Summer 8-15-2015

Dissection of Affective Catecholamine Circuits Using Traditional and Wireless Optogenetics

Jordan Gary McCall
Washington University in St. Louis

Recommended Citation

WASHINGTON UNIVERSITY IN ST. LOUIS

Division of Biology and Biomedical Sciences
Neurosciences

Dissertation Examination Committee:
Michael R. Bruchas, Chair
Joseph D. Dougherty
Robert W. Gereau IV
Erik D. Herzog
Timothy E. Holy

Dissection of Affective Catecholamine Circuits Using Traditional and Wireless Optogenetics
by
Jordan Gary McCall

A dissertation presented to the
Graduate School of Arts & Sciences
of Washington University in
partial fulfillment of the
requirements for the degree
of Doctor of Philosophy

August 2015
St. Louis, Missouri

Table of Contents

Chapter 1 Introduction

Part 1 The development and application of cellular-scale optoelectronic devices for wireless manipulation of intact mammalian neural circuitry

Chapter 2 Injectable, cellular-scale optoelectronics with application for wireless optogenetics

Chapter 3 Fabrication of flexible, multimodal light-emitting devices for wireless optogenetics

Chapter 4 Wireless optofluidic systems for programmable *in vivo* pharmacology and optogenetics

Part 2 Dissecting the role of locus coeruleus circuitry in negative affective behaviors

Chapter 5 CRH engagement of the locus coeruleus noradrenergic system mediates stress-induced anxiety

Chapter 6 Determining the downstream receptor and projection targets that mediate the locus coeruleus-induced negative affective behaviors

Chapter 7 Further discussion and future directions

Appendix 1 Distinct subpopulations of nucleus accumbens dynorphin neurons drive aversion or reward

Appendix 2 Supplementary locus coeruleus experiments

List of Figures and Tables

Chapter 3

Chapter 5

Chapter 6

Chapter 7

Appendix 1

Appendix 2

Acknowledgements

I always thought I would begin my dissertation acknowledgements by saying, "21st century science is a team sport". However, after years of thought and internal debate concerning bowling, golf, and billiards, I cannot in good conscious use this metaphor. Instead I will begin by saying that neuroscience in the 21st century is inherently multidisciplinary and the work presented here would have never happened without good-hearted, dedicated people from many different fields working closely together for many years. What follows next is a diminutive attempt at thanking just some of those who have helped both myself and the science reach places we all previously thought impossible.

At Washington University I will first thank my advisor, Michael Bruchas, PhD, for his steadfast commitment to my work. When Michael and I first met, most of the ideas presented here were seen as dream technology and experiments that we each hoped could one day be achieved. With Michael's unyielding support we made "one day" become reality. One day we will use the neural activity of one mouse on cocaine to wirelessly drive the neural activity of a sober mouse, scientific question be damned.

Next, I would like to thank the members of my committee all of whom have been beyond supportive since the day I arrived in St. Louis. It is my hope that Joseph Dougherty, PhD, Rob

Gereau IV, PhD, Erik Herzog, PhD, and Tim Holy, PhD can all find hallmarks of their advice in these pages and within all of my future works to come. In particular, I would like to thank Erik and Rob for their unending wisdom as both scientists and mentors. The open doors of their offices will continue to open more for countless trainees to come.

Within the Bruchas laboratory I must thank Will Planer for putting up with purchase orders from the most expensive graduate student of all time, or so I suspect. Audra Foshage and Lamley Lawson managed our animal colony with an excellence without which nothing would be in the pages to come. Lamley brings light into every room she enters, another invaluable asset during a graduate career. I thank Adrian Gomez, PhD and Lauren Richmond, PhD for the French press and coffee beans that made writing this dissertation possible. Martin Schmidt, PhD provided boundless conversation about science and life during his time in the lab. If I become Iron Man he can be my War Machine. I thank all of the undergraduate researchers I attempted to mentor: Blessan Sebastian, Dan Hong, and Zach Schools. I hope I prepared you in some way for something and I am eternally grateful for all of the less than glorious work you did in my name. It was a pleasure to work with Mat Araujo, Tayler Sheahan, Skylar Spangler, and Cody Burleson as they rotated through the lab. I thank A-a-ron Norris, MD/PhD for being right when and where I needed him towards the end of my graduate career. There are many years until 40 and I believe the LC and its neighbors will be safe in your hands. Ed Suida [*sic*], PhD is my long lost Polish brother and without him grad school would have been much, much more miserable. Thank you for smoking, Ed.

Elsewhere at Washington University there are many more to thank, but I would like to especially call attention to Sherri Vogt, Judith Golden, PhD, and the rest of the Gereau lab for being great scientific neighbors. Steve Davidson, PhD told the funniest science-related joke I

I am well aware that I am carrying on beyond what many would have the patience to read, but I have saved the most important for last. Despite all of the rich support I receive professionally and academically, none of it compares to my friends and family that would remain if the science were to disappear completely. I am blessed with the love and loyalty of many friends, but the following are those who have been by my side (or rather in my phone) every day of this journey. From the day we met (starting in 1991), these guys have always been the best

and spoken my language completely: Carl Hammarsten (who defends his PhD in Mathematics the same week as I do mine), Matt Connors, Joe Cappa, Trent Pettus, Brett Hickman, Zane Russell, Steve Walther, MD, Alan Strathman, PhD, Seth Stahlheber, Brad Weishar, Sean Diller, JD, Bob Hatley, JD, Marco Cruz Galve, Drew Layton, and Kyle Parker, PhD (who I credit for my return to neuroscience). The Snapchats, texts, emails, phone calls and random weekend visits from these people and their wonderful familial additions make life worth living.

My family, on the other hand, is worth dying for... if that ever becomes necessary. My amazing parents (see Dedication) had the foresight to make five, unique and wonderful offspring. My siblings all bring very different things to the dinner table and as the youngest I have done my best to absorb the best from them all. I thank my sister April for showing me how to put family above all. I thank my sister Wendy for showing me how to fight for what I believe is right. I thank my brother Jonas for leading by quiet example to demonstrate the merits of self-sacrifice. I thank my sister Liza for being my best friend and closest compadre since the day I was born. I love you all and hope I am a decent uncle to all your wonderful children. I also must thank my mother-in-law for worrying about me long before she ever met me.

Finally, I thank my brilliant wife and closest collaborator, Ream Al-Hasani, PhD for making every step of this PhD possible and for being the best thing to ever happen to me. The future, at home and at work, is the brightest thing I see every day.

Jordan McCall

Washington University in St. Louis

August 2015

To my incredible parents, Gary and Tedra McCall,

you deserve all the credit for anything I ever do.

ABSTRACT OF THE DISSERTATION

Dissection of Affective Catecholamine Circuits Using Traditional and Wireless Optogenetics

by

Jordan Gary McCall

Doctor of Philosophy in Biology and Biomedical Sciences

Neurosciences

Washington University in St. Louis, 2015

Professor Michael R. Bruchas, Chair

Parsing the complexity of the mammalian brain has challenged neuroscientists for thousands of years. In the early 21st century, advances in materials science and neuroscience have enabled unprecedented control of neural circuitry. In particular, cell-type selective manipulations, such as those with optogenetics and chemogenetics, routinely provide answers to previously intractable neurobiological questions in the intact, behaving animal.

In this two-part dissertation, I first introduce new minimally invasive, wireless technology to perturb neural activity in the ventral tegmental area dopaminergic system of freely moving animals. I report a series of novel devices for studying and perturbing intact neural systems through optogenetics, microfluidic pharmacology, and electrophysiology. Unlike optogenetic approaches that rely on rigid, glass fiber optics coupled to external light sources, these novel devices utilize flexible substrates to carry microscale, inorganic light emitting diodes (μ-ILEDs), multimodal sensors, and/or microfluidic channels into the brain. Each class of device can be wirelessly controlled, enabling studies in freely behaving mice and achieving previously untenable control of catecholamine neural circuitry.

In the second part of this dissertation, I apply existing cell-type selective approaches to dissect the role of the locus coeruleus noradrenergic (LC-NE) system in anxiety-like and aversive behaviors. The LC-NE system is one of the first systems engaged following a stressful event. While LC-NE neurons are known to be activated by many different stressors, the underlying neural circuitry and the role of this activity in generating stress-induced anxiety has not been elucidated until now. I demonstrate that increased tonic activity of LC-NE neurons is both necessary and sufficient for stress-induced anxiety; a behavior which is driven by LC projections to the basolateral amygdala. Furthermore, this activity and behavior is elicited by corticotropin releasing hormone-containing afferent inputs into the LC from the central amygdala. These studies position the LC-NE system as a critical mediator of acute stress-induced anxiety and offer a potential intervention for preventing stress-related affective disorders.

Together these two objectives provide a rich technological toolbox for neuroscientists and yield important knowledge of how small catecholamine structures with widespread forebrain innervation can selectively mediate higher order behaviors.

Chapter 1

Introduction

INTRODUCTION

The living mammalian brain is a soft, squishy entanglement of millions of different cells. This declarative statement is the impetus for the following work. That single sentence captures two of the greatest challenges faced in neuroscience. The soft nature of the brain limits how we, as scientists trying to understand its functions, can interact with its intact form. The complex arrangement of the cells in the tissue poses incredible hurdles in understanding the anatomical and functional organization of the organ as a whole. These two challenges are not new, neuroscientists and anatomists have been tackling them for thousands of years, but only recently has our mastery of materials and genetics converged to allow increasingly detailed understanding of the soft, squishy entanglement we know as the brain. The following dissertation will introduce new tools for studying the intact circuitry of the living brain and apply a battery of existing techniques towards understanding the role of the locus coeruleus noradrenergic (LC-NE) system in complex negative affective behaviors.

The power of cell-type selective neural manipulations

The complex nature of the brain has long puzzled those who sought to understand its function. As early as 1700 B.C., observations were recorded documenting the observable structure of brain anatomy (Risse, 1972). While these early observations remained as such for many hundreds of years, ever-diligent anatomists slowly began to establish the gross anatomy of the human brain (Arráez-Aybar et al., 2015; Schmitt, 2009). However, the ability to evaluate the function of brain anatomy remained elusive. One of the first major insights into how the nervous system functions came in 1791 when Luigi Galvani discovered that electricity could be used to stimulate nerve fibers in dissected frog legs (Parent, 2004). What is now considered a simple

observation (indeed one regularly taught in undergraduate physiology courses around the world) was at the time a paradigm-shifting discovery: electrical stimulation can be used to exogenously elicit function from neural tissues. Over the next two hundred years, the electrical nature of the central nervous system was exploited to an elegant degree both in understanding the cellular properties of the neuron (Hodgkin and Huxley, 1945) and the functional organization of the cortex (Rasmussen and Penfield, 1947a). In the latter case, very early studies using electrical stimulation gave functional information to the previously established anatomy (Penfield, 1947; Rasmussen and Penfield, 1947a, 1947b). However, the more sophisticated neurochemical and genetic tools became, the more complex the brain appeared to be. So much so that harnessing the power of electricity now seemed too limiting in scope to perturb and observe neuronal function. This limitation arises in large part due to the non-selective nature of exogenously applied current. When a stimulating microelectrode is placed in the brain, the current delivered to the probe agnostically perturbs all of the electrically excitable membranes near it (**Figure 1.1**). These excitable membranes could be neuronal cell bodies, passing axons, axon terminal or dendrites. For gross functional anatomy mapping (i.e. can *x* brain region elicit *y* behavioral response?) and some therapeutic approaches (Clark, 2015; Giugni and Okun, 2014) this approach proved sufficient, however to understand the complex circuitry of the mammalian brain, more selective tools would be necessary.

By the early 21st century, the need for tools that could selectively modulate particular genetically defined neuronal subtypes became clear and numerous groups provided potential answers (Adamantidis et al., 2007; Arenkiel et al., 2007; Armbruster et al., 2007; Banghart et al., 2004; Güler et al., 2012; Lima and Miesenböck, 2005; Zemelman et al., 2002, 2003). Though a complete review of the possible solutions presented is outside the scope of this introduction, it is

important to note that two major solutions emerged from this challenge: one using photons to target exogenously expressed channels, pumps, and receptors (optogenetics) (Yizhar et al., 2011) and one using highly selective ligands to target exogenously expressed channels and receptors (chemogenetics) (Sternson and Roth, 2014). In both such schemes, advances in viral gene delivery enabled, for the first time, cell-type selective targeting of neurons and their projections (Adamantidis et al., 2007; Arenkiel et al., 2007; Krashes et al., 2011). These approaches now enable dynamic control of various types of cellular activity including stimulation (Arenkiel et al., 2007), inhibition (Berndt et al., 2014), modulation (Airan et al., 2009; Siuda et al., 2015), intracellular signaling (Zhang and Cui, 2015) and gene expression (Konermann et al., 2013; Polstein and Gersbach, 2015). Perhaps the most powerful application of these tools is in awake, behaving animals where new fundamental insights into neural function are being made at an extraordinary rate (Tye and Deisseroth, 2012).

The ventral tegmental area dopamine system as a model for progress in neuroscience

In the age of cell-type selective neural manipulations, few brain systems have received as much scientific attention as the ventral tegmental area dopamine (VTA-DA) system (for review see Britt and Bonci, 2013; Ikemoto and Bonci, 2014; Lammel et al., 2014; Nieh et al., 2013; Stamatakis and Stuber, 2012; Tye and Deisseroth, 2012; Walsh and Han, 2014). The VTA-DA system is one of the main sources of dopamine for the forebrain (Björklund and Dunnett, 2007). The VTA-DA system has long been known for its critical role in reward processing (Bozarth and Wise, 1981; Hollerman and Schultz, 1998; Miliaressis and Cardo, 1973; Wise, 1984), but it was not until the rise of optogenetics that the true complexity of this system was revealed. Diverse heterogeneity of cell-types (Tan et al., 2012; Yamaguchi et al., 2015; van Zessen et al., 2012),
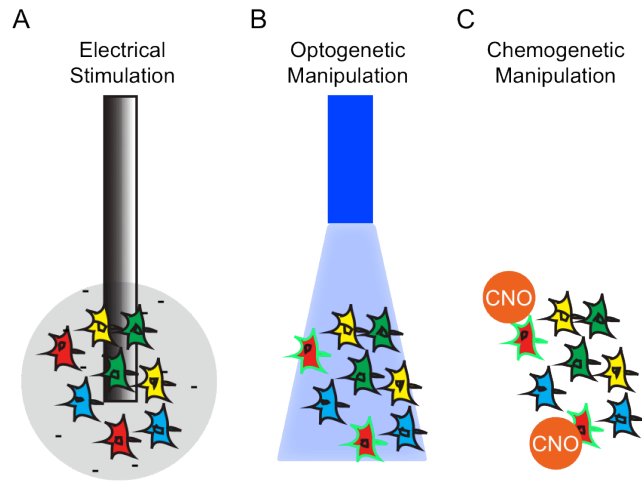
Figure 1.1 Schemes for *in vivo* manipulation of neural circuitry. (**A**) Electrical microstimulation stimulates all cells, terminals, and fibers of passage near the electrode. (**B**) Optogenetics can selectively target genetically-defined cell-types, such as the red cells here. Only cells expressing the opsin (depicted as green outline) will be sensitive to photostimulation. (**C**) Chemogenetics also selectively targets genetically-defined cell-types, but uses a selective ligand (here as CNO), rather than light, to perturb neural activity. **Figure 1.1** layout inspired by (Carter and de Lecea, 2011).

afferent inputs (Lammel et al., 2012; Watabe-Uchida et al., 2012), and efferent projections with non-canonical neurotransmission (Lammel et al., 2011; Root et al., 2014; Stamatakis et al., 2013; Zhang et al., 2015)regulates and contributes to motivation, reward, and emotional regulation with elegant detail.

One of the first studies implementing optogenetics *in vivo* answered a fundamental question about the VTA-DA system (Tsai et al., 2009): how do different phasic or tonic firing patterns contribute to reward-related behaviors? Not only did this study demonstrate that photostimulation could be used to manipulate affective neural circuitry, but it showed that modulation of firing profiles specific cell-types of neurons could be used to drive different behaviors. Several groups have carried on from these findings to clearly define the role of phasic, but not tonic, VTA-DA activity as a neural substrate of reward (Kim et al., 2012b; Lammel et al., 2011; Tan et al., 2012; Witten et al., 2011; van Zessen et al., 2012).

The rich literature of the VTA-DA system provides a model for this two-part dissertation. First, we will utilize our existing knowledge of the VTA-DA system as a testing ground for new technology. The implementation of new technology that interfaces with neural tissue must functionally demonstrate that it can achieve results consistent with what is understood about the brain. Ideally new neural interface technologies will also expand our knowledge of neural function. In **Part 1** of this dissertation, I report a series of novel devices for studying and perturbing intact neural systems through optogenetics, microfluidic pharmacology, and electrophysiology. This technology will be demonstrated with proof-of-principle experiments in the VTA-DA system.

Though the VTA-DA system has been well characterized with modern tools, the same cannot be said for other major monoamine structures such as the dorsal raphe (5-hydroxytryptamine/serotonin) or locus coeruleus (norepinephrine). Recent work has begun to unravel the circuit-level details of the dorsal raphe serotonergic system in motivation and affective procressing (Bruchas et al., 2011; Cohen et al., 2015; McDevitt et al., 2014; Miyazaki et al., 2014; Ogawa et al., 2014; Qi et al., 2014), but very limited work has focused modern tools on the role of locus coeruleus noradrenergic (LC-NE) system (Carter et al., 2010, 2012; Hickey et al., 2014; Vazey and Aston-Jones, 2014) and no so far in these such behaviors. **Part 2** of this dissertation will focus on understanding the role of tonic activity of the LC-NE system in the mediation of stress-induced and stress-related behaviors such as anxiety-like and aversive behaviors. The experimental approaches used by the VTA-DA field will provide a template for how to proceed in dissecting this important catecholamine brain system.

Motivation for the development of flexible, wireless devices for manipulation of intact mammalian neural circuitry

Though much progress can and has been made with traditional approaches to optogenetics (i.e. fiber optics implanted directly into the brain), there remain limitations to the implementation of these approaches in freely behaving animals. An immediate concern is that light delivery with traditional fiber optic approaches requires the animal to be tethered to an external laser or LED light source (Zhang et al., 2010). While this limitation does not prevent study in awake, behaving animals it does limit the scope and type of behaviors one can assess. Interrogation of endogenous neural function is best done in the context of natural behaviors. Any handling or tethering of mice disrupts their natural behavior (Sorge et al., 2014), an observation that can be clearly made from any actogram of behavior following a cage change (Aton et al.,

2005). Furthermore, any obstrusive headstage or cabling would more than likely cause a significant confound in the study of social behavior (Shah et al., 2013). Therefore a conscious effort should be made towards reducing both experimenter and technical interference during the study of animal behavior. To achieve this goal wireless systems present a promising alternative to tethered designs. Wireless observation of neural activity has been achieved by a number of groups (Bertrand, 2015; Harrison et al., 2010; Szuts et al., 2011; Yin et al., 2014), but at the outset of the work presented here no one had yet achieved wireless photostimulation.

Another crucial limitation of traditional fiber optic implants is in controlling the path of light. While there now exist a few options for guiding light at different angles and points along the dorsal-ventral axis of a brain structure (Tye et al., 2011; Zorzos et al., 2010, 2012), basic fiber implants can only deliver light dorsal to the brain structure of interest. This can be problematic when a brain structure is oriented vertically in the dorsal-ventral plane of the brain (i.e. the locus coeruleus) as illuminating the entire structure would either require implanting deeper or increasing the power of the light source. Both of these solutions can cause excess damage to tissue (Yizhar et al., 2011). Therefore developing implantable light sources that can approach brain structures from multiple and unique angles can greatly empower functional dissection of the intact living brain.

The need in the neuroscience community for untethered devices with modular angles of light delivery comes at time when the materials science community has begun to solve many of these issues. Wirelessly powered devices traditionally rely on battery-powered operation, however, batteries traditionally pose two immediate challenges to integration into electronics for small mammals: 1) the batteries must be changed and 2) the batteries add weight to whatever device the animal is required to support. In answer to these challenges, electrical engineers have

8

devised power harvesting strategies that convert ambient energy into usable electrical energy (Anton and Sodano, 2007). While these strategies are often seen as alternative renewable energy sources, the same approach can be used with purposefully broadcasted radiofrequency (RF) signals used to increase the ambient RF energy available for scavenging (Anton and Sodano, 2007; Olgun et al., 2010; Sample and Smith, 2009). This strategy is one that we employ in **Chapter 2 & 3** to create fully untethered devices for wireless photostimulation. These battery-free devices can be powered in most environments without the need to contact the animal.

A second key advance in materials science has been the development of micro-scale light-emitting diodes (μ-ILEDs) (Kim et al., 2010, 2012c). These light sources are small enough that they can readily be transferred to flexible materials (Kim et al., 2012a) which provide ideal material properties for interfacing with biological tissue. μ-ILED technology presents as an excellent solution for spatial targeting in optogenetics. μ-ILEDs can be made that are on the size scale of a few individual cell bodies (as small as $625 \ \mu m^2$) (Kim et al., 2012c) and while the light from these devices spreads further than a single cell, localized activation within a brain structure is an attainable goal. Importantly, μ-ILEDs are extremely efficient (i.e. they convert electrical energy into light without losing too much energy to heating) which is critical for implanting electronics into neural tissue. **Chapter 2** details experiments and modeling (the latter done by collaborators) to ensure that these implanted light sources do not deleteriously heat the tissue. Finally, because of the flexible nature of the fabrication of these μ-ILEDs, they can be implanted on ultrathin substrates that cause substantially less damage to the soft tissue of the brain than conventional implants.

The devices introduced in **Chapters 2 & 3** serve as first generation prototypes of technology that can be used to observed physiology (electrical, optical, and thermal properties) or wirelessly perturb physiology (electrical or optical). These devices lack, however, an interface for delivery of fluids such as viral vectors, therapeutic drugs, or other pharmacological agents. **Chapter 4** presents a new generation of device that maintains the ability to wirelessly photostimulate, but adds fluid delivery capabilities. These optofluidic neural probes represent one of many different possible second generation wireless μ-ILED devices and will serve as a powerful tool for further dissection of neural circuitry.

Motivation for understanding the role of the LC-NE system in negative affective behavior

Anxiety is the manifestation of a complex set of behavioral and physiological responses that can be either beneficial or detrimental to an individual. Under a state of stress and fear, anxiety helps to maintain the arousal and vigilance required to maintain attention and accomplish necessary tasks. After prolonged stress, however, anxiety can become pathological, interfering with an individual's ability to function normally (Gross and Hen, 2004). This neuropsychiatric form of anxiety affects nearly 20% of the U.S. population during their lifetime and leads to significant economic impacts, including loss of productivity and increased health care costs. **Part 2** of this dissertation seeks to establish a greater understanding of the neurobiological basis of anxiety and stress-induced behavioral disorders.

Norepinephrine, stress, and anxiety

The LC-NE system is a small, tightly packed pontine brain region that sends numerous projections to the forebrain and spinal cord. This system is involved in a broad number of physiological functions including arousal, memory, cognition, and stress reactivity (Berridge and Waterhouse, 2003; Snyder et al., 2012; Valentino and Van Bockstaele, 2008). NE acts at

postsynaptic (G_s-coupled β and G_q-coupled α_1) and presynaptic (G_i-coupled α_2) adrenergic receptors throughout the forebrain (**Figure 1.2**) (Berridge and Waterhouse, 2003). The LC-NE system is known to increase activity in response to a wide array of environmental stressors including social and predator stress (Berridge and Waterhouse, 2003; Bingham et al., 2011; Cassens et al., 1981; Curtis et al., 2012; Francis et al., 1999; Snyder et al., 2012; Valentino and Van Bockstaele, 2008). The response of the LC-NE system to stress is particularly important in the context of stress-induced human neuropsychiatric disorders such as posttraumatic stress disorder (PTSD). Noradrenergic neurons within the LC-NE system exhibit three distinct activation profiles: low tonic, high tonic, and phasic activity. It is believed that these neurons function differently in determining behavioral flexibility to various environmental challenges. Low tonic LC discharge (1-2 Hz) is thought to be consistent with an awake state (Aston-Jones and Bloom, 1981a; Carter et al., 2010, 2012), whereas phasic burst activity results from distinct sensory stimuli (Aston-Jones and Bloom, 1981b). Stress and stress-related neuropeptide release (such as corticotrophin-releasing hormone, CRH) is thought to shift LC activity towards a high tonic mode of firing (3-8 Hz) while simultaneously decreasing phasic firing events, whereas endogenous opioid transmission is thought to return tonic firing to baseline (Curtis et al., 2012; Snyder et al., 2012; Valentino and Foote, 1988). Taking a cue from the VTA-DA system, the first study into LC-NE function in affective behaviors will examine different activity profiles of these neurons (Tsai et al., 2009). **Chapter 5** will focus on examining the effects stress-induced and optogenetically-evoked high tonic activity of LC-NE neurons.

Amygdala-LC circuitry and the modulation of stress-induced anxiety-like behavior

There is some evidence that neuropeptidergic inputs to the LC from the central nucleus of the amygdala (CeA), including those containing CRH, may become activated in response to

11

stressors (**Figure 1.2**) (Curtis et al., 2012; Francis et al., 1999; Valentino et al., 1992). Recent anatomical data further support this notion using tract tracing studies and electron microscopy to confirm that CRH containing amydalar monosynaptic projections from the CeA terminate in the LC (Valentino et al., 1992). Given the importance of CRH in stress-induced behavioral responses these projections are situated to significantly impact LC neuronal activity, yet their functional consequences remain unresolved. Engagement of the CRH system has been implicated in stress-induced depression, anxiety, and negative affective responses including dysphoria (Bruchas et al., 2009). Taken together, the prior body of work strongly implicates CeA-LC neural circuit activation in mediating the stress response of the LC-NE system, emphasizing the need for continued dissection of these circuits and systems. The second half of **Chapter 5** focuses on CRH-containing afferent inputs to the LC from the CeA. These studies demonstrate that CRH neurotransmission increases tonic LC-NE activity and drives anxiety-like and aversive behaviors.

Downstream effectors of LC-mediated negative affective behaviors

The LC-NE system has rich and complex combination of receptor and anatomical projection targets. There are at least nine different adrenergic receptors and most have had some implication in anxiety-like behaviors (Brunner et al., 2014; Dixit et al., 2014; Hanke et al., 2012; Kuteeva et al., 2008; Le Maître et al., 2013; Mantsch et al., 2010; Raskind et al., 2007; Wohleb et al., 2011). Furthermore, the LC has a widespread projection network throughout the mammalian forebrain and spinal cord (Berridge and Waterhouse, 2003; Sara, 2009). Of particular interest are the dense projections to the basolateral amygdala, a critical structure in
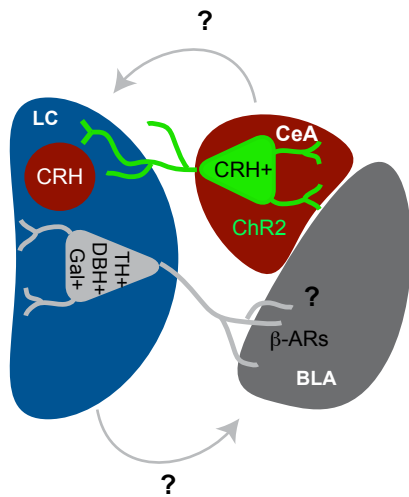
Figure 1.2 Simplified, putative LC-NE system involved in negative affective behaviors. The diagram illustrates CeA neurons terminating in the LC to release CRH and drive increased tonic LC-NE firing causing release of NE into the BLA to drive possibly drive anxiety-like behaviors.

generating negative affect (Berridge and Waterhouse, 2003; Davis, 1992; Valentino and Aston-Jones, 2010). While the anatomical projections from the LC and their cell types have beenstudied for several years, the precise mechanisms by which the LC generates its influence over basolateral amygdala (BLA) function remain undefined. **Chapter 6** will focus on how the LC-BLA projection induces affective behavioral responses via specific receptor systems and cell activity. Understanding the next substrates beyond LC activity will be important for a clear comprehension of how this system produces certain behaviors.

Together, **Part 1** and **Part 2** provide a novel series neural interfacing devices for neuroscientists and off important insight of how small, widely projecting catecholamine structures selectively mediate affective behaviors.

REFERENCES

Adamantidis, A.R., Zhang, F., Aravanis, A.M., Deisseroth, K., and de Lecea, L. (2007). Neural substrates of awakening probed with optogenetic control of hypocretin neurons. Nature *450*, 420–424.

Airan, R.D., Thompson, K.R., Fenno, L.E., Bernstein, H., and Deisseroth, K. (2009). Temporally precise in vivo control of intracellular signalling. Nature *458*, 1025–1029.

Anton, S.R., and Sodano, H.A. (2007). A review of power harvesting using piezoelectric materials (2003–2006). Smart Mater. Struct. *16*, R1.

Arenkiel, B.R., Peca, J., Davison, I.G., Feliciano, C., Deisseroth, K., Augustine, G.J., Ehlers, M.D., and Feng, G. (2007). In vivo light-induced activation of neural circuitry in transgenic mice expressing channelrhodopsin-2. Neuron *54*, 205–218.

Armbruster, B.N., Li, X., Pausch, M.H., Herlitze, S., and Roth, B.L. (2007). Evolving the lock to fit the key to create a family of G protein-coupled receptors potently activated by an inert ligand. Proc. Natl. Acad. Sci. U. S. A. *104*, 5163–5168.

Arráez-Aybar, L.-A., Navia-Álvarez, P., Fuentes-Redondo, T., and Bueno-López, J.-L. (2015). Thomas Willis, a pioneer in translational research in anatomy (on the 350th anniversary of Cerebri anatome). J. Anat. *226*, 289–300.

Aston-Jones, G., and Bloom, F.E. (1981a). Activity of norepinephrine-containing locus coeruleus neurons in behaving rats anticipates fluctuations in the sleep-waking cycle. J. Neurosci. Off. J. Soc. Neurosci. *1*, 876–886.

Aston-Jones, G., and Bloom, F.E. (1981b). Norepinephrine-containing locus coeruleus neurons in behaving rats exhibit pronounced responses to non-noxious environmental stimuli. J. Neurosci. Off. J. Soc. Neurosci. *1*, 887–900.

Aton, S.J., Colwell, C.S., Harmar, A.J., Waschek, J., and Herzog, E.D. (2005). Vasoactive intestinal polypeptide mediates circadian rhythmicity and synchrony in mammalian clock neurons. Nat. Neurosci. *8*, 476–483.

Banghart, M., Borges, K., Isacoff, E., Trauner, D., and Kramer, R.H. (2004). Light-activated ion channels for remote control of neuronal firing. Nat. Neurosci. *7*, 1381–1386.

Berndt, A., Lee, S.Y., Ramakrishnan, C., and Deisseroth, K. (2014). Structure-guided transformation of channelrhodopsin into a light-activated chloride channel. Science *344*, 420–424.

Berridge, C.W., and Waterhouse, B.D. (2003). The locus coeruleus-noradrenergic system: modulation of behavioral state and state-dependent cognitive processes. Brain Res. Brain Res. Rev. *42*, 33–84.

Bertrand, A. (2015). Distributed signal processing for wireless EEG sensor networks. IEEE Trans. Neural Syst. Rehabil. Eng. Publ. IEEE Eng. Med. Biol. Soc.

Bingham, B., McFadden, K., Zhang, X., Bhatnagar, S., Beck, S., and Valentino, R. (2011). Early adolescence as a critical window during which social stress distinctly alters behavior and brain norepinephrine activity. Neuropsychopharmacol. Off. Publ. Am. Coll. Neuropsychopharmacol. *36*, 896–909.

Björklund, A., and Dunnett, S.B. (2007). Dopamine neuron systems in the brain: an update. Trends Neurosci. *30*, 194–202.

Bozarth, M.A., and Wise, R.A. (1981). Intracranial self-administration of morphine into the ventral tegmental area in rats. Life Sci. *28*, 551–555.

Britt, J.P., and Bonci, A. (2013). Optogenetic interrogations of the neural circuits underlying addiction. Curr. Opin. Neurobiol. *23*, 539–545.

Bruchas, M.R., Land, B.B., Lemos, J.C., and Chavkin, C. (2009). CRF1-R activation of the dynorphin/kappa opioid system in the mouse basolateral amygdala mediates anxiety-like behavior. PloS One *4*, e8528.

Bruchas, M.R., Schindler, A.G., Shankar, H., Messinger, D.I., Miyatake, M., Land, B.B., Lemos, J.C., Hagan, C.E., Neumaier, J.F., Quintana, A., et al. (2011). Selective p38α MAPK deletion in serotonergic neurons produces stress resilience in models of depression and addiction. Neuron *71*, 498–511.

Brunner, S.M., Farzi, A., Locker, F., Holub, B.S., Drexel, M., Reichmann, F., Lang, A.A., Mayr, J.A., Vilches, J.J., Navarro, X., et al. (2014). GAL3 receptor KO mice exhibit an anxiety-like phenotype. Proc. Natl. Acad. Sci. U. S. A. *111*, 7138–7143.

Carter, M.E., and de Lecea, L. (2011). Optogenetic investigation of neural circuits in vivo. Trends Mol. Med. *17*, 197–206.

Carter, M.E., Yizhar, O., Chikahisa, S., Nguyen, H., Adamantidis, A., Nishino, S., Deisseroth, K., and de Lecea, L. (2010). Tuning arousal with optogenetic modulation of locus coeruleus neurons. Nat. Neurosci. *13*, 1526–1533.

Carter, M.E., Brill, J., Bonnavion, P., Huguenard, J.R., Huerta, R., and de Lecea, L. (2012). Mechanism for Hypocretin-mediated sleep-to-wake transitions. Proc. Natl. Acad. Sci. U. S. A. *109*, E2635–E2644.

Cassens, G., Kuruc, A., Roffman, M., Orsulak, P.J., and Schildkraut, J.J. (1981). Alterations in brain norepinephrine metabolism and behavior induced by environmental stimuli previously paired with inescapable shock. Behav. Brain Res. *2*, 387–407.

Clark, G.M. (2015). The multi-channel cochlear implant: Multi-disciplinary development of electrical stimulation of the cochlea and the resulting clinical benefit. Hear. Res. *322*, 4–13.

Cohen, J.Y., Amoroso, M.W., and Uchida, N. (2015). Serotonergic neurons signal reward and punishment on multiple timescales. eLife *4*.

Curtis, A.L., Leiser, S.C., Snyder, K., and Valentino, R.J. (2012). Predator stress engages corticotropin-releasing factor and opioid systems to alter the operating mode of locus coeruleus norepinephrine neurons. Neuropharmacology *62*, 1737–1745.

Davis, M. (1992). The role of the amygdala in fear and anxiety. Annu. Rev. Neurosci. *15*, 353–375.

Dixit, M.P., Thakre, P.P., Pannase, A.S., Aglawe, M.M., Taksande, B.G., and Kotagale, N.R. (2014). Imidazoline binding sites mediates anticompulsive-like effect of agmatine in marble-burying behavior in mice. Eur. J. Pharmacol. *732*, 26–31.

Francis, D.D., Caldji, C., Champagne, F., Plotsky, P.M., and Meaney, M.J. (1999). The role of corticotropin-releasing factor–norepinephrine systems in mediating the effects of early experience on the development of behavioral and endocrine responses to stress. Biol. Psychiatry *46*, 1153–1166.

Giugni, J.C., and Okun, M.S. (2014). Treatment of advanced Parkinson's disease. Curr. Opin. Neurol. *27*, 450–460.

Gross, C., and Hen, R. (2004). The developmental origins of anxiety. Nat. Rev. Neurosci. *5*, 545–552.

Güler, A.D., Rainwater, A., Parker, J.G., Jones, G.L., Argilli, E., Arenkiel, B.R., Ehlers, M.D., Bonci, A., Zweifel, L.S., and Palmiter, R.D. (2012). Transient activation of specific neurons in mice by selective expression of the capsaicin receptor. Nat. Commun. *3*, 746.

Hanke, M.L., Powell, N.D., Stiner, L.M., Bailey, M.T., and Sheridan, J.F. (2012). Beta adrenergic blockade decreases the immunomodulatory effects of social disruption stress. Brain. Behav. Immun. *26*, 1150–1159.

Harrison, R.R., Kier, R.J., Leonardo, A., Fotowat, H., Chan, R., and Gabbiani, F. (2010). A wireless neural/EMG telemetry system for freely moving insects. In Circuits and Systems (ISCAS), Proceedings of 2010 IEEE International Symposium on, pp. 2940–2943.

Hickey, L., Li, Y., Fyson, S.J., Watson, T.C., Perrins, R., Hewinson, J., Teschemacher, A.G., Furue, H., Lumb, B.M., and Pickering, A.E. (2014). Optoactivation of locus ceruleus neurons evokes bidirectional changes in thermal nociception in rats. J. Neurosci. Off. J. Soc. Neurosci. *34*, 4148–4160.

Hodgkin, A.L., and Huxley, A.F. (1945). Resting and action potentials in single nerve fibres. J. Physiol. *104*, 176–195.

Hollerman, J.R., and Schultz, W. (1998). Dopamine neurons report an error in the temporal prediction of reward during learning. Nat. Neurosci. *1*, 304–309.

Ikemoto, S., and Bonci, A. (2014). Neurocircuitry of drug reward. Neuropharmacology *76 Pt B*, 329–341.

Kim, D.-H., Ghaffari, R., Lu, N., and Rogers, J.A. (2012a). Flexible and Stretchable Electronics for Biointegrated Devices. Annu. Rev. Biomed. Eng. *14*, 113–128.

Kim, K.M., Baratta, M.V., Yang, A., Lee, D., Boyden, E.S., and Fiorillo, C.D. (2012b). Optogenetic Mimicry of the Transient Activation of Dopamine Neurons by Natural Reward Is Sufficient for Operant Reinforcement. PLoS ONE *7*, e33612.

Kim, R.-H., Kim, D.-H., Xiao, J., Kim, B.H., Park, S.-I., Panilaitis, B., Ghaffari, R., Yao, J., Li, M., Liu, Z., et al. (2010). Waterproof AlInGaP optoelectronics on stretchable substrates with applications in biomedicine and robotics. Nat. Mater. *9*, 929–937.

Kim, T., Jung, Y.H., Song, J., Kim, D., Li, Y., Kim, H., Song, I.-S., Wierer, J.J., Pao, H.A., Huang, Y., et al. (2012c). High-Efficiency, Microscale GaN Light-Emitting Diodes and Their Thermal Properties on Unusual Substrates. Small *8*, 1643–1649.

Konermann, S., Brigham, M.D., Trevino, A.E., Hsu, P.D., Heidenreich, M., Cong, L., Platt, R.J., Scott, D.A., Church, G.M., and Zhang, F. (2013). Optical control of mammalian endogenous transcription and epigenetic states. Nature *500*, 472–476.

Krashes, M.J., Koda, S., Ye, C., Rogan, S.C., Adams, A.C., Cusher, D.S., Maratos-Flier, E., Roth, B.L., and Lowell, B.B. (2011). Rapid, reversible activation of AgRP neurons drives feeding behavior in mice. J. Clin. Invest. *121*, 1424–1428.

Kuteeva, E., Wardi, T., Lundström, L., Sollenberg, U., Langel, U., Hökfelt, T., and Ogren, S.O. (2008). Differential role of galanin receptors in the regulation of depression-like behavior and monoamine/stress-related genes at the cell body level. Neuropsychopharmacol. Off. Publ. Am. Coll. Neuropsychopharmacol. *33*, 2573–2585.

Lammel, S., Ion, D.I., Roeper, J., and Malenka, R.C. (2011). Projection-Specific Modulation of Dopamine Neuron Synapses by Aversive and Rewarding Stimuli. Neuron *70*, 855–862.

Lammel, S., Lim, B.K., Ran, C., Huang, K.W., Betley, M.J., Tye, K.M., Deisseroth, K., and Malenka, R.C. (2012). Input-specific control of reward and aversion in the ventral tegmental area. Nature *491*, 212–217.

Lammel, S., Tye, K.M., and Warden, M.R. (2014). Progress in understanding mood disorders: optogenetic dissection of neural circuits. Genes Brain Behav. *13*, 38–51.

Lima, S.Q., and Miesenböck, G. (2005). Remote control of behavior through genetically targeted photostimulation of neurons. Cell *121*, 141–152.

Le Maître, E., Barde, S.S., Palkovits, M., Diaz-Heijtz, R., and Hökfelt, T.G.M. (2013). Distinct features of neurotransmitter systems in the human brain with focus on the galanin system in locus coeruleus and dorsal raphe. Proc. Natl. Acad. Sci. U. S. A. *110*, E536–E545.

Mantsch, J.R., Weyer, A., Vranjkovic, O., Beyer, C.E., Baker, D. a, and Caretta, H. (2010). Involvement of Noradrenergic Neurotransmission in the Stress- but not Cocaine-Induced Reinstatement of Extinguished Cocaine-Induced Conditioned Place Preference in Mice: Role for beta-2 Adrenergic Receptors. Neuropsychopharmacol. Off. Publ. Am. Coll. Neuropsychopharmacol. *35*, 2165–2178.

McDevitt, R.A., Tiran-Cappello, A., Shen, H., Balderas, I., Britt, J.P., Marino, R.A.M., Chung, S.L., Richie, C.T., Harvey, B.K., and Bonci, A. (2014). Serotonergic versus nonserotonergic dorsal raphe projection neurons: differential participation in reward circuitry. Cell Rep. *8*, 1857–1869.

Miliaressis, E., and Cardo, B. (1973). Self-stimulation versus food reinforcement: comparative study of two different nervous structures, the lateral hypothalamus and the ventral tegmental area of the mesencephalon. Brain Res. *57*, 75–83.

Miyazaki, K.W., Miyazaki, K., Tanaka, K.F., Yamanaka, A., Takahashi, A., Tabuchi, S., and Doya, K. (2014). Optogenetic activation of dorsal raphe serotonin neurons enhances patience for future rewards. Curr. Biol. CB *24*, 2033–2040.

Nieh, E.H., Kim, S.-Y., Namburi, P., and Tye, K.M. (2013). Optogenetic dissection of neural circuits underlying emotional valence and motivated behaviors. Brain Res. *1511*, 73–92.

Ogawa, S.K., Cohen, J.Y., Hwang, D., Uchida, N., and Watabe-Uchida, M. (2014). Organization of monosynaptic inputs to the serotonin and dopamine neuromodulatory systems. Cell Rep. *8*, 1105–1118.

Olgun, U., Chen, C.-C., and Volakis, J.L. (2010). Wireless power harvesting with planar rectennas for 2.45 GHz RFIDs. In 2010 URSI International Symposium on Electromagnetic Theory (EMTS), pp. 329–331.

Parent, A. (2004). Giovanni Aldini: from animal electricity to human brain stimulation. Can. J. Neurol. Sci. J. Can. Sci. Neurol. *31*, 576–584.

Penfield, W. (1947). Some observations on the cerebral cortex of man. Proc. R. Soc. Lond. B Biol. Sci. *134*, 329–347.

Polstein, L.R., and Gersbach, C.A. (2015). A light-inducible CRISPR-Cas9 system for control of endogenous gene activation. Nat. Chem. Biol. *11*, 198–200.

Qi, J., Zhang, S., Wang, H.-L., Wang, H., de Jesus Aceves Buendia, J., Hoffman, A.F., Lupica, C.R., Seal, R.P., and Morales, M. (2014). A glutamatergic reward input from the dorsal raphe to ventral tegmental area dopamine neurons. Nat. Commun. *5*, 5390.

Raskind, M.A., Peskind, E.R., Hoff, D.J., Hart, K.L., Holmes, H.A., Warren, D., Shofer, J., O'Connell, J., Taylor, F., Gross, C., et al. (2007). A parallel group placebo controlled study of prazosin for trauma nightmares and sleep disturbance in combat veterans with post-traumatic stress disorder. Biol. Psychiatry *61*, 928–934.

Rasmussen, T., and Penfield, W. (1947a). The human sensorimotor cortex as studied by electrical stimulation. Fed. Proc. *6*, 184.

Rasmussen, T., and Penfield, W. (1947b). Further studies of the sensory and motor cerebral cortex of man. Fed. Proc. *6*, 452–460.

Risse, G.B. (1972). Rational Egyptian surgery: a cranial injury discussed in the Edwin Smith Papyrus. Bull. N. Y. Acad. Med. *48*, 912–919.

Root, D.H., Mejias-Aponte, C.A., Qi, J., and Morales, M. (2014). Role of glutamatergic projections from ventral tegmental area to lateral habenula in aversive conditioning. J. Neurosci. Off. J. Soc. Neurosci. *34*, 13906–13910.

Sample, A., and Smith, J.R. (2009). Experimental results with two wireless power transfer systems. In IEEE Radio and Wireless Symposium, 2009. RWS '09, pp. 16–18.

Sara, S.J. (2009). The locus coeruleus and noradrenergic modulation of cognition. Nat. Rev. Neurosci. *10*, 211–223.

Schmitt, S. (2009). From physiology to classification: comparative anatomy and Vicq d'Azyr's plan of reform for life sciences and medicine (1774-1794). Sci. Context *22*, 145–193.

Shah, C.R., Forsberg, C.G., Kang, J.-Q., and Veenstra-VanderWeele, J. (2013). Letting a typical mouse judge whether mouse social interactions are atypical. Autism Res. Off. J. Int. Soc. Autism Res. *6*, 212–220.

Snyder, K., Wang, W.-W., Han, R., McFadden, K., and Valentino, R.J. (2012). Corticotropin-releasing factor in the norepinephrine nucleus, locus coeruleus, facilitates behavioral flexibility. Neuropsychopharmacol. Off. Publ. Am. Coll. Neuropsychopharmacol. *37*, 520–530.

Sorge, R.E., Martin, L.J., Isbester, K.A., Sotocinal, S.G., Rosen, S., Tuttle, A.H., Wieskopf, J.S., Acland, E.L., Dokova, A., Kadoura, B., et al. (2014). Olfactory exposure to males, including men, causes stress and related analgesia in rodents. Nat. Methods *11*, 629–632.

Stamatakis, A.M., and Stuber, G.D. (2012). Optogenetic strategies to dissect the neural circuits that underlie reward and addiction. Cold Spring Harb. Perspect. Med. *2*.

Stamatakis, A.M., Jennings, J.H., Ung, R.L., Blair, G.A., Weinberg, R.J., Neve, R.L., Boyce, F., Mattis, J., Ramakrishnan, C., Deisseroth, K., et al. (2013). A unique population of ventral tegmental area neurons inhibits the lateral habenula to promote reward. Neuron *80*, 1039–1053.

Sternson, S.M., and Roth, B.L. (2014). Chemogenetic Tools to Interrogate Brain Functions. Annu. Rev. Neurosci. *37*, 387–407.

Szuts, T.A., Fadeyev, V., Kachiguine, S., Sher, A., Grivich, M.V., Agrochão, M., Hottowy, P., Dabrowski, W., Lubenov, E.V., Siapas, A.G., et al. (2011). A wireless multi-channel neural amplifier for freely moving animals. Nat. Neurosci. *14*, 263–269.

Tan, K.R., Yvon, C., Turiault, M., Mirzabekov, J.J., Doehner, J., Labouèbe, G., Deisseroth, K., Tye, K.M., and Lüscher, C. (2012). GABA neurons of the VTA drive conditioned place aversion. Neuron *73*, 1173–1183.

Tsai, H.-C., Zhang, F., Adamantidis, A., Stuber, G.D., Bonci, A., de Lecea, L., and Deisseroth, K. (2009). Phasic firing in dopaminergic neurons is sufficient for behavioral conditioning. Science *324*, 1080–1084.

Tye, K.M., and Deisseroth, K. (2012). Optogenetic investigation of neural circuits underlying brain disease in animal models. Nat. Rev. Neurosci. *13*, 251–266.

Tye, K.M., Prakash, R., Kim, S.-Y., Fenno, L.E., Grosenick, L., Zarabi, H., Thompson, K.R., Gradinaru, V., Ramakrishnan, C., and Deisseroth, K. (2011). Amygdala circuitry mediating reversible and bidirectional control of anxiety. Nature *471*, 358–362.

Valentino, R., and Aston-Jones, G. (2010). Special issue on neuropeptides in stress and addiction: Overview. Brain Res. *1314*, 1–2.

Valentino, R.J., and Van Bockstaele, E. (2008). Convergent regulation of locus coeruleus activity as an adaptive response to stress. Eur. J. Pharmacol. *583*, 194–203.

Valentino, R.J., and Foote, S.L. (1988). Corticotropin-releasing hormone increases tonic but not sensory-evoked activity of noradrenergic locus coeruleus neurons in unanesthetized rats. J. Neurosci. Off. J. Soc. Neurosci. *8*, 1016–1025.

Valentino, R.J., Page, M., Van Bockstaele, E., and Aston-Jones, G. (1992). Corticotropin-releasing factor innervation of the locus coeruleus region: distribution of fibers and sources of input. Neuroscience *48*, 689–705.

Vazey, E.M., and Aston-Jones, G. (2014). Designer receptor manipulations reveal a role of the locus coeruleus noradrenergic system in isoflurane general anesthesia. Proc. Natl. Acad. Sci. *111*, 3859–3864.

Walsh, J.J., and Han, M.H. (2014). The heterogeneity of ventral tegmental area neurons: Projection functions in a mood-related context. Neuroscience *282C*, 101–108.

Watabe-Uchida, M., Zhu, L., Ogawa, S.K., Vamanrao, A., and Uchida, N. (2012). Whole-Brain Mapping of Direct Inputs to Midbrain Dopamine Neurons. Neuron *74*, 858–873.

Wise, R.A. (1984). Neural mechanisms of the reinforcing action of cocaine. NIDA Res. Monogr. *50*, 15–33.

Witten, I.B., Steinberg, E.E., Lee, S.Y., Davidson, T.J., Zalocusky, K.A., Brodsky, M., Yizhar, O., Cho, S.L., Gong, S., Ramakrishnan, C., et al. (2011). Recombinase-driver rat lines: tools, techniques, and optogenetic application to dopamine-mediated reinforcement. Neuron *72*, 721–733.

Wohleb, E.S., Hanke, M.L., Corona, A.W., Powell, N.D., Stiner, L.M., Bailey, M.T., Nelson, R.J., Godbout, J.P., and Sheridan, J.F. (2011). β-Adrenergic receptor antagonism prevents

anxiety-like behavior and microglial reactivity induced by repeated social defeat. J. Neurosci. Off. J. Soc. Neurosci. *31*, 6277–6288.

Yamaguchi, T., Qi, J., Wang, H.-L., Zhang, S., and Morales, M. (2015). Glutamatergic and dopaminergic neurons in the mouse ventral tegmental area. Eur. J. Neurosci. *41*, 760–772.

Yin, M., Borton, D.A., Komar, J., Agha, N., Lu, Y., Li, H., Laurens, J., Lang, Y., Li, Q., Bull, C., et al. (2014). Wireless Neurosensor for Full-Spectrum Electrophysiology Recordings during Free Behavior. Neuron *84*, 1170–1182.

Yizhar, O., Fenno, L.E., Davidson, T.J., Mogri, M., and Deisseroth, K. (2011). Optogenetics in Neural Systems. Neuron *71*, 9–34.

Zemelman, B.V., Lee, G.A., Ng, M., and Miesenböck, G. (2002). Selective photostimulation of genetically chARGed neurons. Neuron *33*, 15–22.

Zemelman, B.V., Nesnas, N., Lee, G.A., and Miesenbock, G. (2003). Photochemical gating of heterologous ion channels: remote control over genetically designated populations of neurons. Proc. Natl. Acad. Sci. U. S. A. *100*, 1352–1357.

Van Zessen, R., Phillips, J.L., Budygin, E.A., and Stuber, G.D. (2012). Activation of VTA GABA neurons disrupts reward consumption. Neuron *73*, 1184–1194.

Zhang, K., and Cui, B. (2015). Optogenetic control of intracellular signaling pathways. Trends Biotechnol. *33*, 92–100.

Zhang, F., Gradinaru, V., Adamantidis, A.R., Durand, R., Airan, R.D., de Lecea, L., and Deisseroth, K. (2010). Optogenetic interrogation of neural circuits: technology for probing mammalian brain structures. Nat. Protoc. *5*, 439–456.

Zhang, S., Qi, J., Li, X., Wang, H.-L., Britt, J.P., Hoffman, A.F., Bonci, A., Lupica, C.R., and Morales, M. (2015). Dopaminergic and glutamatergic microdomains in a subset of rodent mesoaccumbens axons. Nat. Neurosci. *18*, 386–392.

Zorzos, A.N., Boyden, E.S., and Fonstad, C.G. (2010). Multiwaveguide implantable probe for light delivery to sets of distributed brain targets. Opt. Lett. *35*, 4133–4135.

Zorzos, A.N., Scholvin, J., Boyden, E.S., and Fonstad, C.G. (2012). Three-dimensional multiwaveguide probe array for light delivery to distributed brain circuits. Opt. Lett. *37*, 4841–4843.

Part 1

The development and application of cellular-scale optoelectronic devices for wireless manipulation of intact mammalian neural circuitry

Chapter 2

Injectable, Cellular-Scale Optoelectronics with Applications for Wireless Optogenetics

Author contributions for the above citation:
*Co-first authors. T.-I.K. and **J.G.M.** worked iteratively together to generate working models of the devices and wrote the paper. T.-I.K.and his colleagues (Y.H.J., Y.M.S., H.A.P., R.H.K., S.D.L. G.S., S.K., and M.P.T) were primarily responsible for the design and fabrication of the multimodal devices. **J.G.M.** and his colleague (E.R.S. and R.A.) performed all of the biology-related experiments including any with cells, tissues, or animals. X.H. designed the RF power harvesting systems. Y.L. J.S. and Y.H. were responsible for the thermal modeling. F.G.O. provided the biodisolvable adhesive. J.A.R. and M.R.B. oversaw all experiments, helped design the devices, and helped write the paper.

SUMMARY

Successful integration of advanced semiconductor devices with biological systems will accelerate basic scientific discoveries and their translation into clinical technologies. In neuroscience generally, and in optogenetics in particular, an ability to insert light sources, detectors, sensors and other components into precise locations of the deep brain could yield versatile and important capabilities. Here, we introduce an injectable class of cellular-scale optoelectronics that offers such features, with examples of unmatched operational modes in optogenetics, including completely wireless and programmed complex behavioral control over freely moving animals. The ability of these ultrathin, mechanically compliant, biocompatible devices to afford minimally invasive operation in the soft tissues of the mammalian brain foreshadow applications in other organ systems, with potential for broad utility in biomedical science and engineering.

INTRODUCTION

Electronic systems that integrate with the body provide powerful diagnostic and therapeutic capabilities for basic research and clinical medicine. Recent research establishes materials and mechanical constructs for electronic circuits, light-emitting diodes (LEDs), sensors, and other components that can wrap the soft, external surfaces of the brain, skin and heart, for diverse functions in analytical measurement, stimulation and intervention (Kim et al., 2010, 2011; Mannsfeld et al., 2010; Ordonez et al., 2012; Qing et al., 2010; Sekitani and Someya, 2012; Sekitani et al., 2009; Takeuchi et al., 2004; Tian et al., 2010; Viventi et al., 2010). A significant constraint in operating these devices, however, follows from their surface-mounted configurations and inability to provide direct interaction into the volumetric depths of

25

the tissues. Passive penetrating electrodes or optical fibers with interconnections to externally located electronic control and/or acquisition systems or light sources can be valuable in many contexts, particularly in neuroscience, engineering, and surgery (Anikeeva et al., 2011; Kim and Romero-Ortega, 2012; Mattis et al., 2012; Ordonez et al., 2012; Stark et al., 2012; Takeuchi et al., 2004). Direct biological integration is limited by challenges from tissue lesions during insertion, persistent irritation, and engineering difficulties in thermal management, encapsulation, scalable interconnection, power delivery, and external control. Many of these issues constrain attempts to insert conventional, bulk LEDs into brain tissue (Cao et al., 2013) and to use semiconductor nanowire devices as cellular probes or active, *in vitro* tissue scaffolds (Tian et al., 2010, 2012). In optogenetics, engineering limitations of conventional, tethered fiber optic devices restrict opportunities for *in vivo* use and widespread biological application. As a solution, we developed mechanically compliant, ultrathin multifunctional optoelectronic systems that mount on releasable injection needles for insertion into the depths of soft tissue. These wireless devices incorporate cellular-scale components ranging from independently addressable multicolored microscale, inorganic light-emitting diodes (μ-ILEDs) to colocated, precision optical, thermal, and electrophysiological sensors and actuators.

RESULTS

A scanning electron micrograph (SEM) of an isolated gallium nitride (GaN) μ-ILED, as a constituent component of these systems, is presented in **Figure 2.1A**, as well as an epifluorescent image of a device among cultured human embryonic kidney (HEK293) cells, to illustrate the similar sizes. Each such "cellular-scale" μ-ILED (6.45 μm thick, 50x50 μm^2) uses high-quality epitaxial material grown on sapphire, processed to establish contacts (15x15 μm^2 square pads in

the corners, and an L-shaped current spreading layer for the p-contact) and then released, to allow transfer printing onto narrow, thin plastic strips. The μ-ILEDs are less than one-thousandth the size of conventional LEDs (typically 100 μm thick, with lateral dimensions of 1 mm^2) and fiber optic probes, as discussed below (Kim et al., 2012b). The small sizes of μ-ILEDs allow for spatially precise, cellular-scale delivery of photons, highly effective thermal management, reduced tissue damage, and minimized inflammation for prolonged use *in vivo*.

Combining μ-ILEDs with electronic sensors and actuators yields multifunctional integrated systems that can be configured in single or multilayer formats. The latter option is illustrated in **Figure 2.1B and C**, in which the sensors and/or actuators include a Pt microelectrode for electrophysiological recording or electrical stimulation (Layer #1; a 20x20 μm^2 exposure defines the active area), a microscale inorganic photodetector (μ-IPD) based on an ultrathin silicon photodiode (Layer #2; 1.25 μm thick, 200x200 μm^2), a collection of four μ-ILEDs connected in parallel (Layer #3) and a precision temperature microsensor or microheater (Layer #4; Pt serpentine resistor) (more details in **Figure 2.2-2.4**). Each layer is processed on separate substrates shaped to match a releasable, photolithographically-defined epoxy microneedle (**Figure 2.5**). A thin layer (~500 nm) of epoxy joins each of the layers in a precisely aligned, stacked configuration. The microneedle bonds to the bottom layer with a thin, bio-resorbable adhesive based on a film of purified silk fibroin, which enables removal of the microneedle after implantation (**Figure 2.1D** and **Figure 2.6**). The microelectrodes measure extracellular voltage signals in the direct vicinity of illumination and can also be used for stimulation (**Figure 2.15H**). The temperature sensors determine the degree of local heating, with a precision approaching ~1 mK, and can also be used as microheaters. The μ-IPD can measure the intensity of light from the μ-ILEDs while implanted deep in brain tissue and/or can enable

basic spectroscopic evaluations of absorption, fluorescence, diffuse scattering, and so on (for detailed information see **Figure 2.7 and 2.8**.
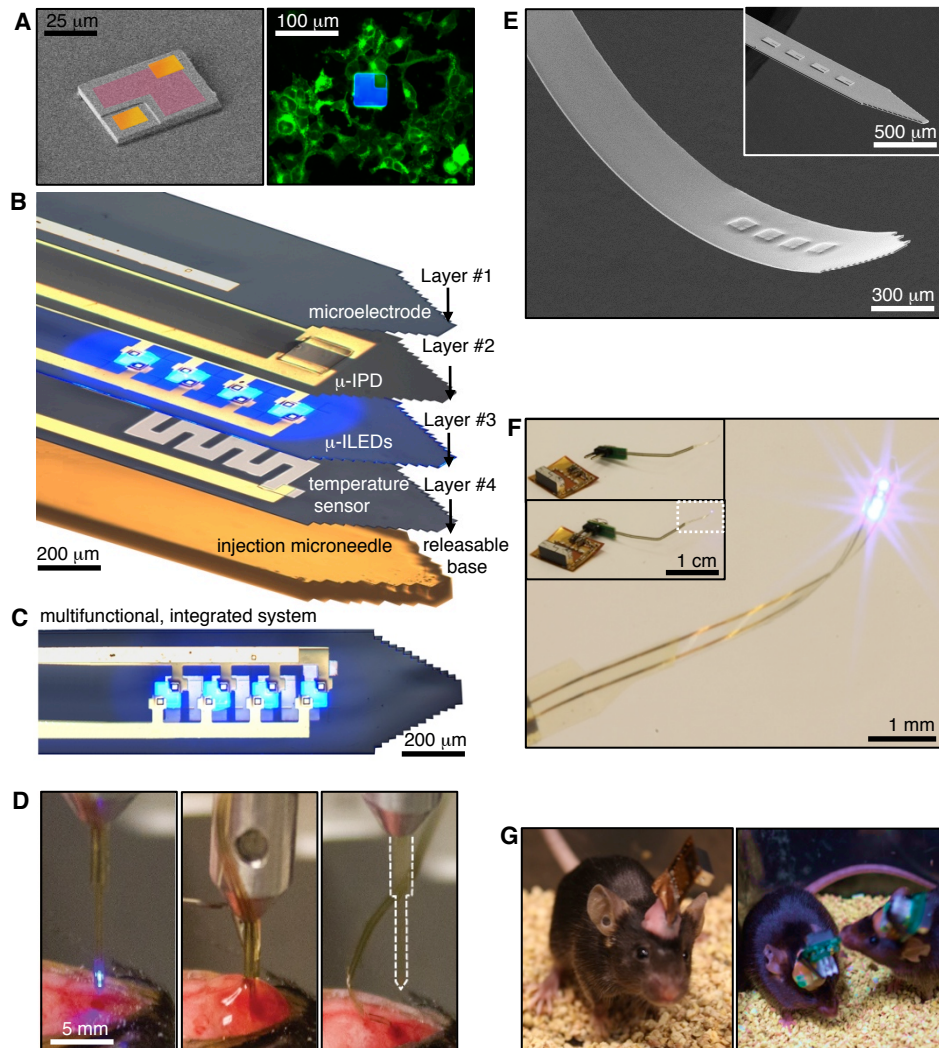
Figure 2.1 Injectable, cellular-scale semiconductor devices, with multifunctional operation in stimulation, sensing and actuation. (A) Left, colorized SEM (left) of a GaN μ-ILED (~6.45 μm thick, and 50x50 μm^2; contacts – gold; spreading layer – red). Right, fluorescent image of a μ-ILED (blue) with cultured HEK293 cells that express an eYFP tagged transmembrane protein (green). **(B)** A multifunctional, implantable optoelectronic device, in a tilted exploded view layout illustrating various components. The system includes layers for electrophysiological measurement (#1; Pt contact pad, microelectrode), optical measurement (#2; silicon μ-IPD), optical stimulation (#3; μ-ILED array), and temperature sensing (#4; serpentine Pt resistor), all bonded to a releasable structural support for injection (microneedle). **(C)** Top view of the integrated device shown in (B). **(D)** Process of injection and release of the microneedle. After insertion, aCSF (center) dissolves the external silk-based adhesive. The microneedle is removed (right) leaving only the active device components in the brain. **(E)** SEM of an injectable array of μ-ILEDs. The total thickness is 8.5 μm. Inset shows rigid device before coating with a passivation layer. **(F)** Integrated system wirelessly powered with RF scavenging. Insets show a connectorized device unplugged (top) and plugged into (bottom) the wireless power system. **(G)** Healthy, freely-moving mice with lightweight, flexible (left) and rigid (right) wireless systems powering GaN μ-LED arrays in the VTA.

A
Temporary substrate
(PDMS coated glass)

Patterned polymer

Lamination

2.5 or 6 µm thick patterned polymer lamination
on temporary substrate (PDMS coated glass)

B
µ-ILEDs

µ-ILED printing (or fabrication of
functional device) on patterned polymer

C
interconnect

Interconnect (Au) & passivation
(Epoxy:SU-8, 2 µm thickness)

D
De-lamination

De-lamination from temporary substrate
and transfer on 250 µm thick epoxy
needle

Figure 2.2 Schematic illustration of steps for fabrication (A) thin (2.5 or 6.0 µm thick) microneedle-shaped polymeric template laminated on a PDMS coated substrate, **(B)** µ-ILEDs integrated by transfer printing, **(C)** patterned passivation layers and interconnects, and **(D)** removal of the device from the PDMS coated substrate and transfer printing onto a releasable, injection microneedle substrate.
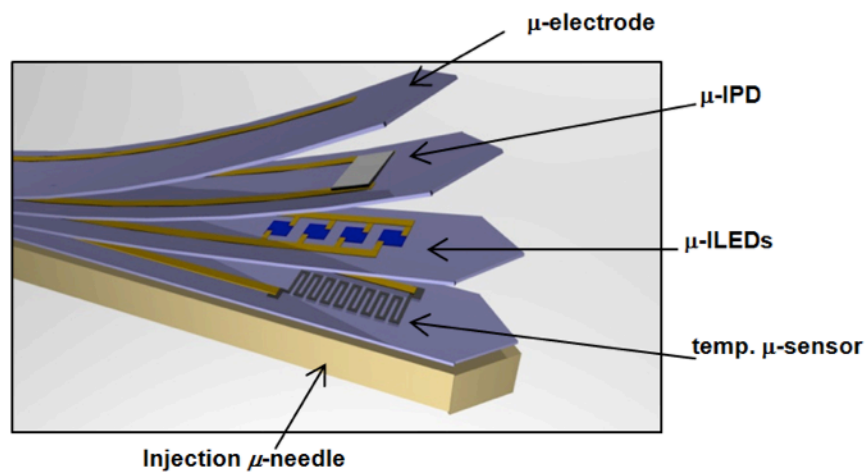
Figure 2.3 Schematic illustration of a printed multifunctional μ-ILED system.
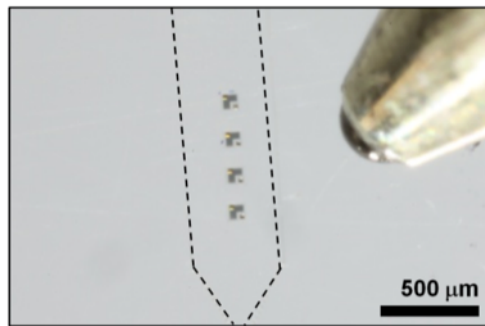
Figure 2.4 Photograph of μ-ILED layout

Photograph of four printed μ-ILEDs next to the tip of a ballpoint pen (right), to set the scale.

Each μ-ILED has lateral dimensions of 100 x100 μm^2, with two 25x25 μm^2 metal pads for

contacts and an L-shape current spreader.
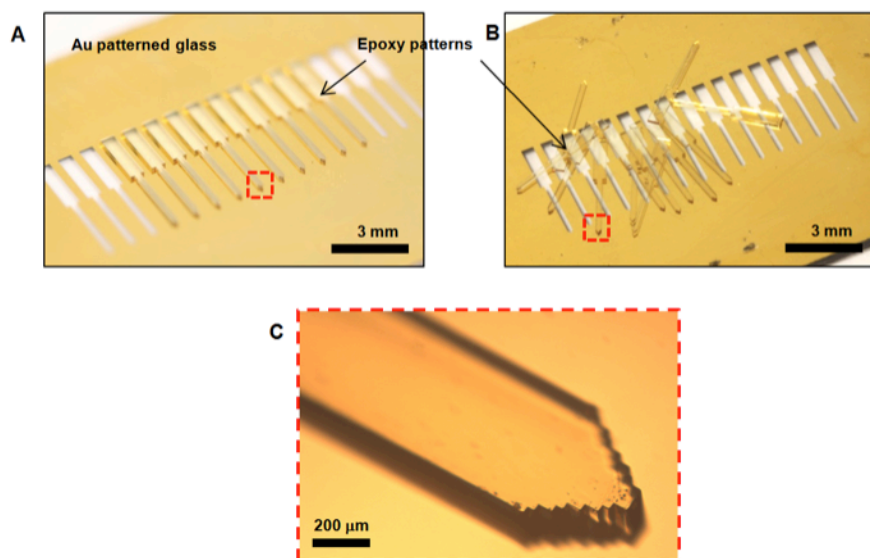
Figure 2.5 Images of injection microneedles

Images of injection microneedles defined photolithographically using a UV-curable epoxy (250 μm thick, SU-8 100). **(A)** Photolithographic patterning of epoxy on a pre-patterned glass substrate **(B)** microneedles delaminated by mechanical force from the glass substrate. **(C)** Tilted optical microscopic image of a single microneedle.
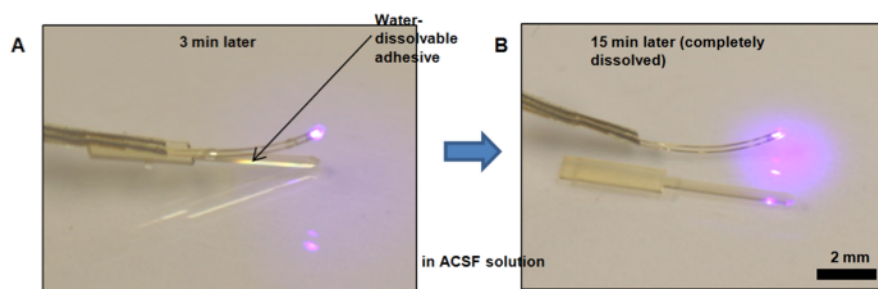
Figure 2.6 Demonstration of silk as an adhesive for injection microneedles

Demonstration of silk as a water soluble, bio-resorbable, releasable adhesive for injection microneedles. **(A)** Image of a device at the initial stages of silk dissolution, after 3 min and **(B)** after full dissolution and mechanical separation, after 15 min.
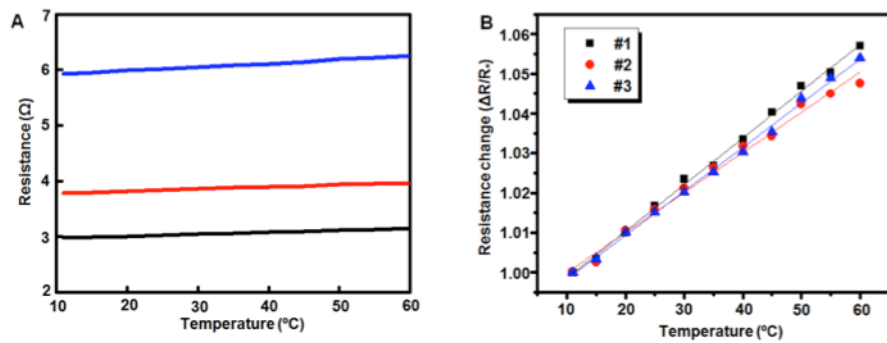
Figure 2.7 Relationship between temperature and resistance of temperature sensors

(A) Change in resistance with temperature. **(B)** Fractional change in resistance as a function of temperature, for three different devices.
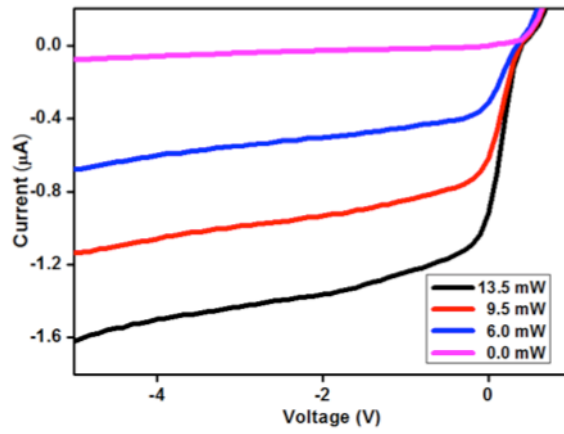
Figure 2.8 Current-voltage (I-V) characteristics of a μ-IPD

Current-voltage (I-V) characteristics of a μ-IPD exposed to different light intensities generated by operation of four μ-ILEDs. Electrical DC input powers into the μ-ILEDs were 0, 6.0, 9.5, 13.5 mW.

Injection of such flexible devices into the brain follows steps shown in **Figure 2.1D**. The injected multifunctional optoelectronic systems, have a total thickness of ~20 μm. This exceptionally thin geometry, low bending rigidity, and high degree of mechanical flexibility (**Figure 2.1E and 2.1F**) allow for minimally invasive operation. Wired control schemes use standard transistor-transistor logic (TTL) and are therefore compatible with any readily available electrical commutator. Details on wired powering strategies and demonstration of wired optogenetic functionality in rodent behavioral assays are presented in **Figures 2.9, 2.10, and 2.11.** Implementation of a wireless power module based on radiofrequency (RF) scavenging is shown in **Figure 2.1F**. A custom flexible polyimide film-based lightweight (~0.7 g) power scavenger or a rigid printed circuit board-based scavenger (~2.0 g) (**Figure 2.1G and Figure 2.12**) can be temporarily mounted on freely moving animals for short-term experimentation without constraint in natural animal behavior (**Figure 2.1G**). The entire system consists of a wireless power transmitter and RF signal generator; an RF source (910 MHz; power output between 0.02 and 0.1 mW); a power supply; an RF power amplifier (gain of 49 dB at 910 MHz; power output between 1.6 and 7.9 W); and a panel antenna (gain of 13 dBi), as in **Figures 2.12 and 2.13**. The low-frequency signal generator provides user-controlled amplitude modulation for programmed operation. The RF power that reaches the animals, under normal operating conditions at a distance of ~1 m, is between 0.15 and 0.77 mW/cm^2, which is substantially smaller than the maximum permissible exposure limits (3.03 mW/cm^2) for humans in controlled environments. Wireless control allows access to complex and ethologically relevant models in diverse environmental settings, including social-interactions, homecage behaviors, wheel running, complex maze navigation tasks, and many other behavioral outputs (**Figure 2.1G and 2.14)**.
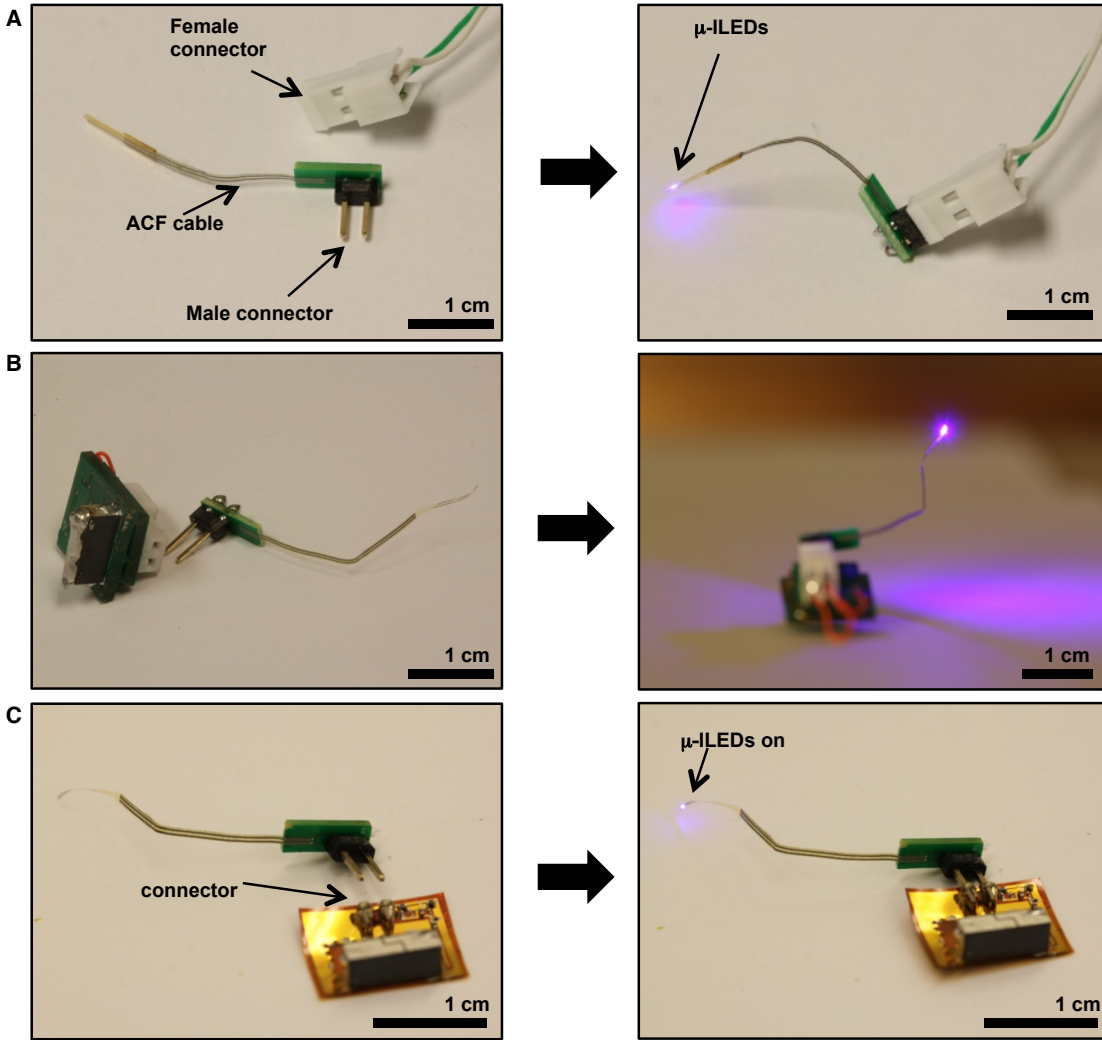
Figure 2.9 Images of connection between power supplies and μ-ILED systems

Images of the plug-in geometry of the connection between power supplies and penetrating μ-ILED systems, for the case of a wired supply **(A)** and RF wireless units **(B and C)**.
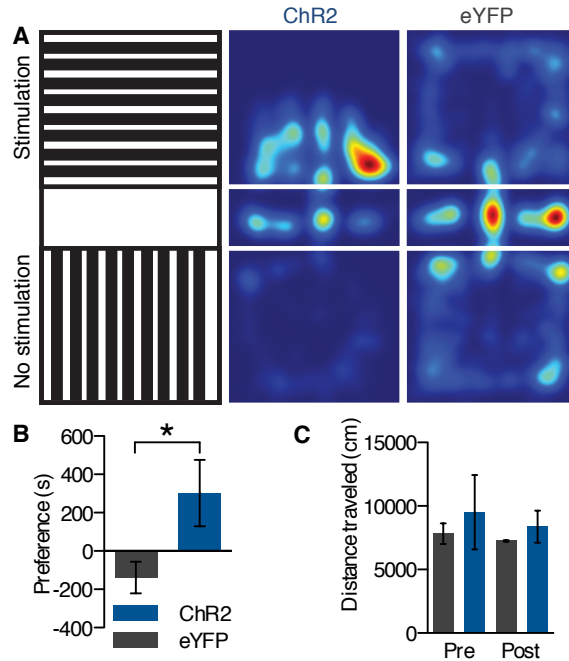
Figure 2.10 μ-ILED devices drive a conditioned place preference using standard TTL signals. To demonstrate wired functionality, we selectively targeted ChR2(H134)-eYFP to VTA-DA neurons (**Figure 2.26A**) and tested that phasic activation (20, 5 ms pulses every minute) of cells with a μ-ILED device is sufficient to drive robust place preference behavior without a change in locomotor activity. Animals were conditioned over three days for 30 minutes. μ-ILED devices were powered and controlled using standard function generator (Tektronix, AFG3022B or AMPI, Master-9). (**A**) Left, Diagram of three-chambered conditioned place preference apparatus. Right, representative heat maps of activity during the post-test, hotter colors represent longer duration at every location in the apparatus. (**B**) Place preference scores, calculated as post-test minus pre-test on the light stimulation-paired side (n = 4-6/group; *p<0.05 t test compared to AAV5-DIO-eYFP controls). (**C**) Total activity during the pre- and post-tests shows no difference between the two groups. All bars represent means ± SEM.
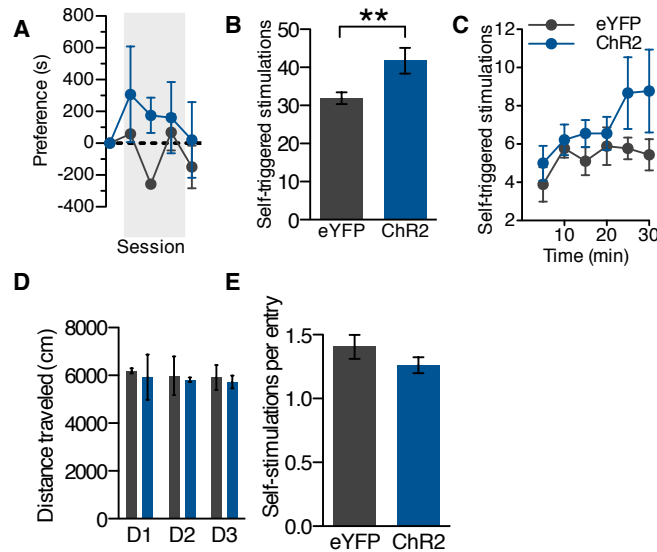
Figure 2.11 Real-time assessment of reward seeking or aversion

Real-time assessment of reward seeking or aversion is possible by pairing an animal's behavioral response with self-triggered stimulation or inhibition (**Figure 2.19-2.21**). Real-time conditioning, animals allowed free access to the apparatus from fig. S18A learn to self-trigger stimulations when 10, 5 ms pulses at 20 Hz light is delivered contingent on entry into the paired chamber. (**A**) Animals did not express either a real-time or conditioned place preference under this experimental design. (**B**) AAV5-DIO-ChR2 mice, however, did have increased numbers of passive, entry-triggered self-stimulations. (**C**) Passive self-stimulation is learned over the course of each trial. (**D**) Importantly, this difference is not due to a change in activity between the two groups (n = 3/group, **p<0.01 t test compared to AAV5-DIO-eYFP controls). (**E**) Animals could receive subsequent stimulations if they remained in the stimulus-paired chamber for 60 seconds. ChR2 mice did not learn to remain in the chamber for these subsequent stimulations.

40
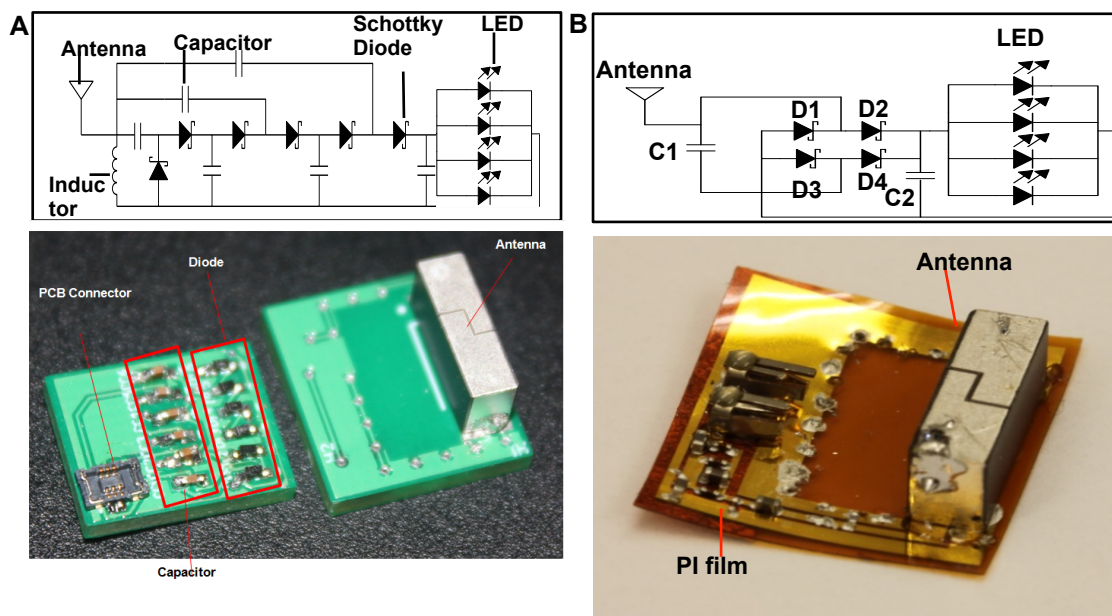
Figure 2.12 Circuit diagrams and pictures if RF powering scavenger

Circuit diagrams for each RF powering scavenger and pictures of RF powering scavenger (left) and RF antenna (right), in a miniaturized PCB layout (**A**) and on polyimide film (**B**). The RF power scavenger contains a RF antenna that works at 910 MHz, an impedance matching inductor, a voltage multiplexer with cascaded combination of Schottky diodes and capacitors, and blue LEDs. The circuit of the RF power scavenger for (**A**) is on two stacked PCB boards that are connected with each other by a PCB connector. For RF power scavenger for (**B**), Au pre-patterned PI film supports all of components connected by silver epoxy.
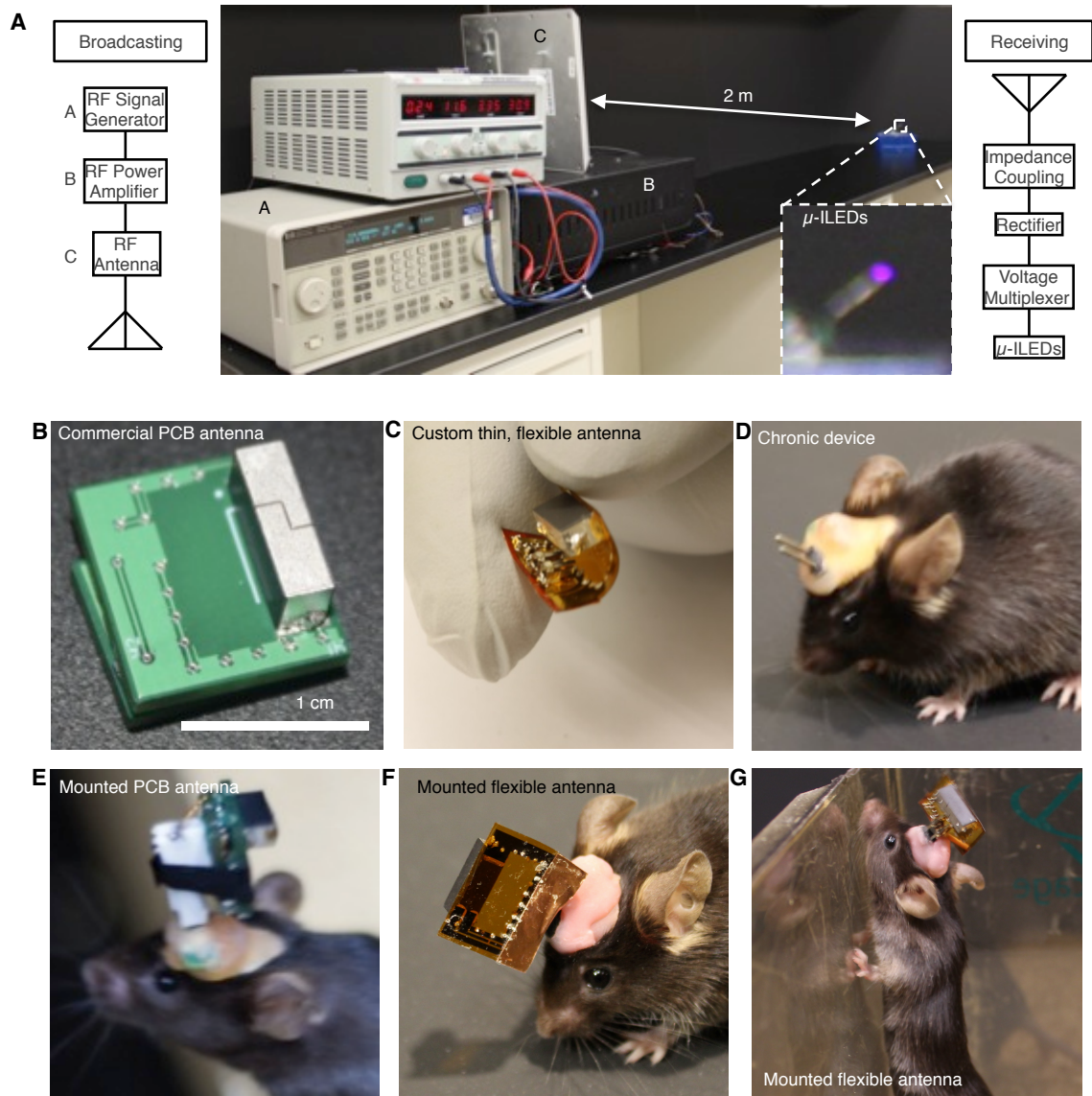
Figure 2.13 Key components for wireless operation using RF power delivery

(A) Photo and diagram explaining the components of the system and demonstrating wireless power. Headstage antennas on PCB board (**B**) and on bent PI (**C**). (**D**) A mouse with a chronically implanted device. The nature of the interconnect allows for temporary coupling to either form of headstage antenna or a wired power source. **(E,F,G)** Mice with acutely mounted headstage antennas.
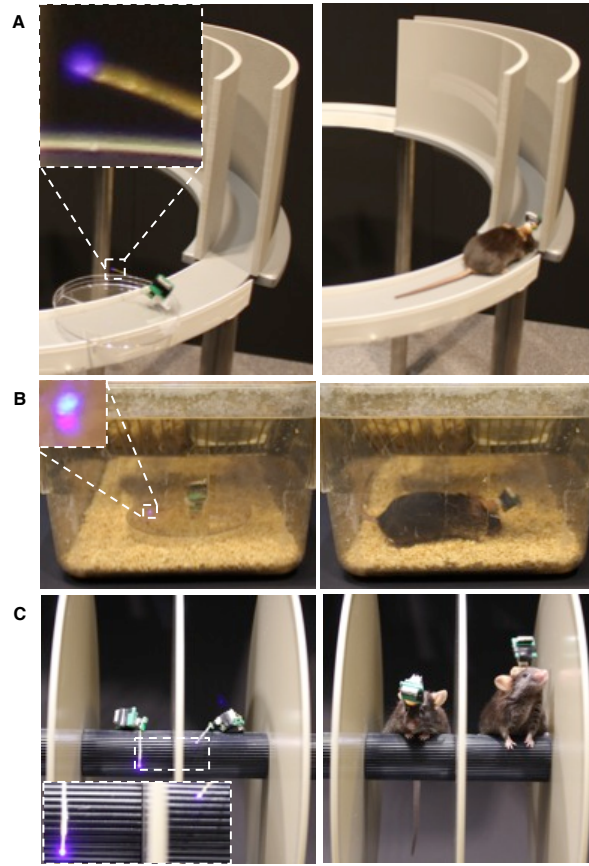
Figure 2.14 Demonstration of wireless capabilities

For all panels the same environment is shown with wireless lit µ-ILEDs (left) and wirelessly stimulated mice (right). (**A**) Wireless mice can explore circular environments with no need for commutators or adaptations to the behavioral apparatus. (**B**) RF modulation can be used to power devices through covered arenas as seen here with a mouse in a traditional homecage environment. (**C**) Multiple wireless devices can be controlled using a single antenna. Here, two implanted mice are receiving identical optical stimulation simultaneously on a standard rotarod- a rotating wheel that provides numerous barriers for use with tethered animals.

The electrical, optical, and thermal characteristics of the devices when operated in biological environments are important for optogenetics and other biomedical applications. The

total optical power density of the four μ-ILEDs in this device as a function of electrical input power is shown in **Figure 2.15A** (more details in **Figure 2.16 and 2.17.** This performance is comparable to similarly designed, state-of-the-art conventional GaN LEDs (Kim et al., 2012b). Many optogenetic constructs can be activated with ~1 mW/mm^2, at wavelengths near 450 nm (Mattis et al., 2012). These conditions are well matched to the output of the GaN μ-ILEDs. Input power of ~1.0 to 1.5 mW (**Figure 2.15A**) is sufficient for both activation of the channelrhodopsin-2 [ChR2(H134)] ion channel and precise control of intracellular signaling [adenosine 3'5'-monophosphate (cAMP and extracellular signal-regulated kinase (ERK 1/2)] via an optically sensitive heterotrimeric guanine nucleotide-binding (G-protein)-coupled receptor (OPTO-β2) (Airan et al., 2009) (**Figure 2.23C and D, Figure 2.18 and 2.19**). Wirelessly, at a distance of 1 m, the RF scavenger puts out 4.08 mW of electrical power resulting in a 7 mW/mm^2 optical power density. Other wavelengths are possible using different types of μ-ILEDs, either in multicolored or uniform arrays. An example of the latter, with blue and red (GaAs) μ-ILEDs, and the former, with green devices (produced using fluorescein sodium salt phosphor on a blue GaN μ-ILED) are shown in **Figure 2.15B**.

μ-ILED induced changes in temperature determined by infrared imaging and by analytical calculation, respectively, are shown in **Figure 2.15, C and D**. The μ-ILEDs were implanted 0.3 mm into an explanted piece of brain tissue held at 37 ^{o}C. The time-averaged temperatures measured at light-pulse (10 ms) frequencies of 3, 5, 10, and 20 Hz with peak light output of 17.7 mW/mm^2 are 37.17º, 37.22º, 37.31º, and 37.46^{o}C, respectively. These results are similar to calculated time-averaged temperatures of 37.20º, 37.34º, 37.68º, and 38.37^{o}C, respectively. Note that, the input power used in these tests is 10 times what is necessary to activate many optogenetic constructs (Mattis et al., 2012). The cellular-scale dimensions of the

μ-ILEDs enable high rates of passive thermal spreading, and the brain tissue itself operates as an efficient heat sink. The latter is apparent in studies of the dependence of operating temperature on tissue thickness, operating power, and frequency (**Figure 2.15E**). As in **Figure 2.15D**, the experiment and theory agree remarkably well in spite of the indirect correlation between infrared imaging results and temperature at the location of the devices (details appear in **Figure 2.20 and 2.21**. Perfusion in living tissue further increases the efficacy of these biological heat sinks. Changes in temperature measured *in vivo* using an integrated temperature sensor (**Figure 2.7**) compared with calculated results are shown in **Figure 2.15F**. Collectively, these results indicate that changes in temperature associated with operation of μ-ILEDs can be less than 0.10 $^{\circ}$C for pulse frequencies less than 20 Hz, typical of many neuronal firing rates. These values are much lower than those that occur in human deep brain stimulation (DBS) regulation, ~2°C (Elwassif et al., 2006). Furthermore, in wireless operation, there is no appreciable change in temperature associated with operation at the headstage antenna or the skull (**Figure 2.22**).

Other components of this multifunctional platform exhibit similarly good characteristics. To demonstrate functionality of the silicon μ-IPD, **Figure 2.15G** shows photocurrents generated by different intensities of light from μ-ILEDs at different pulse frequencies. Finally, the Pt microelectrode has a 400 μm^2 exposure site with ~1.0 MΩ impedance at 1 kHz capable of measuring extracellular potentials on the microvolt scale necessary to distinguish individual action potentials (**Figure 2.15H**), as demonstrated with clear clustering in the principal component analysis of spike data (**Figure 2.15I**).
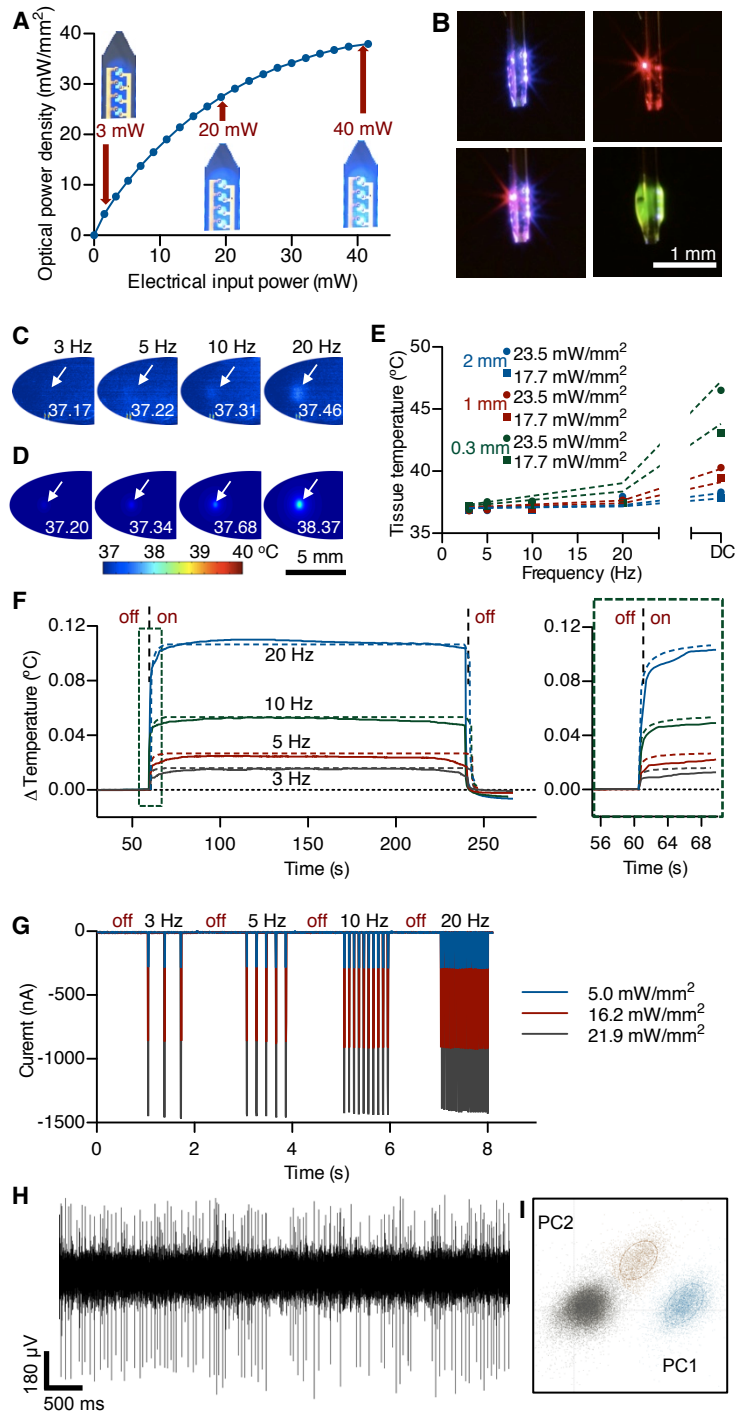
Figure 2.15. Optical, thermal, and electrophysiological studies with corresponding theoretical analyses. **(A)** Total optical power density as a function of electrical input power applied to an array of four GaN μ-ILEDs; optical images show operation at 3, 20 and 40 mW. **(B)** A single device has one 675 nm GaAs μ-ILED and four 450 nm GaN μ-ILEDs that can be activated independently (upper left and upper right) or concurrently (lower left). The same device is coated in a fluorescein sodium salt phosphor for 530 nm light (lower right). **(C)** Measured and **(D)** calculated temperatures in explanted brain tissue near implanted μ-ILEDs at a depth of 0.3 mm and operated at 17.7 mW/mm^2 of light output power. **(E)** Temperatures in a system similar to that of (C, D), as a function of duty cycle in the operation of the μ-ILEDs and at three different implantation depths (0.3, 1.0, 2.0 mm) and two different light output powers (17.7, 23.5 mW/mm^2). **(F)** Change in brain temperature as a function of time, measured using an integrated temperature sensor co-located with an array of four μ-ILEDs in a lightly anesthetized mouse. Results evaluated at a peak input electrical power of 8.65 mW, in 3, 5, 10, and 20 Hz pulses (10 ms duration). The vertical dashed lines indicate onset (at 60 s) and offset (at 240 s) of the μ-ILEDs. Colored dashes lines correspond to theoretical models for the temperature. The right frame shows the time dynamics as the device is powered. **(G)** Change in photocurrent as a function of time, measured using an integrated μ-IPD, for three different light output powers to an array of μ-ILEDs: 5.0 mW/mm^2 (blue trace), 16.2 mW/mm^2 (red trace), and 21.9 mW/mm^2 (black trace) at different pulse frequencies (10 ms pulses at 3, 5, 10, and 20 Hz). **(H)** 5 s extracellular voltage trace of spontaneous neuronal activity gathered using the integrated Pt microelectrode. **(I)** The same data is filtered and sorted using principal components analysis to identify single units.
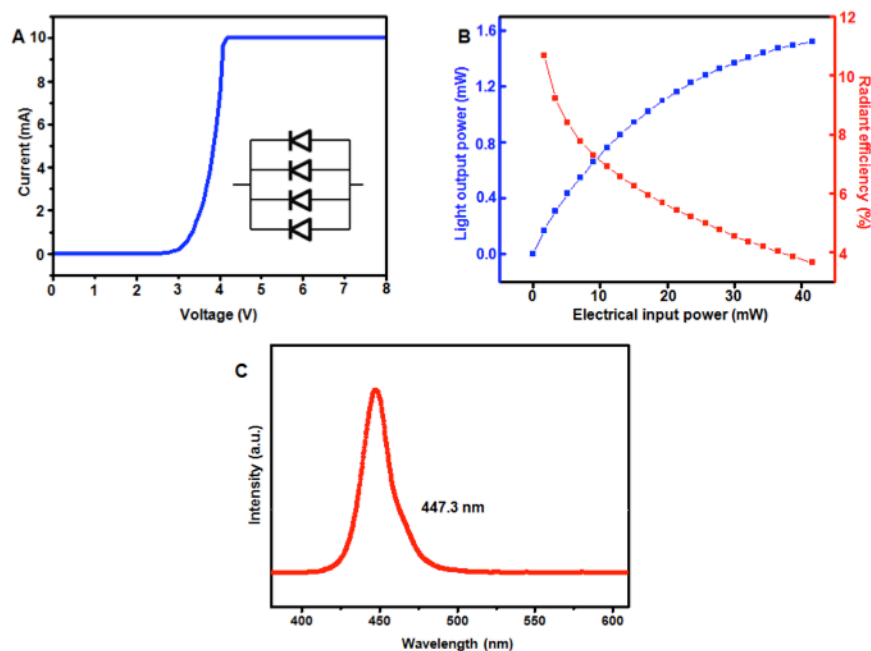
Figure 2.16 Electrical and optical properties of an array of four μ-ILEDs connected in parallel. (A) Current-Voltage (I-V) characteristics, **(B)** light output power and radiant efficiency as a function of electrical input power, and **(C)** light emission intensity as a function of wavelength.
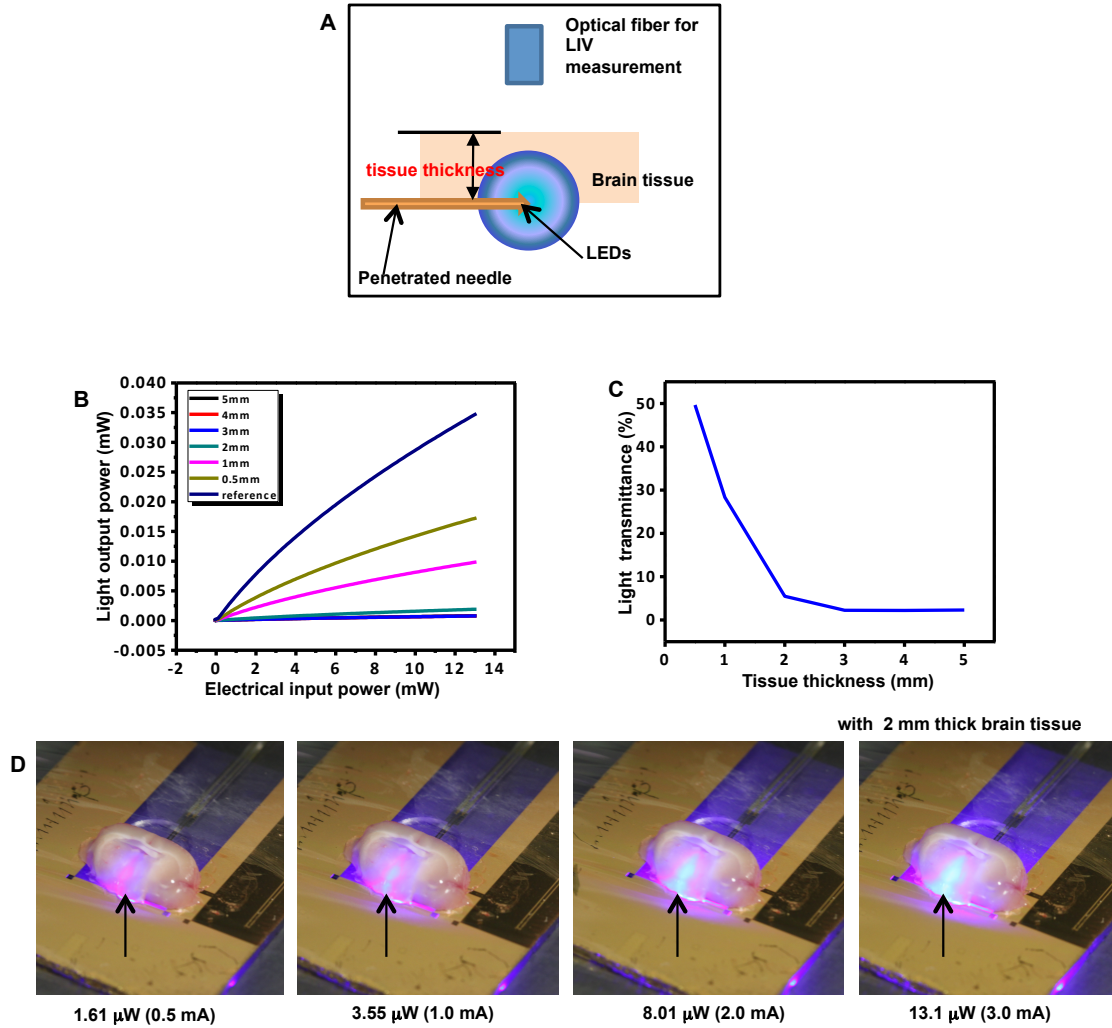
Figure 2.17 Information related to tests of light penetration depth

(A) Schematic illustration of the experimental scheme, **(B)** light output-current and voltage (LIV) results collected using slabs of brain tissue with various thicknesses (0.5, 1, 2, 3, 4, 5 mm) and **(C)** their light transmission through the thickness of the tissue. **(D)** Light extraction through 2 mm thick slabs of brain tissue at various applied powers.
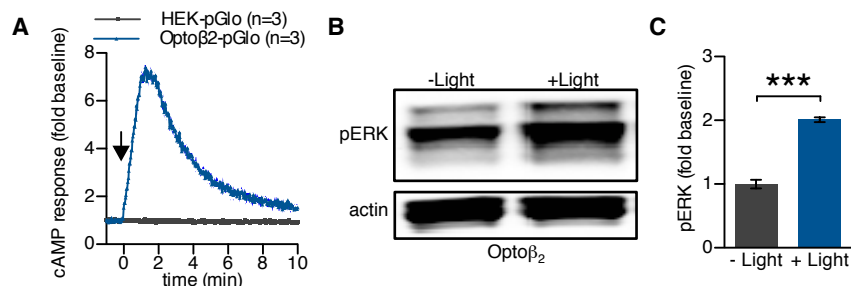
Figure 2.18 *μ*-ILED-induced activation of cAMP and ERK phosphorylation in Optoβ$_2$ expressing cells. (A) Optoβ$_2$ cells co-expressing pGlo show a rapid and transient increase in cAMP following light (450 nm, 5 sec, 0.5 W/cm^2 pulse) stimulation (n=3). HEK293 cells expressing pGlo show no response to the same light stimulation (n=3). Data are expressed as mean ± sem. **(B).** Representative pERK and actin Western Blots for Optoβ$_2$ and HEK293 cells following light (450 nm, 1 min, 0.5 W/cm^2 pulse) stimulation (n=3). **(C).** Quantitation of pERK normalized to actin in light stimulated Optoβ$_2$ and HEK293 cells. (*p<0.05, unpaired, two-tailed t-test).
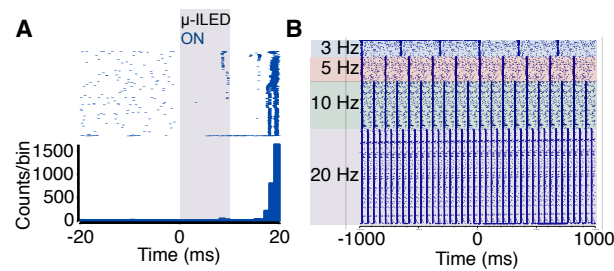
Figure 2.19 μ-ILED-induced modulation of *in vivo* neuronal activity in the VTA via ChR2(H134)-eYFP expressing neurons. (A) Representative peri-light raster plot and histogram demonstrating increased cell firing within 20 ms of onset of a 450 nm, 0.5 W/cm^2 light pulse. (**B**) Raster plot showing activity from the same neuron (A) time locking with various frequencies of light delivery. Each light pulse is centered at 0 ms, the effects of prior and subsequent pulses are apparent in each line of the 2000 ms raster plot.
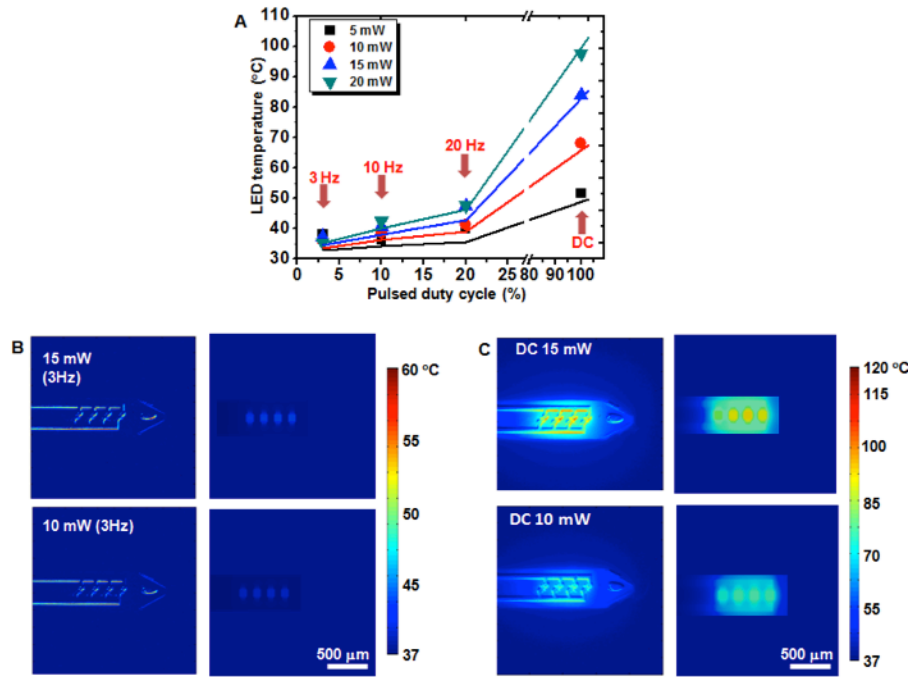
Figure 2.20 Surface temperature of μ-LEDs on an injection microneedle, during operation at various power levels in open air. (A) Measured (dots) and calculated (lines) temperatures of μ-ILEDs at various pulse duty cycles and at DC power levels. All calculated temperatures (lines) are obtained by time-average results at 37 $^{\circ}$C background temperature. The duration time (width) for all pulsed cases is 10 msec. **(B)** Measured (left) and calculated (right) temperatures at 15 and 10 mW applied power. The measured (calculated) temperatures are 37.44 (39.31) and 36.15 (38.54) $^{\circ}$C, respectively, with a 3 Hz pulse. **(C)** Measured (left) and calculated (right) temperature at 15 and 10 mW DC applied power. The measured temperatures (calculated) are 84.01 (86.95) and 86.31 (70.30) $^{\circ}$C, respectively, with a 3 Hz pulse.
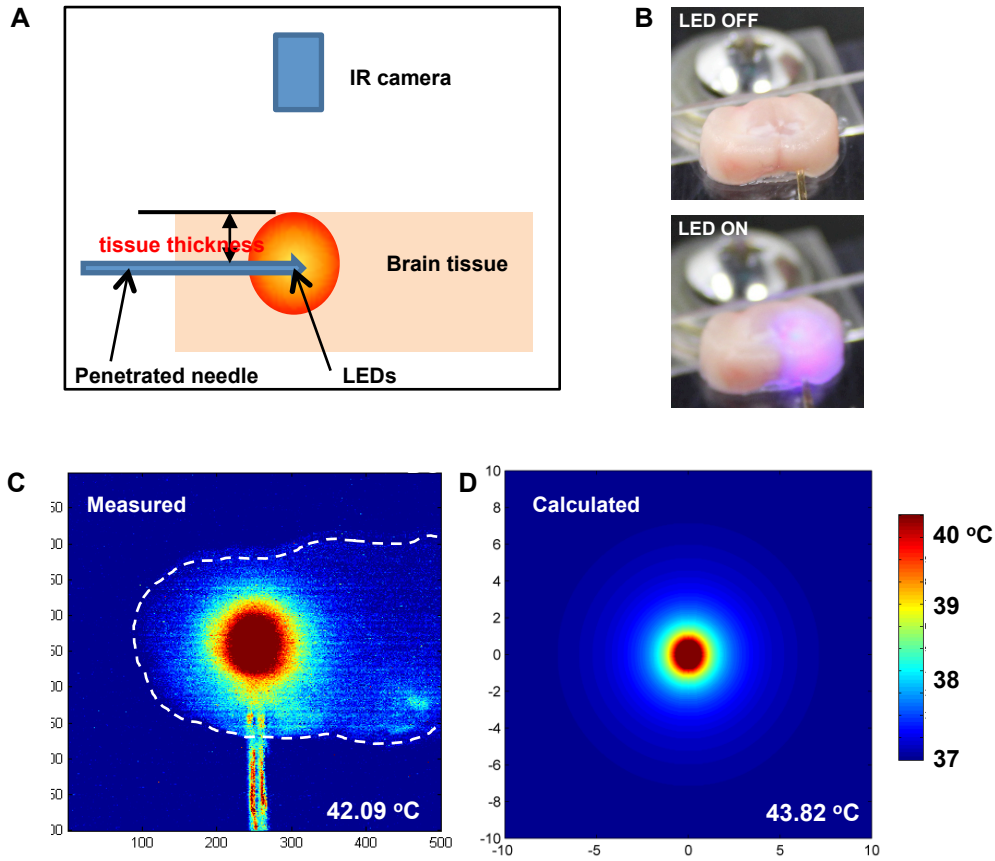
Figure 2.21 Thermal imaging with a calibrated IR camera. **(A)** Schematic illustration and **(B)** pictures of the IR camera stage and μ-ILED devices injected in brain tissue. **(C)** Measured and **(D)** calculated tissue temperature with μ-ILEDs injected into a 0.3 mm thick slab of tissue, evaluated at the surface for the case of 10 mW DC input power. Measured and calculated temperatures are 42.09 and 43.82 °C, respectively.
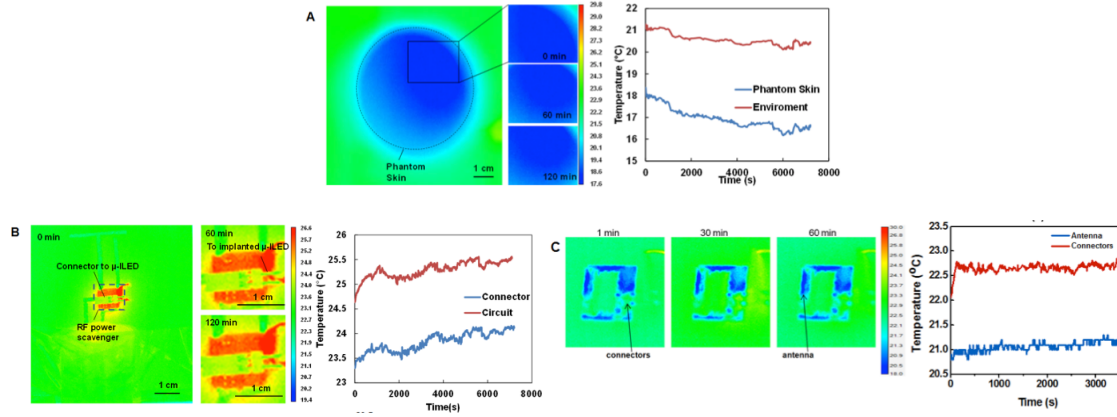
Figure 2.22 IR images of a phantom skin sample and the surrounding environment during prolonged exposure to RF radiation. IR images (left) and extracted average temperatures (right) of a phantom skin sample and the surrounding environment during prolonged exposure to RF radiation, starting at time=0 s. The results indicate no observable effects of heating due to RF. The temperature variations in the phantom skin are small, and mostly due to variations in the environment, without any observable effect, even under constant RF power (**B**) IR images (left) of a RF power scavenger circuit during exposure to constant RF radiation for various times. The images show changes in temperature when RF power is applied, and the μ-ILEDs are turned on, for 0 (left), 60 (right, top), and 120 (right, bottom) min. Spatially averaged changes in temperature (right) of the RF power scavenger circuit and connector during prolonged exposure to constant RF radiation, starting at time=0 s. The temperature change is less than 0.5ºC during this 2 hr period. (**C**) IR images (left) of a thin, lightweight flexible RF power scavenger circuit during exposure to pulsed (10 Hz) RF radiation for various times: 1 (left), 30 (middle), and 60 (right) min. There is no temperature change (right) in the thin, lightweight flexible RF power scavengers (near the antenna and the connectors) during prolonged exposure to pulsed RF radiation at 10 Hz.

For use in optogenetics, such devices eliminate the need for lasers, bulk LEDs, fiber coupling systems, tethers, and optomechanical hardware used in conventional approaches (**Figure 2.9**). Furthermore, the fundamental optics of μ-ILEDs are very different from typical fiber optic implants. Absorbing and reflecting structures around the emissive areas of the μ-ILEDs enable precise delivery of light to cellular sub-regions. **Figure 2.23A and B** compare relative size and the different patterns of light emission from μ-ILEDs to fiber optic probes. Fiber optics typically approach brain structures dorsally. This approach preferentially illuminates cells in the dorsal portion of the targeted region with greater light intensity near the point of light escape (Aravanis et al., 2007) (**Figure 2.23B left**, & **Figure 2.24**). Targeting ventral cell bodies or terminals requires lesion of dorsal regions or the use of substantially greater, and potentially phototoxic (Yizhar et al., 2011), amounts of light to the site of interest. Neither option protects the intact architecture of a complete brain locus. Although recent advances have spatially restricted light from implanted fiber optics (Tye et al., 2011; Zorzos et al., 2012), these approaches require the use of invasive metal cannulae (**Figure 2.23E**) or rely on sophisticated and sensitive optomechanical engineering that may limit their use in awake, behaving animals. The architecture of the μ-ILEDs enables light delivery medial or lateral to the intended target brain region. Native light escape from μ-ILEDs is nearly omni-directional (**Figure 2.23B, center**) but can be restricted to a wide range of angles with absorbing or reflective structures on the device (**Figure 2.23B, right**).

We implanted both μ-ILEDs and fiber optics into animals expressing ChR2(H134)-eYFP (fused with enhanced yellow fluorescent protein) in the locus coeruleus (LC) (**Figure 2.24**). One hour of output-matched photostimulation induced c-fos expression (Carter et al., 2010), a biochemical marker of neuronal activation, in both groups of ChR2(H134)-eYFP-expressing

mice that was not seen in green fluorescent protein (GFP) expressing controls (**Figure 2.23C and D**). The spatial distribution of c-fos expression, however, differed markedly between the fiber optic and μ-ILED groups. μ-ILED devices produced significantly greater activation in the ventral LC (**Figure 2.23D**).

The physical sizes and mechanical properties of the μ-ILED systems reduce lesioning, neuronal loss, gliosis, and immunoreactivity. Glial responses are biphasic with an early phase featuring widespread activation of astrocytes and microglia and a late, prolonged phase hallmarked by restriction of the gliosis to the area closest to the implanted substrate (Szarowski et al., 2003). The μ-ILED devices produced substantially less glial activation and caused smaller lesions than metal cannulae and fiber optics, at both early (2 weeks) and late (4 weeks) phases (**Figure 2.23E**). Furthermore, the brain tolerates the thin, flexible devices better than rigid structures (**Figure 2.23E**), consistent with reports on passive electrode devices (Kozai and Kipke, 2009). Finally, we examined the chronic functionality of the devices and demonstrated that they are well tolerated in freely moving animals with

56
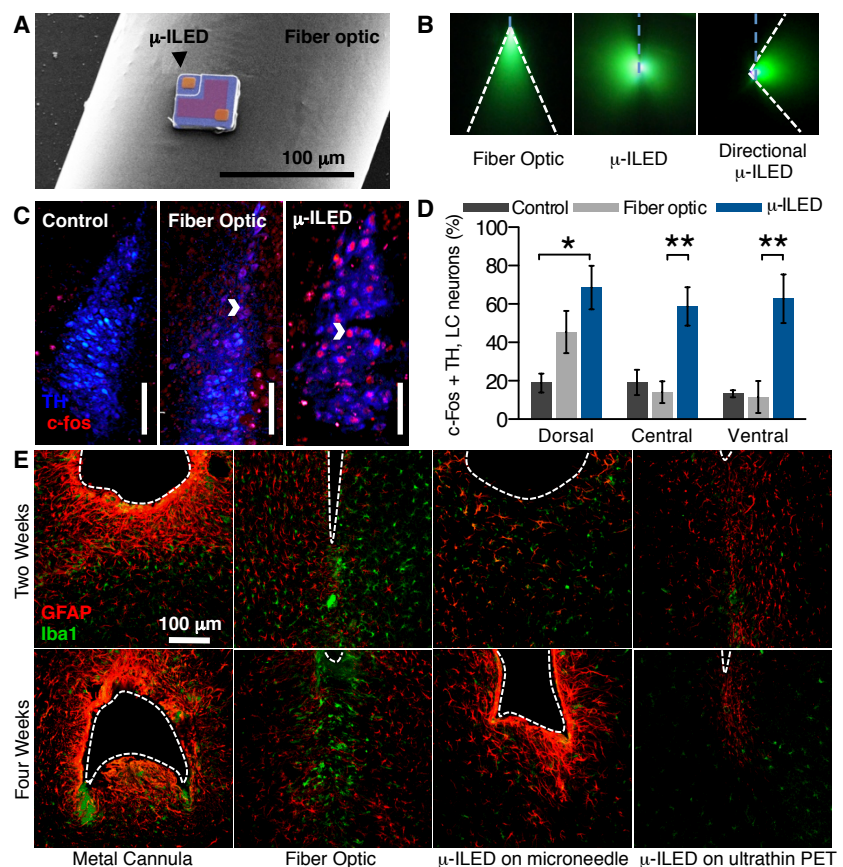
encapsulated sensors and μ-ILEDs, which maintain function over several months (**Figure 2.25**).

Figure 2.23 μ-ILED devices improve spatial targeting and reduce gliosis. (**A**) Colorized SEM (left) of a μ-ILED mounted on a standard 200 μm fiber optic implant. (**B**) Left, a dorsal-ventral oriented light cone (outlined in white) from a 200 μm bare fiber implant (blue dash) emitting 465 nm light in 30 μM fluorescein water. Center, near omnidirectional light escape from a μ-ILED device (blue dash) with four 450 nm μ-ILEDs. Right, lateral light escape (outlined in white) from a modified μ-ILED device (blue dash) to allow unique spatial targeting including flanking positions along the dorsal-ventral axis of brain loci. (**C**) Confocal fluorescence images of 30 μm brainstem slices containing the LC show staining for tyrosine hydroxylase (TH) and c-fos in control (left), fiber optic implanted (center), and μ-ILED device implanted (right) animals following 1 hour 3 Hz photostimulation (15 ms pulses, 5 mW output power). Scale bar = 100 μm. (**D**) Fiber optic and μ-ILED treatments specifically increase co-immunoreactivity. Ventral portions of the LC the μ-ILED devices express a higher proportion of tyrosine hydroxylase (TH, blue) and c-fos (red) co-immunoreactive neurons than fiber optic or control groups (n = 3 slices per brain from 3 brains for each group; Two-way ANOVA with Bonferroni post-hoc; All error bars represent means ± SEM; *$p < 0.05$, **$p < 0.01$). (**E**) Confocal fluorescence images of 30 μm striatal slices show staining for astrocytes (GFAP, red) and activated microglia (Iba1, green) at the ventral tip of each implanted device (dashed outline). Gliosis is smallest with the μ-ILED device at both two- and four-week time points.

A

Fiber-optic implant

Multimodal _μ_-ILED device

Tethered to external laser or LED

To wired TTL power source or
headstage antenna for wireless

cranial surface

brain tissue

- - 200 μm fiber

- - ~20 μm PS

Dorsal LC

Ventral LC

Legend

Neurons expressing ChR2-eYFP

_μ_-ILED (100 x 100 x 6.45 _μm_)

Electrode (platinum)

Photodetector (silicon)

Temperature sensor (platinum)
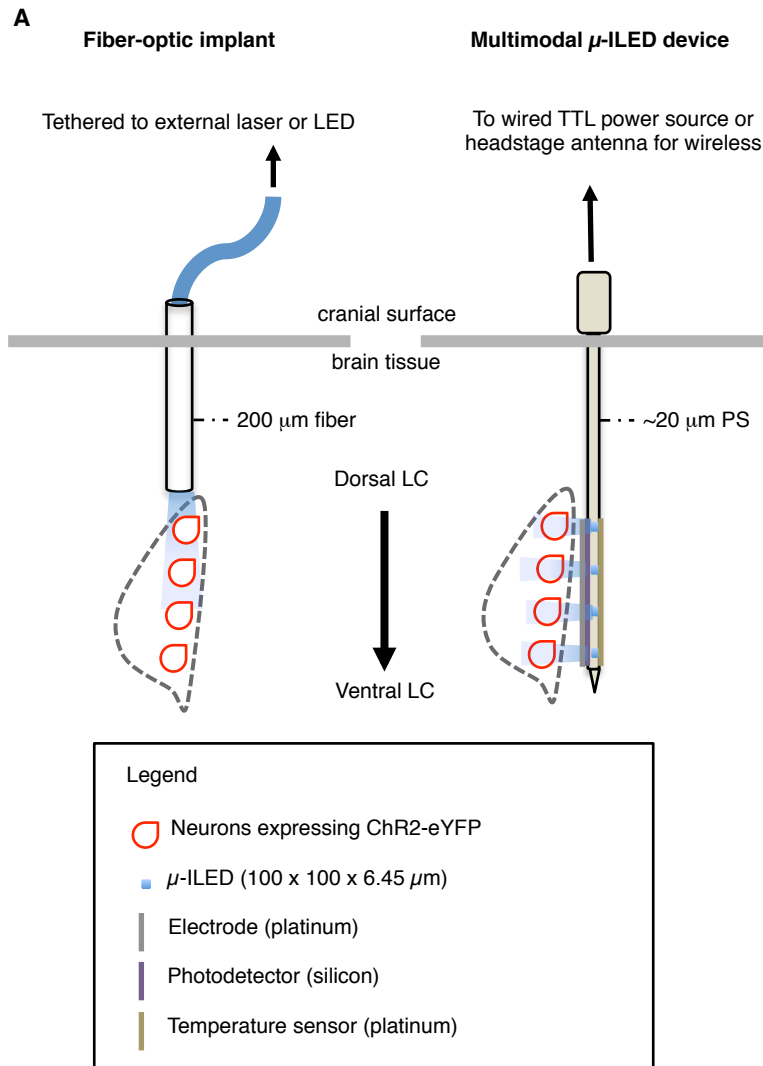
Figure 2.24 Cartoon depicting the experimental strategy used in Fig. 3B & 3C. μ-ILED
devices allow for unique spatial targeting of brain structures (here the locus coeruleus) to provide
consistent illumination along the entire dorsal-ventral plane of the structure.

A

B

1 month after injection

3 months after injection

6 months after injection
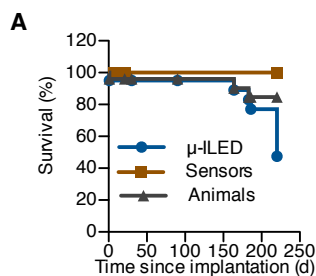
Figure 2.25 The durability of the devices and the constituent component following chronic implantation. (**A**) Survival curve showing viability of μ-ILEDs, fully passivated sensors (temperature and μ-IPD), and animals following device injection. μ-ILEDs were considered viable if the all μ-ILEDs in each array were still emitting sufficient light to activated ChR2. Sensors were considered viable if performance was within 1% of original performance. Components performed reliably within the two-three week timespan of a normal behavioral experiment and often well beyond that range. Detailed information on each point of attrition or censorship is available in **Table 2.1**. (**B)** The μ-ILED devices are robust and capable of functioning properly months after implantation. Working devices one (top), three (center), and six (bottom) months after chronic implantation into freely moving mice.

Table 2.1 Detailed information on the attrition and censoring of devices from Figure 2.25A.
The last working day after implantation was recorded as 0 if the damage occurred prior to or
during implantation.

Device ID	Reason for attrition/censor	Last working day after implantation
S1	Testing period ended, sensor working	21
S2	Testing period ended, sensor working	21
S3	Testing period ended, sensor working	21
S4	Testing period ended, sensor working	21
S5	Testing period ended, sensor working	21
S6	Testing period ended, sensor working	220
S7	Interconnect failure	0
S8	Testing period ended, sensor working	7
L1	Structural damage during implantation	0
L2	Testing period ended, μ-ILEDs working	220
L3	Animal died, device damaged on removal	183
L4	Testing period ended, μ-ILEDs working	220
L5	Testing period ended, μ-ILEDs working	220
L6	Testing period ended, μ-ILEDs working	220
L7	Testing period ended, μ-ILEDs working	220
L8	Testing period ended, μ-ILEDs working	220
L9	Testing period ended, μ-ILEDs working	220
L10	Testing period ended, μ-ILEDs working	220
L11	Testing period ended, μ-ILEDs working	220
L12	Testing period ended, μ-ILEDs working	30
L13	Animal died, device damaged on removal	164
L14	One or more μ-ILED failure	186
L15	Testing period ended, μ-ILEDs working	90
L16	Testing period ended, μ-ILEDs working	90
L17	One or more μ-ILED failure	220
L18	One or more μ-ILED failure	220
L19	One or more μ-ILED failure	220
L20	One or more μ-ILED failure	220

We next implemented a fully wireless system for dissecting complex neurobiology and behavior. Phasic neuronal firing of ventral tegmental area (VTA)-dopaminergic (VTA-DA) neurons encodes salient stimuli and is sufficient for behavioral conditioning (Adamantidis et al., 2011; Kim et al., 2012a; Tsai et al., 2009; Witten et al., 2011). We selectively targeted ChR2(H134)-eYFP to VTA-DA neurons (**Figure 2.26A**) and tested whether mice would engage in wireless, optical self-stimulation (20 5-ms pulses every nose poke) of their dopamine reward pathway. To increase the contextual salience of the stimulation and to demonstrate wireless function of the μ-ILED devices, the mice were free to explore a complex environment (**Figure 2.27A-C**). In the absence of physical reward, the same stimulation of VTA-DA neurons that drives a traditional conditioned place preference (**Figure 2.10**) (Adamantidis et al., 2011; Tsai et al., 2009) is actively sought with a cued nose poke when paired within a discrete environmental context. ChR2(H134)-eYFP mice learned to self-stimulate their dopamine neurons (**Figure 2.26B and C**) and, furthermore, developed a robust place preference (**Figure 2.26D and E**) for the environmental context containing the active nose poke for VTA-DA stimulation. ChR2(H134)-eYFP animals showed strong correlation ($r = 0.8620$, $p = 0.0272$) between the number of active nose pokes and the magnitude of conditioned place preference that was absent in eYFP controls (**Figure 2.26F and Figure 2.27E**). In addition, we examined the effects of wireless tonic stimulation of VTA-DA neurons on anxiety-like behavior. Tonic stimulation (at 5 Hz) reduced anxiety-like behavior, whereas phasic activation of VTA-DA neurons did not have an effect on anxiety-like behavior (**Figure 2.28**). These findings are consistent with the anxiolytic actions of nicotine on VTA-DA neurons, as well as the behavioral phenotypes seen in the *Clock*Δ19 mice that have increased tonic firing of VTA-DA neurons (Coque et al., 2011;

McGranahan et al., 2011) and further establish the utility of wireless optogenetic control in multiple environmental contexts.
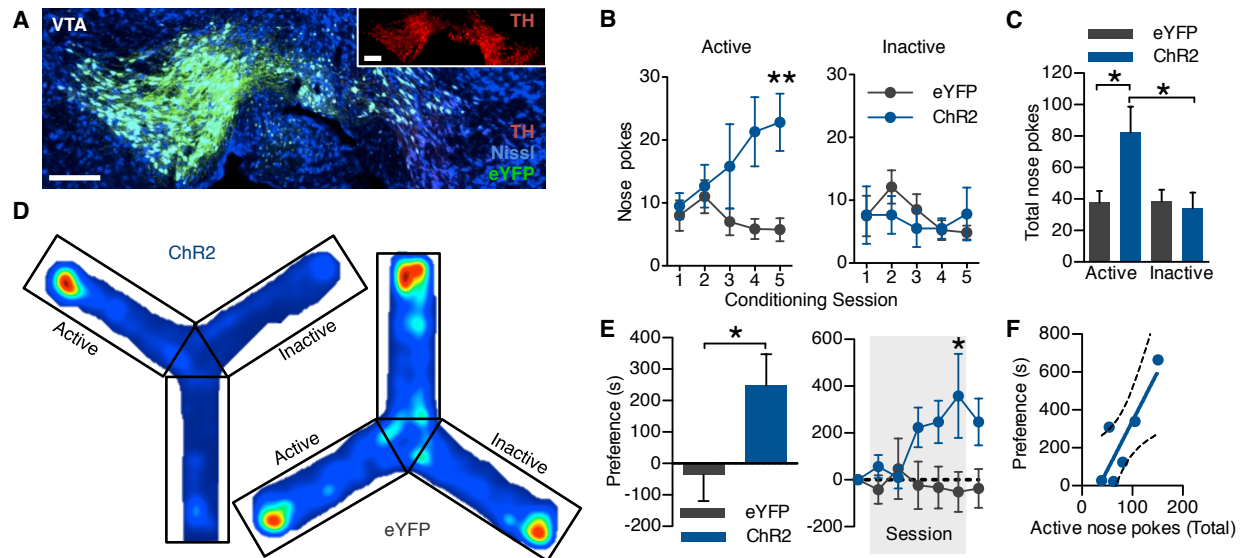
Figure 2.26. **Wirelessly powered μ-ILED devices operantly drive conditioned place preference**. (**A**) Cell-type specific expression of ChR2(H134)-eYFP (green) in dopaminergic, TH (red) containing neurons of the VTA. For clarity, inset shows TH channel alone. All scale bars = 100 μm. (**B**) Operant learning curve on the active (left) and inactive (right) nose poke devices over 5 days of 1-hour trials in the Y-maze. Active pokes drive 1 s of 20 Hz light (5 ms pulses) from the μ-ILED device on a fixed-ratio-1 schedule (n = 6-8 mice/group; Two-way ANOVA with Bonferroni post-hoc; **p < 0.01). (**C**) Mean number of nose pokes ± SEM across all five conditioning sessions. (*p < 0.05 One-way ANOVA with Bonferroni post-hoc) (**D**) Heat maps of activity during the post-test, hotter colors represent longer duration in a location in that part of the apparatus. (**E**) Left, place preference scores calculated as post-test minus pre-test in the active nose poke-paired context. Five days of self-stimulation significantly conditioned a place preference that developed over the course of the training sessions and remained during the post-test (right; *p < 0.05 t-test compared to controls; *p < 0.05 Two-way ANOVA with

Bonferroni post-hoc). All error bars represent means ± SEM (**F**) Scatter plot demonstrating positive correlation (r = 0.8620, p = 0.0272) between post-test preference and total number of active nose pokes during training in the ChR2(H134)-eYFP group.
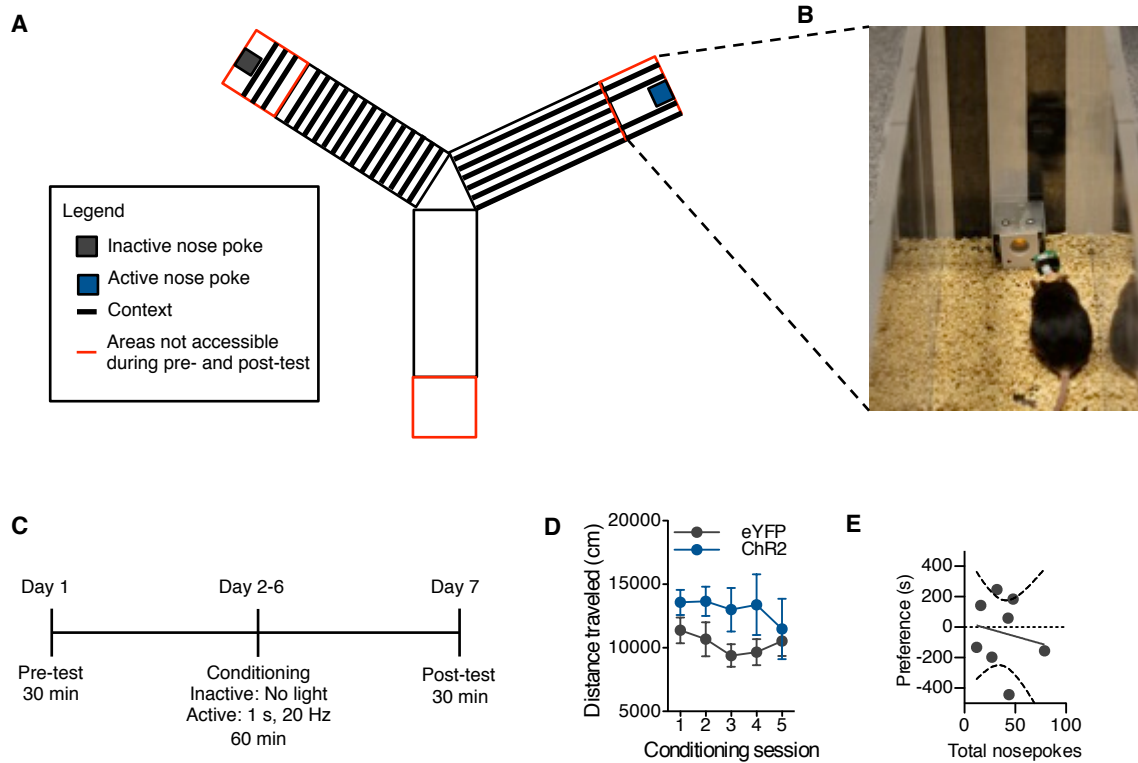
Figure 2.27 Wireless μ-ILED devices drive an operantly conditioned place preference. (**A**) Cartoon and (**B**) photo of Y-Maze with contexts and nose poke devices, red zones were not accessible during pre/post-tests. (**C**) Timeline of experimental approach. (**D**) Total activity during the conditioning shows increase in total ambulation of the ChR2 mice during the first four days of training. (**E**) Scatter plot demonstrating no correlation (r=-0.1707, p=0.6861) between post-test preference and total number of active nose pokes during training in the AAV-DIO-eYFP injected controls.
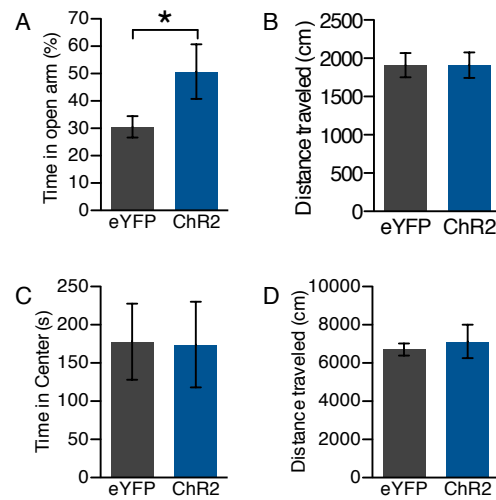
Figure 2.28 Tonic, not phasic, activation of VTA-DA neurons induces anxiolytic-like behavior. (**A**) 5 Hz activation of VTA-DA neurons induces an anxiolytic-like behavioral response in an elevated zero maze independent of (**B**) locomotor effects (n=6-9; *p<0.05 t test compared to AAV5-DIO-eYFP controls). (**C**) Phasic (20, 5 ms pulses of 20 Hz light every minute) stimulation does not influence anxiety-like behavior or (**D**) locomotor activity in the open field test (n=6-8/group).

DISCUSSION

These experiments demonstrate that these devices can be readily used in optogenetic experiments. Future possible uses are in closed-loop operation, where actuators (e.g. heat, light, and electrical) operate in tandem with sensors (e.g. temperature, light, and potential) for altering light stimulation in response to physiological parameters, such as single-unit activity, pH, blood oxygen or glucose levels, or neurochemical changes associated with neurotransmitter release. Many of the device attributes that make them useful in optogenetics suggest strong potential for broader use in biology and medicine. The demonstrated compatibility of silicon technology in these injectable, cellular-scale platforms foreshadows sophisticated capabilities in electronic processing and biological interfaces. Biocompatible deep-tissue injection of semiconductor devices and integrated systems, such as those reported here, will accelerate progress in both basic science and translational technologies.

MATERIALS AND METHODS

Preparation of μ-ILEDs

The fabrication began with epitaxially grown GaN on a sapphire wafer (500 μm thick double polished sapphire with 2" diameter, Cermet Inc.). The GaN stack layers consisted of undoped GaN (3.8 μm), n-type GaN (2 μm), spacer (0.4 μm), MQW (0.14 μm), and p-type GaN (0.2 μm). Residual metal ions and GaN oxide on the surface were removed by rinsing with diluted HCl (33 %). L-shaped current spreading layers of Ni (15 nm) and Au (15 nm) were formed by sputter deposition (AJA ATC 2000), followed by annealing at 500 $^{\circ}$C for 5 min in an oxygen and nitrogen atmosphere to form an ohmic contact. After exposing n-type regions defined using photolithography (40 x 40 μm^2 recessive square with thick AZ 2035, Microchem Inc) and etched using chorine based-inductively coupled plasma reactive ion etching (ICP RIE,

Plasmatherm, SLR-770), both n- and p- contact pads, each 25 x25 μm^2 in dimension, of 15 nm of Cr and 300 nm of Au were deposited by electron beam evaporation (Temescal, FC-1800). To define the lateral dimensions of the devices (100x100 μm^2), chorine based ICP RIE was used to remove GaN down to the sapphire substrate, with negative tone photoresist as an etching mask (AZ 2070, Micorchem Inc).

After deposition of a passivation layer of SiN_x (200 nm) by plasma enhanced chemical vapor deposition (PECVD; STS, Mesc Multiple) the processed substrate was bonded to a silicon wafer using a layer of palladium (Pd)-indium (In) chemical alloy, followed by laser lift off (KrF, intensity,~0.9 J/cm^2) to remove the sapphire from the μ-ILEDs. Here, the laser light triggered thermal decomposition at the GaN-sapphire interface, allowing easy mechanical removal of sapphire substrate upon heating to 70 ^{o}C on a hotplate. Wet etching with 5 wt% diluted HCl selectively removed the underlying unalloyed In layer, leaving residual porous structures of In-Pd alloy that served as anchors to tether the μ-ILEDs to the silicon wafer. In this configuration, the devices were easily lifted onto the surfaces of microstructured (3 μm in diameter, 1.2 μm in height, and 5 μm in space) slabs of poly(dimethylsiloxane) (PDMS; Sylgard 184, Dow Corning) via the action of van der Waals forces. Etching the exposed unalloyed Pd and passivation layer (SiN_x) removed all of residual metal on the μ-ILEDs. The result was an array of μ-ILEDs on microstructured PDMS, suitable for manipulation by transfer printing, for integration onto microneedles.

Fabrication of releasable, injection microneedles

To fabricate penetrating polymeric microneedles, suitable shapes were first defined in layers of Cr (15 nm) and Au (300 nm) deposited on a glass slide (5 x 3.5 cm^2) by photolithography and wet etching. Photo-curable epoxy (SU-8 100, Microchem Inc) was then spin cast (1100 rpm for

250 μm and 1800 rpm for 150 μm thickness) on the slide, and ultraviolet light was passed (380 mJ/cm^2) through the backside to define a pattern of exposure in the epoxy, with the geometry of the microneedle. Developing away the unexposed regions followed by thermal annealing (150 ^{o}C for 10 min) defined and fully cured the epoxy to complete the fabrication of microneedles, typically in array geometries. Poor adhesion between the glass and the epoxy allowed easy mechanical removal of the microneedles, with tweezers, stamps or other implements. The left image of **Figure 2.6** shows an array of epoxy microneedles on glass. The left and right three microneedles were removed before this image was collected.

To fabricate 6 μm thick (or 2.5 μm thick for μ-ILED) polyester device substrates (Mylar$^®$ film, Chemplex$^®$ industries) with similar microneedle layouts, the films were first laminated on a PDMS coated substrate. Patterns of Cr (100 nm thickness) in microneedle geometries were used as etching masks for oxygen plasma RIE (March polymer RIE) of the exposed regions of the films. Wet etching of the Cr completed the fabrication.

Fabrication of sensors

For microelectrodes and temperature sensors, 6 μm thick, patterned polyester films on PDMS coated glass, formed according to procedures described above, were used. To fabricate the electrophysiological sensor, 100 μm wide and 100 nm thick lines of Pt were formed on the needle by photolithography and lift-off using negative tone resist (AZ 2070, Microchem Inc). To measure electrophysiological signals from a single neuron, an epoxy passivation layer (SU-8 2, Microchem Inc.) defined 20 x 20 μm^2 openings to the underlying Pt, as the sensing locations. For temperature sensors, 20 nm thick and 20 μm wide Pt serpentine structures served as resistors, connected by Au electrodes at both ends.

For the photodetectors, the top silicon layer of an silicon on insulator (SOI) wafer (1.25 μm thick silicon on a 400 nm thick layer of silicon dioxide on a silicon substrate, Soitec) was p- and n- doped sequentially through masking layers of silicon dioxide (900-nm thick) deposited by plasma-enhanced chemical vapor deposition and patterned by photolithography and etching. For p-doping, the sample was exposed to a boron source for 30 min at 1000 ^{o}C in an N_2 environment. The n- doping used a phosphorous source under the same conditions for 10 min. A single cell had a size of 200 μm x 200 μm including p- and n- doped parts with 200 μm x 40 μm (active area: 200 μm x 120 μm), isolated by reactive ion etching through the silicon layer in a geometry patterned by photolithography. The buried oxide layer of the SOI wafer was partially etched to slightly undercut slicon layer. Next, photolithography defined photoresist structures at the four corners of each square cell to hold the silicon layers to the underlying silicon wafer during complete removal of the silicon dioxide layer with HF.

Measurements on μ-IPD

The current responses of μ-IPDs at different current injection levels (0 to 9 mA) into four blue μ-ILEDs, in an array, were measured at biases of -5V to 5V. For time-dependent light response measurements, AC current with four different frequencies (i.e., 3, 5, 10, and 20 hz) were applied to the μ-ILEDs using a pulse generator (Global Specialities®). The current resonse of the μ-IPDs at a bias of -3V were measured for 8 s with a sampling rate of 160 Hz.

Impedance measurements on microelectrode

Impedance was measured using a potentiostat (Gamry instruments, reference 600) with phoshate buffered saline (PBS, Sigma-Aldrich). The PBS solution was diluted in 1 liter

deionized water for 0.01 M, pH 7.4 at 25 $^{\circ}$C. To measure impedance, we appied frequency ranging from 11.0 KHz to 1 KHz.

Fabrication of μ-ILED arrays and interconnects on microneedles

1.   A PDMS stamp with posts (100 × 100 μm and heights of 100 μm) was positioned above μ-ILEDs on a structured PDMS slab and then used to remove an μ-ILED, one at a time, for integration onto a thin UV curable adhesive coated on a 2.5 μm thick microneedle shaped substrate (patterned polyester film on PDMS coated glass, fabricated using steps similar to those described above for the sensors). The printing was performed using a modified mask aligner (Karl Suss, MJB). To form interconnected arrays of μ-ILEDs, the SiN$_x$ passivation layer was first removed by reactive ion etching (RIE; Plasmatherm 790). Coating with an adhesion promoter (Dow, AP3000) and then a layer of photosensitive benzocyclobutene (6 μm thick; BCB) prepared the devices for backside exposure to ultraviolet light, through the transparent substrate. This light exposed the BCB in all regions except those above the opaque n-, and p-contact pads. Developing away the unexposed BCB (Advanced Developer, DS2100) and blowing with a stream of N$_2$ removed the residual developer, to complete the patterning process for via holes. After fully curing the BCB in an Ar atomosphere in a glove box at 210 $^{\circ}$C for 3 hr, remaining BCB residues on the contacts were removed by oxygen RIE. To form metallization lines to the contacts, 15 nm of Cr and 300 nm of Au were sputter deposited, and then wet etched through a photopatterned layer of photoresist. Finally, an epoxy layer (2 μm thick, SU-8 2 Microchem) was spin cast and cured to form insulating coatings on the electrodes.

Forming multi-functional μ-ILED systems on releasable injection microneedles

Separately fabricated thermal and electrophysiological sensors and printed μ-ILEDs, each on polyester thin film substrates, were stacked in an aligned configuration on a penetrating epoxy microneedle substrate using a modified mask aligner (Karl Suss, MJB). A thin layer of UV curable epoxy (SU-8 2) served as an adhesive for bonding the sensors and the μ-ILEDs. For bonding the entire stack to the penetrating microneedle, a thin layer of purified silk (7 wt%) was used, to allow release of after implantation. After curing or drying, the adhesives in all cases have thicknesses of a few hundred nanometers.

Characterization of optical and thermal properties

Optical measurements of the emission spectra and light output were obtained with a spectrometer (HR4000 and FOIS-1 fiber optics integrating sphere, Ocean Optics). Thermal measurements were performed using a MWIR-based InDb thermal imager (InfraScope, GFI) with a base temperature of 37°C.

Wired powering

μ-ILED devices were connected to a function generator (AMPI, Master-9 or Tektronix, AFG3022B) and TTL modulation (low 0V, high 4V) was used to power the μ-ILEDs at the stated frequencies and pulse widths.

Wireless powering and RF powering scavenger

The wireless power transmitter includes a low-frequency signal generator, an RF signal generator, a power supply, a RF power amplifier, and a panel antenna. The low-frequency signal generator outputs an amplitude modulation signal to modulate the RF power generator. The RF

power amplifier that is powered by the power supply enlarges the modulated RF signal from the RF signal generator. The RF power is then transmitted from the panel antenna on 75 μm thick polyimide layer or commercialized PCB board. The RF signal generator has a power output from -10 to -17 dBm at 910 MHz, which corresponds to a power ranging from 0.1 mW to 0.02 mW. The power amplifier has a gain of 49 dB, thus the power output from the power amplifier is from 1.6 to 7.9 W. Under an antenna gain of 13 dBi and at a distance that is approximately 1 meter away from the antenna, the RF power that reaches the mice is approximately 4 mW, given an exposure area of the mice of ~32 cm^2. Mice with chronically implanted μ-ILED devices were acutely connected to the headstage antenna immediately prior to any wireless photostimulation.

Numerical modeling of temperature in the μ-ILEDs

A three dimensional (3D) model was established to study the temperature distributions in the system in the pulsed mode and DC mode. Eight-node, hexahedral brick elements in the finite element software ABAQUS were used to discretize the geometry. The μ-ILEDs are modeled as heat sources. The bottom surface of device was set as a constant temperature, while the other surfaces are free heat convection boundary with the convection heat transfer coefficient 25 W/(m^2·K). The initial temperature of the device was set as the environmental temperature T_∞. The dimensions and layout of the device can be found in the main text. The microelectrodes and the sensors were neglected in the finite element simulations due to their small thickness (~300 nm) compared to that of other layer (~6 μm). The thermal conductivity, density and thermal capacity are 317 W/(m·K), 19300 kg/m^3 and 130 J/(kg·K) for Au, 0.2 W/(m·K), 1190 kg/m^3 and 1200 J/(kg·K) for epoxy (Solano et al., 2008), 0.15 W/(m·K), 1050 kg/m^3 and 1270 J/(kg·K) for polyester (Mattsson et al., 2007), 230 W/(m·K), 2330 kg/m^3 and

700 J/(kg·K) for μ-ILEDs (Kim et al., 2012b), and 0.29 W/(m·K), 1050 kg/m³ and 2180 J/(kg·K) for BCB (Modafe et al., 2005).

Figure 2.18A shows the time-average temperature of μ-ILEDs operated in pulsed modes (3, 10, and 20 Hz) and DC mode at 5, 10, 15 and 20 mW input power when the background temperature is $T_\infty = 37$ °C. The finite element results (line) agree well with the experimental measurements (dot). **Figure 2.18B and C** show the surface temperature distribution from experiments and finite element simulations. They agree reasonably well with each other and the discrepancy is due to the assumption of heat source only for μ-ILEDs since other parts (e.g., Au interconnect) may also serve as heat sources.

Analytical modeling of temperature in the tissue

An analytical model was established to obtain the steady temperature in the tissue when the device is inserted into the mouse brain tissue. The μ-ILED is modeled as a disk heat source with a radius $r_0 = L/\sqrt{\pi}$ corresponding to the same area of μ-ILED ($L \times L$) and a heat generation of $Q(t)$. Since the thickness of tissue (~4 mm) is much larger than that of device (~100 μm), we ignore the device structure in the analytical modeling. Once we have the temperature due to a single μ-ILED, the temperature due to four *μ*-ILEDs can be obtained by the superposition theorem.

The heat transfer equation in cylindrical coordinate with the origin as the center of μ-ILED is

$$\frac{\partial^2 T}{\partial r^2} + \frac{1}{r}\frac{\partial T}{\partial r} + \frac{\partial^2 T}{\partial z^2} - \frac{c\rho}{k}\frac{\partial T}{\partial t} = 0 \tag{1}$$

72

where k is thermal conductivity of tissue, ρ is density of tissue, c is specific heat capacity of tissue. The thermal diffusivity of tissue is $\alpha = k/(c\rho)$. By setting $\theta = T - T_\infty$, where T_∞ is the remote temperature, the above equation becomes

$$\frac{\partial^2 \theta}{\partial r^2} + \frac{1}{r}\frac{\partial \theta}{\partial r} + \frac{\partial^2 \theta}{\partial z^2} = \alpha \frac{\partial \theta}{\partial t} \tag{2}$$

Boundary conditions involve the adiabatic condition on the top surface ($z=-h_0$) and a constant temperature $T_\infty = 37\ ^\circ C$ on the bottom surface ($z=h_1$). At the μ-ILED interface ($z=0$), discontinuous heat flow $Q(t)$ is assumed as a means to introduce the input pulsed power. Let's consider a unit pulsed power $P(t)$ for time between 0 an t_0 with a period T, which can be expanded into Fourier Series

$$P(t) = \begin{cases} 1 & 0 < t \le t_0 \\ 0 & t_0 < t \le T \end{cases} = a_0 + \sum_{n=1}^{\infty} a_n \cos n\omega t + \sum_{n=1}^{\infty} b_n \sin n\omega t \tag{3}$$

where $\omega = 2\pi/T, a_0 = t_0/T, a_n = 2\sin(n\omega t_0)/(n\omega T), b_n = 2[1-\cos(n\omega t_0)]/(n\omega T)$. For each $\cos(nwt)$ [or $\sin(nwt)$] in the power expression of Eq. (3), we can assume the solution of Eq. (2) to be $\theta(r,z,t) = \psi(r,z)\exp(n\omega t i)$. Equation (2) then becomes

$$\frac{\partial^2 \psi}{\partial r^2} + \frac{1}{r}\frac{\partial \psi}{\partial r} + \frac{\partial^2 \psi}{\partial z^2} - q^2 \psi = 0 \tag{4}$$

where $q^2 = \dfrac{n\omega i}{\alpha}$. Equation (4) can be solved by applying the Hankel transformation. For $-h_0 \le z \le 0$, we obtain the solution as

$$\psi(r,z;n\omega) = \int_0^{+\infty} A_0 \left[\exp(z\sqrt{s^2+q^2}) + \exp(-z\sqrt{s^2+q^2} - 2h_0\sqrt{s^2+q^2}) \right] J_0(sr)s\,ds, \tag{5}$$

73

where $A_0 = \dfrac{r_0 J_1(sr_0)}{2k_s s\sqrt{s^2+q^2}} \dfrac{1-\exp(-2h_1\sqrt{s^2+q^2})}{1+\exp(-2h_0\sqrt{s^2+q^2}-2h_1\sqrt{s^2+q^2})}$.

The temperature increase due to the power of $\cos(nwt)$ [or $\sin(nwt)$] is then equal to

$|\psi(r,z;n\omega)|\cos(n\omega t+\beta_n)$ [or $|\psi(r,z;n\omega)|\sin(n\omega t+\beta_n)$] where $\tan(\beta_n)=\mathrm{Im}(\psi)/\mathrm{Re}(\psi)$. The

temperature due to the power $P(t)$ in Eq. (3) is given by

$$\psi(r,z,t)=a_0\psi(r,z;0)+\sum_{n=1}^{\infty}a_n|\psi(r,z;n\omega)|\cos(n\omega t+\beta_n)+\sum_{n=1}^{\infty}b_n|\psi(r,z;n\omega)|\sin(n\omega t+\beta_n) \quad (6)$$

The temperature due to the four μ-ILEDs with total power $Q(t)=Q_0*P(t)/4$ can then be given by

$$\psi_{tot}(r,z,t)=\frac{Q_0}{4}\sum_{i=1}^{4}\psi_i(r,z,t) \tag{7}$$

In vitro experiments, the thermal conductivity k of the issue is 0.6 W/(m·K), the density ρ is

1040 Kg/m^3, the specific heat c is 3650 J/(kg·K)(Elwassif et al., 2006). The predicted surface

temperature ($z=-h_0$) agrees well with experimental measurement as shown in **Figure 2.19 and

Figure 2.15D and E**. In vivo experiments, there is a heat loss due to blood flow and we fit an

effective power to be 0.62 mW at 3Hz. Then the predicted the time-averaged temperature at the

location of temperature sensor ($z=-6$ μm) agrees very well with that in experiments at other

frequencies with ~5% error. To further verify the analytical solution in Eq. (7), a full 3D finite

element model for the device/tissue system is also established. The time history of average

temperature in **Figure 2.15F** shows a good agreement between finite element simulation and

experimental measurement.

Preparation of phantom skin and IR measurement of RF scavenger

The potential localized heating effect of RF power is characterized using a phantom skin sample that is placed in the RF field. The phantom skin (Esler et al., 2010; Ito et al., 2001) is a gelatin-based material that is made of the combination of water, agar, polyethylene, sodium chloride, sodium azide (Sigma-Aldrich Co.), and TX 151 (Oil Center Research), and has similar electrical properties as animal skin at the RF range. The thermal imaging is taken using an infrared camera (A655sc, FLIR Systems, Inc.), which has high resolution and a measurement accuracy at ±2% of the reading value.

Experimental subjects

Adult (25–35 g) male C57BL/6J and TH::IRES-Cre backcrossed to C57BL/6J mice were group-housed, given access to food pellets and water *ad libitum* (except where noted) and maintained on a 12 h:12 h light:dark cycle (lights on at 7:00 AM). All animals were held in a facility in the lab 1 week prior to surgery, post-surgery and throughout the duration of the behavioral assays to minimize stress from transportation and disruption from foot traffic. All procedures were approved by the Animal Care and Use Committee of Washington University and conformed to US National Institutes of Health guidelines.

Viral preparation

Plasmids coding pAAV-EF1a-DIO-EFYP, pAAV-EF1a-double floxed-hChR2(H134R)-EYFP-WPRE-HGHpA, and pLenti-EF1a-hChR2(H134R)-EYFP-WPRE were obtained from Addgene (Addgene.org) originally from the Deisseroth Laboratory at Stanford University. The DNA was amplified with a Maxiprep kit (Promega) and packaged into AAV5 serotyped viruses by the WUSTL Hope Center Viral Core. LV-PGK-GFP was provided by the WUSTL viral core

facility. The final viral concentration was 2-5 x 10^{12} genome vg/mL for the adeno-associated viruses and 1.1-1.3 x 10^8 IU/ml for all the lentivirus used.

Table 2.2

Plasmid	Source	Packaged by	Serotype	Titer
pAAV-EF1a-DIO-EFYP	Deisseroth Laboratory (Stanford)	WUSTL Hope Center Viral Core	AAV5	5 x 10^12 vg/ml
pAAV-EF1a-double floxed-hChR2(H134R)-EYFP-WPRE-HGHpA	Deisseroth Laboratory (Stanford)	WUSTL Hope Center Viral Core	AAV5	2 x 10^13 vg/ml
pLenti-EF1a-hChR2(H134R)-EYFP-WPRE	Deisseroth Laboratory (Stanford)	WUSTL Hope Center Viral Core	N/A	1.1 x 10^8 IU/ml
pRRLsinPGK-GFPppt	Sands Laboratory (WUSTL)	WUSTL Hope Center Viral Core	N/A	1.3 x 10^8 IU/ml

Stereotaxic surgery

After the animals were acclimatized to the holding facility for seven to nine days, they were anaesthetized in an induction chamber (4% Isolflurane) and placed in a stereotaxic frame (Kopf Instruments, Model 1900) where they were maintained at 1-2% isoflurane. A craniotomy was performed and mice were injected with 1ul of AAV5-DIO-ChR2 or AAV5-DIO-eYFP, LV-Ef1α-ChR2-eYFP, or LV-Ef1α-GFP unilaterally into the VTA (stereotaxic coordinates from bregma: -3.20 anterior-posterior (AP), +/−0.50 medial-lateral (ML), −4.90 mm dorsal-ventral (DV)), LC (-5.45 AP, +/- 1.25 ML, -4.00 DV), or the ventral striatum (1.3 AP, +/- 1.0 ML, -4.00

DV). Mice were then implanted with metal cannula (PlasticsOne; coordinates adjusted from viral injection 0.00 AP, +/- 0.25 ML, +1.00 DV), fiber optic implants (coordinates adjusted from viral injection 0.00 AP, +/- 0.25 ML, +1.00 DV)(Sparta et al., 2011), or a μ-ILED device (same coordinates as viral injection). Custom adapters (WUSTL Instrument Machine Shop) for the Kopf cannula holder (Model 1966) were used to implant the fiber optics and the μ-ILED devices. For biodissolvable samples, the device was implanted at the desired target, ACSF was applied to the portion of the device that remained outside of the skull to facilitate dissolution of the adhesive, and then the epoxy needle was removed after a delay of 15 minutes. The implants were secured using two bone screws (CMA, 743102) and affixed with TitanBond (Horizon Dental Products) and dental cement (Lang Dental). Mice were allowed to recover for 3-5 weeks prior to behavioral testing; this interval also permitted optimal AAV expression and Cre recombinase activity.

Immunohistochemistry

Immunohistochemistry was performed as described (Bruchas et al., 2011). Briefly, mice were anesthetized with pentobarbital and intracardially perfused with ice-cold 4% paraformaldehyde in phosphate buffer (PB). Brains were dissected, post-fixed for 24 hr at 4 ºC and cryoprotected with solution of 30% sucrose in 0.1M PB at 4ºC for at least 24 hr, cut into 30 μm sections and processed for immunostaining. 30 μm brain sections were washed three times in PBS and blocked in PBS containing 0.5% Triton X-100 and 5 % normal goat serum. Sections were then incubated for ~16 hr at room temperature in rabbit anti c-fos antibody (1:20000, Millipore), guinea pig anti-GFAP (1:500, Synaptic Systems), rabbit anti-Iba1 (1:300, Wako Chemicals) and/or chicken anti-TH (1:2000, Aves Labs). Following incubation, sections were washed three times in PBS and then incubated for 2 hr at room temperature in Alexa Fluor 488

goat anti-mouse IgG (1:500, Invitrogen), Alexa Fluor 594 goat anti-rabbit IgG (1:500, Invitrogen-), goat anti-chicken Alexa Fluor 633(1:500, Invitrogen) and/or goat anti-guinea pig Alexa Fluor 546(1:500, Invitrogen) were then washed three times in PBS and followed by three 10-min rinses in PB and mounted on glass slides with Vectashield (Vector Labs) and sealed with nail polish for microscopy. All sections were imaged on both epifluorescent (Olympus BX61) and confocal (Olympus Fluoview 500) microscopes. Gain and exposure time were constant throughout, and all image groups were processed in parallel using Adobe Photoshop CS5 (Adobe Systems).

Table 2.3

Antibody	Species	Dilution	Source
GFAP	Guinea Pig	1:500	Synaptic Systems
Iba1	Rabbit	1:300	Wako Chemicals
TH	Chicken	1:2000	Aves Labs
c-fos	Rabbit	1:20,000	Millipore
Alexa Fluor 488 anti-mouse IgG	Goat	1:500	Invitrogen
Alexa Fluor 594 anti-rabbit IgG	Goat	1:500	Invitrogen
Alexa Fluor 633 anti-chicken IgG	Goat	1:500	Invitrogen
Alexa Fluor 546 anti-guinea pig IgG	Goat	1:500	Invitrogen
Alexa Fluor 594 anti-chicken IgG	Goat	1:500	Invitrogen

Cell culture and transfection of NOPR-YFP expressing, HEK293 Cells

A single 50 x 50 x 6.45 µm µ-ILED was printed onto a standard glass coverslip (Fisherbrand, 12-545-80). The glass was coated with Poly-L-lysine (Sigma-Aldrich, P4707) to facilitate cell adhesion. Stable HEK293 cells expressing pcDNA3 containing nociceptin opioid peptide receptor-YFP (NOPR-YFP) were generated as previously described (Zhang et al., 2012). The NOPR-YFP expressing cells were grown on the coverslip in a 24-well plate and placed in a 37 °C 5% CO_2 incubator. Cells were washed three times with PBS and then fixed in 4% paraformaldehyde for 20 min, washed in PBS, washed in 0.1 M PB, and mounted using VECTASHIELD (Vector Laboratories) and sealed with clear nail polish. Images were captured using Metamorph 7.6 (Molecular Devices) and processed with ImageJ 1.44o (NIH).

cAMP Assay

HEK293 cells were co-transfected with Optoβ$_2$ (Airan et al., 2009) (pGloSensor-22F cAMP plasmid (Promega E2301) in 96-well format. Using a SynergyMx microplate reader (BioTek; VT, USA), baseline luminescence recordings were taken. In the presence of 9-cis retinal (1µM), cells were exposed to µ-ILED light (450 nm, 5 sec, 0.5 W/cm^2 pulse) and relative luminescent units taken every 2 sec using GloSensor cAMP Assay (Promega). Relative luminescent units were normalized to an initial 1 min recording of baseline. Data are expressed as ± S.E.M.

Immunoblotting

Western blots for phospho-MAPKs were performed as described previously (Zhang et al., 2012). Briefly, Optoβ$_2$ expressing HEK293 cells were serum-starved 4-6 h prior to treatment. Cells were light treated (450 nm, 1 min, 0.5 W/cm^2 pulse), lysed in 70 µl of lysis buffer (50 mM Tris-HCl, 300 mM NaCl, 1 mM EDTA, 1 mM Na3VO4, 1 mM NaF, 10% glycerol, 1% Nonidet

P-40, 1:100 of phosphatase inhibitor mixture set 1 (Calbiochem), and 1:100 of protease inhibitor mixture set 1 (Calbiochem)), sonicated for 20 s, centrifuged for 15 min (14000 x g, 4 °C). 50 μg of total protein was loaded onto non-denaturing 10% bisacrylamide precast gels (Invitrogen) and run at 150 V for 1.5 h. Blots were transferred to nitrocellulose (Whatman, Middlesex, UK) for 1.5 h at 30 mV, blocked in TBS/5% bovine serum albumin for 1 hr, incubated overnight at 4 °C with a 1:1000 dilution of goat-anti- rabbit phospho-ERK 1/2 (Thr-202/Tyr-204) antibody (Cell Signaling) and mouse actin (1:20,000, AbCam). Following overnight incubation, membranes were washed 4 x 15 min in TBST (Tris- buffered saline, 1% Tween 20) and then incubated with IRDye 800- and 700 conjugated affinity-purified anti-rabbit or anti-mouse IgG at a dilution of 1:5000 (pERK) or 1:20,000 (actin) in a 1:1 mixture of 5% milk/TBS and Li-Cor blocking buffer (Li-Cor Biosciences, Lincoln, NE) for 1 h at room temperature, washed 3 x 10 min in TBST, 1 x 10 min in TBS and analyzed using the Odyssey infrared imaging system (Li-Cor Biosciences). Band intensity was measured using Odyssey software following background subtraction and integrated band density in high-resolution pixels calculated. All subtypes of ERK (1 and 2) were quantified together. All pERK bands were normalized to actin, as an equal protein loading control and plotted using GraphPad (GraphPad Prism 5.0) software. Statistical significance was taken as * $p < 0.05$ as determined by unpaired two-tailed t-test.

In vivo *electrophysiology*

To demonstrate the ability of the incorporated electrode, spontaneous cellular activity was monitored in the deep midbrain (**Figure 2.15H**). For light modulated responses, an array of 16 (35-μm tungsten wires, 150-μm spacing between wires, 150-μm spacing between rows, Innovative Physiology) was epoxied to a rigid μ-ILED device and lowered into the VTA of a

lightly (~1% isoflurane) anesthetized, TH-Cre mouse expressing ChR2(H134)-eYFP in the VTA (**Figure 2.17**). Two skull screws were arbitrarily placed anterior to bregma on either side of the midline and used to ground the electrode array. In either approach, voltage readings from each electrode were bandpass-filtered with activity between 250 and 8,000 Hz analyzed as spikes. The signal was amplified and digitally converted using commercially available hardware and software (Omniplex and PlexControl, Plexon). Spikes were sorted using principal component analysis and/or evaluation of t-distribution with expectation maximization (Offline sorter, Plexon).

Light path visualization

A 200 μm, 0.48 NA diameter fiber optic coupled to a 465 nm blue LED (Plexon) or devices with four, 100 x 100 x 6.45 μm 450 nm blue μ-ILEDs were adjusted to have the same (~280 μW) light output. The light sources were submerged in 30 μM fluorescein sodium salt (Sigma-Aldrich, F6377) (Tye et al., 2011) in deionized water and the photos were taken in a dark room with an exposure of 1/1000 s and an f-number of 5.6 from ~50 cm away for all images. Each photo was cropped using Photoshop (Adobe Systems), but no other processing was used.

c-fos expression

C57BL/6J mice were injected with LV-Ef1α-ChR2-eYFP or LV-PGK-GFP into the LC as described above. Three weeks later, animals were anesthetized, mounted on the stereotaxic instrument, and fiber optics or μ-ILED devices were acutely implanted to target the LC. 5 mW, 3 Hz blue light stimulation was delivered for 1 hour (Carter et al., 2010), animals were perfused immediately following, and immunohistochemistry was performed as above. Slices from the LC originated from approximately -5.45 mm caudal to bregma were mounted and imaged. For

quantification, the LC was divided into three (dorsal, central, and ventral) 100 x 100 μm compartments. TH and c-fos labeled channels were separated, the compartment mask was applied, an exclusive threshold was set and positive staining for each channel was counted in a blind-to-treatment fashion using Metamorph. The counts from each channel were then overlaid and percent TH+ cells expressing c-fos were reported.

Immuno-glial response in implanted tissues

C57BL/6J mice (n=16) were implanted with devices into the ventral striatum and allowed to recover for either 2 or 4 weeks before perfusion. Immunohistochemistry was performed as described.

Conditioned Place Preference

VTA injected (AAV5-DIO-eYFP or AAV5-DIO-ChR2-eYFP; n=4-6/group) mice were trained in an unbiased, balanced three- compartment conditioning apparatus as described (Bruchas et al., 2011). Briefly, mice were pre-tested by placing individual animals in the small central compartment and allowing them to explore the entire apparatus for 30 min. Time spent in each compartment was recorded with a video camera (ZR90; Canon) and analyzed using Ethovision 8.5 (Noldus). Mice were randomly assigned to light and no-light compartments and received no light in the morning and light (20, 5 ms pulses every minute) in the afternoon at least 4 h after the morning training on three consecutive days. CPP was assessed on day 5 by allowing the mice to roam freely in all three compartments and recording the time spent in each. Scores were calculated by subtracting the time spent in the light stimulus-paired compartment post-test minus the pre-test.

Real-time Place Preference

VTA injected (AAV5-DIO-eYFP or AAV5-DIO-ChR2-eYFP; n=3/group) TH-Cre mice were trained in an unbiased, balanced three-compartment conditioning apparatus as described (Lammel et al., 2012; Stamatakis and Stuber, 2012; Tan et al., 2012). Mice were trained in the same conditioning apparatus as described above, and the pretesting phase (day 1) was identical. However, on days 2–4, mice were still allowed to freely roam all three compartments. On these conditioning days, entry into one compartment was paired with 20, 5 ms pulses of light that would repeat every minute the animal remained in the light-paired chamber. On day 5, the post-testing was identical as the above. Scores were calculated by subtracting the time spent in the light stimulus-paired compartment each day minus the pre-test.

Operantly Conditioned Place Preference

VTA injected (AAV5-DIO-eYFP or AAV5-DIO-ChR2-eYFP; n=6-8/group) TH-Cre mice were prepared for nose poke training by mildly restricting daily food to four grams to stabilize body weight and facilitate behavioral responding. Mice were trained in an unbiased, balanced three-compartment Y-Maze. Each arm of the Y-Maze was 50 cm by 10 cm, a 50 cm^2 equilateral triangle connected all three arms (for a total area of 1550 cm^2), and each arm was outfitted with a unique context (white, horizontal black stripes, or vertical black stripes). At the distal end of each of the striped arms a nose poke device (Med Associates, ENV-313M). On day 1, the headstage antenna was attached and mice were pre-tested by placing individual animals in the intersection of the three arms and allowing them to explore the entire apparatus for 30 min. During the pre-test and post-test sessions, a wall was placed to prohibit access to the nose poke apparatus and the final 15 cm of each arm. On days 2-6, the headstage antenna was attached and mice were allowed access to the entire Y-Maze for 1 hour. During these conditioning sessions a cue light was on to indicate a stimulation could be achieved nose poke and turned off for 500 ms

following a poke on either device. A nose poke on the active device triggered an optical stimulation (20 pulses, 20 Hz, 5 ms pulse duration) on a fixed ratio-1 schedule, while a poke on the inactive device resulted in the cue light turning off for 500 ms. Nose pokes were recorded using a Med Associates TTL-I/O Interface connected to the Noldus Ethovision I/O Box. On day 7, the post-testing was conducted in an identical manner as the pre-test. All activity and position data was recorded using Ethovision and analyzed using Microsoft Excel and GraphPad Prism 5.0. Place preference scores were calculated by subtracting the time spent in the active nose poke-paired compartment each day minus the pre-test.

Open Field Test

OFT testing was performed in a sound attenuated room maintained at 23ºC. Lighting was measured and stabilized at 200 lux, and performed in the afternoon between 13:00–1600 hrs. The open field was a 55 x 55 cm square enclosure and was cleaned with 70% ethanol between testing trials. For testing, VTA injected (AAV5-DIO-eYFP or AAV5-DIO-ChR2-eYFP; n=6-8/group) TH-Cre mice were connected to cables coupled to a function generator and placed in the center of the open field and allowed to roam freely for 15 min. During the entire trial, animals received 20, 5 ms pulses of photostimulation. Movements were video- recorded and analyzed using Ethovision. The center was defined as a square comprised of 50% the total area of the OFT. Time in the center expressed as percentages total time was the primary measure of anxiety-like behaviors.

Elevated Zero Maze

EZM testing was performed in a sound attenuated room maintained at 23ºC. Lighting was 200 lux, and performed in the afternoon between 13:00–1600 hrs. The EZM (Harvard

Apparatus) was made of grey plastic (Dimensions: 200 cm in circumference comprised of four 50 cm sections: two opened, two closed. The maze was elevated 50 cm above the floor and had a path width of 4 cm with a 0.5 cm lip on each open section) and was cleaned with 70% ethanol between trials. For testing, VTA injected (AAV5-DIO-eYFP or AAV5-DIO-ChR2-eYFP; n=6-9/group) TH-Cre mice were connected to the headstage antenna and placed at the threshold of a closed section facing the open section and allowed to roam freely for 9 min. For the first and the final 3 minutes of each trial there was no photostimulation. For minutes 4-6, animals received 5 Hz, 5 ms width stimulation. Movements were video- recorded and analyzed using Ethovision (Noldus). Open section times expressed as percentages total time the primary measures of anxiety-like behaviors.

Data Analysis/Statistics

Data are expressed as means ± SEM. Data were normally distributed, and differences between groups were determined using independent t-tests or one-way ANOVA, or two-way ANOVAs followed by post hoc Bonferroni comparisons if the main effect was significant at $p < 0.05$. Statistical analyses were conducted using Prism 5.0 (GraphPad).

Genotyping of mouse lines

DNA was isolated from tail tissue obtained from weanling mice (21-28 days of age), and PCR screening was performed using the following primers: Cre recombinase (forward: 5'- GCA TTA CCG GTC GAT GCA ACG AGT GAT GAG-3' and reverse: 5'- GAG TGA ACG AAC CTG GTC GAA ATC AGT GCG-3') yielding a 400-bp PCR product in Cre positive animals. Fatty acid-binding protein intestinal primers (forward: 5'- TGG ACA GGA CTG GAC CTC

TGC TTT CCT AGA-3' and reverse: 5'- TAG AGC TTT GCC ACA TCA CAG GTC ATT

CAG-3') were used as positive controls and yield a 200-bp PCR product.

REFERENCES

Adamantidis, A.R., Tsai, H.-C., Boutrel, B., Zhang, F., Stuber, G.D., Budygin, E.A., Touriño, C., Bonci, A., Deisseroth, K., and de Lecea, L. (2011). Optogenetic interrogation of dopaminergic modulation of the multiple phases of reward-seeking behavior. J. Neurosci. Off. J. Soc. Neurosci. *31*, 10829–10835.

Airan, R.D., Thompson, K.R., Fenno, L.E., Bernstein, H., and Deisseroth, K. (2009). Temporally precise in vivo control of intracellular signalling. Nature *458*, 1025–1029.

Anikeeva, P., Andalman, A.S., Witten, I., Warden, M., Goshen, I., Grosenick, L., Gunaydin, L.A., Frank, L.M., and Deisseroth, K. (2011). Optetrode: a multichannel readout for optogenetic control in freely moving mice. Nat. Neurosci. *15*, 163–170.

Aravanis, A.M., Wang, L.-P., Zhang, F., Meltzer, L.A., Mogri, M.Z., Schneider, M.B., and Deisseroth, K. (2007). An optical neural interface: in vivo control of rodent motor cortex with integrated fiberoptic and optogenetic technology. J. Neural Eng. *4*, S143–S156.

Bruchas, M.R., Schindler, A.G., Shankar, H., Messinger, D.I., Miyatake, M., Land, B.B., Lemos, J.C., Hagan, C.E., Neumaier, J.F., Quintana, A., et al. (2011). Selective p38α MAPK deletion in serotonergic neurons produces stress resilience in models of depression and addiction. Neuron *71*, 498–511.

Cao, H., Gu, L., Mohanty, S.K., and Chiao, J.-C. (2013). An integrated μLED optrode for optogenetic stimulation and electrical recording. IEEE Trans. Biomed. Eng. *60*, 225–229.

Carter, M.E., Yizhar, O., Chikahisa, S., Nguyen, H., Adamantidis, A., Nishino, S., Deisseroth, K., and de Lecea, L. (2010). Tuning arousal with optogenetic modulation of locus coeruleus neurons. Nat. Neurosci. *13*, 1526–1533.

Coque, L., Mukherjee, S., Cao, J.-L., Spencer, S., Marvin, M., Falcon, E., Sidor, M.M., Birnbaum, S.G., Graham, A., Neve, R.L., et al. (2011). Specific role of VTA dopamine neuronal firing rates and morphology in the reversal of anxiety-related, but not depression-related behavior in the ClockΔ19 mouse model of mania. Neuropsychopharmacol. Off. Publ. Am. Coll. Neuropsychopharmacol. *36*, 1478–1488.

Elwassif, M.M., Kong, Q., Vazquez, M., and Bikson, M. (2006). Bio-heat transfer model of deep brain stimulation induced temperature changes. Conf. Proc. Annu. Int. Conf. IEEE Eng. Med. Biol. Soc. IEEE Eng. Med. Biol. Soc. Annu. Conf. *1*, 3580–3583.

Esler, B., Lyons, T., Turovets, S., and Tucker, D. (2010). Instrumentation for low frequency EIT studies of the human head and its validation in phantom experiments. J. Phys. Conf. Ser. *224*, 012007.

Ito, K., Furuya, K., Okano, Y., and Hamada, L. (2001). Development and characteristics of a biological tissue-equivalent phantom for microwaves. Electron. Commun. Jpn. Part Commun. *84*, 67–77.

Kim, Y., and Romero-Ortega, M.I. (2012). Material considerations for peripheral nerve interfacing. MRS Bull. *37*, 573–580.

Kim, D.-H., Viventi, J., Amsden, J.J., Xiao, J., Vigeland, L., Kim, Y.-S., Blanco, J.A., Panilaitis, B., Frechette, E.S., Contreras, D., et al. (2010). Dissolvable films of silk fibroin for ultrathin conformal bio-integrated electronics. Nat. Mater. *9*, 511–517.

Kim, D.-H., Lu, N., Ma, R., Kim, Y.-S., Kim, R.-H., Wang, S., Wu, J., Won, S.M., Tao, H., Islam, A., et al. (2011). Epidermal Electronics. Science *333*, 838–843.

Kim, K.M., Baratta, M.V., Yang, A., Lee, D., Boyden, E.S., and Fiorillo, C.D. (2012a). Optogenetic Mimicry of the Transient Activation of Dopamine Neurons by Natural Reward Is Sufficient for Operant Reinforcement. PLoS ONE *7*, e33612.

Kim, T., Jung, Y.H., Song, J., Kim, D., Li, Y., Kim, H., Song, I.-S., Wierer, J.J., Pao, H.A., Huang, Y., et al. (2012b). High-Efficiency, Microscale GaN Light-Emitting Diodes and Their Thermal Properties on Unusual Substrates. Small *8*, 1643–1649.

Kozai, T.D.Y., and Kipke, D.R. (2009). Insertion shuttle with carboxyl terminated self-assembled monolayer coatings for implanting flexible polymer neural probes in the brain. J. Neurosci. Methods *184*, 199–205.

Lammel, S., Lim, B.K., Ran, C., Huang, K.W., Betley, M.J., Tye, K.M., Deisseroth, K., and Malenka, R.C. (2012). Input-specific control of reward and aversion in the ventral tegmental area. Nature *491*, 212–217.

Mannsfeld, S.C.B., Tee, B.C.-K., Stoltenberg, R.M., Chen, C.V.H.-H., Barman, S., Muir, B.V.O., Sokolov, A.N., Reese, C., and Bao, Z. (2010). Highly sensitive flexible pressure sensors with microstructured rubber dielectric layers. Nat. Mater. *9*, 859–864.

Mattis, J., Tye, K.M., Ferenczi, E.A., Ramakrishnan, C., O'Shea, D.J., Prakash, R., Gunaydin, L.A., Hyun, M., Fenno, L.E., Gradinaru, V., et al. (2012). Principles for applying optogenetic tools derived from direct comparative analysis of microbial opsins. Nat. Methods *9*, 159–172.

Mattsson, C.G., Thungstrom, G., Bertilsson, K., Nilsson, H.E., and Martin, H. (2007). Development of an infrared thermopile detector with a thin self-supporting SU-8 membrane. In 2007 IEEE Sensors, pp. 836–839.

McGranahan, T.M., Patzlaff, N.E., Grady, S.R., Heinemann, S.F., and Booker, T.K. (2011). α4β2 nicotinic acetylcholine receptors on dopaminergic neurons mediate nicotine reward and anxiety relief. J. Neurosci. Off. J. Soc. Neurosci. *31*, 10891–10902.

Modafe, A., Ghalichechian, N., Powers, M., Khbeis, M., and Ghodssi, R. (2005). Embedded benzocyclobutene in silicon: An integrated fabrication process for electrical and thermal isolation in MEMS. Microelectron. Eng. *82*, 154–167.

Ordonez, J., Schuettler, M., Boehler, C., Boretius, T., and Stieglitz, T. (2012). Thin films and microelectrode arrays for neuroprosthetics. MRS Bull. *37*, 590–598.

Qing, Q., Pal, S.K., Tian, B., Duan, X., Timko, B.P., Cohen-Karni, T., Murthy, V.N., and Lieber, C.M. (2010). Nanowire transistor arrays for mapping neural circuits in acute brain slices. Proc. Natl. Acad. Sci. *107*, 1882–1887.

Sekitani, T., and Someya, T. (2012). Stretchable organic integrated circuits for large-area electronic skin surfaces. MRS Bull. *37*, 236–245.

Sekitani, T., Yokota, T., Zschieschang, U., Klauk, H., Bauer, S., Takeuchi, K., Takamiya, M., Sakurai, T., and Someya, T. (2009). Organic Nonvolatile Memory Transistors for Flexible Sensor Arrays. Science *326*, 1516–1519.

Solano, B., Rolt, S., and Wood, D. (2008). Thermal and mechanical analysis of an SU8 polymeric actuator using infrared thermography. Proc. Inst. Mech. Eng. Part C J. Mech. Eng. Sci. *222*, 73–86.

Sparta, D.R., Stamatakis, A.M., Phillips, J.L., Hovelsø, N., van Zessen, R., and Stuber, G.D. (2011). Construction of implantable optical fibers for long-term optogenetic manipulation of neural circuits. Nat. Protoc. *7*, 12–23.

Stamatakis, A.M., and Stuber, G.D. (2012). Activation of lateral habenula inputs to the ventral midbrain promotes behavioral avoidance. Nat. Neurosci. *15*, 1105–1107.

Stark, E., Koos, T., and Buzsaki, G. (2012). Diode probes for spatiotemporal optical control of multiple neurons in freely moving animals. J. Neurophysiol. *108*, 349–363.

Szarowski, D.H., Andersen, M.D., Retterer, S., Spence, A.J., Isaacson, M., Craighead, H.G., Turner, J.N., and Shain, W. (2003). Brain responses to micro-machined silicon devices. Brain Res. *983*, 23–35.

Takeuchi, S., Suzuki, T., Mabuchi, K., and Fujita, H. (2004). 3D flexible multichannel neural probe array. J. Micromechanics Microengineering *14*, 104.

Tan, K.R., Yvon, C., Turiault, M., Mirzabekov, J.J., Doehner, J., Labouèbe, G., Deisseroth, K., Tye, K.M., and Lüscher, C. (2012). GABA neurons of the VTA drive conditioned place aversion. Neuron *73*, 1173–1183.

Tian, B., Cohen-Karni, T., Qing, Q., Duan, X., Xie, P., and Lieber, C.M. (2010). Three-Dimensional, Flexible Nanoscale Field-Effect Transistors as Localized Bioprobes. Science *329*, 830–834.

Tian, B., Liu, J., Dvir, T., Jin, L., Tsui, J.H., Qing, Q., Suo, Z., Langer, R., Kohane, D.S., and Lieber, C.M. (2012). Macroporous nanowire nanoelectronic scaffolds for synthetic tissues. Nat. Mater. *11*, 986–994.

Tsai, H.-C., Zhang, F., Adamantidis, A., Stuber, G.D., Bonci, A., de Lecea, L., and Deisseroth, K. (2009). Phasic firing in dopaminergic neurons is sufficient for behavioral conditioning. Science *324*, 1080–1084.

Tye, K.M., Prakash, R., Kim, S.-Y., Fenno, L.E., Grosenick, L., Zarabi, H., Thompson, K.R., Gradinaru, V., Ramakrishnan, C., and Deisseroth, K. (2011). Amygdala circuitry mediating reversible and bidirectional control of anxiety. Nature *471*, 358–362.

Viventi, J., Kim, D.-H., Moss, J.D., Kim, Y.-S., Blanco, J.A., Annetta, N., Hicks, A., Xiao, J., Huang, Y., Callans, D.J., et al. (2010). A Conformal, Bio-Interfaced Class of Silicon Electronics for Mapping Cardiac Electrophysiology. Sci. Transl. Med. *2*, 24ra22–ra24ra22.

Witten, I.B., Steinberg, E.E., Lee, S.Y., Davidson, T.J., Zalocusky, K.A., Brodsky, M., Yizhar, O., Cho, S.L., Gong, S., Ramakrishnan, C., et al. (2011). Recombinase-driver rat lines: tools, techniques, and optogenetic application to dopamine-mediated reinforcement. Neuron *72*, 721–733.

Yizhar, O., Fenno, L.E., Davidson, T.J., Mogri, M., and Deisseroth, K. (2011). Optogenetics in Neural Systems. Neuron *71*, 9–34.

Zhang, N.R., Planer, W., Siuda, E.R., Zhao, H.-C., Stickler, L., Chang, S.D., Baird, M.A., Cao, Y.-Q., and Bruchas, M.R. (2012). Serine 363 is required for nociceptin/orphanin FQ opioid receptor (NOPR) desensitization, internalization, and arrestin signaling. J. Biol. Chem. *287*, 42019–42030.

Zorzos, A.N., Scholvin, J., Boyden, E.S., and Fonstad, C.G. (2012). Three-dimensional multiwaveguide probe array for light delivery to distributed brain circuits. Opt. Lett. *37*, 4841–4843.

Chapter 3

Fabrication of flexible, multimodal light-emitting devices for wireless optogenetics

Author contributions for the above citation:
*Co-first author J.G.M., T-.i.K., G.S., X.H., Y.H.J., and R.A. performed the experiments. **J.G.M**., T-.i.K., G.S., X.H., R.A., F.G.O., M.R.B. and J.A.R. developed the protocol. **J.G.M.**, T-.i.K., G.S., X.H., M.R.B. and J.A.R. wrote the manuscript.

SUMMARY

The rise of optogenetics provides unique opportunities to advance materials and biomedical engineering as well as fundamental understanding in neuroscience. This protocol describes the fabrication of optoelectronic devices for studying intact neural systems. Unlike optogenetic approaches that rely on rigid fiber optics tethered to external light sources, these novel devices utilize flexible substrates to carry wirelessly powered microscale, inorganic light-emitting diodes (μ-ILEDs) and multimodal sensors inside the brain. We describe the technical procedures for construction of these devices, their corresponding radiofrequency power scavengers, and their implementation *in vivo* for experimental application. In total, the timeline of the procedure, including device fabrication, implantation, and preparation to begin *in vivo* experimentation, can be completed in approximately 3–8 weeks. Implementation of these devices allows for chronic (tested up to six months), wireless optogenetic manipulation of neural circuitry in animals navigating complex natural or homecage environments, interacting socially, and experiencing other freely-moving behaviors.

INTRODUCTION

Optogenetics is a relatively new field of neuroscience that gives researchers the ability to control cellular signaling and neural activity in a cell-type selective manner. *In vivo* applications of optogenetics have rapidly aided in the understanding of neural circuit function in behavioral models (Adamantidis et al., 2007; Carter et al., 2010; Fenno et al., 2011; Jennings et al., 2013; Kim et al., 2013a; Lammel et al., 2012; Stuber et al., 2011; Tye et al., 2011; Yizhar et al., 2011; Zhang et al., 2010). Despite the success of these studies, tethered fiber optic approaches have restricted opportunities for the study of more complex, ethologically relevant behavioral paradigms such as enclosed homecage behavior, spontaneous pain, wheel-running, and freely-

91

moving social interactions. Here we present a protocol for the fabrication of flexible devices that carry wirelessly powered microscale, inorganic light-emitting diodes (μ-ILEDs) and multimodal sensors to study neural circuitry in awake, freely moving animals. The devices described in this protocol are robust, self-contained, multifunctional, and capable of wireless operation with conventional electronics and power supplies. These fully electronic systems eliminate the need for high-powered light sources, fiber coupling fixtures and optomechanical hardware for *in vivo* optogenetic experiments. The following protocol is based on technology and approaches developed jointly in our two laboratories (See Chapter 2) (Al-Hasani et al., 2013; Kim et al., 2010a, 2012a, 2012b, 2013b; Li et al., 2013).

Development of the protocol and comparison with traditional light sources

This protocol is the result of advances in material science that have led to the development of flexible electronics, biodissolvable adhesives, microscale sensors, and high efficiency μ-ILEDs (See Chapter 2) (Hwang et al., 2012; Kim et al., 2010a, 2012a, 2012b; Tao et al., 2012). While other groups have successfully implemented wireless schemes and LEDs for optogenetics (Cao et al., 2013; Iwai et al., 2011; Wentz et al., 2011; Zhao et al., 2009), the protocol described here provides a completely customizable approach for combining various materials engineering approaches to design and implement devices that can be optimized for an individual laboratory's experimental needs.

The current standard in neuroscience for light delivery into the depth of the brain is to use chronically implanted fiber optics (Sparta et al., 2011), which offer substantial advantages over acute delivery of fibers via metal cannulae (See Chapter 2) (Kim et al., 2013b; Zhang et al., 2010). These chronic implants, however, have their own limitations. Principally, light from fiber

optic implants can only escape from the tip of the implant to illuminate ventral brain structures. While adaptations to this ventral light delivery are possible (Tye et al., 2011; Zorzos et al., 2010, 2012) (available commercially at www.doriclenses.com), the range of customizability can be limited and often restricts the user to only delivering light without the capability of observing physiology. Furthermore, μ-ILEDs create opportunities to restrict or expand spatial targeting by selecting from a range of sizes (625-10,000 μm^2), altering the number and arrangement of μ-ILEDs, and using reflective materials to direct light. This protocol provides a basis from which any combination of μ-ILEDs and sensors can direct light within the brain and measure physiological function without the restriction of enforced light trajectory.

Various strategies have been employed for delivering multiple wavelengths of light into the same animal (Stark et al., 2012; Zorzos et al., 2010, 2012). These approaches require establishing an extensive network of optics and tethered optical equipment external to the behaving animal. Depending on the laboratory behavioral space, such setups can restrict experimental possibilities and requires advanced experience with optics to maintain optimal conditions. This protocol may require access to external facilities for some labs, but the end result is a device that can be operated with basic laboratory equipment already likely to be present in most neuroscience laboratories. Furthermore, the rescue and recycling of these devices for re-use is relatively easy, meaning that these devices can be used for several rounds of behavioral experimentation with different sets of animals. For light-evoked activation of channelrhodopsin-2 [ChR2 (H134)], optically sensitive seven-transmembrane domain receptors (i.e. OPTO-α_1, OPTO-$\beta_{2,}$), and other blue light-sensitive optogenetic constructs, GaN μ-ILEDs are appropriate (See Chapter 2) (Airan et al., 2009; Kim et al., 2013b; Yizhar et al., 2011). A device utilizing these 450 nm-emitting μ-ILEDs will be the focus of this protocol. However, it is

important to note that µ-ILEDs emitting at other relevant wavelengths are also possible to fabricate for use in other contexts (See Chapter 2) (Kim et al., 2013b; Park et al., 2009) . The combination of µ-ILEDs of different wavelengths provides the user with access to activation spectra of multiple optogenetic constructs with a single implanted, electronic device. Furthermore, the electronic nature of these devices ensures that they can be operated wirelessly. Wireless optogenetic manipulation of neural circuitry has been achieved by other means (Iwai et al., 2011; Wentz et al., 2011), but these approaches can restrict behaviors accessible to study because the animal is required to remain in a fixed environment. By utilizing radiofrequency (RF) power scavenging, the devices and approaches contained in this protocol free the user of constraints on behavioral assays, thereby allowing for experimental testing in any space.

Applications of the protocol

While the focus of this protocol is on the creation of devices engineered to deliver µ-ILEDs into the brain for optogenetic applications, this same protocol can be used to fabricate devices to measure electrophysiological, thermal, and other properties of intact brain tissue (See **Optional Section 3.1** for details). The flexible nature of these devices provides the potential to extend their application into other intact tissues such as the peripheral nervous system and the circulatory system/cardiac tissue of larger organisms.

Experimental design

Subjects. This protocol and these devices have been optimized for use in adult (25–35 g) male C57BL/6J mice and mutant mice backcrossed to the C57BL/6J mouse strain. However, as the optogenetic toolbox expands to other mammals (Cavanaugh et al., 2012; Diester et al., 2011;

Gerits and Vanduffel, 2013; Han et al., 2009; Ruiz et al., 2013; Witten et al., 2011) these devices will likely have broader utility in other animal models. Specifically, larger organisms such as rats and non-human primates will tolerate the ~700 mg wireless antenna with greater ease than mice. Unlike animals with polished fiber optic implants, animals with chronically implanted μ-ILEDs can be housed with other animals, as the metal pin connectors cannot be damaged by cage mates. Prior to beginning this protocol, all the procedures described herein should be approved by the Animal Care and Use Committee of the investigating institution and conform to US National Institutes of Health guidelines regarding animal research. For this protocol, all procedures were approved by the Animal Care and Use Committee of Washington University and conformed to US National Institutes of Health guidelines.

Controls As noted elsewhere (See Chapter 2) (Kim et al., 2013b; Sparta et al., 2011; Yizhar et al., 2011), the proper controls for *in vivo* optogenetics are mice that express genetically-encoded fluorescent reporters in the absence of an opsin. These control mice will account for any disturbance from viral injection, device implantation, heating confounds from light delivery, and fluorophore fluorescence within the brain. Another important confound to consider when conducting light-evoked single-unit electrophysiological experiments is the potential for generating neural activity downstream of retinal stimulation. These devices prevent the external light escape that is common with fiber optic implants, but activity from the visual system has the potential to activate the retina and retinal ganglion cells from within the brain, depending on the brain region (Kravitz et al., 2013). Recordings performed with an external light stimuli can control for these effects. Additionally, properly counter-balanced within-subject experimental

designs are possible with these devices by withholding power to the devices during the behavioral testing period.

Limitations While these devices offer numerous advantages over traditional fiber optic implants; the technology is not intended to replace protocols that work well to manipulate neural circuitry *in vivo* (Sparta et al., 2011; Zhang et al., 2010). The greatest limitation associated with this procedure is the accessibility to the facilities and the technical skill required to fabricate these devices and their scavenging antennas. That being said, subsequent recovery and re-fabrication of the devices is straightforward and accessible to any laboratory. Once the protocol is followed there are few considerations when designing behavioral experiments. First, depending on the panel antenna employed, the signal can be polarized. In current designs, both the panel antenna and the antenna on the scavenger are directional with linear polarization. A maximum efficiency of power transmission and reception is achieved when the polarizations of both antennas are aligned. The power transmitted by the panel antenna can typically be adjusted to accommodate mismatches that can occur in most practical situations. Such issues can be avoided entirely by use of a transmission antenna with circular polarization or multiple panel antennas. Care should also be taken to ensure that the animal's surroundings do not interfere with the RF signal by powering a free-standing device in the behavioral context (See Chapter 2) (Kim et al., 2013b). Wireless control of these devices is compatible with a wide-range of behavioral assays. In our hands, the devices have performed well in tests of anxiety-like behavior (open field test, elevated zero maze), reward-related behavior (conditioned place preference, operant behaviors, and self-stimulation), social behaviors (social defeat stress and social aversion), pain behaviors (Hargreaves test), and homecage behaviors[11]. In our experience, commonly used materials for behavioral apparatus (wood, polyvinyl chloride (PVC), Poly(methyl methacrylate)

(PMMA; Plexiglass/Perspex) and the metal from cage lids) do not interfere with the RF signal, but can reduce the overall power if they are positioned between the panel antenna and the headstage scavenger (see **Table 3.1**).

Second, the current protocol only provides wireless access to power the μ-ILEDs and not to receive information from the sensors. This backwards data stream restriction is largely one based on the weight that an animal can endure on the headstage. For a mouse, electrophysiological, temperature, and photo sensors currently require a wired connection. For larger mammals, the devices can be integrated with existing telemetry setups, provided they do not interfere with the RF signal (Harrison et al., 2010; Szuts et al., 2011) (commercially available at www.plexon.com). Finally, independent control of individual μ-ILEDs is also possible with these devices, but the described protocol has not been optimized for these conditions in a wireless control mode. If independent control is a desired feature, it is recommended that smaller connections featuring a number of channels are employed over the pin connectors that we present here (many options commercially available at www.omnetics.com).

Upon completion of the protocol presented here, users can expect to have devices with 4 μ-ILEDs that can be wirelessly powered with suitable light output from two meters away. In our experience, more μ-ILEDs can be added to a single device with relative ease (the maximum we have tested is 25 (5 x 5) μ-ILEDs from a single power scavenger). Furthermore, the radiofrequency power scavenging approach is appropriately suited for powering multiple μ-ILED devices (presumably in multiple animals) using a different power scavenging headstage antenna for each device. The upper limit on the number of simultaneously powered devices is primarily dependent on the spatial constraints of the experimental space and apparatus to achieve equal powering to all devices.

Notes on the materials and equipment used in this protocol: Accurate injection of these devices into brain tissue requires an stereotaxic adapter for standard cannula holders. The basic principle of this adapter is that the μ-needle can mounted in-line with the existing stereotaxic system. The dimensions of such an adapter will vary by stereotaxic alignment system make and model, but most university machine shops should be able to fashion such an adapter. The adapter presented in this protocol was specifically designed for use with the KOPF Single Cannula Holder (Model 1966). It is also possible that other commercially available electrode holders may be capable of accurately targeting the devices (e.g. KOPF Model 1768). More detailed information on the machining and dimensions of the adapter for the KOPF Model 1966 can be found in (**Figure 3.6).**

In order to deliver pulse trains of light, the devices can be controlled using a traditional function generator to drive amplitude modulation of the wireless powering equipment. Amplitude modulation is an internal function available on most RF generators. This function allows an internally or externally supplied modulating signal to control the amplitude of the output RF signal. The internal modulating signal is usually a sinusoidal waveform with a much lower frequency compared to that of the RF output. For the positive region of the sinusoidal signal, the RF generator can output an RF signal whose amplitude is modulated by the low frequency sinusoidal signal, and change from 0 to the maximum set power and then back to 0. For the negative region of the modulating signal, the output RF signal maintains at 0. An external TTL modulating signal is preferable in terms of modulating the amplitude of the output RF signal. Here, the high state of the TTL causes the RF generator to output a constant set power, while in the low state of the TTL, the RF generator outputs 0 power. Thus, the TTL modulating

method is more suitable for generating constant light intensity during the high state of the TTL. The pulse width and frequency of photostimulation should be determined and based on physiologically relevant conditions (Adamantidis et al., 2011; Jennings et al., 2013; Sparta et al.; Tye and Deisseroth, 2012; Tye et al., 2011)

Post-mortem rescue of the devices for reuse is a delicate, but straightforward process. The dental cement presented here (Lang Dental) allows for such rescue. Other cements and bonding agents can inhibit the process and destroy internal components. It may be necessary to use a stronger bonding agent in some scenarios (see **Table 3.1**). In such cases, the re-usability might be compromised.

MATERIALS

Reagents

Preparation of releasable polymer template

- UV curable epoxy (SU-8 2 & 100 photoresist, Microchem) ! CAUTION Partially cured or uncured epoxy needle can induce excess chemical contamination in the brain**.**

- SU-8 developer (Microchem)

- Isopropyl alcohol (IPA) !CAUTION Isopropyl alcohol is flammable.

- Acetone !CAUTION Acetone is flammable.

- Silk adhesive (Details are shown in other papers (Hwang et al., 2012; Kim et al., 2010a; Tao et al., 2012), see REAGENT SETUP).

- BCB (Benzocyclobutene, DS-4022 35, Dow corning)

- BCB developer (Advanced Developer, DS2100, Dow corning)

- Water soluble tape (3M)

- Photoresists (AZ 1518, AZ 2070, Capital Scientific)

- AZ 300 MIF developer (Capital Scientific)

- Hydrofluoric acid (HF) !CAUTION HF is extremely corrosive. Wear gloves and use eye protectionwhen using HF.

- Chrome (Cr) etchant, gold (Au) etchant, palladium (Pd) etchant (Transene Inc.)

- Polydimethylsiloxane (PDMS, Sylgard184, Dow corning)

- Polyethylene terephthalate (PET, polyester film, 2.5 and 6 μm thick, Mylar® film, Chemplex® Inc.)

Preparation of μ-ILEDs

- Gallium nitride (GaN) LED epitaxial materials grown on sapphire substrates (Cermet Cop.)

Injection of virus and μ-ILEDs into targeted brain structure

- Isoflurane, USP (Isothesia, Butler Schein, cat. no. 029405)! CAUTION Prior to beginning this protocol, the Animal Care and Use Committee of the investigating institution should approve all procedures and conform to US National Institutes of Health guidelines regarding animal research. ! CAUTION Ensure proper ventilation and gas scavenging methods are in place to prevent potential inhalation of excess isolflurane.

- Betadine solution (Purdue Products, cat. no. 67618015017)

- Ethanol (Sigma-Aldrich, cat. no. 362808) ! CAUTION Ethanol is flammable.

- Hydrogen peroxide, 3% USP (Select Medical Products, cat. no. 117)

- Lidocaine ointment USP, 5% (Fougera)

- Ophthalmic ointment (Altalube Ophthalmic Product)

- Adhesive Luting Cement (C&B-Metabond, Parkell Inc., cat. no. S380) ! CAUTION

- Light cured bonding adhesive (VLC One Step Prime & Bond Adhesive, cat. no. 305-006-

030) ! CAUTION

- Dental cement (Jet Denture Repair, Lang Dental, cat. no.1223, see REAGENT SETUP) ! CAUTION Methyl Methacrylate Monomer, Stabilized is a flammable liquid. It may also cause skin irritation; avoid contact with skin, eyes, and clothing. Use with adequate ventilation.

- 0.9% Sodium Chloride Inj., USP ((9 mg/ml NaCl), Hospira, cat. no. RL-0497(9/04))

- Enroflaxin (Baytril, Bayer, cat. no. R30901)

- Antibiotic ointment (Neosporin, Johnson & Johnson, cat. no. 174-73087Q)

- Viruses of interest (Adeno-associated virus and lentiviruses are available from the WUSTL Hope Center Viral Core , https://hopecenter.wustl.edu/?page_id=99 and/or the University of North Carolina Viral Vector Core, http://genetherapy.unc.edu/services.htm), Herpes Simplex Viruses are available from the MIT Viral Core, http://mcgovern.mit.edu/technology/viral-vector) ! CAUTION Follow the appropriate safety precautions pertaining to the particular virus in use. It may be necessary to obtain a higher Biosafety Level certification prior to use.

- Artificial cerebral spinal fluid (ACSF; Tocris, cat. no. 3525 or custom, see REAGENT S ETUP (2011; Zhang et al., 2010)

- Animal(s) to be injected with μ-ILED device. The procedure describes how to use a μ-IL ED device with a mouse, as previously described (See Chapter 2) (Kim et al., 2013b). ! C AUTION Prior to beginning this protocol, the Animal Care and Use Committee of the in vestigating institution should approve all procedures and conform to US National Institut es of Health guidelines regarding animal research.

Behavioral procedures using RF power scavenging

- Thermal grease (Wakefield Solutions, cat. no. 120-2)

EQUIPMENT

Preparation for μ-ILEDs and Multifunctional Sensors

- Sputter ((AJA international, ATC 200) metal deposition for Au (gold), Ni (nickel), Pt (platinum), etc.)

- Rapid thermal annealing (RTA) !CAUTION High temperature, semi-transparent *L*-shaped current spreading layer on p-side on GaN LED should be used in thin metal layers (15/15 nm Ni/Au) followed by 500°C annealing.

- Mask aligner (Karl Suss, MJB)

- Inductively coupled plasma (ICP) etcher (PlasmaTherm SLR-700, etching for GaN)

- Reactive ion etcher (RIE, PlasmaTherm 790, etching for SiNx)

- Plasma enhancement-chemical vapor deposition (PE-CVD, STS mixed frequency nitride deposition system)

- Wafer bonder (Electronic Visions, EV501)

- Laser lift off (LLO, Krypton Fluoride (KrF)(0.9 J/cm^2, 248 nm wavelength, IPG Photonics (http://www.ipgphotonics.com/microprocessing.htm)) or Yttrium aluminum garnet (YAG):Nd laser (0.3 J/cm^2, 266 nm Single pulse with 5 ns exposure, Sandia National Lab) ! CAUTION Avoid eye contact with the laser. Always wear eye protection.

- Digital multimeter (Fluke 115 or other commercially available multimeter)

- Printed circuit board (PCB) for headstage connection (General Circuits Co.)

- Male pins for headstage PCB (2.54 mm spacing male pins (Sunlight Inc, P2540-H254-S180).

Measurement of µ-ILED

- Ocean Optics (Ocean Optics HR4000) (for measuring wavelength spectrum, light output power)

- Probe station (Agilent 4155) (current-voltage (I-V) characteristics).

- Pulse generator (Global specialties, 4001)

- Oscilloscope (Agilent , DSOX2004A, 70 MHz)

- IR camera (QFI InfraScope II)

Injection of virus and µ-ILEDs into targeted brain structure

- Stereotaxic alignment system (KOPF Model1900) ! CAUTION Prior to beginning this protocol, the Animal Care and Use Committee of the investigating institution should approve all procedures and conform to US National Institutes of Health guidelines regarding animal research**.**

- Stereotaxic alignment indicator (KOPF Model 1905)

- 40X Centering Microscope (KOPF 1915)

- Stereotaxic drill (KOPF Model 1911) and #66 drill bit (KOPF cat. no. 8669)

- Stereotaxic single cannula holder (KOPF Model 1966)

- Stereotaxic adapter for cannula holder (**See Figure 3.6)**, WUSTL Machine Shop or other)

- Anchoring screws (CMA Microdialysis, cat. no. 7431021)

- Needles (Becton-Dickinson, cat. no. 305111)

- Micro-injection syringes (Hamilton, cat. no. 88011)

- Infusion pump and controller (UltraMicroPump III, World Precision Intstruments, cat. nos. UMP3 and UNC4)

- Forceps (Miltex, cat. no. 6-100)

- Surgical scissors (Miltex, cat. no. 18-1430)

- Hemostats (Miltex, cat. no. MH7-26)

- Microspatula (Chemglass, cat. no. CG-1982-12)

- Electric clippers (Wahl, cat. no. 8064-900)

Behavioral procedures using RF power scavenging

- RF generator (Agilent, N5181 MXF)

- Function generator with standard transistor-transistor logic (TTL) (AMPI Master-9 or other)

- RF amplifier (Empower RF systems Inc. 1100/BBM2E4AJP)

- RF antenna (ARC wireless solutions, ARC-PA0913B01, ARC 902-928 MHz 12.5dBi, Flat Panel)

- DC power supply (Mastech, cat. no. HY5005E-2)

- Relevant behavioral assay apparatus (university machine shops, MED Associates, Harvard Apparatus or other)

- Wireless headstage antenna (see PROCEDURE)

- Printed circuit board (PCB) for wireless headstage antenna (General Circuits Co.)

- Ceramic antenna (W3012, Pulse Electronics)

- Schottky diode (Digi-Key, cat. no. MMDL301T1G)

- Power meter (Bird Electronic Corp.,Thruline 43)

- Two SMA Male to N Male Precision cables (Pasternack, cat. no. PE304-120)

- Fan-cooled heat sink (Fischer Elektronik, cat. no. LA 17/200 24V)

Behavioral procedures using a wired connection

- Animal(s) with injected µ-ILED device ! CAUTION Prior to beginning this protocol, the Animal Care and Use Committee of the investigating institution should approve all procedures and conform to US National Institutes of Health guidelines regarding animal research**.**

- Relevant behavioral assay apparatus (university machine shops, MED Associates, Harvard Apparatus or other)

- Function generator for standard transistor-transistor logic (TTL) (AMPI Master-9 or other)

- BNC cables (Cables to Go, various lengths and catalog numbers)

- Electrical rotary joint (Moog, cat. no. SRA-73683 (du Hoffmann et al., 2011))

- BNC-to-banana plug adapter (Fluke BP881 or other)

- Wire (30 gauge wire, Artistic Wire) and female connector (Single modality devices: TE Connectivity, cat. no. AMP 3-640441-2; Multimodal devices or independent µ-ILED control: TE Connectivity, cat. no. AMP 87631-4)

REAGENT SETUP

Silk adhesive Boil cocoons of the Bombyx mori silkworm for 30 minutes in a solution of 0.02M Na_2CO_3 to remove the sericin protein. Rinse the extracted fibroin with distilled water and dry in ambient air for 12 hours. After drying, dissolve the fibroin in a 9.3M LiBr solution at 60 ° C for 4 hours, yielding a 20 wt.% aqueous solution, and subsequently dialyze the solution against distilled water using a dialysis cassette at room temperature for 48 hours until the solution reaches a concentration of 8 wt.%.

Dental cement The dental cement can be prepared as described elsewhere (Sparta et al., 2011) by combining the Jet Denture Repair Powder with the Jet Liquid (methyl methacrylate). A starting point is 350 µl of methyl methacrylate monomer added to 225 mg of powder. In some cases, the viscosity must be adjusted (by increasing or decreasing the amount of methyl methacrylate in the mixture) to properly secure the flexible device in place and/or mount the PCB in the headcap. ▲CRITICAL STEP Adjusting the viscosity alters the working time of the cement.

Virus Each type of virus has different handling instructions, but all must be stored on ice until immediately prior to the injection. In some cases, dilution of stock titers requires obtaining more of the reagent in which the viral prep was initially concentrated.

ACSF If not purchased, the solution can be prepared following the recipes described elsewhere (2011; Zhang et al., 2010).

EQUIPMENT SETUP

Preparation of amplifier with proper heat sink The RF amplifier (1100/BBM2E4AJP, Empower RF Systems Inc.) requires an additional cooling system during operation. Thermal grease applied on top of the heat sink (LA 17/200 24V, Fischer Elektronik Inc.) facilities thermal contact with the amplifier, which is affixed to the sink using screws. The DC power supply operates both the amplifier and the fan attached to the heat sink, by supplying power with voltages of 24 V and 10 V, respectively.

PROCEDURE

Preparation of µ-ILEDs ● TIMING 7 d

1 | Clean the wafer surface of GaN LED stacks (450 nm emission wavelength; p-type

GaN/multi-quantum well (MQW)/spacer/n-type GaN/undoped GaN) grown on sapphire substrate with 5 wt % diluted HCl for 5 min. ▲CRITICAL STEP Proper cleaning enables reduced turn-on voltages and improved efficiencies, both of which minimize production of heat by the operating μ-ILEDs.

2 | Deposit metals (Ni/Au, 15/15 nm) immediately after cleaning ▲CRITICAL STEP The deposition should be carried out degree vacuum levels of ~10^{-6} torr or less.

3 | Form *L*-shape patterned metals (Ni/Au) onto the p-type GaN semiconductor layer by photolithography and wet etching with Cr and Ni etchants followed by removal of the photoresist (PR) with acetone (**Figure 3.1A**).

4 | Anneal the wafer for 10 min at 500 $^{\circ}$C in 20% oxygen and 80% Argon atmosphere to generate *p*-ohmic contact. ▲CRITICAL STEP The annealed metal layers should be semi-transparent after this step.

5 | Generate 40 x40 μm^2 square hole patterns in a negative tone PR (AZ 2070 PR) and etch (chlorine gas based RIE etching) the p-GaN layer, MQW, spacer to open n-side GaN (**Figure 3.1B**).

A
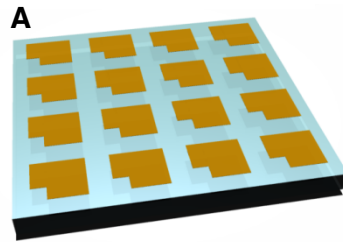
Deposit *L*-shape current spreading layer

B

Etch n-side GaN

C
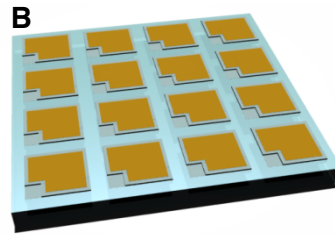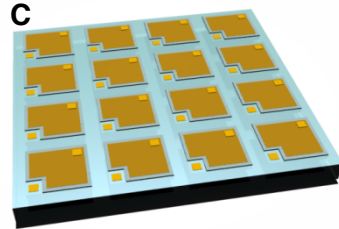
Deposit p- and n-contact pads

D
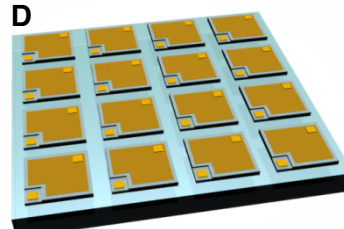
Etch space and fabricate complete *μ*-ILEDs on sapphire

E
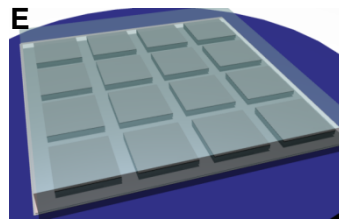
Deposit SiNx and bond to silicon wafer using In-Pd bonding

F
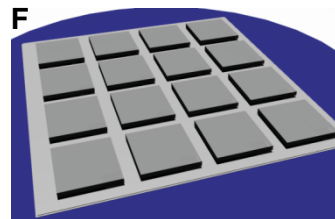
Laser lift off and remove sapphire

G
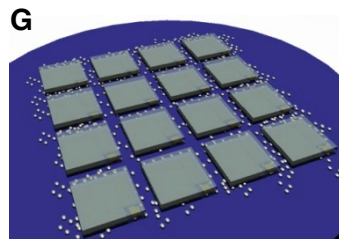
Etch bonded metal layer

H
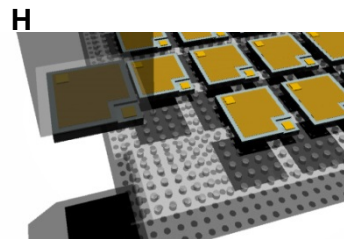
Pick up *μ*-ILEDs using a structured PDMS slab

Figure 3.1 Fabrication procedure for injectable μ-ILEDs. (**A**) L-shape current spreading layer (patterning of Ni/Au (15/15 nm) layers followed by 500 ºC annealing) is formed on GaN blue lighting LED stacks grown on sapphire. (**B**) In order to expose n-type GaN semiconductors, etch rectangular shape of p-type one, multi quantum well (MQW), and spacer layers by reactive ion etching. (**C**) Generation of n- and p-contact pads (Cr/Au (15/300 nm) 25 x25 μm^2 squares) on n- and p-type GaN sides. (**D**) Etch 20 μm width trench to define 100 x 100 μm^2 or smaller than 100 x 100 μm^2 lateral dimensions. (**E**) Bonding μ-ILEDs on sapphire with silicon wafer using In-Pd metallic alloy bond. (**F**) Expose laser on sapphire and mechanically remove sapphire from μ-ILEDs. (**G**) Wet etch the bonded metallic layer located on wafer. (**H**) Transfer of all μ-ILEDs onto structured PDMS slabs and selectively pick up single μ-ILEDs using a polydimethyl siloxane (PDMS) stamp. [Part d, f, g and h reproduced with permission from (Kim et al., 2012a) © 2012 Wiley]

6 | Generate 25 x25 μm^2 square hole patterns in PR for n- and p-type metal contact pads and deposit Cr/Au (10/300 nm) using an electron beam evaporator. Then, remove PR (**Figure 3.1C**).

7 | Deposit a low stress layer (200 nm) of SiNx on the substrate, using plasma enhanced-chemical vapor deposition (PE-CVD). Next, pattern a negative tone PR (AZ 2070) to serve as a mask for etching the SiNx and the GaN to define the lateral dimensions of array of μ-ILEDs. Devices with dimensions of 100 x 100 μm^2 or less are formed with 20 μm spacings (**Figure 3.1D**).

8 | Deposit a layer of SiNx onto the μ-ILEDs to protect the devices and metal pads from further processes. Bond the LED wafer to a silicon substrate using indium (In)-palladium (Pd) metallic alloy. This bonding uses Cr/Pd (15 /150 nm) on the LED substrate and Cr/Pd/In (15/150/900 nm) on the silicon. The bonding occurs on contact with a pressure of 400 bar and temperature of 220 ^{o}C for 2 hr (**Figure 3.6E**).

9 | Use laser illumination through the sapphire to release the μ-ILEDs (**Figure 3.1F**). Details of this laser lift-off (LLO) technique appear elsewhere(Kim et al., 2012a; Wong et al., 2000).

10 |Etch unalloyed metal by immersion in 5 wt% HCl for 30 min (**Figure 3.1G**).

11 |Retrieve all μ-ILEDs onto substrate of PDMS with patterns of surface relief, in the geometry of cylindrical pillars with 3 μm diameter and 1.4 μm height and 5 μm spacing. Remove residual metals, including In-Pd alloy and Crare by Pd and Cr etchants (**Figure 3.1H**).

12 |Prepare a PDMS stamp with a single relief feature consisting of a post with 100 x 100 μm^2 lateral dimensions and 100 μm height. Using a mask aligner for photolithography, retrieve a single μ-ILED with the stamp and transfer it to a needle shaped structure of PET adhered to a

thin layer of PDMS on a transparent temporary substrate (**Figure 3.2A** and **B**).

13 |Remove passivation layer, SiNx (deposited in procedure 8) with RIE and spin coat a photosensitive benzocyclobutene (6 μm thick, BCB) onto the μ-ILED.

14 |Pass ultraviolet (UV) light through the backside of the substrate and develop the BCB with BCB developer (**Figure 3.2C**) to obtain holes for n- and p-side contacts (**Figure 3.2C,** lower inset) !CAUTION Make sure that BCB covers the μ-ILED surface. Non-uniform coatings of BCB generate interference fringes that are readily visible. (**Figure 3.2C,** upper inset) After further curing BCB, anneal the samples at 250 ^{o}C on a hot plate for 3 hr. ▲CRITICAL STEP The annealing should be carried out in Ar atmosphere to avoid high temperature damage to the BCB and polymeric layers. ?TROUBLESHOOTING

15 |Deposit Cr/Au (15/300 nm) by sputtering, and form metal interconnects using positive tone PR (AZ 15198) followed by metal etching (**Figure 3.2D**).

Deterministic device assembly by transfer printing and formation of electrical interconnects ● TIMING 1 d

16 |Remove μ-ILEDs fabricated on each temporary substrate as shown in **Figure 3.2A** with water-soluble tape (**Figure 3.2E**). Remove water-soluble tapes in DI water (**Fig. 2f**) and place the devices on slabs of PDMS (**Figure 3.2G**). ▲CRITICAL STEP Steps 16-20 describe device assembly for μ-ILEDs alone. If you are assembling a multifunctional device, follow the instructions in **Optional Section 3.1** before proceeding.

17 |Connect each of the devices with anisotropic conductive film (ACF) cable to a PCB board (**Figure 3.2H**). ▲ CRITICAL STEP Apply pressure and high temperature (~150 ^{o}C) during ACF cable bonding. ?TROUBLESHOOTING

A 6 (or 2.5) μm thick PET

PDMS-coated glass slide

B Stamp

μ-ILED

Transferred μ-ILEDs on stamp

200 μm

C Chrome mask

Backside exposure

Wave pattern

Uniform

D Metal interconnection

E Water soluble tape

Adhesive dissolved in water

F Residual polymer film

G PDMS slab

ACF cable

H PCB with pin connector

I PDMS coating for waterproofing

J Blue μ-ILEDs (450 nm)

K μ-needle

Biodissolvable adhesive

L 250 μm thick

Figure 3.2 Procedure for fabrication of injectable, multifunctional electronics. (**A**) Thin (~2.5 μm thick) needle-shaped polyethylene terephthalate (PET) is attached on temporary Polydimethylsiloxane (PDMS) coated glass substrate. (**B**) Schematic and photograph demonstrating the transfer printing of four μ-ILEDs onto the tip of the PET using a PDMS stamp. (**C**) Passivation approach with photocurable benzocyclobutene (BCB) polymer. The backside of BCB coated substrate is exposed to ultraviolet light. The wave pattern in the upper inset shows ununiformed coating of BCB. The lower inset shows successful uniformed coating. (**D**) The metal interconnection (Cr/Au) is generated by sputtering, photolithography and metal etching to electrically connect the four μ-ILEDs. (**E**) The connected device is picked up with water soluble tape. (**F**) The substrate is separated from the tape after the adhesive is dissolved in the water. The inset shows the μ-ILEDs on freestanding thin, flexible, needle-shaped PET. (**G**) The device is electrically connected to the ACF cable. The PDMS slabs on top and bottom are compressed using high temperature (~150ºC) to bond the ACF cable. (**H**) The other side of the ACF cable is connected to the PCB with pin connector for wireless or wired powering schemes. (**I**) The ACF cable and PCB is coated with PDMS for waterproofing. (**J**) Blue (450 nm) μ-ILEDs are powered. The μ-ILEDs and electrical connection should be checked prior to injection (**K**) The device is assembled with injection μ-needle using biodissolvable silk adhesive. (**I**) Image of a completed device ready for injection into brain tissue.
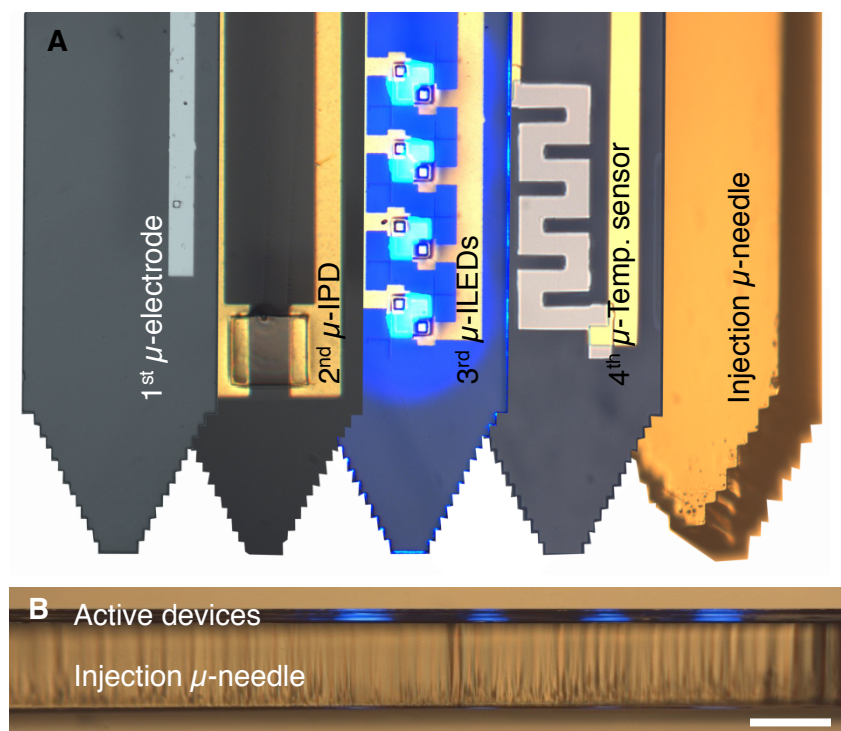
Figure 3.3 Multifunctional sensors and optoelectronics. (**A**) Representative scheme for multifunctional, injectable electronics formed on injectable needle. The devices include electrophysiological sensor (m-electrode); 1st layer), silicon photodiode (m -IPD; 2nd layer), four microscale inorganic light-emitting diodes (m-ILEDs; 3rd layer), and temperature sensor (m-temp. sensor; 4th layer) based on platinum resistor are formed on injectable m-needle fabricated from epoxy polymer. (**B**) Side view of such a device reveals the ultrathin nature of the active components of the device. Scale bar applies to both panels and = 200 mm.

18 | Assemble all devices onto injection μ-needle formed in SU-8 epoxy. The entire region of injection device should be electrical insulated for *in vivo use.* Cover the flexible device with SU-8 polymer and the other parts with PDMS for waterproofing (**Figure 3.2I**). Temporarily fix the device to the PDMS slab. Drop PDMS solution (Sylgard 180, Dow corning, weight ratio=10:1 (silicone elastomer precursor: curing agent), see details at http://www.dowcorning.com/applications/search/default.aspx?r=131en) onto the ACF cable and PCB except for the pin connection area. After baking the PDMS in the oven at 70℃ for 2 hrs, the entire area except pin adapter is electrically passivated by PDMS.

19 | To check functionality, power the device by connecting to a power supply capable of delivering more than 1 mW (Figure 3.2J). Use silk adhesive to bond the devices to the injection μ-needle (**Figure 3.2K and l**).

Fabrication of wireless power harvester and preparation of wireless operation● **TIMING 1 d**

20 | Build either the robust, PCB-based (option A) or thin, flexible (option B) wireless power harvester. ▲ CRITICAL STEP Both options perform equally, but each have advantages. The PCB-based option is more easily contrasted and more durable, but weighs more than the flexible version. We recommend using the PCB-based harvester for experiments that involve social interaction, while the flexible version is more ideal for experiments involving only a single animal.

A)   **Construction of the PCB-based wireless power harvester.**

i.   Build the wireless power harvester from two stacked PCB circuits (**Figure 3.4B**); General Circuits Co., Ltd.). Each PCB includes top and bottom layers that are mostly

covered by solid copper ground planes.

ii.   Mount the electrical components on the PCB boards through soldering. The first PCB circuit (labeled as 5 in **Figure 3.4B**) contains a ceramic antenna (W3012, Pulse Electronics) operated at 915 MHz with a clearance space of 10.8×8.25 mm to the surrounding ground plane.

iii.   Connect a capacitor (8.2 pF in capacitance) between the feed line of the antenna and the ground plane to match the impedance of the antenna with the following circuit. A secondary PCB circuit (labeled as 6 in **Figure 3.4B**) contains a voltage multiplier circuit constructed with 6 pairs of capacitors (47 nF in capacitance) and Schottky diodes (MMDL301T1G) in cascaded connection (See Chapter 2) (Kim et al., 2013b).

iv.   Mount the connector that is used for the μ-LEDs to the secondary PCB circuit. Join the PCB circuits and the connector with flexible copper wires (**Figure 3.4C**), and bond together with resin epoxy (**Figure 3.4D**). **Figure 3.3I** shows a schematic illustration of the power harvester. The circuit parts, which are labeled with number 5 to 7, correspond to the same number shown in **Figure 3.3B and 3.3E**.

B) **Construction of the thin, flexible wireless power harvester.**

i.   Fabricate the flexible PCB circuit on 75 μm thick Kapton film (**Figure 3.4F**). Coat the film with a 6 μm thick layer of copper using electron beam evaporation.

ii.   Pattern the copper to form pads for the electrical components and interconnection. Spin cast and pattern 1 μm thick polyimide film to expose the electrical contact pads, while passivating the interconnection (**Figure 3.4F**).

iii.   Attach a ground plane made of copper tape (**Figure 3.4G**) to the bottom of the Kapton film and connect with copper pattern on the top of the Kapton film through channels

filled with solder. A schematic illustration of the flexible PCB circuit appears in **Figure 3.4J**

21 |Setup the wireless power transmission system. The system consists of an RF signal generator (N5181A, Agilent Technologies, Inc.), an RF amplifier (1100/BBM2E4AJP, Empower RF Systems Inc.), a DC power supply (U8031A, Agilent Technologies, Inc.), an antenna (ARC-PA0913B01, ARC Wireless), and a power meter (Thruline 43, bird electronic corp.) (**Figure 3.4A**). Connect the amplifier to RF signal generator and an antenna using coaxial cables (SMA Male to N Male Precision Cable Using 160 Series Coax, Pasternack Inc.).The RF signal generator provides a 915 MHz RF signal with a power of -15 to -20 dBm. The signal is amplitude-modulated through the internal function of the generator to create a pulsed signal with frequency of 10 Hz, and a carrier frequency of 915 MHz. Alternatively, an external TTL function generator can be connected to the RF signal generator to modulate the pulse width and frequency. This signal is directed to the RF amplifier, which amplifies the signal to 30 to 33 dBm.

22 |Connect the power supply to the RF amplifier and the exhaust fan of the heat sink of the amplifier (see EQUIPMENT SETUP) to provide DC voltages of 24 V and 10 V to the RF, respectively. Measure the intensity of the output power of the amplifier and then connect the amplifier to the antenna to RF power to power the μ-LEDs at a 1~2 meter distance (**Figure 3.4E and H**).

Injection of virus and μ-ILEDs into targeted brain structure ● TIMING 1 d

23 |Mount the μ-ILED device in the custom-built cannula holder adapter or other electoral device holder (see EQUIPMENT SETUP) (**Figure 3.5A and 3.6**). To do so, grasp the exposed region of the μ-needle (**Figure 3.5B**). ▲ CRITICAL STEP The device must be placed along

A — (labels: 4, 3, 2, 1)

B — Voltage multiplier; Antenna & impedance matching; Connector (labels: 6, 5)

C — Copper wire

D

E — (labels: 5, 7, 6)

F — Antenna; Impedance matching; Voltage multiplier

G — Antenna; Connector; Kapton film; Ground plane

H

I — (labels: 6, 5, 7); Antenna

J — Antenna

118
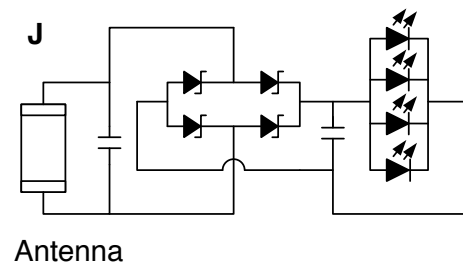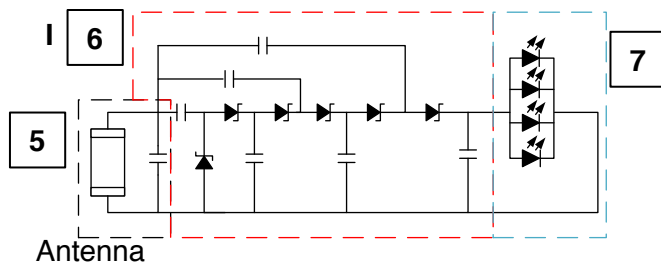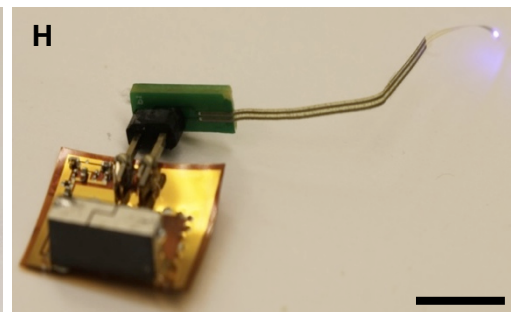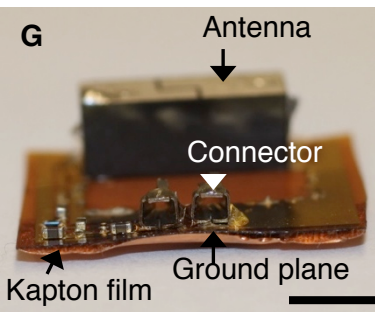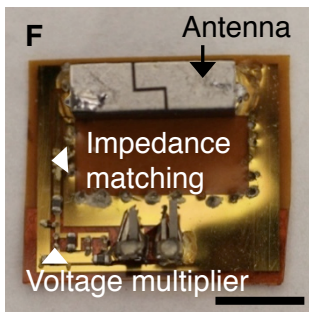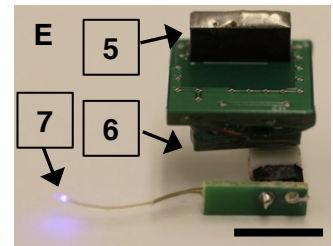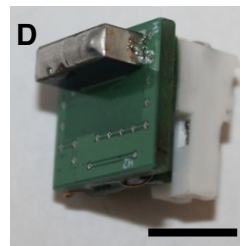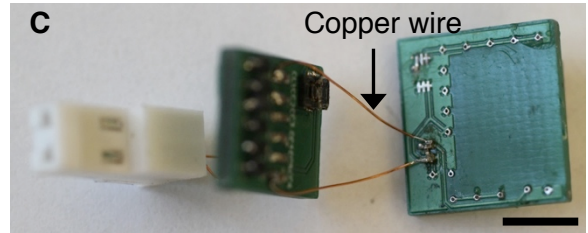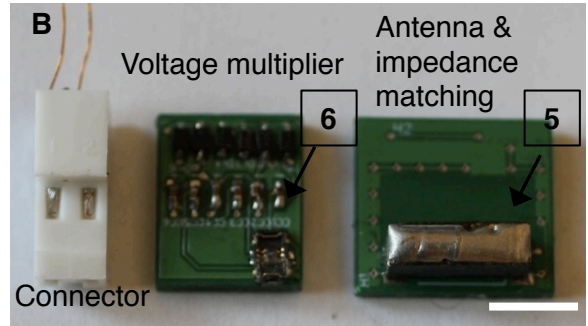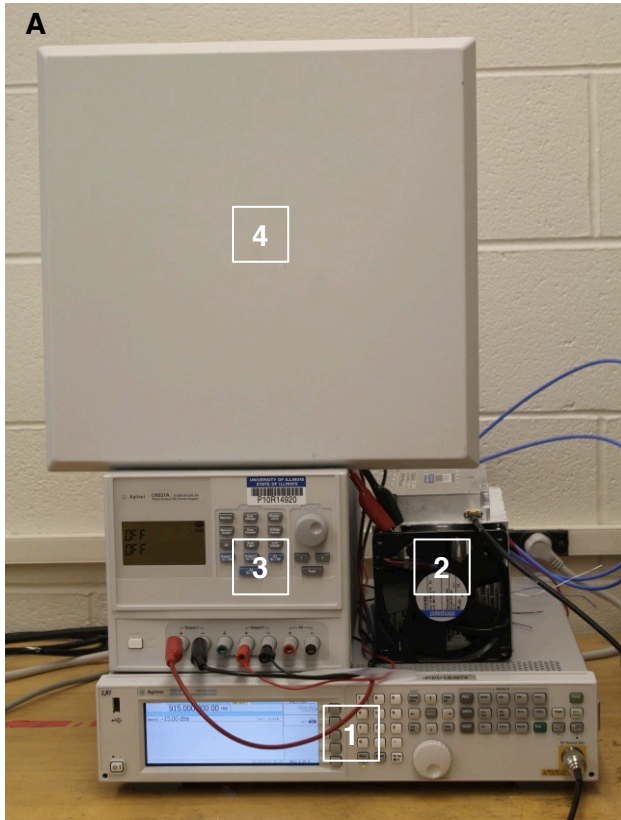
Figure 3.4 Wireless operation and equipment. (**A**) An experimental setup for wireless power transmission. The setup contains a RF signal generator (1), a RF power amplifier (2), a DC power supply (3), and a panel antenna (4). Components for the wireless power harvester for μ-ILED powering with stacked PCB circuits (5: circuit contains a ceramic antenna and a capacitor is connected between the feed line of the antenna and the ground plane to match the impedance of the antenna with the next circuit. 6: a second circuit contains a voltage multiplier constructed with 6 pairs of capacitors and Schottky diodes in a cascaded connection), before (**B**) and after (**C**) connecting with copper wire. A completed wireless power harvester alone (**D**) and with (**E**) connection to μ-ILED device (7) for wireless operation. Top (**F**) and side views (**G**) of a flexible wireless power harvester on Kapton film with similar components as the wireless harvester on PCB circuits. (**H**) A completed flexible wireless power harvester with connection to μ-ILED device for wireless operation. All scale bars are 5 mm. (**I**) A schematic of the PCB-based power harvester. The numbered circuit components correspond to the same number shown in Fig. 3b and 3e. (**J**) A schematic of the wireless power harvester.

the midline of the adapter to achieve proper spatial targeting. ? TROUBLESHOOTING

24 |Anesthetize the mouse in an isoflurane induction chamber using 4% isoflurane and a flow rate of 1.5 L/min O_2. ▲ CRITICAL STEP Prior to beginning this protocol, all procedures should be approved by the Animal Care and Use Committee of the investigating institution and conform to US National Institutes of Health guidelines regarding animal research**.** ▲ CRITICAL STEP Ensure that the animal is sufficiently anesthetized prior to transferring to the stereotaxic frame. The animal should have no response to a toe pinch and its breathing rate should reduce to ~1 Hz.

25 |Transfer the animal to the stereotaxic frame, ensuring proper airflow of isoflurane to the nose cone (~2.5% isoflurane; 1.5 L/min O_2). ▲ CRITICAL STEP Isoflurane levels should be monitored throughout the surgery to maintain sufficient anesthesia (no toe pinch response) and breathing (1 Hz). For longer duration surgery, isoflurane levels may be decreased to as low as 1%. Sterile, aseptic conditions should be used at all times to avoid infection.▲ CRITICAL STEP Proper placement in the stereotaxic frame is required for accurate injection of virus and devices. ? TROUBLESHOOTING

26 |Apply ophthalmic ointment to protect the eyes during surgery.

27 |Shave a 2 x 1 cm area on the animal's scalp (**Figure 3.5C**).

28 |Inject 0.1 mL of Enroflaxin into the hindlimb (i.m.) and 0.3 mL saline solution (0.9% (w/v), s.c.) to prevent infection and dehydration, respectively.

29 |Using a cotton swab, apply 70% ethanol (vol/vol) and betadine to the shaved area.

30 |Carefully grasp the tissue with the forceps and, using the scissors, make an incision the length of the shaved area of the animal's scalp (**Figure 3.5D**). ▲ CRITICAL STEP Ensure that all surgical instruments are sterilized prior to each animal surgery.

31 |After the skin separates, use the forceps and scissors to clean and remove any remaining periosteum on the skull surface.

32 |Identify the skull sutures, lambda and bregma. Carefully level the skull according to the manufacturer's recommend steps for your stereotaxic frame. For the KOPF Model 1900, use the stereotaxic alignment indicator. It is critical that both lambda and bregma be level, as well as achieving a level plane laterally across the skull. ? TROUBLESHOOTING

33 |Once the skull is level, move the drill to the coordinates you have selected for anchor screw placement. Carefully drill a hole with a diameter just wide enough for the screws to catch and not so deep as to penetrate the skull (**Figure 3.5E**). ▲ CRITICAL STEP Proper anchoring is crucial to ensure that the headcap remains affixed to the skull for the duration of the behavioral experiments. Generally, anchor screws should be placed on either side of the midline within 2 mm of the site of implantation. ? TROUBLESHOOTING

34 |Use the forceps and microspatula to properly anchor the screws into the skull (**Figure 3.5F**)

35 |Move the drill above the injection site. Drill a hole that penetrates the skull, but not the dura. ▲ CRITICAL STEP Drilling through the dura can cause widespread damage, bleeding, and inflammation under the skull.

36 |Align the infusion pump and lower the injection needle to the dorsal-ventral stereotaxic coordinates of the targeted structure of interest (**Figure 3.5G**). ▲ CRITICAL STEP A beveled needle can penetrate the dura safely. If a blunt needle is used the dura should be pierced using a sharp, sterile needle.

37 |Using the microcontroller, infuse the virus at a maximum rate of 100 nl/minute. Volume of virus will vary depending on the brain structure and serotype of virus used (Cardin et al., 2010; Fenno et al., 2011; Gradinaru et al., 2010; Osakada and Callaway, 2013; Osakada et

al., 2011; Yizhar et al., 2011; Zhang et al., 2010). ▲ CRITICAL STEP All viruses should be kept on ice prior, but special care should be taken with lentiviruses and herpes simplex viruses to prolonged exposure to temperatures above 4ºC. ? TROUBLESHOOTING

38 |Once the infusion is complete, allow the injection needle to remain in place for one minute for every 100 nl of virus infused. Slowly remove the needle from the injection site.

39 |Position the cannula holder above the drill hole (**Figure 3.5H**). Take care to orient the μ-ILED/other functionalities in the direction suitable for the experiment in order to properly illuminate the opsin expressing brain region of interest. ▲ CRITICAL STEP For injection into rodents, rinse with ethanol to sterilize the device prior to injection. For other mammals and primates it might be necessary to use room temperature Ethylene Oxide (EtO) gas sterilization (http://www.anpro.com/sterilizers/anprolene/indexanprolene.html) ?TROUBLESHOOTING

40 |Slowly lower the device into the brain to the desired dorsal-ventral coordinates.

41 |Using a syringe needle, slowly apply ACSF to the skull to dissolve the silk-based adhesive. The brain tissue will dissolve the adhesive inside the skull. Wait at least ten minutes to allow for complete dissolution of the adhesive (**Figure 3.5I**). ▲ CRITICAL STEP The adhesive must be completely dissolved prior to μ-needle removal. If not, the final placement of the flexible substrates will be affected.

42 |Slowly remove the μ-needle. Monitor the position of the flexible substrates to ensure that zero movement occurs. If the adhesive is completely dissolved, the μ-needle will remove with ease and without movement (**Figure 3.5J**).

43 |Prepare the dental cement according the REAGENT SETUP.

44 |Using the microspatula, carefully apply a layer of dental cement directly to point of injection

to fully secure the placement of the device (**Figure 3.4K**). ▲ CRITICAL STEP Allow this layer of cement to completely cure prior to building the structure of remaining headcap.

45 |Once the initial layer of cement is fully cured, position the PCB-based connector in the desired orientation. Apply a small amount of dental cement to secure it to the base layer (**Figure 3.5l**). ▲ CRITICAL STEP The orientation of the connector will determine the orientation of the RF headstage antenna.

46 |Finish the headstage by completely encapsulating the device-related hardware in dental cement. Be sure to leave the pins of the connector exposed to allow for connections to RF or wired functional generator. (**Figure 3.5M and N**). ? TROUBLESHOOTING

47 |Using a sterile spatula, detach any scalp skin from the cement. If the skin and the cement are connected, the headstage will be less stable over time.

48 |Liberally apply (~1g) the antibiotic ointment and lidocaine ointment to the entire incision area.

49 |Remove the animal from the stereotaxic frame and place it in a clean homecage position on top of a heating pad for recovery. The animal should recover rapidly (<15 minutes) and can be returned to its homecage once it displays normal, awake locomotor behaviors. Because the only exposed portion of the devices are the metal connector pins, the animals can be group-housed for the duration of their experimental lifetime. However, if one chooses, the pins can be capped using a dummy connector.

50 |The μ-needle should be clear of any components of the device. Remove from the cannula holder adapter and sterilize for re-use (**Figure 3.5O**) as described in **Optional Section 2 and Figure 3.8.**

Preparation for behavioral testing ● TIMING ~5 days

51 |House mice until the time at which proteins would be expected to be expressed. The choice

of viral expression system will determine expression time, and hence this wait time prior to
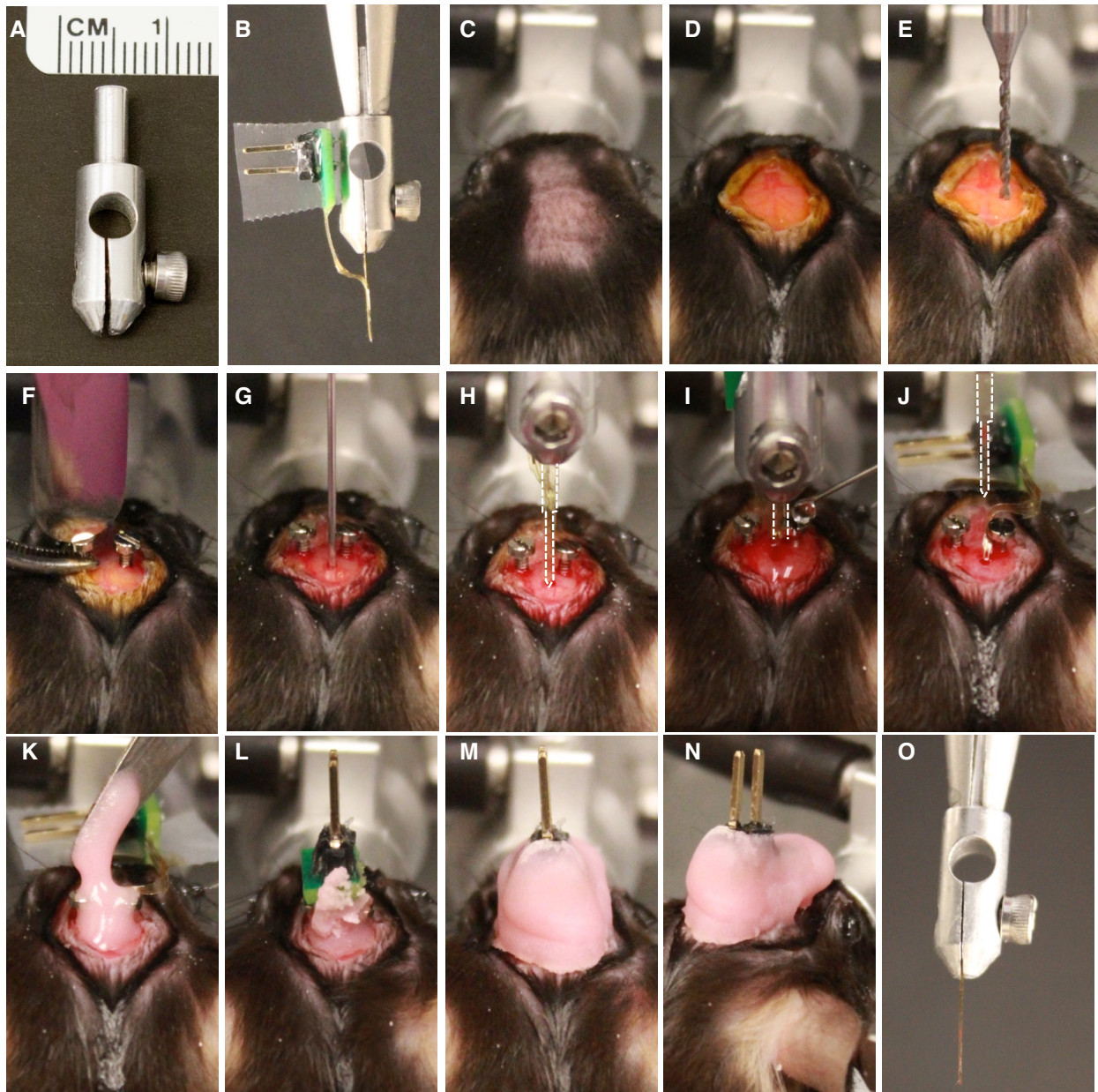
Figure 3.5 Surgical procedure for injection of virus and µ-ILED devices into mouse brain.

(**A**) Custom-built adapter for accurate stereotaxic placement of device (see EQUIPMENT SETUP). (**B**) Mounted µ-ILED device, ready for injection into the animal. The exposed µ-needle is grasped with the adapter and a small piece of tape is used to secure the PCB during surgery. (**C**) A properly mounted mouse with head shaved and eyes-lubricated is ready for surgery. (**D**) Betadine and ethanol is used to prevent infection and the scalp is open to expose the skull. (**E**) After leveling the skull, the drill is used to create pilot holes for the bone screws. (**F**) Forceps and a spatula or jewelry screwdriver is used to drive the screws into the skull. (**G**) The syringe needle is lowered to the desired coordinates to deliver the virus containing the optogenetic construct. (**H**) A µ-ILED device prepared to be driven into the brain using the same craniotomy as the viral injection. Dashed lines outline the shape of the device for clarity. (**I**) The µ-ILED device is lowered into the tissue and ACSF is applied to the skull surface to dissolve any external silk adhesive. (**J**) After a 15 minute waiting period, the µ-needle is carefully retracted from the skull. (**K**) Dental cement is applied directly to the craniotomy site to secure the µ-ILED device in its targeted position. (**L**) The PCB connector is secured above the bone screws using a second layer of dental cement. (**M,N**) The PCB connector is completely encapsulated in dental cement, taking care to ensure that no bonds are made directly to the soft tissue. (**O**) The adapter is shown following surgery, containing only the µ-needle. All procedures were approved by the Animal Care and Use Committee of Washington University and conformed to US National Institutes of Health guidelines.
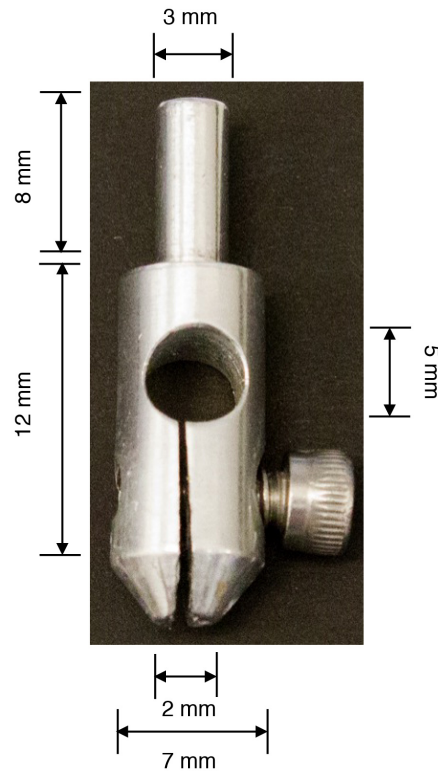
Figure 3.6 Machining of the cannula holder adapter. This adapter is specifically designed for use with the KOPF Model 1966 Cannula Holder. The adapter is fashioned from aluminum with an 8 mm stalk (3 mm in diameter) that can be held by the Model 1966. The main body of the adapter is 14 mm in length with a 7 mm diameter. There are two orthogonal bore holes through the body. The first is a 5 mm hole from which the center slit is created through to the tip of the adapter. The second is a 2 mm screw-hole so that a screw can be tightened to reduce the size of the center slit to hold the μ-needle. It is important that the center point of the adapter be in-line with the center point of the cannula holder itself to ensure accurate device injection. Note that this adapter is merely a suggestion, but we acknowledge there can be many other solutions to the problem of accurate injection of the devices. Most stereotaxic instrument manufacturers offer custom-built holders and it is likely that many standard electrode holders can be modified to suit the needs of the individual laboratory (e.g. KOPF Model 1768).

behavioral experimentation. This duration will vary from one to six weeks. For adeno-associated viral expression typical wait times are 2-3 weeks for expression at cell bodies (See Chapter 2) (Cardin et al., 2010; Kim et al., 2013b; Lammel et al., 2012; Yizhar et al., 2011; Zhang et al., 2010).

52 |At least five days before experimentation, handle animals to acclimate the animals to manipulation. In particular, connectors should be fitted to the headstage and any areas of the body that will be injected should be gently touched in order to habituate the animal to the manipulations they will experience during behavioral testing (e.g. the nape of the neck for subcutaneous, the abdomen for intraperitoneal, etc.).

53 |Also habituate animals to the method of powering the devices. If a wired approach is used, animals should be connected to the wires and allowed to explore a homecage environment for at least 20 minutes once a day for three days. If a wireless approach is used, the RF headstage antenna should be connected in the homecage for the same duration. ▲ CRITICAL STEP To eliminate locomotor confounds, the animals must be habituated to carrying the added weight of the antennas.

54 |Perform wired (option A) or wireless (option B) behavioral tests. ▲ CRITICAL STEP The timing of the photostimulation will depend on the parameters and goals of the study, but the pulse generation options are well suited for a wide variety of approaches. Any traditional function generator can either power the devices or provide TTL input into the RF signal generator to modulate the pulse width and frequency of the light pulses. If the photostimulation needs to be contingent on the animal's behavior this can be achieved by using live video tracking connected to a TTL output (Noldus Ethovision 9.0 with Trial and Hardware Control and I/O Box or other) or triggering a TTL signal from infrared beam breaks (Med Associates or other).

A) Wired optogenetic behavioral control ● TIMING variable

i. Once habituated to the connecting cables, power the devices using a traditional function generator. The pulse width and frequency of photostimulation should be determined and based on physiologically relevant conditions (Adamantidis et al., 2011; Jennings et al., 2013; Sparta et al.; Tye and Deisseroth, 2012; Tye et al., 2011). The timing of the photostimulation will greatly depend on the parameters and goals of the study.

ii. Connect the cable to the function generator using the BNC-to-banana plug adapter.

iii. Route the cabling. For most wired behaviors, the best approach is to route the cabling through an electrical rotary joint as described previously (du Hoffmann et al., 2011).

iv. Carefully scruff the animal and connect the free end of the cable to the headstage of the animal. Place the animal in the behavioral apparatus (**Figure 3.7A)** and perform desired behavioral test.

v. Following the behavioral test, scruff the animal, and remove the cable from the headstage.

B) Wireless optogenetic behavioral control ● TIMING variable

i. Connect the function generator to the RF Signal generator, the RF signal generator to the RF power amplifier, and the RF power amplifier to the panel antenna. Be sure that the power supply is connected to the heat sink (see EQUIPMENT SETUP) to avoid damaging the amplifier. Connect the power supply to the RF amplifier. It is reasonable to assume that wireless operation of the devices would be compatible with any behavioral assay in which the behavioral apparatus itself does not interfere with the RF signal, but care should be taken to ensure proper powering of the devices in every behavioral apparatus used. CRITICAL STEP To avoid unnecessary powering of the devices, do not engage the power supply until

| Wired operation | Wireless operation with lightweight scavenger | Wireless operation with PCB scavenger |
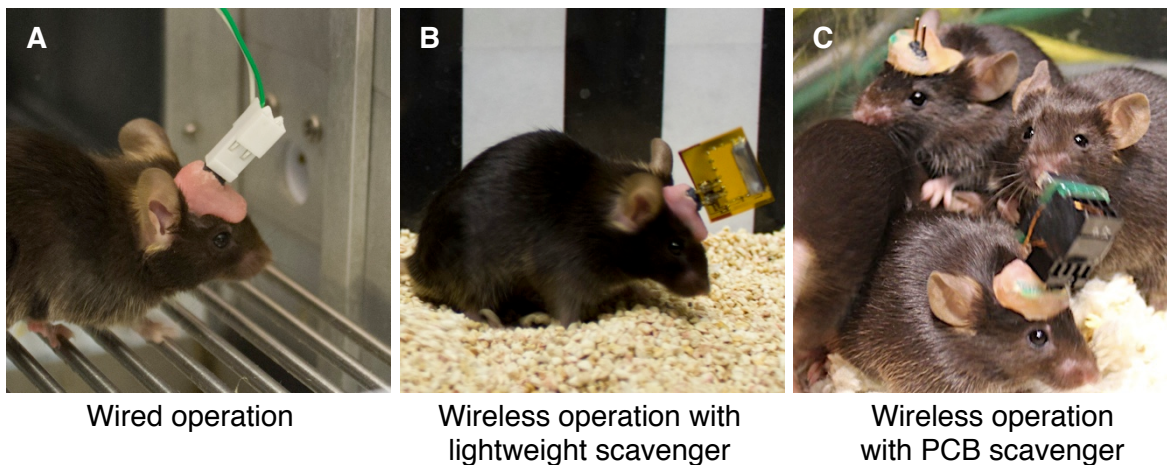
Figure 3.7 Expected results following viral and device injection. Once a device is injected, the standard connection allows for temporary coupling multiple means of powering in a variety of behavioral assays: (**A**) A mouse connected for wired powering in a standard operant behavioral chamber, (**B**) the same mouse prepared for wireless powering using the lightweight, flexible power scavenger in a conditioned place preference environment, (**C**) Two mice with implanted devices amongst cage mates. The mouse in the foreground has a PCB-style RF scavenger for powering in a homecage environment. All procedures were approved by the Animal Care and Use Committee of Washington University and conformed to US National Institutes of Health guidelines.

the beginning of the behavioral session. ? TROUBLESHOOTING.▲

ii. Carefully scruff the animal(s) and attach the RF scavenging antenna(s). Place the animal(s) in the behavioral apparatus and perform the behavioral test (**Figure 3.7B** and **C)**.

iii. Following the behavioral test, carefully scruff the animal and remove the scavenging antenna.

iv. After the final behavioral session, if desired kill animals and use tissue for any manner of post-mortem evaluation (See Chapter 2) (Kim et al., 2013b). ? TROUBLESHOOTING

Optional Section 1| Combining multifunctional sensors and optoelectronics

One hallmark of these devices is their ability to both deliver light into the brain and record information from the brain. Depending on the experiment, users may wish to outfit the devices with a variety of multiple and optional modalities. Each different modality can be combined with any other modality; devices can have between one and four different modalities incorporated. However, if the electrophysiological sensor is incorporated it should be the outermost layer to have direct exposure to the tissue. The following steps provide information on adding functional layers to the devices. If these optional modalities are desired, **Optional Section 1** should be completed prior to Step 16 of the main PROCEDURE.

A) Fabrication of temperature sensors (4th layer shown in Figure 3.3**)**

i. Generate PR patterns on a needle-shaped piece of PET (same substrates used in procedure 12) and deposit platinum (Pt, 10 nm) by sputtering. Remove PR by acetone and generate Cr/Au (15/300 nm) metal lines that connect to the Pt resistor.

ii. Calibrate the temperature sensor. Dip the temperature sensor into deionized (DI) water and

measure reference resistance using digital multimeter. With precisely controlled temperature of the DI water, measure the changes in resistance. Since the resistance change (ΔR) of the Pt resistor depends linearly on the temperature change (ΔT), the formula for estimated temperature is $\Delta T \sim k \cdot \Delta R$ where k is constant.

B) Fabrication of µ-IPDs

CRITICAL (2nd layer shown in Figure 3.3**)**, Additional details of this method are shown in a previous publication (Kim et al., 2008).

i. Deposit SiO$_2$ by PECVD on a silicon-on-insulator (SOI) wafer, with a top silicon layer thickness of approximately 1 µm.

ii. Generate PR patterns to pattern the SiO$_2$ using hydrofluoric acid (HF).

iii. Remove PR and clean the wafer surface by RCA cleaning. First perform SC (standard cleaning)-1 with 1:1:5 solution of ammonium hydroxide (NH$_4$OH):Hydrogen peroxide(H$_2$O$_2$):DI water at 80 ^{o}C for 15 min. Second remove the SiO$_2$ layer using 1:50 solution of HF:DI water. Finally perform SC-2 with a 1:1:6 solution of hyrdrochloric acid (HCl):H$_2$O$_2$:DI water at 80 ^{o}C for 15 min (RCA Cleaning: http://inside.mines.edu/fs_home/cwolden/chen435/clean.htm).

iv. Carry out solid state doping of the silicon to form a p-type region.

v. Repeat above Steps 4 to 6 from for n-type doping.

vi. Generate PR hole patterns on the entire wafer surface and etch the silicon layer, to define the lateral dimensions of the photodetectors.

vii. Etch the buried oxide (BOx) layer using HF

viii. Retrieve a ~1 µm thick thin Si membrane photodiode using a PDMS slab and release it onto

131

the needle-shaped PET substrate (described in PROCEDURE, Step12)

ix. Form metal (Cr/Au, 15/300 nm) lines for interconnect.

C) Fabrication of μ-electrode for electrophysiological sensor (1st layer shown in Figure 3.3)

i. Generate PR (AZ 2030) lift off patterns

ii. Deposit Pt (30 nm) a needle-shaped piece of PET (described in PROCEDURE Step 12) by sputtering. Generate a pattern of SU-8 2 (2 μm thick) with 20 x 20 μm^2 square opening. ▲ CRITICAL STEP Additional oxygen descum to remove residual PR layer is recommended. The impedance of the Pt μ-electrode should be ~1.0 MΩ at 1 kHz.

Optional Section 2| Recycling the optoelectronic devices for re-use

1| After sacrificing the animal, use forceps to forcibly remove the headcap from the surface of the skull. Thoroughly remove any visible biological tissue or other build-up from the sides and bottom of the headcap. Take care not to damage the flexible aspect of the device. Once removed and cleaned, the headcap is ready for dissolution (**Figure 3.8A**).

2| Place the headcap into a glass beaker and add methyl methacrylate until the headcap is entirely submerged (**Figure 3.8B**). Cover the beaker with tin foil and place in a properly ventilated fume hood overnight. ! CAUTION Methyl Methacrylate Monomer is a flammable liquid. It may also cause skin irritation; avoid contact with skin, eyes, and clothing. Use with adequate ventilation.

3| Following overnight incubation, the dental cement should be completely dissolved. The device and bone screws should be clearly visible in the beaker (**Figure 3.8C**). Wearing

gloves and using forceps, remove these items from the beaker. The screws can be cleaned, sterilized, and used for another surgery. The device will normally become inactive after dissolution of the
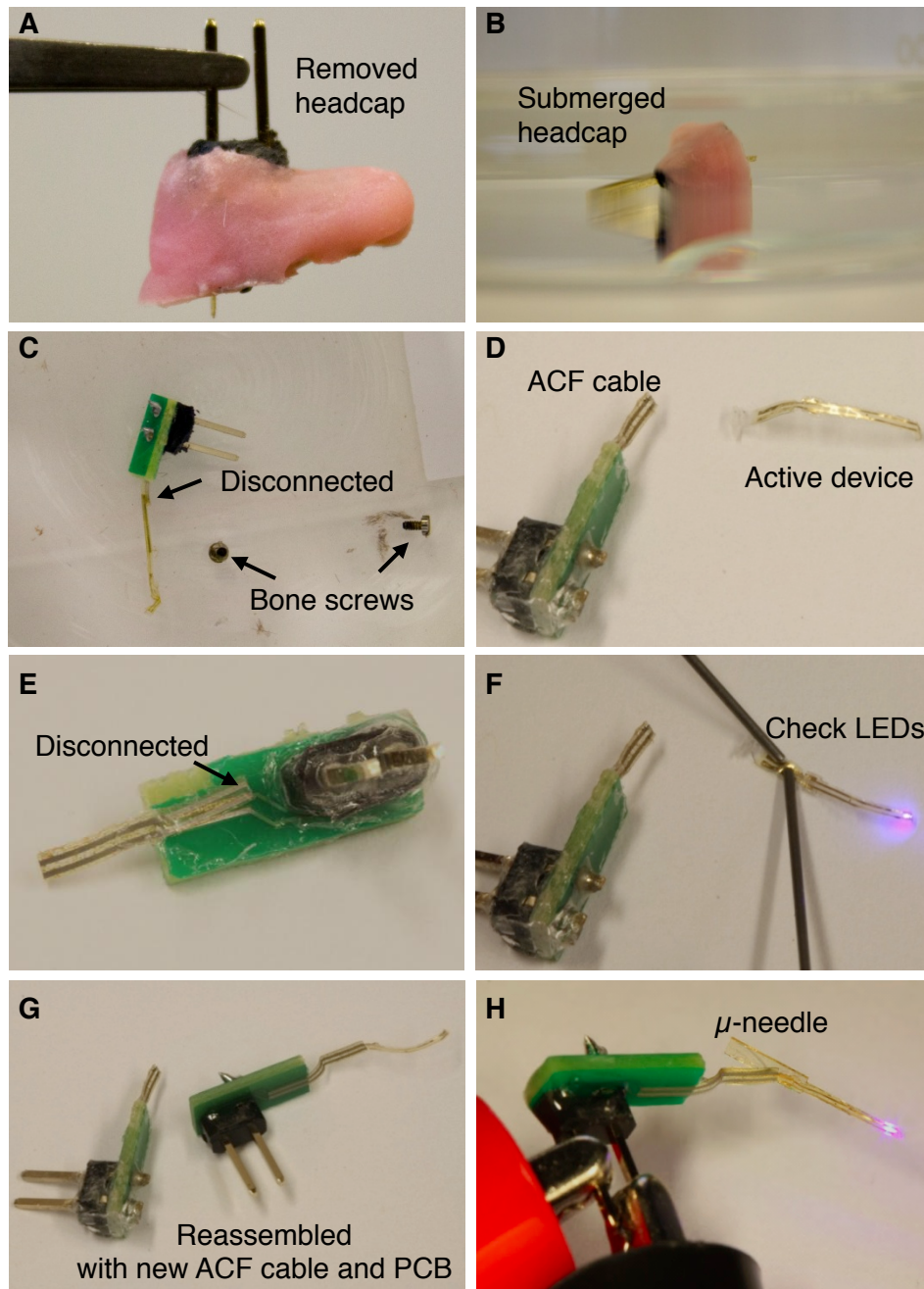
Figure 3.8 µ-ILED device recycling and re-fabrication for subsequent use. (**A**) The same headcap from Fig. 4, removed from the animal post-mortem and cleaned of biological material. (**B**) The headcap should then be fully submerged in methyl methacrylate. (**C**) Following overnight incubation in the stabilized methyl methacrylate monomer, the PCB, connector, µ-ILED device, and bone screws will be freely available in the solution. (**D,E**) Both connections with the ACF cable will also dissolve, rendering the device non-functional. (**F**) The device should be checked for reuse. If non-functional, the device should be discarded and a new device should be fabricated. (**G**) The working device is reassembled with new ACF cable and PCB. (**H**) The electrical connection through the new ACF cable should be checked after the device is attached with injection µ-needle again.

4 | headcap due to concurrent dissolution of the adhesive connecting the ACF cable to both the device and the PCB (**Figure 3.8D and E**). Prior to proceeding to Step 4, use a multimeter to check that all µ-ILEDs still function properly (**Figure 3.8F**). If any of the µ-ILEDs have electrical failure, discard the device and begin the fabrication process anew. ? TROUBLESHOOTING

5 | Discard the original PCB, and reassemble the device as described in Step 17 (**Figure 3.2G and H**).

6 | Apply PDMS to the entire device construction to provide passivation and waterproofing for operation *in vivo* as in Step 19 (**Figure 3.2I**).

7 | Attach the µ-needle using the silk adhesive and test the device to ensure proper electrical connection as done previously in Steps 18 and 20 of the PROCEDURE (**Figure 3.2J-L, 3.8G, and H**). The device is now ready for injection into a fresh animal starting at Step 24 of the PROCEDURE.

? TROUBLESHOOTING

Troubleshooting advice can be found in **Table 3.1**.

● TIMING

Steps 1–22, Preparation of µ-ILEDs, deterministic device assembly, and fabrication of wireless harvester: 9 d

Steps 22-50, Viral and device injection: 1 d for procedure, 1–6 weeks for expression

Steps 51-63, Behavioral experimentation: 5 d for preparation, variable by experiment

Optional Section 1, Combining multifunctional sensors and optoelectronics: 1-4 d depending on modalities

Optional Section 2, Rescuing the optoelectronics for re-use: 2 d

ANTICIPATED RESULTS

Following successful fabrication and implementation of μ-ILEDs, wireless manipulation of intact mammalian neural circuitry is possible. While our group has demonstrated the feasibility of using these devices to investigate reward-related and anxiety-like behaviors (See Chapter 2) (Kim et al., 2013b), nearly any behavioral assay should be accessible with these devices. In particular, behaviors that require complete freedom of movement such as social interactions, wheel running, and homecage behaviors are now possible (**Figure 3.7C**). Users can expect injected devices to maintain function for many months, as we have tested devices up to six months following injection and observe that the devices retain their operational functionality (See Chapter 2) (Kim et al., 2013b). Furthermore, we show here that these devices can be reused in other animals to avoid the lengthy process of remaking new devices for each experiment. Depending on the nature of the experiment, a single panel antenna can power numerous headstage devices. If the stimulation parameters are the same across animals, this approach can greatly increase the experimental throughput for a variety of behavioral assays. Though not presented in detail here, a reasonable extension of this protocol would be to incorporate other existing microscale sensors such as pH, blood oxygen, glucose levels, or neurochemical detection onto μ-ILED devices (Clark et al., 2009; Kim et al., 2010b). In sum, the protocol described here should provide researchers the ability to use optogenetics to wirelessly control and study intact mammalian neural circuitry in a minimally invasive manner.

Table 3.1 ?TROUBLESHOOTING

Step	Problem	Possible reason	Possible solution(s)
14	Electrical device failure	Un-uniform coating of BCB passivation on μ-ILED	Spincoat BCB again and redo the process.
17, Optional Section 2	ACF cable bonding failure	Insufficient temperature and/or pressure when bonding	Be certain to apply enough pressure (~1 or 2 MPa) and temperature (150 ºC)
24	Device is damaged prior to or during mounting for surgery	The electrical components are grasped by the cannula holder adapter	Only grasp the upper, exposed portion of the μ-needle. No portion of the electrical components should be grasped with the cannula holder adapter. Be careful to apply appropriate pressure so as to avoid crushing the μ-needle.
25, 32	Inaccurate tissue targeting	Improperly aligned skull	Follow the instructions provided for your laboratory's stereotaxic equipment for ear bar placement and skull leveling. Species-specific ear bars may be required. If the suture lines for identifying bregma/lambda on the skull are difficult to visualize, a surgical microscope and/or treating the skull with hydrogen peroxide can be a helpful addition. It may be necessary to wait longer after penetration prior to removal of the μ-needle.
33, 36	Headcap falls off in homecage/during behavior	Insufficient anchoring or cement application	Dental cement is ideal for reusablility, but other adhesives such as VLC One Step Adhesive and C&B Metabond offer stronger bonds to the screws and skull surface. While two screws are normally sufficient, larger the PCB interfaces may require more anchor screws.

37, 63	Little or no expression of the viral construct	Improper handling and injection of the virus	Thaw virus as close in time to the surgery as possible. Maintain virus on ice until the time of injection. Depending on the promoter that drives expression, some systems will not provide sufficient opsin expression. This should be empirically determined prior to any attempted behavioral experiments.
40	Dissolution of silk adhesive during sterilization	Too much exposure to ethanol	Most aqueous solutions will dissolve the silk adhesive. Do not soak the devices in ethanol as this will promote dissolution of the adhesive. In our experience, rinsing the device with ethanol for ~15 seconds is sufficient to prevent widespread inflammation in mouse brain tissue (See Chapter 2) (Kim et al., 2013b). Care should be taken to use appropriate sterilization techniques in higher mammals to avoid immune responses, such as EtO gas sterilization.
54Bi	Insufficient RF power is reaching the headstage scavenger	The behavioral apparatus is between the panel antenna and scavenger (in an enclosure)	Connect a freestanding device to the scavenging headstage and place it in the behavioral enclosure. Using the gain on the RF signal generator adjust the RF power until sufficient power is available to power the μ-ILEDs to the desired light output. If problems powering the device persist, consider reducing the distance between the panel antenna and the scavenger.

Optional Section 2	Headcap does not fully-dissolve	Insoluble dental cement was used, not enough solvent, or extend duration of exposure to solvent	Some dental cements will not dissolve in methyl methacrylate. Consider using the exact recommended cements where possible. If using Jet Denture Repair, add more solvent or wait a longer durations for cap to dissolve.

REFERENCES

Adamantidis, A.R., Zhang, F., Aravanis, A.M., Deisseroth, K., and de Lecea, L. (2007). Neural substrates of awakening probed with optogenetic control of hypocretin neurons. Nature *450*, 420–424.

Adamantidis, A.R., Tsai, H.-C., Boutrel, B., Zhang, F., Stuber, G.D., Budygin, E.A., Touriño, C., Bonci, A., Deisseroth, K., and de Lecea, L. (2011). Optogenetic interrogation of dopaminergic modulation of the multiple phases of reward-seeking behavior. J. Neurosci. Off. J. Soc. Neurosci. *31*, 10829–10835.

Airan, R.D., Thompson, K.R., Fenno, L.E., Bernstein, H., and Deisseroth, K. (2009). Temporally precise in vivo control of intracellular signalling. Nature *458*, 1025–1029.

Cao, H., Gu, L., Mohanty, S.K., and Chiao, J.-C. (2013). An integrated µLED optrode for optogenetic stimulation and electrical recording. IEEE Trans. Biomed. Eng. *60*, 225–229.

Cardin, J.A., Carlén, M., Meletis, K., Knoblich, U., Zhang, F., Deisseroth, K., Tsai, L.-H., and Moore, C.I. (2010). Targeted optogenetic stimulation and recording of neurons in vivo using cell-type-specific expression of Channelrhodopsin-2. Nat. Protoc. *5*, 247–254.

Carter, M.E., Yizhar, O., Chikahisa, S., Nguyen, H., Adamantidis, A., Nishino, S., Deisseroth, K., and de Lecea, L. (2010). Tuning arousal with optogenetic modulation of locus coeruleus neurons. Nat. Neurosci. *13*, 1526–1533.

Cavanaugh, J., Monosov, I.E., McAlonan, K., Berman, R., Smith, M.K., Cao, V., Wang, K.H., Boyden, E.S., and Wurtz, R.H. (2012). Optogenetic inactivation modifies monkey visuomotor behavior. Neuron *76*, 901–907.

Clark, J.J., Sandberg, S.G., Wanat, M.J., Gan, J.O., Horne, E.A., Hart, A.S., Akers, C.A., Parker, J.G., Willuhn, I., Martinez, V., et al. (2009). Chronic microsensors for longitudinal, subsecond dopamine detection in behaving animals. Nat. Methods *7*, 126–129.

Diester, I., Kaufman, M.T., Mogri, M., Pashaie, R., Goo, W., Yizhar, O., Ramakrishnan, C., Deisseroth, K., and Shenoy, K.V. (2011). An optogenetic toolbox designed for primates. Nat. Neurosci. *14*, 387–397.

Fenno, L., Yizhar, O., and Deisseroth, K. (2011). The Development and Application of Optogenetics. Annu. Rev. Neurosci. *34*, 389–412.

Gerits, A., and Vanduffel, W. (2013). Optogenetics in primates: a shining future? Trends Genet. TIG.

Gradinaru, V., Zhang, F., Ramakrishnan, C., Mattis, J., Prakash, R., Diester, I., Goshen, I., Thompson, K.R., and Deisseroth, K. (2010). Molecular and Cellular Approaches for Diversifying and Extending Optogenetics. Cell *141*, 154–165.

Han, X., Qian, X., Bernstein, J.G., Zhou, H., Franzesi, G.T., Stern, P., Bronson, R.T., Graybiel, A.M., Desimone, R., and Boyden, E.S. (2009). Millisecond-Timescale Optical Control of Neural Dynamics in the Nonhuman Primate Brain. Neuron *62*, 191–198.

Harrison, R.R., Kier, R.J., Leonardo, A., Fotowat, H., Chan, R., and Gabbiani, F. (2010). A wireless neural/EMG telemetry system for freely moving insects. In Circuits and Systems (ISCAS), Proceedings of 2010 IEEE International Symposium on, pp. 2940–2943.

Al-Hasani, R., McCall, J.G., Foshage, A.M., and Bruchas, M.R. (2013). Locus Coeruleus Kappa Opioid Receptors modulate Reinstatement of Cocaine Place Preference through a Noradrenergic Mechanism. Neuropsychopharmacology.

Du Hoffmann, J., Kim, J.J., and Nicola, S.M. (2011). An inexpensive drivable cannulated microelectrode array for simultaneous unit recording and drug infusion in the same brain nucleus of behaving rats. J. Neurophysiol. *106*, 1054–1064.

Hwang, S.-W., Tao, H., Kim, D.-H., Cheng, H., Song, J.-K., Rill, E., Brenckle, M.A., Panilaitis, B., Won, S.M., Kim, Y.-S., et al. (2012). A Physically Transient Form of Silicon Electronics. Science *337*, 1640–1644.

Iwai, Y., Honda, S., Ozeki, H., Hashimoto, M., and Hirase, H. (2011). A simple head-mountable LED device for chronic stimulation of optogenetic molecules in freely moving mice. Neurosci. Res. *70*, 124–127.

Jennings, J.H., Sparta, D.R., Stamatakis, A.M., Ung, R.L., Pleil, K.E., Kash, T.L., and Stuber, G.D. (2013). Distinct extended amygdala circuits for divergent motivational states. Nature *496*, 224–228.

Kim, D.-H., Ahn, J.-H., Choi, W.M., Kim, H.-S., Kim, T.-H., Song, J., Huang, Y.Y., Liu, Z., Lu, C., and Rogers, J.A. (2008). Stretchable and Foldable Silicon Integrated Circuits. Science *320*, 507–511.

Kim, D.-H., Viventi, J., Amsden, J.J., Xiao, J., Vigeland, L., Kim, Y.-S., Blanco, J.A., Panilaitis, B., Frechette, E.S., Contreras, D., et al. (2010a). Dissolvable films of silk fibroin for ultrathin conformal bio-integrated electronics. Nat. Mater. *9*, 511–517.

Kim, R.-H., Kim, D.-H., Xiao, J., Kim, B.H., Park, S.-I., Panilaitis, B., Ghaffari, R., Yao, J., Li, M., Liu, Z., et al. (2010b). Waterproof AlInGaP optoelectronics on stretchable substrates with applications in biomedicine and robotics. Nat. Mater. *9*, 929–937.

Kim, S.-Y., Adhikari, A., Lee, S.Y., Marshel, J.H., Kim, C.K., Mallory, C.S., Lo, M., Pak, S., Mattis, J., Lim, B.K., et al. (2013a). Diverging neural pathways assemble a behavioural state from separable features in anxiety. Nature *496*, 219–223.

Kim, T., Jung, Y.H., Song, J., Kim, D., Li, Y., Kim, H., Song, I.-S., Wierer, J.J., Pao, H.A., Huang, Y., et al. (2012a). High-Efficiency, Microscale GaN Light-Emitting Diodes and Their Thermal Properties on Unusual Substrates. Small *8*, 1643–1649.

Kim, T., Kim, R.-H., and Rogers, J.A. (2012b). Microscale Inorganic Light-Emitting Diodes on Flexible and Stretchable Substrates. IEEE Photonics J. *4*, 607–612.

Kim, T., McCall, J.G., Jung, Y.H., Huang, X., Siuda, E.R., Li, Y., Song, J., Song, Y.M., Pao, H.A., Kim, R.-H., et al. (2013b). Injectable, Cellular-Scale Optoelectronics with Applications for Wireless Optogenetics. Science *340,* 211–216.

Kravitz, A.V., Owen, S.F., and Kreitzer, A.C. (2013). Optogenetic identification of striatal projection neuron subtypes during in vivo recordings. Brain Res. *1511*, 21–32.

Lammel, S., Lim, B.K., Ran, C., Huang, K.W., Betley, M.J., Tye, K.M., Deisseroth, K., and Malenka, R.C. (2012). Input-specific control of reward and aversion in the ventral tegmental area. Nature *491*, 212–217.

Li, Y., Shi, X., Song, J., Lu, C., Kim, T. -i., McCall, J.G., Bruchas, M.R., Rogers, J.A., and Huang, Y. (2013). Thermal analysis of injectable, cellular-scale optoelectronics with pulsed power. Proc. R. Soc. Math. Phys. Eng. Sci. *469*, 20130142–20130142.

Osakada, F., and Callaway, E.M. (2013). Design and generation of recombinant rabies virus vectors. Nat. Protoc. *8*, 1583–1601.

Osakada, F., Mori, T., Cetin, A.H., Marshel, J.H., Virgen, B., and Callaway, E.M. (2011). New Rabies Virus Variants for Monitoring and Manipulating Activity and Gene Expression in Defined Neural Circuits. Neuron *71*, 617–631.

Park, S.-I., Xiong, Y., Kim, R.-H., Elvikis, P., Meitl, M., Kim, D.-H., Wu, J., Yoon, J., Yu, C.-J., Liu, Z., et al. (2009). Printed Assemblies of Inorganic Light-Emitting Diodes for Deformable and Semitransparent Displays. Science *325*, 977–981.

Ruiz, O., Lustig, B.R., Nassi, J.J., Cetin, A.H., Reynolds, J.H., Albright, T.D., Callaway, E.M., Stoner, G.R., and Roe, A.W. (2013). Optogenetics through windows on the brain in the nonhuman primate. J. Neurophysiol.

Sparta, D.R., Stamatakis, A.M., Phillips, J.L., Hovelsø, N., van Zessen, R., and Stuber, G.D. (2011). Construction of implantable optical fibers for long-term optogenetic manipulation of neural circuits. Nat. Protoc. *7*, 12–23.

Sparta, D.R., Jennings, J.H., Ung, R.L., and Stuber, G.D. Optogenetic strategies to investigate neural circuitry engaged by stress. Behav. Brain Res.

Stark, E., Koos, T., and Buzsaki, G. (2012). Diode probes for spatiotemporal optical control of multiple neurons in freely moving animals. J. Neurophysiol. *108*, 349–363.

Stuber, G.D., Sparta, D.R., Stamatakis, A.M., van Leeuwen, W.A., Hardjoprajitno, J.E., Cho, S., Tye, K.M., Kempadoo, K.A., Zhang, F., Deisseroth, K., et al. (2011). Excitatory transmission from the amygdala to nucleus accumbens facilitates reward seeking. Nature *475*, 377–380.

Szuts, T.A., Fadeyev, V., Kachiguine, S., Sher, A., Grivich, M.V., Agrochão, M., Hottowy, P., Dabrowski, W., Lubenov, E.V., Siapas, A.G., et al. (2011). A wireless multi-channel neural amplifier for freely moving animals. Nat. Neurosci. *14*, 263–269.

Tao, H., Brenckle, M.A., Yang, M., Zhang, J., Liu, M., Siebert, S.M., Averitt, R.D., Mannoor, M.S., McAlpine, M.C., Rogers, J.A., et al. (2012). Silk-Based Conformal, Adhesive, Edible Food Sensors. Adv. Mater. *24*, 1067–1072.

Tye, K.M., and Deisseroth, K. (2012). Optogenetic investigation of neural circuits underlying brain disease in animal models. Nat. Rev. Neurosci. *13*, 251–266.

Tye, K.M., Prakash, R., Kim, S.-Y., Fenno, L.E., Grosenick, L., Zarabi, H., Thompson, K.R., Gradinaru, V., Ramakrishnan, C., and Deisseroth, K. (2011). Amygdala circuitry mediating reversible and bidirectional control of anxiety. Nature *471*, 358–362.

Wentz, C.T., Bernstein, J.G., Monahan, P., Guerra, A., Rodriguez, A., and Boyden, E.S. (2011). A wirelessly powered and controlled device for optical neural control of freely-behaving animals. J. Neural Eng. *8*, 046021.

Witten, I.B., Steinberg, E.E., Lee, S.Y., Davidson, T.J., Zalocusky, K.A., Brodsky, M., Yizhar, O., Cho, S.L., Gong, S., Ramakrishnan, C., et al. (2011). Recombinase-driver rat lines: tools, techniques, and optogenetic application to dopamine-mediated reinforcement. Neuron *72*, 721–733.

Wong, W.S., Sands, T., Cheung, N.W., Kneissl, M., Bour, D.P., Mei, P., Romano, L.T., and Johnson, N.M. (2000). InxGa1−xN light emitting diodes on Si substrates fabricated by Pd–In metal bonding and laser lift-off. Appl. Phys. Lett. *77*, 2822–2824.

Yizhar, O., Fenno, L.E., Davidson, T.J., Mogri, M., and Deisseroth, K. (2011). Optogenetics in Neural Systems. Neuron *71*, 9–34.

Zhang, F., Gradinaru, V., Adamantidis, A.R., Durand, R., Airan, R.D., de Lecea, L., and Deisseroth, K. (2010). Optogenetic interrogation of neural circuits: technology for probing mammalian brain structures. Nat. Protoc. *5*, 439–456.

Zhao, Y., Larimer, P., Pressler, R.T., Strowbridge, B.W., and Burda, C. (2009). Wireless Activation of Neurons in Brain Slices Using Nanostructured Semiconductor Photoelectrodes. Angew. Chem. Int. Ed. *48*, 2407–2410.

Zorzos, A.N., Boyden, E.S., and Fonstad, C.G. (2010). Multiwaveguide implantable probe for light delivery to sets of distributed brain targets. Opt. Lett. *35*, 4133–4135.

Zorzos, A.N., Scholvin, J., Boyden, E.S., and Fonstad, C.G. (2012). Three-dimensional multiwaveguide probe array for light delivery to distributed brain circuits. Opt. Lett. *37*, 4841–4843.

(2011). Artificial cerebrospinal fluid (ACSF). Cold Spring Harb. Protoc. *2011*, pdb.rec065730.

Chapter 4

Wireless optofluidic systems for programmable *in vivo* pharmacology and optogenetics

Author contributions for the above citation:
*Co-first author. J.W.J. and **J.G.M.** worked iteratively together to generate working models of the optofluidic neural probes, designed all of the experiments, and wrote the paper. J.W.J. and his colleagues (G.S., M.K. S.L., K.I.J., Y.L.) were primarily responsible for the design and fabrication of the optofluidics. **J.G.M.** and his colleagues (R.A., D.Y.H., G.P.S., L.X., P.G.) performed all of the biology-related experiments. Y.Z. J.Y.S., Y.S., Z.H. and Y.H. were responsible for the thermal and fluid modeling. W.Z.R. provided the rats. M.R.B. and J.A.R. oversaw all experiments, helped design the devices, and helped write the paper.

SUMMARY

In vivo pharmacology and optogenetics hold tremendous promise for dissection of neural circuits, cellular signaling and manipulating neurophysiological systems in awake, behaving animals. Existing neural interface technologies, such as metal cannulas connected to external drug supplies for pharmacological infusions and tethered fiber optics for optogenetics, are not ideal for minimally-invasive, untethered studies on freely behaving animals. Here we introduce wireless optofluidic neural probes that combine ultrathin, soft microfluidic drug delivery with cellular-scale inorganic light-emitting diode (μ-ILED) arrays. These probes are orders of magnitude smaller than cannulas and allow wireless, programmed spatiotemporal control of fluid delivery and photostimulation. We demonstrate these devices in freely moving animals to modify gene expression, deliver peptide ligands, and provide concurrent photostimulation with antagonist drug delivery to manipulate mesoaccumbens reward-related behavior. The minimally-invasive operation of these probes forecasts utility in other organ systems and species, with potential for broad application in biomedical science, engineering, and medicine.

INTRODUCTION

Fundamental insights into the function of the central and peripheral nervous system often follow from advances in tools and methodologies for neuroscience research. Technologies for deep brain optical manipulation of neural activity allow for many types of basic research into neural circuits (Tye and Deisseroth, 2012), intracellular signaling (Siuda et al., 2015; Zhang and Cui, 2015), gene expression (Konermann et al., 2013; Polstein and Gersbach, 2015) and other biological processes. Additional levels of control follow from combined use of such approaches with pharmacological delivery (Jennings et al., 2013; Stamatakis et al., 2013; Walsh et al., 2014). Furthermore, the potential of these combinatorial approaches for clinical impact was recently

145

demonstrated using combined optical and pharmacological intervention to inform and modify traditional, electrical deep brain stimulation to be more effective for off-label psychiatric disorders (Creed et al., 2015). A key technological challenge has been the development of miniaturized, self-contained systems that are capable of providing such functionality with wireless control in feely moving, awake animal models. Conventional methods rely on metal tubes (cannulas) and fiber optic cables to deliver drugs and light, respectively. Typically each modality requires connection to separately located light and fluid sources that physically tethers the animals and restricts their natural movement. Recent advances have combined cannulas and fiber optics into small, multifunctional fibers that have capabilities in fluid delivery and photostimulation, but which retain similar requirements for multiple, external connections (Canales et al., 2015). All these technologies use rigid materials as neural interfaces leading to adverse consequences for chronic use. The tissue benefit of mechanical compliance was recently demonstrated comparing standard systems against systems that combine soft electrodes and microfluidic structures in epidural implants (Minev et al., 2015) (See Table 4.1 for feature comparison).

The approach we report here describes complete platforms that include power supplies, control electronics, wireless interfaces, active fluidic handling systems and efficient light sources, into compact, head-mounted devices that interface with thin, mechanically compliant multifunctional neural probes. The result is a set of unique capabilities in programmed delivery of multiple types of pharmacological agents and monochromatic light to discretely targeted regions of the deep brain. These systems, which we refer to as wireless optofluidic neural probes, create important opportunities in neuroscience research that combines *in vivo* pharmacology with

146

	Optofluidic neural probes	Electronic dura mater (Minev et al., 2015)	Multifunctional Fiber (Canales et al., 2015)	NeuroMedicator (Spieth et al., 2012)
Operation	Wireless	Tethered	Tethered	Tethered
Modality	Optical & Fluidic	Fluidic & Electrical	Optical, Fluidic & Electrical recording	Fluidic only
Programmable operation	Yes	No	No	Yes
Mechanical property of the probe	Soft, flexible	Soft, flexible	Flexible	Rigid
	Modulus: ~ 1 Mpa	Modulus: ~ 1 Mpa	Not reported	Modulus: ~170 GPa
	Stiffness: 13-18 N/m	Not reported	Stiffness: 107-149 N/m	Not reported
Optical property	Optically transparent	Optically transparent	Not transparent	Not transparent
Number of independent drug channels	4	1	2	2
Drug leakage	No leakage	No leakage	No leakage	Leakage by diffusion
Dimensions	80 um in thickness	200 um in thickness	400-700 um in diameter (for multimodal fibers)	250um in thickness

Table 4.1. Comparison of various neural probes with related capabilities, related to Figure 4.1.

wireless optogenetics. Examples in awake, freely moving animals demonstrate the sophisticated levels of spatiotemporal control over neural circuit functions that are possible without physically contacting the animal. Specifically, optical manipulation of projections from the ventral tegmental area dopaminergic system into the nucleus accumbens can elicit place preference behaviors that can be blocked, in a temporally-precise programmable manner, by site-specific infusion of a dopamine receptor antagonist. These and related studies represent the sort of versatile, complex experimental options provided by the technology we report here.

RESULTS

Ultrathin, Soft Neural Probes Have Wireless Capabilities For Programmed Drug Delivery and Photostimulation

Figure 4.1 A-C show schematic illustrations and photographs of a multichannel, soft microfluidic system, in which two thin, narrow pieces of the elastomer polydimethylsiloxane (PDMS) bond together to form a set of four channels each with 10×10 μm^2 cross-sectional areas in a platform that has a total thickness of 50 μm. This type of microfluidic probe (**Figure 1, B and C**) is transparent (> 95 % throughout across wavelengths from 400 nm to 700 nm) and mechanically soft (modulus ~1 MPa; bending stiffness 13-18 N/m), thereby enabling both optical access and minimally invasive use in soft neural tissue (see Chapter 2) (Canales et al., 2015; Capadona et al., 2012; Jeong et al., 2015; Kim et al., 2013b; Kozai et al., 2012; Minev et al., 2015; Subbaroyan et al., 2005; Wu et al., 2013). The former characteristic facilitates integration of microscale inorganic light-emitting diodes (μ-ILEDs) on a filament of polyethylene terephthalate (PET) with thickness of 6 μm (**Figure 4.1D**). These μ-ILEDs (each with thicknesses of 6.54 μm and lateral dimensions of 100×100 μm^2; **Figure 4.1E**) (see Chapter 2) (Kim et al., 2013b) provide spatially- and temporally-precise delivery of light in regions adjacent to the outlets of the microfluidic channels. Active infusion of multiple drugs through these four individual channels (**Figure 4.1F**) can be controlled independently from the μ-ILEDs. This system allows for tandem pharmacological and optogenetic manipulation of neural circuitry, with potential for application in optopharmacology where the use of light to activate compounds requires high spatiotemporal control of both drug and light delivery (Kramer et al., 2013) (**Figure 4.1G**).

Figures 4.1G, H and **I** provide comparisons of this type of compliant optofluidic probe to a standard metal cannula (see also **Figure 4.2**). The latter is hard, rigid, and displaces large amounts of brain tissue (diameter ~500 μm), whereas the former is soft, flexible, and minimally invasive (total thickness ~ 80 μm). The low bending stiffness (13-18 N/m, compared to > 5 MN/m for the 26 gauge cannula) of the optofluidic probes (**Figure 4.3**) facilitates adaptation to the micromotions associated with movement, respiration, and blood flow (Gilletti and Muthuswamy, 2006). This probe property minimizes mechanically induced damage or irritation of the brain tissue in chronic applications (Lee et al., 2005). X-ray computed tomographic images of mice implanted with these two types of fluidic delivery systems highlight the notable differences in scale and impact on the tissue (**Figures 4.1H and I**).

Thermo-mechanical-fluidic Characteristics of the Optofluidic Devices

Figure 4.4A presents a schematic diagram of the overall system, with emphasis on the fluid-controlling hardware. The schemes for fluid handling and pumping represent extensions of recently reported drug delivery systems that use rigid, single-channel and single-reservoir microfluidics and wired control interfaces (Spieth et al., 2012). Each of the four channels connects to a separate reservoir whose base consists of an active layer (2:1 mixture of PDMS and expandable microspheres, Expancel 031 DU 40, AkzoNobel) that initiates pumping through expansion induced by Joule heating in an underlying element (serpentine traces of gold with thickness of 185 nm). A dramatic increase in the volume of the active layer follows from thermally induced, irreversible expansion of hollow polymer microspheres that encapsulate hydrocarbon gas (**Figure 4.4B**). The supporting substrate (FR4) has a low thermal conductivity (0.4 W/m·K), thereby minimizing the electrical power needed to reach the temperatures required for this type of thermal actuation. The four reservoirs exist as molded features in a cyclic olefin

polymer (COP), chosen for its low water vapor permeability ($0.023\text{g}\cdot\text{mm/m}^2\cdot\text{day}$). Thin copper membranes (thicknesses of 3 μm) seal the outlets of the reservoirs to prevent evaporation. This design allows delivery of multiple drugs without the repeated insertion of a delivery probe.
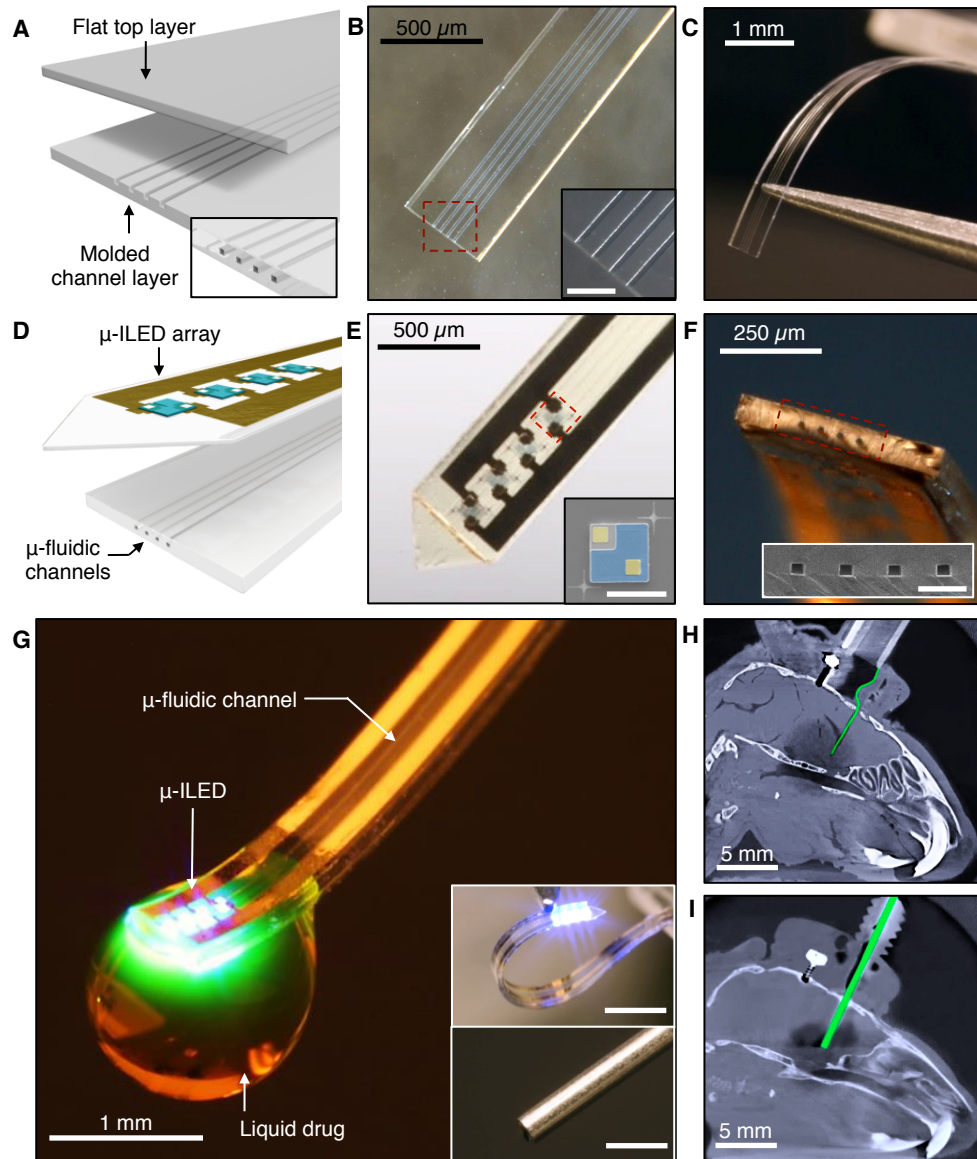
Figure 4.1 Ultrathin, Soft Neural Probes with Wireless Capabilities in Programmed Drug Delivery and Photostimulation (A) Schematic diagram of the assembly of a soft microfluidic probe. Bonding thin, molded (bottom) and unmolded (top) layers of PDMS together yields a system that includes four separately addressable microfluidic channels each with cross sections of 10×10 μm^2, and a total thickness of 50 μm and width of 500 μm, as illustrated in the inset at the bottom right. **(B)** Optical micrograph of a microfluidic probe formed in this way. (Inset) Magnified view of the channels. Scale bar, 100 μm. **(C)** Picture that illustrates the soft, compliant mechanics of the device. **(D)** Schematic diagram of the integration of a soft microfluidic probe with a flexible array of μ-ILEDs (each with lateral dimensions of 100x100 μm^2, and thicknesses of 6.54 μm) and metal interconnect traces on a film of PET (thickness of 6 μm). **(E)** Optical micrograph of an integrated probe, which we refer to as an optofluidic system. (Inset) Colorized SEM of a representative μ-ILED (contact electrodes, yellow; spreading layer, blue). Scale bar, 100 μm. **(F)** Tilted view of an optofluidic probe that shows the tip end. (Inset) SEM of the outlets of the microfluidic channels. Scale bar, 50 μm. **(G)** Optofluidic neural probe during simultaneous drug delivery and photostimulation. (Insets) Comparison of such a device (top) and a conventional metal cannula (bottom; outer and inner diameters of ~500 and 260 μm, respectively). Scale bars, 1 mm. **(H & I)** X-ray computed tomographic images of the mouse models with **(H)** an optofluidic neural probe and **(I)** a metal cannula implanted into the brain. Both devices are colorized green.
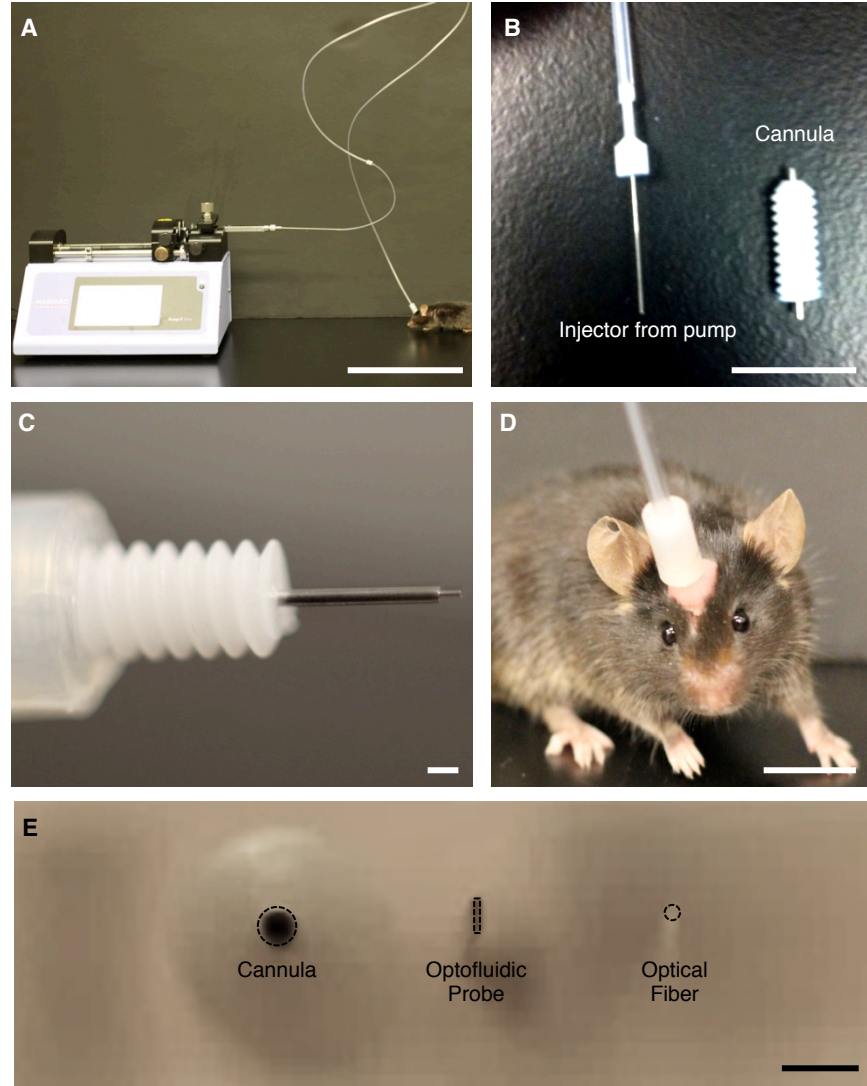
Figure 4.2 Conventional cannulae to deliver drugs into the brain via an external pump. Related to Figure 4.1. **(A)** Example of microinfusion pump system set up and connected to an awake behaving mouse. Scale bar, 10 cm. **(B)** Injector and metal cannula (500 μm diameter metal tube). Scale bar, 1 cm. **(C)** Connected injector/cannula (Note: 500 μm projection beyond cannula termination). Scale bar, 1 mm. **(D)** Mouse with cannula implanted into dorsal striatum, connected to microinfusion pump. Scale bar, 1 cm. **(E)** Top views of a metal cannula, an optofluidic probe, and an optical fiber. Metal cannula: 500 μm in diameter; Optofluidic probe: ~80 μm in thickness; Optical fiber: 125 μm in diameter including a cladding. Scale bar, 1mm.
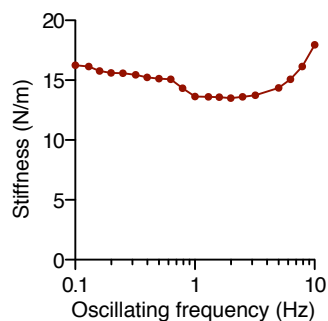
Figure 4.3 Bending stiffness measurement of the optofluidic probe at physiological frequency range (respiration, heat beat, etc). Related to Figure 4.1. Dynamic mechanical analyzer (DMA Q800) in the single cantilever mode was used to measure the bending stiffness.

As illustrated in **Figure 4.4C**, activating a Joule heating element launches expansion of the corresponding active layer (**Figure 4.4B)**. The resulting pressure in the reservoir ruptures the thin copper membrane and pumps the drug, with nearly 100% efficiency in volume delivery (0.5 µl in this case; **Figure 4.4D**), through the respective microfluidic channel. Quantitative measurements and numerical modeling based on finite element analyses (FEA) capture the thermal and mechanical aspects of operation. Because the modulus of the COP material (~ 2.6 GPa) is much higher than that of the expandable polymer (~ 3.0 MPa), deformations induced by thermal actuation are almost exclusively accommodated by the latter, as shown by both experimental and FEA results (**Figure 4.4D and Figure 4.5, A-C**). Quantitative studies (**Figure 4.4D**) indicate a negligible amount (< 8.5%) of infusion for heating of the active layer to temperatures below ~75 $^{\circ}$C, followed by a rapid increase above ~82 $^{\circ}$C, finally reaching complete infusion (> 99.5% of the volume of the reservoir) at ~87 $^{\circ}$C. This nonlinear behavior originates from the nonlinear thermal expansion properties (**Figure 4.4B**). FEA results for the spatiotemporal temperature distribution of isolated Joule heating elements agree with IR images, as shown in **Figure 4.2E**, thereby validating the use of computation in design optimization (**Figure 4.5D**). The increase in temperature decays rapidly along both the thickness and in-plane directions (**Figure 4.4F and H**), to allow efficient individual control of the reservoirs. Computed

153

and measured temperatures at representative locations for times before, during and immediately after actuation appear in **Figure 4.4G**. The average temperature of the drug in the reservoir remains in a range (< 60 ºC) compatible with many neuroactive compounds (Callahan et al., 2001; Joyce et al., 1984; Steger et al., 1996). Calculations based on a simplified fluid dynamics model (see SI for details) indicate that the drug cools significantly as it flows down the microfluidic channels before reaching the outlets and penetrating the targeted tissue (< 0.1 ºC higher than the temperature of the surroundings).

Wireless Optofluidic Devices Can Deliver Multiple Fluids and Photostimulation

Figure 4.6A (left) provides a schematic illustration of control hardware and associated electronics, along with the key components that directly support the array of μ-ILEDs and the soft microfluidic probe. A battery-powered infrared (IR) wireless module enables independent control of fluid delivery and optical activation. The system uses serial communication between a separate IR transmitter (950 nm wavelength) and the receiver, to provide programmable activation of individual heaters in the array (heater 1, 2, 3, or 4) and the μ-ILEDs (in this case 5, 10, 20, or 40 Hz with 10 ms pulse width; Figure S4A). A thin, flexible printed circuit board (PCB) serves as a substrate for a microcontroller (556-ATTINY84-20MU, Atmel), transistors, and an IR detector with wide sensing angle (120˚; IR Sensor IC 38 kHz, Vishay Semiconductors). Two small, rechargeable lithium ion batteries (GM300910H, PowerStream Technology; **Figure 4.7B**) provide power. The entire collection of components (including the optofluidic probe, microfluidic reservoirs and actuators, the wireless module, and two batteries) is sufficiently lightweight (~ 1.8 g) to allow head mounting on adult mice and rats (**Figure 4.7C**). The wireless module and rechargeable batteries release from the optofluidics to allow quick replacement, thus facilitating long-term operation in various behavioral experiments.
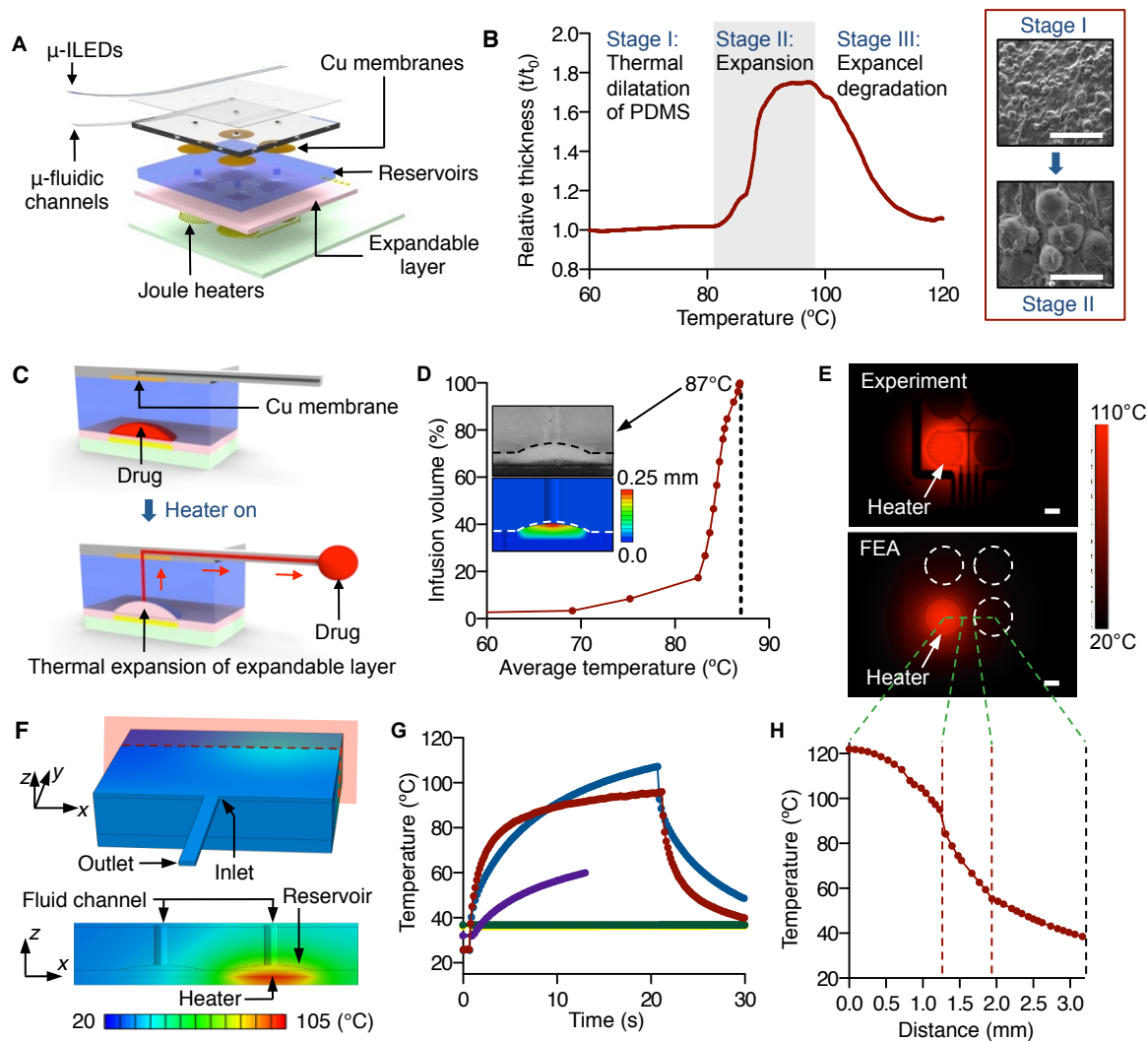
Figure 4.4 Thermo-Mechanical-Fluidic Characteristics of the Wireless Optofluidic System

(A) Exploded view schematic diagram that illustrates an array of μ-ILEDs mounted on top of a soft microfluidic system that includes four separate microfluidic channels, each connected to a set of fluid reservoirs that include copper membranes as hermetic seals, expandable composite materials as mechanical transducers, and microscale Joule heating elements as actuators. **(B)** Characteristics of a thermally expandable composite material. (Left) Thickness variation of this material as a function of temperature. (Right) SEM images (scale bar, 100 μm) show the expansion of microspheres upon application of heat at ~110 ˚C. **(C)** Actuation principle for drug

155

delivery. Before actuation, drug remains in the reservoir (top). Upon activation of the Joule heater, the expandable composite layer increases in volume to push drug through the connecting microfluidic channel (bottom). **(D)** Dependence of the infused volume, as a percentage of the total volume of the reservoir, on temperature of the composite material. The dashed line indicates ~100% infusion at 87 ºC. (Inset top) Cross sectional SEM image that shows complete filling of a reservoir with composite material by thermal expansion, for a state of 100% infused volume. (Inset bottom) Corresponding distribution of vertical displacements in the composite material under the deformed configuration. **(E)** Comparison of temperature distributions for the system with a bare heater in IR images (top) and FEA modeling results (bottom). The images show the temperature distribution after activating the heater for 20 s. **(F)** Calculated temperature distribution at the surface of the entire three-dimensional computational model (top), and that at the cross-section defined by the red plane in the top (bottom). **(G)** Computed (blue) and measured (red) temperature at the location of a thermal actuator, immediately before, during, and after operation. The violet, green and yellow curves correspond to calculations at the reservoir, the microfluidic inlet and outlet, respectively. **(H)** Temperature profile from the center of the powered heater to the center of adjacent, unpowered heater, corresponding to the FEA model in (E). The two red lines represent the boundaries of the two heaters.
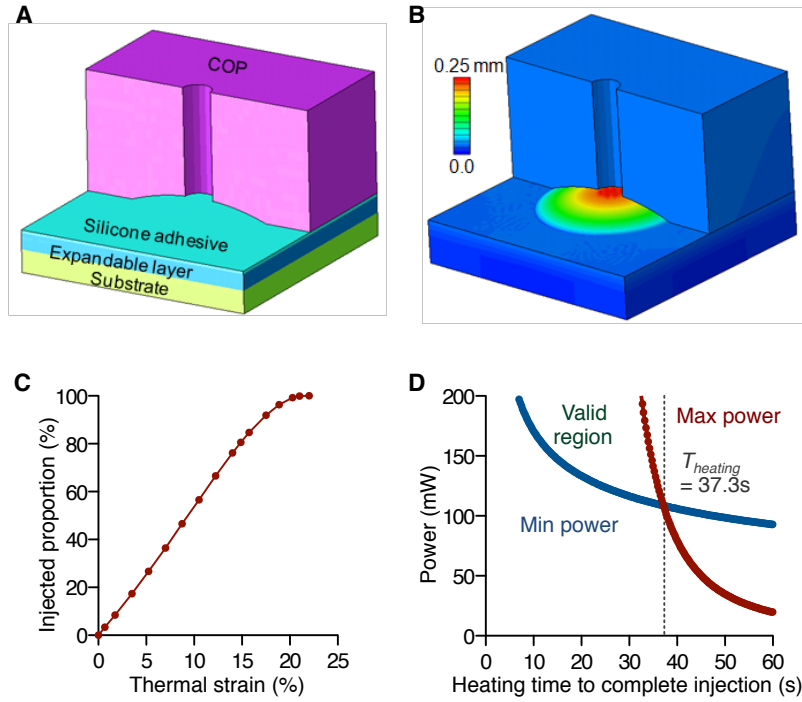
Figure 4.5. Results of thermo-mechanical modeling on the actuation process. Related to Figure 4.4. **(A)** Schematic of the full 3D model of FEA. **(B)** Distribution of the out-of-plane (i.e., the thickness direction) displacement in the structure, by applying a thermal strain of 22.4% to the area covered by the heater (corresponding to heating the thermal expandable layer to an average temperature of 87 $^{\circ}$C). **(C)** The injected proportion of drug as a function of the thermal strain in the expandable layer. **(D)** Power analyses for a safe and sufficient injection. The minimum and maximum powers are plotted as functions of the heating time to complete the injection.

Figure 4.6A (right) demonstrate wireless operation of drug delivery and optical stimulation with a compact, self-contained device in a 3D-printed enclosure. Upon wireless triggering, the microcontroller activates a selected heater for drug delivery. The infusion rates non-linearly increase up to ~ 5.2 µl/min, such that most of the fluid is delivered within 13 seconds after initiating actuation (**Figure 4.6B**). The time dynamics of the expansion process and the geometries of the reservoirs and channels define these rates. Therefore, engineering the geometries of reservoirs and the dimensions of the channels can modulate the flow rate for different applications. Demonstration experiments using aqueous solutions of colored dyes and phantom brain tissue (0.6 % agarose gel) verify these operational characteristics, as shown in **Figure 4.6C** and **D**. **Figure 4.6E** shows results for total volumes of fluid delivered from a set of reservoirs in a representative device.
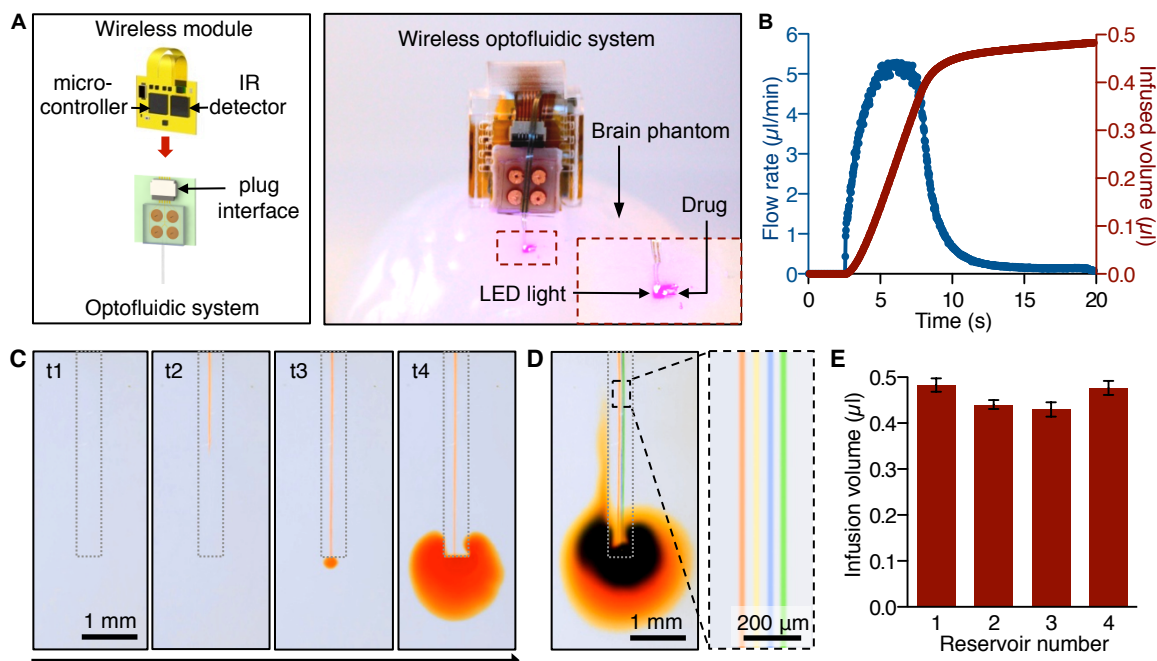
Figure 4.6 Wireless Optofluidic Devices Are Capable of Delivery of Multiple Fluids and Optical Manipulation. (A) Complete wireless optofluidic system. (Left) Schematic illustration of the electronics, power and wireless control system that plugs into the construct shown in Figure 2A. (Right) Demonstration of wireless drug delivery and optical stimulation by operation of the optofluidic system in a brain tissue phantom (0.6% agarose gel). **(B)** Flow rate in a microfluidic channel (blue) and total infused volume (red) as a function of time before, during and after actuation. **(C)** Time sequence of optical images that demonstrates delivery of liquid (aqueous solution with orange dye) into brain phantom tissue (0.6 % agarose gel) through a microfluidic channel: t1 = 0 s (onset of actuation), t2 = 3.1 s, t3 = 3.8 s, t4 = 15.2 s. **(D)** Images that show capabilities in separate delivery of different liquids (aqueous solutions with red, yellow, blue and green dyes) through four individual microfluidic channels. The image on the right provides a magnified view. **(E)** Total infusion volumes from each of four reservoirs in representative devices (average of three devices).

159

Component	Weight (g)
Package Case	0.705
Battery (2)	0.66
PCB	0.15
Optofluidic Device	0.34
Total	1.855
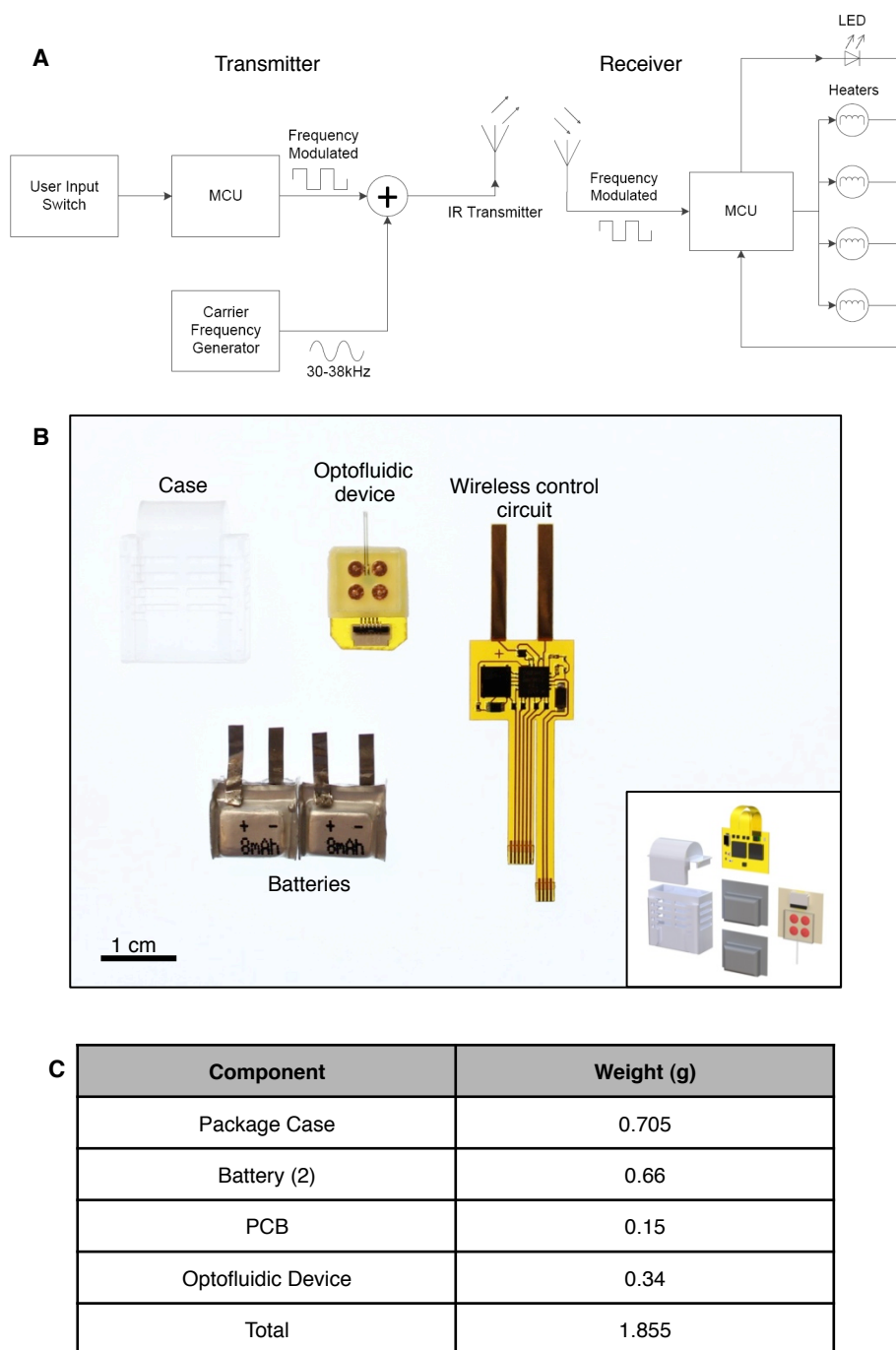
Figure 4.7 Design of wireless control system. Related to Figure 4.6 (A) Overall design of

transmitter (remote controller) and receiver circuit. **(B)** Picture of optofluidic drug delivery

device system components including a case, an optofluidic device, wireless control circuit, and

lithium ion batteries. **(C)** Weight of an optofluidic system.

Optofluidic Devices Are Suitable for Wireless Pharmacology and Optical Manipulation in Awake, Behaving Animals

For application *in vivo,* the optofluidic drug delivery device can be chronically packaged with the platform for wirelessly triggered operation that includes infrared remote control, battery power, fluid reservoirs and pumps with associated control electronics, all contained in a small head stage (**Figure 4.8A, Figure 4.9A** and **B**). To extend the lifetime of operation and reduce the impact on smaller organisms, the packaged electronics for the optofluidic device can be acutely affixed to an awake animal for acute device operation (**Figure 4.8B**). Mice with the fully encapsulated, chronically implanted wireless optofluidic devices interfaced to the dorsal striatum perform the rotarod test of sensorimotor control equally as well as cannula-implanted controls (**Figure 4.8C and Figure 4.9C**). Furthermore when allowed to choose when and how to run on a wheel, optofluidic-implanted mice run equally as often and as much as cannula-implanted controls (**Figure 4.8D and Figure 4.9D**) and have equivalent baseline anxiety-like behavior in the open field test (**Figure 4.8E**). These results indicate that even small mammals such as mice tolerate the chronically implanted probes equally as well as mice with conventional cannulas targeting the same brain structure. It is important to note that the cannulated mice in these experiments were not connected to an external drug supply. Such tethering can restrict movement and impacts performance on all of these tests, while the optofluidic device-implanted mice are fully integrated with both the device and the fluid supply. In addition to comparable behavioral responses, the mechanical compliance and smaller overall tissue displacement of the microfluidic channels reduce lesioning and immunoreactive glial responses from deep brain implantation (**Figure 4.8F-J**). Additionally, the optofluidic devices provide access to four channels of drug, viral, or other fluid administration compared to a single channel for the cannula in a significantly

161

A

B

C

D

E

F Wild Type Mouse
Horizontal section

G

H

I Cannula
Nissl   Iba1   GFAP   Merge

J Optofluidic
Nissl   Iba1   GFAP   Merge

162
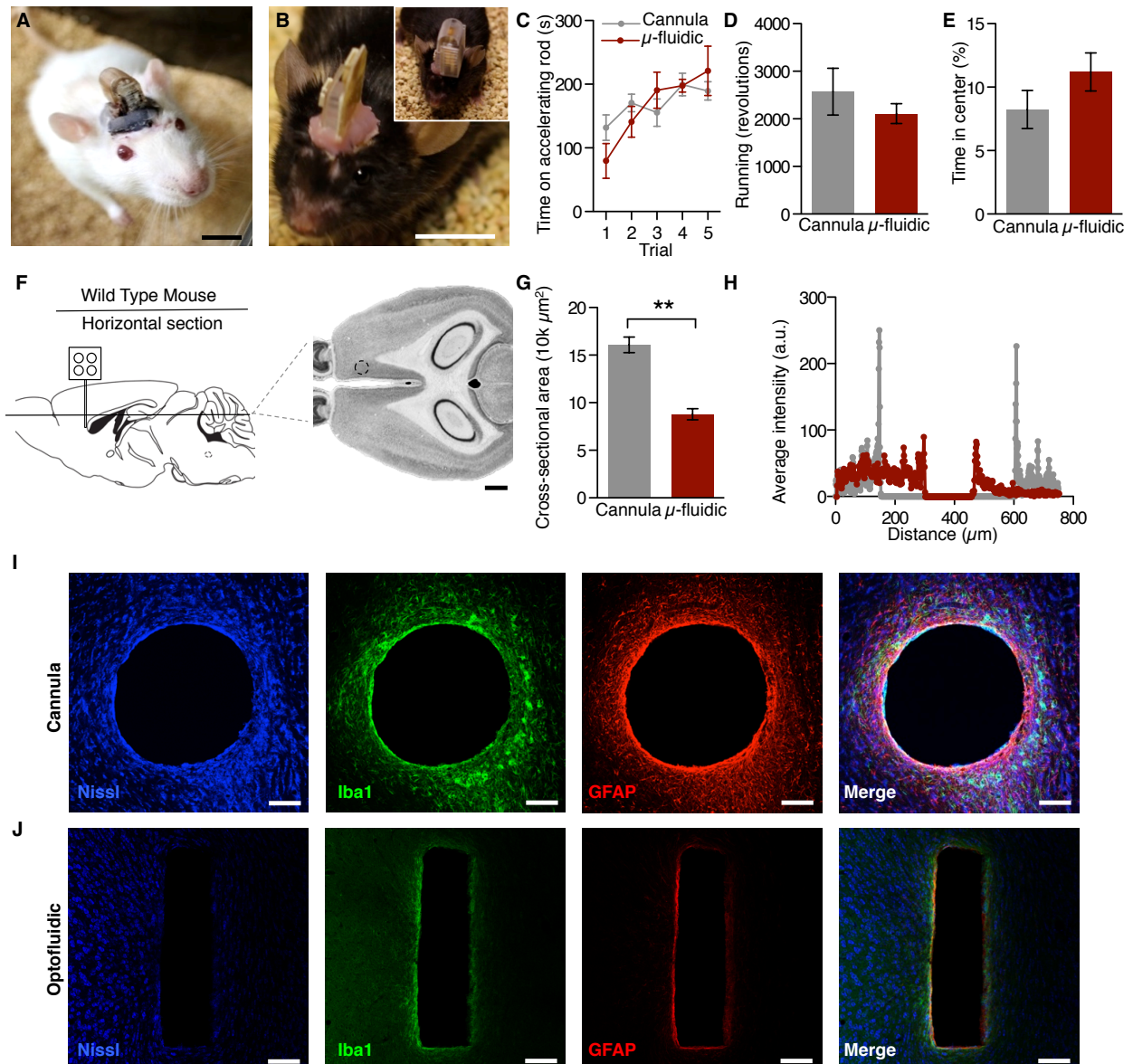
Figure 4.8 Optofluidic Devices Are Suitable for Wireless Pharmacology in Awake, Behaving Animals. (A & B) Images of a freely behaving **(A)** Sprague-Dawley rat and **(B)** a C57Bl6 mouse mounted with wireless power systems that are capable of drug delivery and photostimulation deep into brain tissue. All animals are healthy and freely moving, shown here one week following surgery. Scale bars, 1 cm. **(C-E)** Wild-type (C57Bl6) mice tolerate the microfluidic devices as well as traditional cannulas and do not exhibit any notable deficits in **(C)** motor coordination, **(D)** spontaneous locomotor activity, or **(E)** anxiety-like behavior. **(F)** Schematic and Mouse Brain Library atlas image of histological approach for inflammation and lesion study. Dashed circle indicates approximate injection site. Scale bar, 1 mm. **(G)** Mean ± SEM cross-sectional area of lesions from cannulas and optofluidic probes (Student's T-Test, **p<0.01, n=3/group). **(H)** Representative linescan of fluorescence intensity from cannula (gray) and optofluidic probe (red) lesions. **(I & J)** Representative confocal fluorescence images of 30 μm horizontal striatal slices show immunohistochemical staining for Nissl bodies (blue), astrocytes (GFAP, red) and activated microglia (Iba1, green) and overall lesion from a cannula **(I)** and an optofluidic device. All histological and confocal settings were kept consistent across groups. **(J)**. In the rightmost panels, the shape and scale of the lesion from the cannula or optofluidic device is overlaid on the image of the other device (dashed lines). Scale bars, 100 μm.
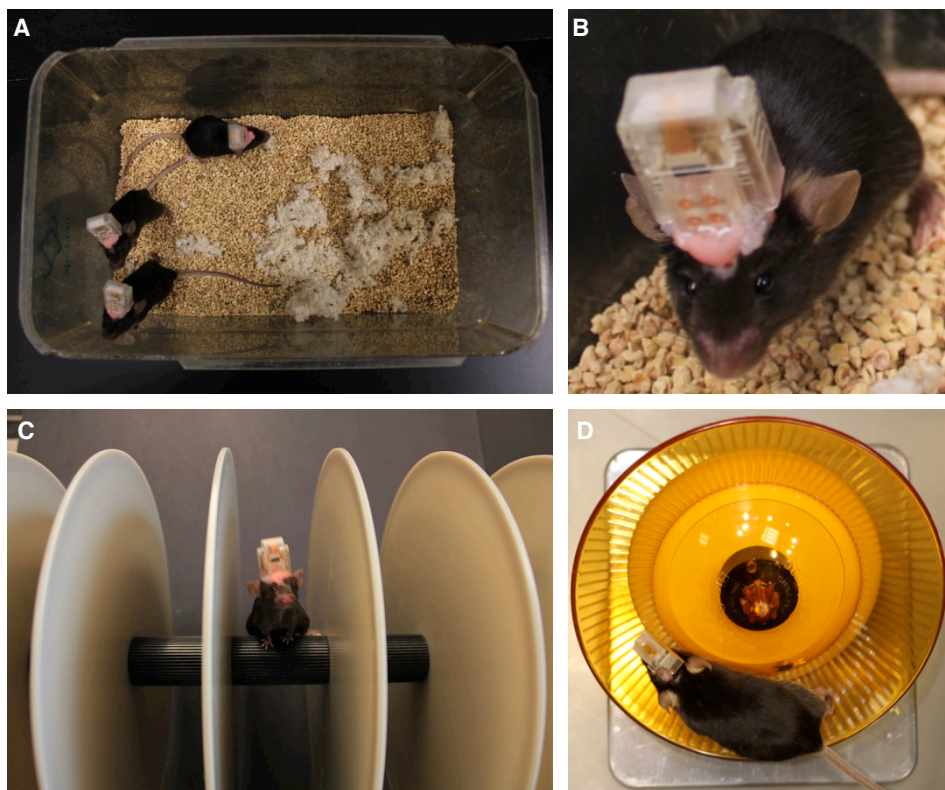
Figure 4.9 Demonstration of chronically implanted, fully enclosed and wireless microfluidic devices in various environments, related to Figure 4.8A-E. (A & B) Group-housed homecage environment. **(C)** Rotarod test. **(D)** Spontaneous run on a running wheel.

smaller cross-sectional area (**Figure 4.8G**) of the brain. These thin, flexible optofluidic neural probes are better tolerated by the brain than rigid implants, consistent with previous reports of ultrathin, flexible deep brain implants (see Chapter 2) (Canales et al., 2015; Capadona et al., 2012; Kim et al., 2013b; Kozai and Kipke, 2009; Kozai et al., 2012).

Wireless Virally-mediated Recombination and Visualization of Fluid Delivery

As a demonstration of the optofluidic probes' ability to delivery multiple, independent fluids through a single implant in an awake, behaving animal we loaded two reservoirs with two different adeno-associated viruses to allow for recombination-dependent fluorescent visualization of successful fluid ejection. First, we delivered a virus expressing Cre recombinase (AAV5-PGK-Cre) into the dorsal striatum of a Cre-conditional tdTomato reporter mouse line developed by the Allen Institute for Brain Science (**Figure 4.10A**) (Madisen et al., 2010). We observed robust Cre-dependent expression of tdTomato in a distinct radius below the ventral tip of the microfluidic channels, thereby indicating efficient remote-controlled, virally-induced *in vivo* recombination (**Figure 4.10A**). When we counted the number of tdTomato$^+$ cells emanating from the tip of the implant we found the majority of the Cre-induced fluorescent reporter expression to be within 500 μm of the injection site (**Figure 4.10B**). Next, in a separate group of animals, we delivered the same AAV5-PGK-Cre as well as a Cre-dependent eYFP reporter virus (AAV5-Ef1a-DIO-eYFP). In these animals we clearly observed co-expression of both tdTomato and eYFP (**Figure 4.10C-E**) indicating successful, combinatorial viral-mediated recombination *in vivo*. These are proof-of-principle experiments, but the same approach could be used to wirelessly alter gene expression at multiple timepoints without the need for multiple, disruptive surgeries or physical connection to viral infusion hardware. Together these results further demonstrate the optofluidic neural probes can be used for *in vivo* remote-controlled, independent

165

delivery of fluids within an isolated region through individual and distinct channels running along a single implant.
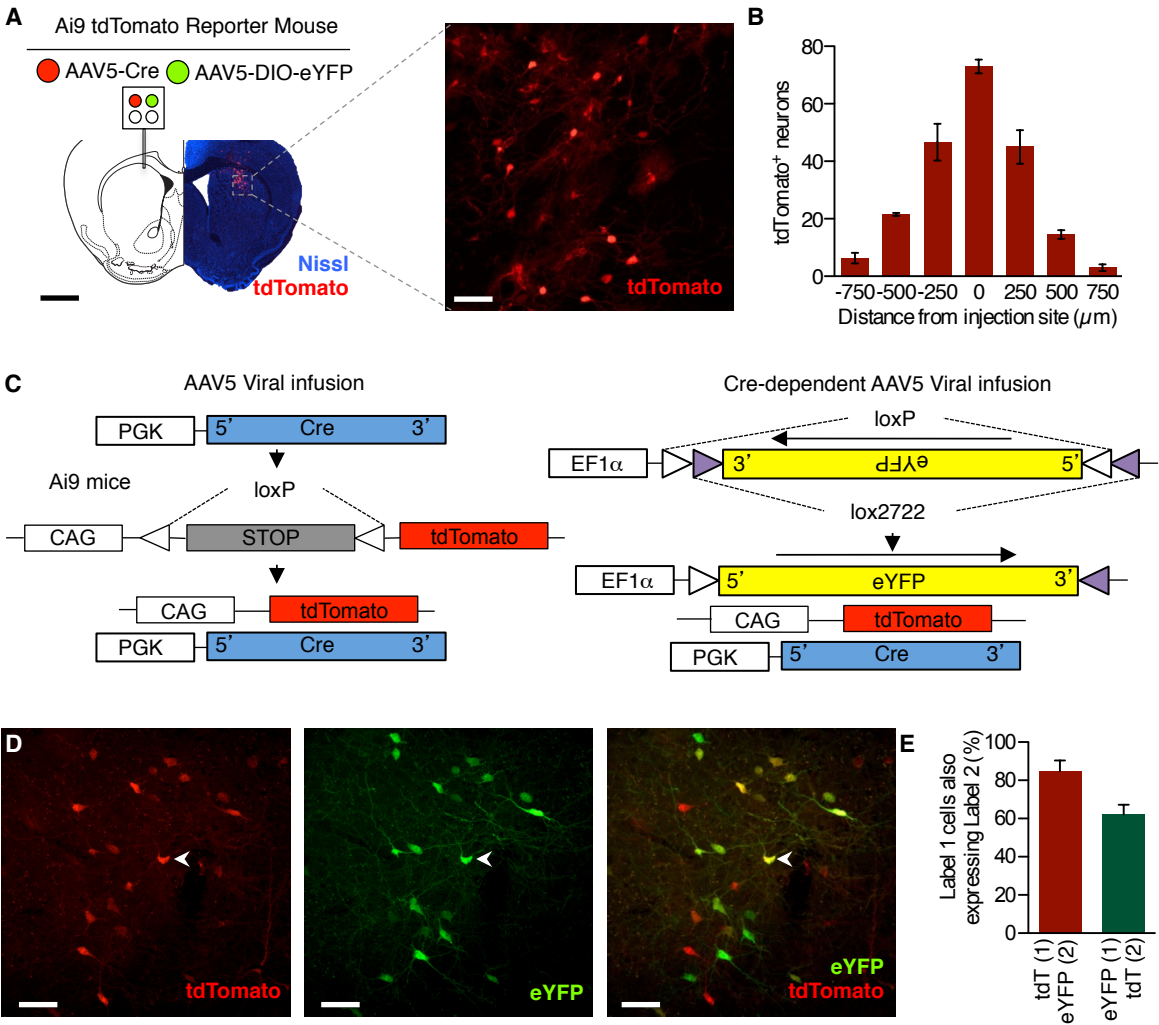
Figure 4.10 Wireless Virally-mediated Recombination Visualizes the Spread of Fluid Delivery. (A) Schematic of viral delivery experiment depicting loading of two distinct viruses into a single microfluidic device, fluorescence image depicts bolus of Cre-mediated recombination (imaged as expressed tdTomato, red; Nissl, blue) near the tip of the implanted microfluidic device. Right, enlarged maximum projection of 35 confocal fluorescence images (tdTomato, red). Black scale bar, 1 mm; white scale bar, 25 μm. **(B)** Quantification of the spread of AAV5-PGK-Cre viral recombination. Cells counted in serial coronal slices from point of infusion (n=3 slices per brain from 3 brains). **(C)** Viral recombination scheme for the dual viral approach taken in (**D & E**). **(D)** Representative maximum projection of 35 confocal fluorescence images of 30 μm coronal striatal slices demonstrate efficient virally-induced gene expression (Left-tdTomato, red; middle - eYFP, green, Right-overlay) following wireless delivery of viruses. Chevron indicates example co-localization of tdTomato and eYFP. Scale bar, 25 μm. **(E)** Quantification of co-localization of tdTomato (tdT) and eYFP (n=3 slices per brain from 3 brains).

Untethered, Programmed Pharmacological Infusion Alters the Behavior of Freely Moving Animals

The capability to load a single device with multiple fluids for independent, remote-controlled delivery offers the user the advantage of either multiplexed therapeutic treatments or easily controlled within-subject study designs. As a demonstration of the latter, we implanted microfluidic devices unilaterally into the ventral tegmental area (VTA) of wild-type (C57Bl6) mice. Previous reports have demonstrated a remarkably stereotyped rotation behavior to unilateral μ-opioid receptor (MOPR) activation in the VTA (Devine and Wise, 1994; Jenck et al., 1988). As a proof-of-principle within-subject *in vivo* pharmacology experiment, two chambers of each device were loaded with different pharmacological agents; one with the synthetic opioid peptide and MOPR agonist, [D-Ala^2, N-MePhe^4, Gly-ol]-enkephalin (DAMGO, 200 pmol, Tocris), and one with artificial cerebral spinal fluid (ACSF) as a vehicle control. In a counter-balanced design, we then wirelessly delivered either the DAMGO or vehicle into the VTA of freely behaving animals over a distance of ~1 m away from the animal (**Figure 4.11A** and **B**). Consistent with previous reports (Calenco-Choukroun et al., 1991; Devine and Wise, 1994; Jenck et al., 1988; Latimer et al., 1987), when DAMGO was infused into the VTA the animals showed a robust increase in overall locomotor activity (**Figure 4.11C-E**). In particular, the unilateral administration causes stereotypical rotations contralateral to injection site that is completely absent when the same animals receive the wireless ACSF infusion (**Figure 4.11B, C and E**). This experiment demonstrates the utility of the optofluidic probes for self-contained, within-subject experiments to wirelessly deliver multiple chemicals into the brain without any physical contact with the animal for completely unconstrained freely moving behavior.
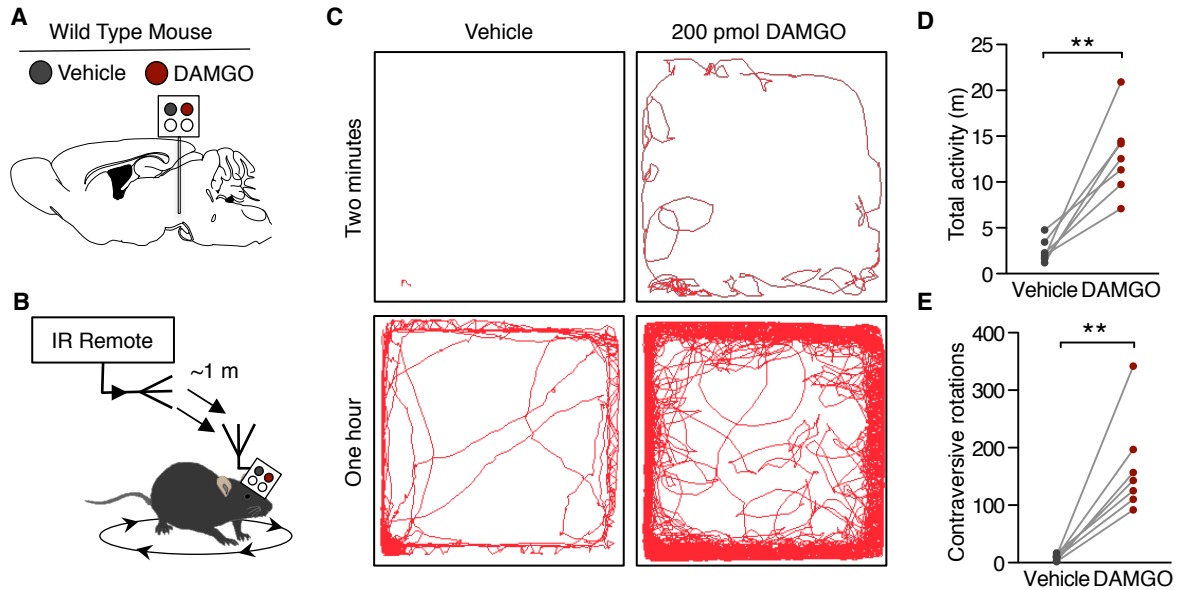
Figure 4.11 Untethered Delivery of Opioids into the Ventral Tegmental Area Causes Stereotypical, Repeated Rotation Behavior. (A) Schematic of the opioid peptide delivery experiment depicting loading of an agonist (200 pmol DAMGO, Tocris) and its vehicle into single microfluidic device. **(B)** Cartoon of wireless scheme for the DAMGO-induced rotation experiment. **(C)** Representative traces of movement from the same animal over the course of two minutes and one hour clearly show an increase in overall movement and rotations. **(D-E)** Within-subject, counter-balanced experiments demonstrate robust wireless, DAMGO-induced changes in ambulatory behavior. Intra-VTA DAMGO causes a significant increase in **(D)** overall locomotion and **(E)** contraversive 360° rotations (n=7, Paired Student's T-Test, **p<0.01).

Concomitant Wireless Photostimulation with Pharmacological Antagonism Modulates a Dopamine Receptor-1-sensitive Real-Time Place Preference

We next determined the *in vivo* optofluidic capabilities of these devices. Real-time place preference has become a common tool for neuroscientists to assess the behavioral valence of photostimulated neural circuits or cell bodies in a freely moving animal (Jennings et al., 2013; Kim et al., 2013a; Siuda et al., 2015; Stamatakis and Stuber, 2012; Stamatakis et al., 2013; Tan et al., 2012). In related behavioral models, phasic optogenetic activation of VTA dopaminergic (VTA-DA) neurons is rewarding (see Chapter 2) (Kim et al., 2012, 2013b; Tsai et al., 2009; Witten et al., 2011). However, we previously failed to observe that wireless phasic activation of VTA-DA cell bodies was sufficient for a real-time place preference (see Chapter 2) (Kim et al., 2013b). Because of the pronounced heterogeneity of VTA projections (Gunaydin et al., 2014; Lammel et al., 2011, 2012, 2015; Stamatakis et al., 2013; Stuber et al., 2015), we sought to selectively target VTA-DA projections into the shell of the nucleus accumbens (NAcSh). To do this, we selectively targeted channelrhodopsin-2 fused with eYFP (AAV5-EF1a-ChR2(H134)-eYFP) to VTA-DA neurons of TH-Cre mice and implanted an integrated optofluidic probe adjacent to the NAcSh (**Figure 4.12A and B; Figure 4.13A-C**). In this experiment, we found that photostimulation of the NAcSh-projecting VTA-DA fibers resulted in an increase in c-fos expression, a widely used biochemical marker of neuronal activation, in both the accumbens and the ventral tegmental area (presumably through antidromic activation) (**Figure 4.13D and E**). To test whether any of the observed behavioral phenotypes were dopamine-dependent, we filled one chamber of the optofluidic device with the selective dopamine receptor D_1 (DRD1) antagonist SCH23390 (400 ng, Tocris) (Billard et al., 1984; Gunaydin et al., 2014; Hyttel, 1983). We found that phasic photostimulation (8 x 10 ms light pulses at 20 Hz every 5s) of VTA-NAcSh terminals

was able to drive a robust real-time place preference (**Figure 4.12C and D**). Importantly, in a counter-balanced design, this place preference was completely blocked by wireless pharmacological delivery of SCH23390 prior to photostimulation in the real-time place preference task, indicating that optogenetically-induced dopamine release into the NAcSh elicits the real-time place preference via DRD1 activation. There was no effect of either the photostimulation or the drug treatment on TH-Cre$^-$ control animals that did not express ChR2(H134)-eYFP (**Figure 4.12E and F)** and no treatment group displayed a significant effect on locomotor activity (**Figure 4.12**). These findings demonstrate that completely self-contained, remote-controlled optofluidic neural probes can be easily incorporated into optogenetic studies to introduce pharmacological agents into the immediate region of targeted photostimulation in a programmed fashion that is time-locked and dependent on the behavior.

DISCUSSION

The wireless optofluidic neural probes presented here represent a compelling technology for programmable drug delivery and optical manipulation of deep brain tissue in freely moving animals. The resulting device platform has multifunctional capabilities in a single, soft implant that provides powerful options for *in vivo* pharmacology and wireless optogenetics, many of which would be impossible to reproduce with conventional metal cannulas and/or optical fibers.

A key advantage of these systems is the spatial specificity inherent in the multimodal brain/device interface. Previous demonstrations of wireless drug delivery have focused on defuse infusion of drug into the subcutaneous space of rats and, recently, humans (Farra et al., 2012; Hoare et al., 2009, 2011; Timko et al., 2014). While these devices are capable of on-demand fluid delivery, they are unable to couple to the types of microfluidic channels necessary for

A TH-Cre VTA^ChR2

NAc ● SCH23390

B VTA — TH, ChR2-eYFP / NAc — Nissl, ChR2-eYFP

C No stimulation | Stimulation

μ-ILED

μ-ILED +SCH

D Time in stimulation side (%) — ***

μ-ILED   μ-ILED +SCH

E Time in stimulation side (%)

μ-ILED   μ-ILED +SCH

F Time in stimulation side (s) — **, **, ****

μ-ILED   μ-ILED +SCH   μ-ILED   μ-ILED +SCH

G Total activity (m)
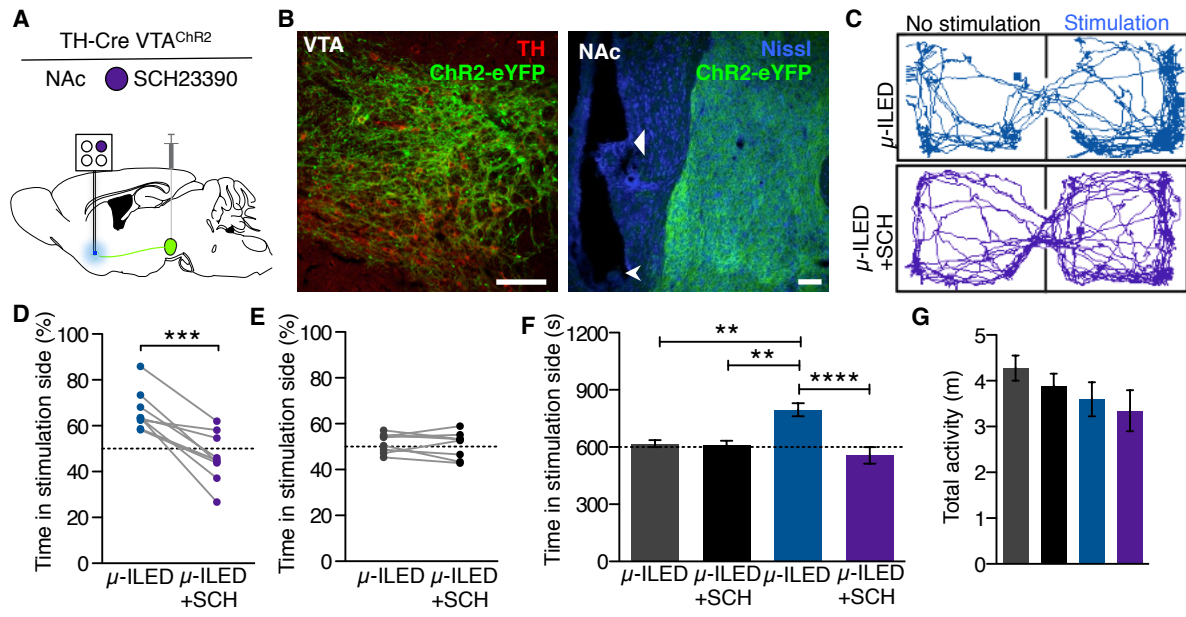
Figure 4.12 Wireless DRD1 Antagonism in the NAcSh Blocks Photostimulation-induced Real-Time Preference of Freely Moving Animals. (A) Schematic of the optofluidic experiment. AAV5-EF1a-DIO-ChR2-eYFP was injected into the VTA and six weeks later an optofluidic probe loaded with SCH23390 (400 ng, Tocris) was implanted in the NAc of TH-Cre animals. **(B)** Representative confocal fluorescence images depicting cell-type specific expression of ChR2-eYFP in (right) dopaminergic, TH containing neurons of the VTA (TH, red; ChR2-eYFP, green) and (left) their projections in the NAc (Nissl, blue; ChR2-eYFP, green). Triangular arrow indicates the ventral tip of the microfluidic channels and the chevron indicates the ventral tip of the optofluidic device. All scale bars for the figure are 100 μm. **(C-G)** Phasic photostimulation (8 pulses at 20 Hz, 10 ms pulse width upon entry and every 5 s the animal remains in the chamber) of NAc-projecting terminals from the VTA of TH-Cre animals drives a real-time place preference. **(C)** Representative traces of movement during the real-time place testing experiment of one TH-Cre$^{VTA:ChR2}$ animal show a SCH23390-sensitive preference for the photostimulation-paired chamber. **(D)** All TH-Cre$^{VTA:ChR2}$ animals show a real-time place preference that is significantly reduced following wireless intra-NAc delivery of SCH23390 (n=9, Paired Student's T-Test, ***$p<0.001$). **(E)** In Cre$^-$ control animals, neither the photostimulation or the SCH23390 treatment affects real-time preference behavior (n=8, Paired Student's T-Test, $p=0.6234$). **(F)** Grouped analysis confirms that the SCH23390-sensitive place preference is selective for the TH-Cre$^+$ animals (n=8-9/group, One-way ANOVA, Bonferroni Post-Hoc, **$p<0.01$, ****$p<0.0001$). **(G)** There is no significant difference between any groups for overall locomotor activity (n=8-9/group, One-way ANOVA).
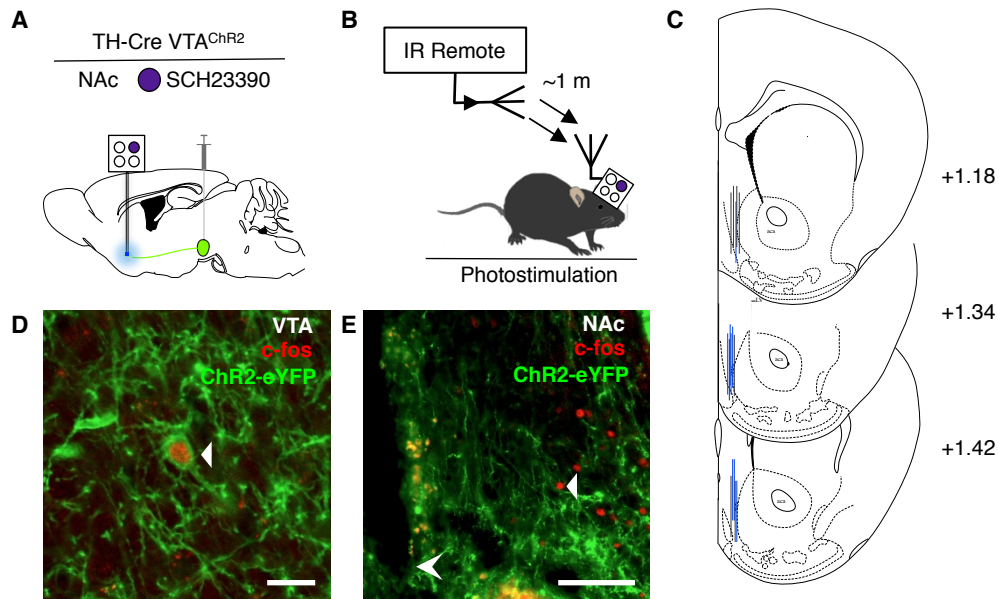
Figure 4.13 Further analysis of optofluidic real-time place preference experiment, related to Figure 4.12 (A) Schematic of the optofluidic experiment. **(B)** Cartoon of wireless scheme for the RTPP experiment. **(C)** Hit map of optofluidic placements for the experiments in Figure 7. Blue lines represent the most ventral 1 mm of device in Cre[+] animals, grey lines repersent the most ventral 1 mm of device in Cre[-] animals. **(D)** Antidromic c-fos expression in the VTA following 1 hour of photostimulation. Triangular arrow indicates example c-fos expression. Scale bar, 10 μm. **(E)** Orthodromic c-fos expression in the NAcSh following 1 hour photostimulation. Triangular arrow indicates example c-fos expression. Arrowhead indicates ventral tip of optofluidic device. Scale bar, 100 μm.

discrete, targeted fluid delivery into deep brain tissue. The wireless optofluidic probes reported here overcome this challenge with a single device that causes a single, static lesion to brain tissue, where fluids and photons arrive at precisely the same micro-region of the brain. This co-localization targets the same cells with both drugs and photostimulation. One interesting possibility is in delivery of viral vectors for expression of exogenous receptors (light-sensitive ion channels, receptors, pumps, etc. or DREADD receptors), ligands for these or endogenous receptors, and photostimulation all to the same brain region and cell population. The compact, self-contained construction eliminates the repeated micro-lesions associated with internal cannulas and the angled lesions associated with exterior fiber optics dramatically reducing overall trauma to the brain (**Figure 4.8F and G**). This minimally invasive operation facilitates a within-subject experimental design, thereby reducing the number of animals one needs to account for the behavioral variability that arises from any significant disruption of brain tissue. The soft neural interfaces enabled by these ultrathin, compliant probes also create new opportunities for chronic neuroscience research and preclinical investigation, as demonstrated not only here but also in recent studies of other soft device technologies for use in the epidural space (Minev et al., 2015). Importantly, the materials and designs presented here represent significant advances over these and other neural interfaces, all of which rely on tethered operation and lack capabilities in both wireless operation and photostimulation (Table S1)(Canales et al., 2015; Minev et al., 2015; Spieth et al., 2012). An important perspective is that the platforms reported here can easily be adapted for a wide range of other types of passive or active electronics technologies, including electrical microstimulation.

For any configuration, the value of the technology to the community depends on the extent to which it can be widely adopted. In this context, a relevant consideration is that the

hardware for control and power management consists of readily available electronics hobbyist components. Aside from a simple IR remote control, the animal carries a small IR receiver system with little observable impact on its behavior (**Figure 4.8**). In fact, after the initial surgery to implant and secure the device to the skull, the experimental subject never needs to come in contact with a human again. Complete operation of these optofluidic neural probes, including delivery of up to four distinct pharmacological agents, viruses, or other fluids, as well as photostimulation can all be achieved wirelessly in any domain through which the IR signal can pass.

Areas for further improvement include dynamic control of fluid flow. While the reported devices provide for multiple delivery events, each operates with identical rates of infusion (**Figure 4.6B**). Engineered variations in the dimensions of the reservoirs and channels represent one means to define different flow conditions. Another limitation is in refilling devices. With the current layouts, reuse of the microfluidics reservoirs and channels can be challenging. To overcome these restrictions, implementing replaceable fluid-containing cartridges (analogous to ink jet printer cartridges) might represent an attractive future design feature.

Even in existing embodiments, the device capabilities allow previously intractable experiments such as altering gene expression in freely behaving animals while living in their native home cage environments (**Figure 4.9 and 4.10**). The optofluidic neural probes can also provide photostimulation and delivery of pharmacological agents in a closed-loop manner based on the animals' behavior **(Figure 4.12)**. Integration with real-time video acquisition of socially interacting animals (de Chaumont et al., 2012; Kunwar et al., 2015) would allow fully automated, programmed fluid delivery that could be tuned entirely to the social interactions of the animal. Beyond the possibilities in optogenetics, all which require genetic modification, an

176

interesting application could be in optopharmacology. The use of photo-sensitive compounds that act as photo-switches or ligands that bind to channels or receptors upon photo-conversion (Kramer et al., 2013) could exploit the high spatiotemporal control of both fluid and light delivery afforded by these optofluidic probes. Optopharmacological agents have been enthusiastically received in neuroscience for *in vitro* applications (Banghart and Sabatini, 2012; Callaway and Katz, 1993; Carter and Sabatini, 2004; Matsuzaki et al., 2001), but their use *in vivo* has been limited. Although compelling findings exist addressing the external visual nervous system and the surface of the cortex (Mourot et al., 2012; Noguchi et al., 2011; Polosukhina et al., 2012; Tochitsky et al., 2014), optopharmacological application in the deep brain remains a significant challenge. Optofluidic devices that provide access to the UV spectrum with advanced μ-ILEDs could target these highly selective photosensitive tools to spatially isolated regions of the central nervous system in non-genetically altered mammals.

Beyond basic research, the operation and architecture of the probes reported here will allow for a smooth translation to non-human primate models as well as applications in clinical medicine. Therapeutic solutions for a diverse set of pathologies (e.g. local neurooncotherapy, pharmacologically-refined deep brain stimulation, delivery of agents to mitigate traumatic brain injury etc.) will benefit from the untethered and fully-contained, programmable operation of devices similar in design to these optofluidic neural probes. Such centrally targeted drug delivery holds the promise of more tissue- and cell-type selective therapies that avoid perturbing off-target organ systems. With these exciting future directions in mind, the results of our studies establish strategies for minimally-invasive, ultrathin wireless optofluidic neural probes that can serve as a starting point for new generations of fluid neural interfaces.

MATERIALS AND METHODS

Fabrication of Ultrathin, Flexible Optofluidic Probes

Fabrication of flexible microfluidic probes started with creating microfluidic channel patterns in a 25-µm-thick PDMS layer (Sylgard 184, Dow Corning) using a molding process. For fabrication of a mold, photo-curable epoxy (SU-8 10, Microchem Inc.) was spin-coated (3000 rpm for 10 µm thickness) on a silicon wafer and UV-exposed (120 mJ/cm^2) through a mask pattern. Removing the unexposed region by developing, followed by thermal annealing (95°C for 2 min) completed the mold for the fluidic channels. To facilitate release of patterned PDMS from the mold, the mold was chemically treated with evaporated anti-stiction agent (chlorotrimethylsilane, Sigma-Aldrich) for 20 min. PDMS was casted on the mold and pressed with a glass slide (5 × 3.5 cm^2) that was treated with Pt inhibitor solution (5% AEAPS (3-(2-Aminoethylamino) Propylmethyldimethoxysilane, Sigma-Aldrich) and 95% methanol) for 45 min; this inhibitor treatment facilitated release of the thin PDMS layer from the glass slide by deactivating Pt at the glass-PDMS interface, which is a catalyst for polymerization of PDMS. The glass slide and the mold were clamped, and the PDMS between them was cured for 50 min at 70°C. Then, the glass slide with the patterned thin PDMS layer was carefully detached from the Si mold.

In the meantime, a flat, thin PDMS layer (20 µm thick) was prepared by spin-casting PDMS (2000 rpm for 60 s) on a polycarbonate (PC) membrane and cured at 70°C for 1 hour. The PC was chosen as a substrate for handling due to its surface property allowing easy release of PDMS. Both this flat PDMS layer on the PC membrane and the patterned PDMS layer on the glass slide were oxygen plasma–treated to activate their surfaces and bonded together to form

microfluidic probes. After removing the PC membrane, the microfluidic probes were released from the glass slide without damage due to the Pt inhibitor treatment of the glass surface.

The fabrication of the μ-ILED array on a thin PET layer (6 μm thick) was previously presented (see Chapters 2 & 3) (Kim et al., 2013b; McCall et al., 2013) (See SI for fabrication details). The μ-ILED array was integrated onto the microfluidic probe using a double-sided adhesive (25 μm thick; ARclear 8154, Adhesives Research), and the fabrication was completed. The result was an ultra-thin (~80 μm thick), soft, and flexible optofluidic probe, suitable for long-term implantation in the soft brain tissue.

Fabrication of Optofluidic Drug Delivery Devices With Thermal Actuators

Heater patterns were defined photolithographically on Cr/Au (5 nm/185 nm thick) deposited FR-4 substrates (G10 glass epoxy sheet, ePlastics). The expandable layer (250 μm thick) was prepared on top of heaters on the FR-4 substrate by spin-coating thermally expandable polymer (2:1 mixture of PDMS (elastomer:curing agent = 10:1) and expandable microspheres (Expancel 031 DU 40, AkzoNobel) and cured in a 70°C oven for 12 hours. Hemispherical reservoirs, which were patterned in cyclic olefin polymer, were aligned on the heaters and bonded using a double-sided adhesive (25 μm thick; ARclear® 8154, Adhesives Research). Then, parylene C (6 μm thick) was deposited on the inner walls of the reservoirs to further improve vapor impermeability as well as chemical resistance.

For drug loading, the reservoirs were first treated with oxygen plasma (March RIE) for 30 seconds to make the inner surface hydrophilic. A syringe with a blunt needle was used to place the drug of interest into the reservoirs. To prevent fluid evaporation, the outlets of the

reservoirs were hermetically sealed with Cu membranes (3 µm thick) after drug loading. Then, the inlets of an optofluidic probe were aligned and bonded with the outlets of the reservoirs.

Fabrication of µ-ILED Arrays on Flexible Microneedles

The fabrication of the µ-ILED was previously described (see Chapters 2 & 3) (Kim et al., 2013; McCall et al., 2013). The GaN epi-layers, which were grown on a sapphire wafer (500 µm thick with 2" diameter, Cermet Inc.), consisted of undoped GaN (3.8 µm), n-GaN (2 µm), spacer (0.4 µm), multi-quantum well (0.14 µm), and p-GaN (0.2 µm). A sapphire surface were rinsed with diluted HCl (33 %) to remove GaN oxide layer followed by sputter deposition (AJA ATC 2000) of current spreading layers of Ni/Au (15 nm/15 nm). Post-annealing at 500 ^{o}C for 5 min formed an Ohmic contact between the metal and the GaN. After etching n-type regions with inductively coupled plasma reactive ion etching (ICP RIE, Plasmatherm, SLR-770), n- and p-pads of 15 nm/300 nm of Cr/Au were deposited by electron beam evaporation (Temescal, FC-1800). To define the entire LEDs with 100×100 µm^2, ICP RIE was used to remove GaN down to the sapphire substrate, with negative photoresist (AZ 2070, Micorchem Inc) as an etching mask. A passivation layer of SiN$_x$ (200 nm) was deposited by plasma enhanced chemical vapor deposition (PECVD; STS, Mesc Multiple) followed by wafer bonding between a silicon wafer with Cr/Pd/In layers (15 nm/150 nm/900 nm) and a sapphire substrate to make metallic alloy. The LEDs were removed from a sapphire wafer by laser lift-off (KrF, intensity of ~0.9 J/cm^2) and additional heating up to 70 ^{o}C for melting of In metal on a hot plate. Wet etching with HCl (5w%) removed the residual In layer, leaving porous structures of InPd alloy that acted as anchors to hold the LEDs to the silicon wafer during following etching processes with Pd and Cr metals. Entire LEDs were easily transferred onto PDMS slab which has micro-pillar (3 µm in diameter, 1.2 µm in height, and 5 µm in space) via the van der Waals forces. Finally, wet etching

of the residual Pd completed the fabrication of μ-ILEDs on PDMS, which were ready for transfer printing.

To transfer the μ-ILEDs, a PDMS stamp with micro-post (100 × 100 μm^2 and heights of 100 μm) was used to pick up the μ-ILED from a structured PDMS slab. The μ-ILED on the micro-post was integrated onto a thin UV curable adhesive (Kim et al., 2014) coated 6 μm-thick PET film which was micropatterned with a needle shape by using a mask aligner (Karl Suss, MJB). After transferring the μ-ILEDs, the SiN$_x$ passivation layer was removed by reactive ion etching (Plasmatherm 790). Photosensitive benzocyclobutene (6 μm thick) was spin-coated with 2000 rpm for 30 sec followed by UV exposure from bottom side through the transparent glass substrate. UV light exposed all regions except the opaque n- and p- pads which are made of thick metals. Developing away (Advanced Developer, DS2100) the unexposed region completed the patterning process for via holes on to both pads. After fully curing in a glove box without water/oxygen gases at 210 ^{o}C for 2 hr, metal interconnections was deposited with 15 nm/300 nm of Cr/Au and patterned using photolithography and wet etching. Finally, the entire area except contact pads for connection was encapsulated with 2 μm-thick SU-8 and hard-cured for waterproof.

Preparation of Releasable Metal Microneedles for Injection

To prepare injection metal microneedles, thin metal foil of Stainless steel (50 μm thickness) was purchased from Goodfellow Corporation. Needle shapes were designed with 500 μm width / 6 mm length from the tip to the mid-point and 1 mm width / 7 mm length from the mid-point to the end. Metal foil was defined with laser mill which has focal point of 35 μm. Detaching of cut needles from the residual foil and cleaning with IPA completed the preparation.

For bonding of an optofluidic probe to the injection microneedle, a thin layer of purified silk (7 wt%) or an adhesive from the water soluble PVA tape were used, to allow release after implantation – it takes about 5 min for resolution of the adhesives inside saline solution.

Measurement of Device Temperature During Thermal Actuation

The temporal response of devices during thermal actuation was characterized by thermal imaging with an infrared camera (A655sc, FLIR Systems, Inc.), which has measurement accuracy at ±2% of the reading value.

Thermal Characterization of Thermally Expandable Polymer

To measure the volumetric expansion dependent on temperature, we increased the temperature of the expandable polymer in an environmental chamber (Thermotron SM 1.0). The temperature was increased by 10°C per hour from 20°C to 130°C for 11 hours. The thermal expansion of the polymer was imaged with a camera (Logitech 720p Webcam C905), while the temperature was simultaneously recorded with a K-Type thermocouple probe (OMEGA®) connected to an analog channel of a NI DAQ board (myDAQ, National Instruments). The thermocouple probe was attached to the polymer with heat paste to enhance the thermal contact conductance. The images of the expanding polymer were analyzed by a custom code with Image Processing Tool Box of Matlab (MathWorks).

Fluid Flow Rate Measurement

The flow rate was measured by tracking 2 μm green fluorescent microspheres (F-8827, Thermo Fisher Scientific) diluted to distilled water by 100:1. Before injecting the tracer, the microsphere solution was sonicated for 5 minutes to eliminate any aggregation. The video was

captured by a digital high speed camera (Phantom v7.3, Vision Research) and an inverted optical microscope (Leica) with a 20X objective (Leica) and wide-field fluorescence light source (X-Cite 120Q, Excelitas Technologies) at the frame rate of 20,000 frames per seconds. The video was analyzed by Matlab (Mathworks) with an open source code for particle image velocimetry (http://www.fast.u-psud.fr/pivmat/) to calculate the microsphere displacement between the each frame. Then, the volumetric flow rate was calculated by multiplying the cross-section area with the flow speed.

Delivered Fluid Volume Measurement

Delivered fluid volume was characterized by measuring device weight change per actuation with a high-precision analytical balance (XS105, Mettler Toledo) and converting it to volume.

Thermo-Mechanical-Fluidic Simulation

Three dimensional (3D) finite element analysis (FEA) was carried out using the software ABAQUS to analyze the thermal conduction and mechanical deformation of the optofluidic drug delivery devices. For a given power applied to the heater, the transient thermal analyses were carried out first to calculate the spatial and temporal variations of temperature in the device. The thermal expansion of expandable polymer could be then determined based on the nonlinear thermal expansion curve (**Figure 4.4B**) and the increase of temperature obtained from thermal analyses. In the subsequent simulation of mechanical deformations, the volume average of thermal expansion was applied as a uniform thermal expansion strain, to the area of expandable polymer underneath the operating heater for simplification. The injected volume of drug could be then determined based on the deformed configuration of the entire device.

In the thermal analyses, 8-node linear heat transfer elements were used, and the refined meshes were adopted to ensure the accuracy. A volume heat source was applied within the operating heater. The free surfaces of the device have natural convection with the surrounding air. In the simulation of bare heater on the expandable polymer, the polymer was adhered to a plastic case that was put on a large petri-dish, and therefore a constant temperature (equal to room temperature) was applied to the bottom surface of plastic case. In the simulation of entire operating device, the probe was inserted into a brain for interaction with neural tissues. In this case, one side surface of device was in contact with the brain, and therefore should have a constant temperature approximately equal to the body temperature. The material parameters used in the simulations are summarized in Supplementary Table 1. The calculated temperature distributions are shown in **Figure 4.4E** for the bare-heater system, which agrees reasonably well with the corresponding experimental measurement.

In the mechanical analyses, 8-node 3D solid elements were used for all materials, with refined meshes to ensure the accuracy. Since each reservoir is relatively far from each other, only one reservoir was modeled in the mechanics analyses, as schematically shown in **Figure 4.5A** and **B**. The physical contact between the top surface of adhesive layer and the spherical surface of reservoir was taken into account during the thermal expansion. The calculations show that the deformation induced by thermal actuation is mainly accommodated by the expandable layer, which is in agreement with the experiment results (**Figure 4.4D**). For a given thermal expansion strain applied to the area of expandable polymer underneath the heater, the injected proportion of drug was obtained in **Figure 4.5C**, which shows a saturation in the injection for the thermal strain exceeding ~22%.

Besides the thermal-mechanical simulations described above, a simplified computational fluid dynamics model was adopted to estimate the cooling of heated drug in the channel, before its reaction with neural tissues. Here, FLUID 142 element (in the software ANSYS) was used to simulate the drug as a type of fluid flowed through the channel. For simplification, the straight channel was assumed to be embedded in a cylindrical substrate that is sufficiently large. A constant fluid temperature was adopted at the inlet of the channel, and the zero pressure condition was set at the outlet. The free (i.e., outer) surface of the substrate have natural convection with the surrounding air. The fludic parameters include the density (1060 kg/m^3), the thermal conductivity (0.6 W/m/K), and the specific heat (4.184 kJ/kg/K). The calculations show that the fluid temperature drops rapidly along the channel and the maximum temperature increase at the outlet is less than 0.1 ^{o}C.

Table 4.2 The thermal and mechanical properties of various components in the microfluidic drug device, where E denotes the modulus, v is the Poisson ratio, and ρ is the density, c_p is the specific heat and k is the thermal conductivity.

Component	ρ (kg/m^3)	c_p (J/kg/K)	k (W/m/K)	E (MPa)	v
Silicone adhesive	1050	1100	0.18	1	0.49
Expandable polymer	970	1460	0.24	3	0.48
COP	1020	1000	0.14	2600	0.35
Au heater	19280	129	318.00	78000	0.44

Substrate (FR-4)	1200	1750	0.45	24000	0.13

Experimental subjects

Adult (25–35 g) male C57BL/6J and TH::IRES-Cre backcrossed to C57BL/6J mice were group-housed, given access to food pellets and water *ad libitum* and maintained on a 12 h:12 h light:dark cycle (lights on at 7:00 AM). All mice were held in a facility in the lab 1 week prior to surgery, post-surgery and throughout the duration of the behavioral assays to minimize stress from transportation and disruption from foot traffic. Adult (275-325g) male Lewis rats (LEW/CRL) were purchased from Charles River and housed in a climate-controlled facility with a 12:12-h light-dark cycle under standard conditions. All procedures were approved by the Animal Care and Use Committee of Washington University and conformed to US National Institutes of Health guidelines.

Viral Preparation

Plasmids coding pAAV-EF1a-DIO-EFYP and pAAV-EF1a-double floxed-hChR2(H134R)-EYFP-WPRE-HGHpA were obtained from Addgene (Addgene.org) originally from the Deisseroth Laboratory at Stanford University. The DNA was amplified with a Maxiprep kit (Promega) and packaged into AAV5 serotyped viruses by the WUSTL Hope Center Viral Core. AAV5-PGK-Cre was acquired from the UNC Vector Core.

Table 4.3 Details on origin and titer of viral constructs used.

Plasmid	Source	Packaged by	Serotype	Titer
pAAV-EF1a-DIO-EFYP	Deisseroth Laboratory (Stanford)	WUSTL Hope Center Viral Core	AAV5	5 x 10^12 vg/ml
pAAV-EF1a-double floxed-hChR2(H134R)-EYFP-WPRE-HGHpA	Deisseroth Laboratory (Stanford)	WUSTL Hope Center Viral Core	AAV5	2 x 10^13 vg/ml
AAV5-PGK-Cre	UNC Vector Core	UNC Vector Core	AAV5	3.2 x 10^12 VM/mL

Stereotaxic Surgery

After the mice were acclimatized to the holding facility for seven to nine days, they were anaesthetized in an induction chamber (4% Isolflurane) and placed in a stereotaxic frame (Kopf Instruments, Model 1900) where they were maintained at 1-2% isoflurane. For the baseline locomotor, anxiety, and inflammation assays, mice were implanted with the microfluidic device into the dorsal striatum (stereotaxic coordinates from bregma (mm): anterior-posterior (AP): +1.10, medial-lateral (ML): +/−1.50, dorsal-ventral (DV): −4.00). For the test of viral expression, mice were implanted with the microfluidic device into the dorsal striatum (stereotaxic

coordinates from bregma (mm): AP: +1.00, ML: +/−1.50, DV: −3.00). For the DAMGO-induced rotation experiment, mice were implanted with the microfluidic device above the VTA (stereotaxic coordinates from bregma (mm): AP:-3.10, ML: +/- 0.50, DV: -4.25). For the optofluidics experiment, a craniotomy was performed and TH-Cre mice were injected with 1 µl of AAV5-EF1a-ChR2(H134)-eYFP unilaterally into the VTA (stereotaxic coordinates from bregma (mm): AP:-3.20, ML:+/−0.50, DV: −4.90). Five weeks later, mice were then implanted with the optofluidic device adjacent to the NAcSh (stereotaxic coordinates from bregma: +1.30 AP, +/−0.20 ML, −4.80 mm DV). A standard electrode holder (KOPF 1770) was adapted to implant the microfluidic and optofluidic devices. For biodissolvable samples, the device was implanted at the desired target, ACSF was applied to the portion of the device that remained outside of the skull to facilitate dissolution of the adhesive, and then the epoxy needle was removed after a delay of 15 minutes. The implants were secured using two bone screws (CMA, 743102) and affixed with dental cement (Lang Dental). C57Bl6 mice were allowed to recover for 5 days prior to behavioral testing. Ai9 mice were allowed to recover three weeks following surgery for viral expression. TH-Cre mice were allowed to recover one week following the final surgery (for a total of six weeks to (permit optimal AAV expression and Cre recombinase activity at VTA-NAc terminals). Post-surgery, all rats received subcutaneous injections of buprenorphine hydrochloride (0.05 mg/kg, Reckitt Benckiser Healthcare Ltd., USA) for pain management, and of ampicillin (50 mg/kg, Sage Pharmaceuticals, USA) to prevent infection at the implantation site.

Immunohistochemistry

Immunohistochemistry was performed as described (see Chapter 2) (Kim et al., 2013b)
Briefly, mice were anesthetized with pentobarbital and intracardially perfused with ice-cold 4%
paraformaldehyde in phosphate buffered saline (PBS). Brains were dissected, post-fixed for 24
hr at 4 ºC and cryoprotected with solution of 30% sucrose in 0.1M PB at 4ºC for at least 24 hr,
cut into 30 μm sections and processed for immunostaining. 30 μm brain sections were washed
three times in PBS and blocked in PBS containing 0.5% Triton X-100 and 5 % normal goat
serum. Sections were then incubated for ~16 hr at room temperature in rabbit anti c-fos antibody,
guinea pig anti-GFAP, rabbit anti-Iba1 and/or chicken anti-TH. Following incubation, sections
were washed three times in PBS and then incubated for 2 hr at room temperature in Alexa Fluor
488 goat anti-rabbit IgG, Alexa Fluor 594 goat anti-rabbit IgG, Alexa Fluor 633 goat anti-
chicken, and/or goat anti-guinea pig Alexa Fluor 546, then washed three times in PBS, incubated
for 1 hr in Neurotrace 435/455 Blue Fluorescent Nissl stain (1:400), then washed three times in
PBS, and followed by three 1washes in PB and mounted on glass slides with HardSet
Vectashield (Vector Labs). All sections were imaged on both epifluorescent and confocal
microscopes. Gain and exposure time were constant throughout each experiment, and all image
groups were processed in parallel using Adobe Photoshop CS5 (Adobe Systems).

Table 4.4 Details on origin, species, and dilution of antibodies used.

189

Antibody	Species	Dilution	Source
GFAP	Guinea Pig	1:500	Synaptic Systems
Iba1	Rabbit	1:300	Wako Chemicals
TH	Chicken	1:2000	Aves Labs
c-fos	Rabbit	1:1000	Santa Cruz
Alexa Fluor 488 anti-rabbit IgG	Goat	1:1000	Invitrogen
Alexa Fluor 594 anti-rabbit IgG	Goat	1:1000	Invitrogen
Alexa Fluor 633 anti-chicken IgG	Goat	1:1000	Invitrogen
Alexa Fluor 546 anti-guinea pig IgG	Goat	1:1000	Invitrogen
Alexa Fluor 594 anti-chicken IgG	Goat	1:1000	Invitrogen
Neurotrace 435/455	N/A	1:400	Life Technologies

Immuno-Glial Response in Implanted Tissues

C57BL/6J mice (n=6) were implanted with microfluidic devices into the dorsal striatum and allowed to recover for four weeks before perfusion. Immunohistochemistry was performed as described.

c-fos Expression

TH-Cre animals expressing AAV5-EF1a-ChR2(H134)-eYFP unilaterally in the VTA and implanted with optofluidic devices in the NAcSh were photostimulated at 10 Hz for 1 hour (see Chapter 2) (Kim et al., 2013b), animals were perfused immediately following, and immunohistochemistry was performed as above.

Rotarod Assay

An accelerating Rotarod (Ugo Basile, Comerio, Italy) was used as described previously (Golden et al., 2013; Montana et al., 2009) to assess motor coordination C57Bl6 mice (cannulas or microfluidic devices were implanted in the dorsal striatum as described, n= 5/group) received two training sessions separated by 1 h. The first training session consisted of two trials of 120 s spent walking on the Rotarod at a fixed speed of 4 rpm. The second training session consisted of one trial of 120 s at 4 rpm. All mice completed the first training session without falling in five attempts or less; all mice completed the second training session in two attempts or less without a fall. One hour after the second training session, latency to fall as the Rotarod accelerated from 4 to 40 rpm over 5 min was assessed. Five consecutive acceleration trials were performed, with 10 min between each trial.

Spontaneous Running Assay

C57Bl6 mice (cannulas or microfluidic devices were implanted in the dorsal striatum as described, n=9-10/group) mice were habituated to locked low profile, wireless running wheels (ENV-044, Med Associates) for one hour. Following this habituation the wheels were unlocked and the animals were allowed to run freely for 2 hours. Revolutions of the wheel were counted as the primary means of assessing spontaneous running.

Open Field Test

OFT testing was performed in a sound attenuated room maintained at 23ºC. Lighting was measured and stabilized at 2000 lux, and performed in the afternoon between 13:00–1600 hrs. The open field was a 50 x 50 cm square enclosure and was cleaned with 70% ethanol between testing trials. For testing, C57Bl6 mice (cannulas or microfluidic devices were implanted in the dorsal striatum as described, n=10/group) were placed in the center of the open field and allowed to roam freely for 30 min. Movements were video recorded and analyzed using Ethovision. The center was defined as a square comprised of 50% the total area of the OFT. Time in the center expressed as percentages total time was the primary measure of anxiety-like behaviors.

Contraversive Rotation/Locomotor Testing Assay

C57Bl6 mice with microfluidic devices implanted above the VTA were placed in the center of the same arena used for the OFT and allowed to roam freely for 1 hr. Wireless infusion of vehicle or DAMGO was initiated and movements were video recorded and analyzed using Ethovision. Rotations were defined as full 360º revolutions in the path of movement.

Real-Time Place Preference

TH-Cre$^{VTA-NAc:ChR2}$ animals were placed in a custom-made unbiased, balanced two-compartment conditioning apparatus (52.5 x 25.5 x 25.5 cm) as described previously (Jennings et al., 2013; Kim et al., 2013a; Stamatakis and Stuber, 2012; Stamatakis et al., 2013; Tan et al., 2012). Mice were allowed to freely roam the entire apparatus for 20 min. Entry into one compartment triggered photostimulation (8, 10 ms light pulses at 20 Hz every 5s) while the animal remained in the light-paired chamber. Entry into the other chamber ended the photostimulation. The following day SCH23390 (400 ng, Tocris) was administered 10 minutes prior to the testing. Mice were counterbalanced so that ~50% received the SCH23390 on day 1, there was no difference between animals that received the drug on day 1 or day 2. The side paired with photostimulation was counterbalanced across mice and across sessions. Time spent in each chamber and total distance traveled for the entire 20-minute trial was measured using Ethovision 8.5 (Noldus Information Technologies, Leesburg, VA). The triggered wireless photostimulation was elicited using a Noldus I/O Box coupled to an Arduino microcontroller that controlled the output of the of IR remote control.

Data Analysis/Statistics

Data are expressed as means ± SEM. Data were normally distributed, and differences between groups were determined using independent t-tests or one-way ANOVA followed by post hoc Bonferroni comparisons if the main effect was significant at $p < 0.05$. Paired t-tests were used in within subject design experiments. Statistical analyses were conducted using Prism 5.0 (GraphPad).

Genotyping of Mouse Lines

DNA was isolated from tail tissue obtained from weanling mice (21-28 days of age), and PCR screening was performed using the following primers: Cre recombinase (forward: 5'- GCA TTA CCG GTC GAT GCA ACG AGT GAT GAG-3' and reverse: 5'- GAG TGA ACG AAC CTG GTC GAA ATC AGT GCG-3') yielding a 400-bp PCR product in Cre positive animals. Fatty acid-binding protein intestinal primers (forward: 5'- TGG ACA GGA CTG GAC CTC TGC TTT CCT AGA-3' and reverse: 5'- TAG AGC TTT GCC ACA TCA CAG GTC ATT CAG-3') were used as positive controls and yield a 200-bp PCR product.

REFERENCES

Banghart, M.R., and Sabatini, B.L. (2012). Photoactivatable neuropeptides for spatiotemporally precise delivery of opioids in neural tissue. Neuron *73*, 249–259.

Billard, W., Ruperto, V., Crosby, G., Iorio, L.C., and Barnett, A. (1984). Characterization of the binding of 3H-SCH 23390, a selective D-1 receptor antagonist ligand, in rat striatum. Life Sci. *35*, 1885–1893.

Calenco-Choukroun, G., Daugé, V., Gacel, G., Féger, J., and Roques, B.P. (1991). Opioid delta agonists and endogenous enkephalins induce different emotional reactivity than mu agonists after injection in the rat ventral tegmental area. Psychopharmacology (Berl.) *103*, 493–502.

Callahan, W.J., Narhi, L.O., Kosky, A.A., and Treuheit, M.J. (2001). Sodium Chloride Enhances the Storage and Conformational Stability of BDNF and PEG-BDNF. Pharm. Res. *18*, 261–266.

Callaway, E.M., and Katz, L.C. (1993). Photostimulation using caged glutamate reveals functional circuitry in living brain slices. Proc. Natl. Acad. Sci. U. S. A. *90*, 7661–7665.

Canales, A., Jia, X., Froriep, U.P., Koppes, R.A., Tringides, C.M., Selvidge, J., Lu, C., Hou, C., Wei, L., Fink, Y., et al. (2015). Multifunctional fibers for simultaneous optical, electrical and chemical interrogation of neural circuits in vivo. Nat. Biotechnol. *33*, 277–284.

Capadona, J.R., Tyler, D.J., Zorman, C.A., Rowan, S.J., and Weder, C. (2012). Mechanically adaptive nanocomposites for neural interfacing. MRS Bull. *37*, 581–589.

Carter, A.G., and Sabatini, B.L. (2004). State-dependent calcium signaling in dendritic spines of striatal medium spiny neurons. Neuron *44*, 483–493.

De Chaumont, F., Coura, R.D.-S., Serreau, P., Cressant, A., Chabout, J., Granon, S., and Olivo-Marin, J.-C. (2012). Computerized video analysis of social interactions in mice. Nat. Methods *9*, 410–417.

Creed, M., Pascoli, V.J., and Lüscher, C. (2015). Addiction therapy. Refining deep brain stimulation to emulate optogenetic treatment of synaptic pathology. Science *347*, 659–664.

Devine, D.P., and Wise, R.A. (1994). Self-administration of morphine, DAMGO, and DPDPE into the ventral tegmental area of rats. J. Neurosci. Off. J. Soc. Neurosci. *14*, 1978–1984.

Farra, R., Sheppard, N.F., McCabe, L., Neer, R.M., Anderson, J.M., Santini, J.T., Cima, M.J., and Langer, R. (2012). First-in-Human Testing of a Wirelessly Controlled Drug Delivery Microchip. Sci. Transl. Med. *4*, 122ra21–ra122ra21.

Gilletti, A., and Muthuswamy, J. (2006). Brain micromotion around implants in the rodent somatosensory cortex. J. Neural Eng. *3*, 189–195.

Golden, J.P., DeMaro, J.A., Knoten, A., Hoshi, M., Pehek, E., Johnson, E.M., Gereau, R.W., and Jain, S. (2013). Dopamine-Dependent Compensation Maintains Motor Behavior in Mice with Developmental Ablation of Dopaminergic Neurons. J. Neurosci. *33*, 17095–17107.

Gunaydin, L.A., Grosenick, L., Finkelstein, J.C., Kauvar, I.V., Fenno, L.E., Adhikari, A., Lammel, S., Mirzabekov, J.J., Airan, R.D., Zalocusky, K.A., et al. (2014). Natural neural projection dynamics underlying social behavior. Cell *157*, 1535–1551.

Hoare, T., Santamaria, J., Goya, G.F., Irusta, S., Lin, D., Lau, S., Padera, R., Langer, R., and Kohane, D.S. (2009). A magnetically triggered composite membrane for on-demand drug delivery. Nano Lett. *9*, 3651–3657.

Hoare, T., Timko, B.P., Santamaria, J., Goya, G.F., Irusta, S., Lau, S., Stefanescu, C.F., Lin, D., Langer, R., and Kohane, D.S. (2011). Magnetically Triggered Nanocomposite Membranes: A Versatile Platform for Triggered Drug Release. Nano Lett. *11*, 1395–1400.

Hyttel, J. (1983). SCH 23390 - the first selective dopamine D-1 antagonist. Eur. J. Pharmacol. *91*, 153–154.

Jenck, F., Bozarth, M., and Wise, R.A. (1988). Contraversive circling induced by ventral tegmental microinjections of moderate doses of morphine and [D-Pen2, D-Pen5]enkephalin. Brain Res. *450*, 382–386.

Jennings, J.H., Sparta, D.R., Stamatakis, A.M., Ung, R.L., Pleil, K.E., Kash, T.L., and Stuber, G.D. (2013). Distinct extended amygdala circuits for divergent motivational states. Nature *496*, 224–228.

Joyce, J.R., Bal, T.S., Ardrey, R.E., Stevens, H.M., and Moffat, A.C. (1984). The decomposition of benzodiazepines during analysis by capillary gas chromatography/mass spectrometry. Biol. Mass Spectrom. *11*, 284–289.

Kim, K.M., Baratta, M.V., Yang, A., Lee, D., Boyden, E.S., and Fiorillo, C.D. (2012). Optogenetic Mimicry of the Transient Activation of Dopamine Neurons by Natural Reward Is Sufficient for Operant Reinforcement. PLoS ONE *7*, e33612.

Kim, S.-Y., Adhikari, A., Lee, S.Y., Marshel, J.H., Kim, C.K., Mallory, C.S., Lo, M., Pak, S., Mattis, J., Lim, B.K., et al. (2013a). Diverging neural pathways assemble a behavioural state from separable features in anxiety. Nature *496*, 219–223.

Kim, T., McCall, J.G., Jung, Y.H., Huang, X., Siuda, E.R., Li, Y., Song, J., Song, Y.M., Pao, H.A., Kim, R.-H., et al. (2013b). Injectable, Cellular-Scale Optoelectronics with Applications for Wireless Optogenetics. Science *340,* 211–216.

Konermann, S., Brigham, M.D., Trevino, A.E., Hsu, P.D., Heidenreich, M., Cong, L., Platt, R.J., Scott, D.A., Church, G.M., and Zhang, F. (2013). Optical control of mammalian endogenous transcription and epigenetic states. Nature *500*, 472–476.

Kozai, T.D.Y., and Kipke, D.R. (2009). Insertion shuttle with carboxyl terminated self-assembled monolayer coatings for implanting flexible polymer neural probes in the brain. J. Neurosci. Methods *184*, 199–205.

Kozai, T.D.Y., Langhals, N.B., Patel, P.R., Deng, X., Zhang, H., Smith, K.L., Lahann, J., Kotov, N.A., and Kipke, D.R. (2012). Ultrasmall implantable composite microelectrodes with bioactive surfaces for chronic neural interfaces. Nat. Mater. *11*, 1065–1073.

Kramer, R.H., Mourot, A., and Adesnik, H. (2013). Optogenetic pharmacology for control of native neuronal signaling proteins. Nat. Neurosci. *16*, 816–823.

Kunwar, P.S., Zelikowsky, M., Remedios, R., Cai, H., Yilmaz, M., Meister, M., and Anderson, D.J. (2015). Ventromedial hypothalamic neurons control a defensive emotion state. eLife e06633.

Lammel, S., Ion, D.I., Roeper, J., and Malenka, R.C. (2011). Projection-Specific Modulation of Dopamine Neuron Synapses by Aversive and Rewarding Stimuli. Neuron *70*, 855–862.

Lammel, S., Lim, B.K., Ran, C., Huang, K.W., Betley, M.J., Tye, K.M., Deisseroth, K., and Malenka, R.C. (2012). Input-specific control of reward and aversion in the ventral tegmental area. Nature *491*, 212–217.

Lammel, S., Steinberg, E.E., Földy, C., Wall, N.R., Beier, K., Luo, L., and Malenka, R.C. (2015). Diversity of transgenic mouse models for selective targeting of midbrain dopamine neurons. Neuron *85*, 429–438.

Latimer, L.G., Duffy, P., and Kalivas, P.W. (1987). Mu opioid receptor involvement in enkephalin activation of dopamine neurons in the ventral tegmental area. J. Pharmacol. Exp. Ther. *241*, 328–337.

Lee, H., Bellamkonda, R.V., Sun, W., and Levenston, M.E. (2005). Biomechanical analysis of silicon microelectrode-induced strain in the brain. J. Neural Eng. *2*, 81–89.

Madisen, L., Zwingman, T.A., Sunkin, S.M., Oh, S.W., Zariwala, H.A., Gu, H., Ng, L.L., Palmiter, R.D., Hawrylycz, M.J., Jones, A.R., et al. (2010). A robust and high-throughput Cre reporting and characterization system for the whole mouse brain. Nat. Neurosci. *13*, 133–140.

Matsuzaki, M., Ellis-Davies, G.C., Nemoto, T., Miyashita, Y., Iino, M., and Kasai, H. (2001). Dendritic spine geometry is critical for AMPA receptor expression in hippocampal CA1 pyramidal neurons. Nat. Neurosci. *4*, 1086–1092.

McCall, J.G., Kim, T., Shin, G., Huang, X., Jung, Y.H., Al-Hasani, R., Omenetto, F.G., Bruchas, M.R., and Rogers, J.A. (2013). Fabrication and application of flexible, multimodal light-emitting devices for wireless optogenetics. Nat. Protoc. *8*, 2413–2428.

Minev, I.R., Musienko, P., Hirsch, A., Barraud, Q., Wenger, N., Moraud, E.M., Gandar, J., Capogrosso, M., Milekovic, T., Asboth, L., et al. (2015). Biomaterials. Electronic dura mater for long-term multimodal neural interfaces. Science *347*, 159–163.

Montana, M.C., Cavallone, L.F., Stubbert, K.K., Stefanescu, A.D., Kharasch, E.D., and Gereau, R.W. (2009). The Metabotropic Glutamate Receptor Subtype 5 Antagonist Fenobam Is Analgesic and Has Improved in Vivo Selectivity Compared with the Prototypical Antagonist 2-Methyl-6-(phenylethynyl)-pyridine. J. Pharmacol. Exp. Ther. *330*, 834–843.

Mourot, A., Fehrentz, T., Le Feuvre, Y., Smith, C.M., Herold, C., Dalkara, D., Nagy, F., Trauner, D., and Kramer, R.H. (2012). Rapid optical control of nociception with an ion-channel photoswitch. Nat. Methods *9*, 396–402.

Noguchi, J., Nagaoka, A., Watanabe, S., Ellis-Davies, G.C.R., Kitamura, K., Kano, M., Matsuzaki, M., and Kasai, H. (2011). In vivo two-photon uncaging of glutamate revealing the structure–function relationships of dendritic spines in the neocortex of adult mice. J. Physiol. *589*, 2447–2457.

Polosukhina, A., Litt, J., Tochitsky, I., Nemargut, J., Sychev, Y., De Kouchkovsky, I., Huang, T., Borges, K., Trauner, D., Van Gelder, R.N., et al. (2012). Photochemical Restoration of Visual Responses in Blind Mice. Neuron *75*, 271–282.

Polstein, L.R., and Gersbach, C.A. (2015). A light-inducible CRISPR-Cas9 system for control of endogenous gene activation. Nat. Chem. Biol. *11*, 198–200.

Spieth, S., Schumacher, A., Holtzman, T., Rich, P.D., Theobald, D.E., Dalley, J.W., Nouna, R., Messner, S., and Zengerle, R. (2012). An intra-cerebral drug delivery system for freely moving animals. Biomed. Microdevices *14*, 799–809.

Stamatakis, A.M., and Stuber, G.D. (2012). Activation of lateral habenula inputs to the ventral midbrain promotes behavioral avoidance. Nat. Neurosci. *15*, 1105–1107.

Stamatakis, A.M., Jennings, J.H., Ung, R.L., Blair, G.A., Weinberg, R.J., Neve, R.L., Boyce, F., Mattis, J., Ramakrishnan, C., Deisseroth, K., et al. (2013). A unique population of ventral tegmental area neurons inhibits the lateral habenula to promote reward. Neuron *80*, 1039–1053.

Steger, P.J., Martinelli, E.F., and Mühlebach, S.F. (1996). Stability of high-dose morphine chloride injection upon heat sterilization: comparison of UV-spectroscopy and HPLC. J. Clin. Pharm. Ther. *21*, 73–78.

Stuber, G.D., Stamatakis, A.M., and Kantak, P.A. (2015). Considerations when using cre-driver rodent lines for studying ventral tegmental area circuitry. Neuron *85*, 439–445.

Subbaroyan, J., Martin, D.C., and Kipke, D.R. (2005). A finite-element model of the mechanical effects of implantable microelectrodes in the cerebral cortex. J. Neural Eng. *2*, 103–113.

Tan, K.R., Yvon, C., Turiault, M., Mirzabekov, J.J., Doehner, J., Labouèbe, G., Deisseroth, K., Tye, K.M., and Lüscher, C. (2012). GABA neurons of the VTA drive conditioned place aversion. Neuron *73*, 1173–1183.

Timko, B.P., Arruebo, M., Shankarappa, S.A., McAlvin, J.B., Okonkwo, O.S., Mizrahi, B., Stefanescu, C.F., Gomez, L., Zhu, J., Zhu, A., et al. (2014). Near-infrared–actuated devices for remotely controlled drug delivery. Proc. Natl. Acad. Sci. *111*, 1349–1354.

Tochitsky, I., Polosukhina, A., Degtyar, V.E., Gallerani, N., Smith, C.M., Friedman, A., Van Gelder, R.N., Trauner, D., Kaufer, D., and Kramer, R.H. (2014). Restoring Visual Function to Blind Mice with a Photoswitch that Exploits Electrophysiological Remodeling of Retinal Ganglion Cells. Neuron *81*, 800–813.

Tsai, H.-C., Zhang, F., Adamantidis, A., Stuber, G.D., Bonci, A., de Lecea, L., and Deisseroth, K. (2009). Phasic firing in dopaminergic neurons is sufficient for behavioral conditioning. Science *324*, 1080–1084.

Tye, K.M., and Deisseroth, K. (2012). Optogenetic investigation of neural circuits underlying brain disease in animal models. Nat. Rev. Neurosci. *13*, 251–266.

Walsh, J.J., Friedman, A.K., Sun, H., Heller, E.A., Ku, S.M., Juarez, B., Burnham, V.L., Mazei-Robison, M.S., Ferguson, D., Golden, S.A., et al. (2014). Stress and CRF gate neural activation of BDNF in the mesolimbic reward pathway. Nat. Neurosci. *17*, 27–29.

Witten, I.B., Steinberg, E.E., Lee, S.Y., Davidson, T.J., Zalocusky, K.A., Brodsky, M., Yizhar, O., Cho, S.L., Gong, S., Ramakrishnan, C., et al. (2011). Recombinase-driver rat lines: tools, techniques, and optogenetic application to dopamine-mediated reinforcement. Neuron *72*, 721–733.

Wu, F., Tien, L., Chen, F., Kaplan, D., Berke, J., and Yoon, E. (2013). A multi-shank silk-backed parylene neural probe for reliable chronic recording. In 2013 Transducers Eurosensors XXVII: The 17th International Conference on Solid-State Sensors, Actuators and Microsystems (TRANSDUCERS EUROSENSORS XXVII), pp. 888–891.

Zhang, K., and Cui, B. (2015). Optogenetic control of intracellular signaling pathways. Trends Biotechnol. *33*, 92–100.

Part 2

Dissecting the role of locus coeruleus circuitry in negative affective behaviors

Chapter 5: CRH engagement of the locus coeruleus noradrenergic system mediates stress-induced anxiety

Chapter 6: Determining the downstream receptor and projection targets that mediate locus coeruleus-induced negative affective behaviors

Chapter 5

CRH engagement of the locus coeruleus noradrenergic system mediates stress-induced anxiety

Author contributions for the above citation:
J.G.M designed, performed, and analyzed all of the experiments (except for the slice physiology) and wrote the paper. R.A. helped design and perform behavioral experiments. E.R.S. helped analyzed the *in vivo* electrophysiology experiments. R.A., A.J.N., and D.Y.H performed some of the surgeries. D.Y.H. helped perform the immunohistochemistry and built hundreds of fiber optic implants. C.P.F. designed, performed, and analyzed the slice physiology experiments. M.R.B. oversaw all of the work, helped design the experiments, and helped write the paper.

SUMMARY

The locus coeruleus noradrenergic (LC-NE) system is one of the first systems engaged following a stressful event. While numerous groups have demonstrated that LC-NE neurons are activated by many different stressors, the underlying neural circuitry and the role of this activity in generating stress-induced anxiety has not been elucidated. Using a combination of *in vivo* chemogenetics, optogenetics, and retrograde tracing we determine that increased tonic activity of the LC-NE system is necessary and sufficient for stress-induced anxiety and aversion. Selective inhibition of LC-NE neurons during stress prevents subsequent anxiety-like behavior. Exogenously increasing tonic, but not phasic, activity of LC-NE neurons is alone sufficient for anxiety-like and aversive behavior. Furthermore, endogenous corticotropin releasing hormone[+] (CRH[+]) LC inputs from the amygdala increase tonic LC activity, inducing anxiety-like behaviors. These studies position the LC-NE system as a critical mediator of acute stress-induced anxiety and offer a potential intervention for preventing stress-related affective disorders.

INTRODUCTION

Anxiety is a complex set of behavioral and physiological responses that can be both beneficial and detrimental to an individual. In stressful conditions, acute anxiety helps to maintain the arousal and vigilance required to sustain attention, accomplish necessary tasks, and avoid repeated exposures to dangerous conditions (Gross and Hen, 2004). Recent basic neuroscience has elucidated circuits in the extended amygdala that are either natively anxiogenic or anxiolytic, building a circuit-based pathology that may yield more selective therapeutic approaches (Felix-Ortiz et al., 2013; Jennings et al., 2013; Kheirbek et al., 2013; Kim et al., 2013a; Tye et al., 2011). However, the extended amygdala does not act alone in its control over

202

anxiogenesis, as elegant recent work reveals parallel systems for anxiety in the septohypothalamic circuitry related to persistent, stress-induced anxiety (Anthony et al., 2014; Heydendael et al., 2014). Additionally, the great majority of these studies propose mechanisms mediated by the fast-acting, small molecule neurotransmitters, GABA and glutamate. However, clinically, we know that neuromodulators such as norepinephrine and various neuropeptides play pivotal roles in long-term outcomes following stress exposure (Raskind et al., 2003, 2007, 2013). Here we propose a separate neuromodulatory system underlying immediate, acute stress-induced anxiety, which serves to alter risk aversion behavior immediately following a stressful event.

The locus coeruleus-noradrenergic system (LC-NE) is a small, tightly packed pontine brain region that sends numerous projections to the forebrain and spinal cord. The LC-NE system is involved in a broad number of physiological functions including arousal, memory, cognition, pain processing, behavioral flexibility, and stress reactivity (Berridge and Waterhouse, 2003; Carter et al., 2010; Hickey et al., 2014; Snyder et al., 2012; Tervo et al., 2014; Valentino and Van Bockstaele, 2008; Vazey and Aston-Jones, 2014).. Numerous environmental stressors, including social and predator stress, activate the LC-NE system (Bingham et al., 2011; Cassens et al., 1981; Curtis et al., 1997, 2012; Francis et al., 1999; Lechner et al., 1997; Reyes et al., 2008; Valentino and Van Bockstaele, 2008; Valentino et al., 1991). Thus, the LC system is thought to comprise a major component of the centrally mediated components of the classical fight-or-flight response The response of the LC-NE systems to stress is particularly important in the context of stress-induced human neuropsychiatric disorders such as posttraumatic stress disorder (PTSD) where both basic and clinical research have revealed noradrenergic antagonism to be a very promising therapeutic target (Olson et al., 2011; Raskind et al., 2003, 2007, 2013).

Noradrenergic neurons within the LC-NE system exhibit three distinct activation profiles: low tonic, high tonic, and phasic activity. It has been proposed that these neurons function differently to determine behavioral flexibility to various environmental challenges. Low tonic LC discharge (1-2 Hz) is thought to be consistent with an awake state (Aston-Jones and Bloom, 1981a; Bloom, 1981; Carter et al., 2010, 2012) whereas phasic burst activity results from distinct sensory stimuli such as flashes of light, auditory tones, and brief touch (Aston-Jones and Bloom, 1981b; Foote et al., 1980; Rasmussen et al., 1986). Stressful events and stimuli shift LC activity towards a high tonic mode of firing (3-8 Hz) and stress-related neuropeptide release, such as corticotropin-releasing hormone (CRH) is thought to drive the high tonic state while simultaneously decreasing phasic firing events (Curtis et al., 1997, 2001, 2012; Jedema and Grace, 2004; Page and Abercrombie, 1999; Reyes et al., 2008; Snyder et al., 2012; Valentino and Foote, 1988). We were particularly interested in examining the role of this high tonic activity of LC-NE neurons during stress and defining the endogenous substrates that drive this increased LC-NE activity.

While phasic modulation of the LC is thought to be mediated by fast, small molecule neurotransmission, neuropeptide transmission is thought to control tonic LC-NE activity. Anatomical evidence suggests that neuropeptidergic inputs to the LC from the central nucleus of the amygdala (CeA), including those containing CRH, may become activated in response to stressors (Reyes et al., 2008; Valentino et al., 1992). Anatomical data support this notion using tract tracing studies and electron microscopy to suggest that CRH-containing amygdalar monosynaptic projections from the CeA terminate in the LC (Reyes et al., 2008). Given the importance of CRH in stress-induced behavioral responses such as dysphoria, anxiety, and aversion (Bruchas et al., 2009; Dunn et al., 2004; Francis et al., 1999; Gafford et al., 2012; Heinrichs et al., 1994; Koob, 1999; Land et al., 2008), these projections are situated to

204

significantly impact LC neuronal activity, yet the functional consequences of these inputs remain unresolved.

Here we dissect the locus coeruleus circuitry in the context of stress-induced negative affective behavior. In particular, we use chemogenetics and optogenetics to focus on the role of neural activity of locus coeruleus noradrenergic (LC-NE) neurons in generating these behaviors. We find that LC-NE neurons have increased activity during stress and that blocking this elevated activity suppresses acute stress-induced anxiety. Furthermore, optogenetic activation and release of endogenous amygdalar CRH into the LC promotes anxiety-like and aversive behavior. We conclusively show that LC and its afferent circuitry are critical for encoding and producing stress-induced anxiety.

Results

Selective inhibition of LC-NE neurons during stress suppresses subsequent anxiety

Numerous groups have reported that tonic activity of LC-NE neurons increases in response to stress (Bingham et al., 2011; Cassens et al., 1981; Curtis et al., 1997, 2012; Francis et al., 1999; Lechner et al., 1997; Reyes et al., 2008; Valentino and Van Bockstaele, 2008; Valentino et al., 1991), but it has previously been untenable to selectively inhibit the activity of only these NE neurons and assess their role in stress-induced behaviors. To examine the role of LC-NE neurons in stress-induced anxiety-like behavior in mice, we implemented a restraint stress paradigm (Chmielarz et al., 2013; Schaefer et al., 2000; Sim et al., 2013), which was immediately followed by anxiety testing in the open field test (OFT) (**Figure 5.1A**). Following 30 minutes of restraint stress, wild-type (C57BL/6J) mice produce a robust stress-induced anxiety phenotype and have increased immediate early gene (*cfos*) expression, consistent with

increased activity of these neurons (**Figure 5.1B-D, Figure 5.2A & B**). To determine whether this increase in activity is necessary for the resultant anxiety-like behavior, we selectively targeted the inhibitory designer receptor exclusively activated by designer drug (Ga_i-coupled; hM4Di DREADD (Armbruster et al., 2007) to LC-NE neurons by injecting a Cre-dependent AAV into the LC of tyrosine hydroxylase-IRES-Cre mice (*Th*-Cre) (**Figure 5.1E**). When the receptor is activated with its ligand, Clozapine-n-oxide (CNO; 10 mg/kg (Li et al., 2013; Mahler et al., 2014; Penzo et al., 2015; Vazey and Aston-Jones, 2014)) prior to stress, there is a robust and significant decrease in stress-induced c-fos$^+$ LC-NE neurons indicating the selective hM4Di DREADD approach is effective at reducing LC-NE neuronal activity (**Figure 5.1F**) during stress exposure.

Next, we used the Cre-dependent, AAV-hM4Di DREADD approach to test whether inhibition of LC-NE neurons during restraint stress can prevent subsequent stress-induced anxiety in the OFT (**Figure 5.1G**). Stressed control animals that do not express the Cre-dependent hM4di (*Th*-$^{CreLC:hM4Di-}$) show a significant stress-induced anxiety-like behavior compared to unstressed animals regardless of Cre-dependent hM4Di expression (*Th*-Cre $^{LC:hM4Di-}$ and *Th*-Cre $^{LC:hM4Di+}$) seen in both time spent in the center and entries into the center of the OFT (**Figure 5.1H & I**). Stressed *Th*-Cre $^{LC:hM4Di+}$ animals, however, did not exhibit anxiety-like behavioral responses and instead have behavior similar to and not statistically different from both non-stressed *Th*-Cr $^{LC:hM4Di+}$ and *Th*-Cre $^{LC:hM4Di-}$ mice that did not experience the stressor (**Figure 5.1H & I**). Interestingly, hM4Di DREADD-mediated inhibition of LC-NE neurons prior to stress did not alter stress induced fecal output suggesting that the inhibition of LC-NE neurons suppresses acute stress-induced behavioral anxiety, but leaves other physiological responses intact (**Figure 5.1J**) (Bruchas et al., 2009; Konturek et al., 2011; Larauche et al., 2009).

Importantly, the hM4i DREADD manipulation has no effect on baseline anxiety levels (**Figure 5.1H, I, L)** and none of the manipulations affected gross locomotor activity in the OFT (**Figure 5.1K**). These findings suggest that stress-induced increases in LC-NE activity are required to produce an acute stress-induced anxiety state.
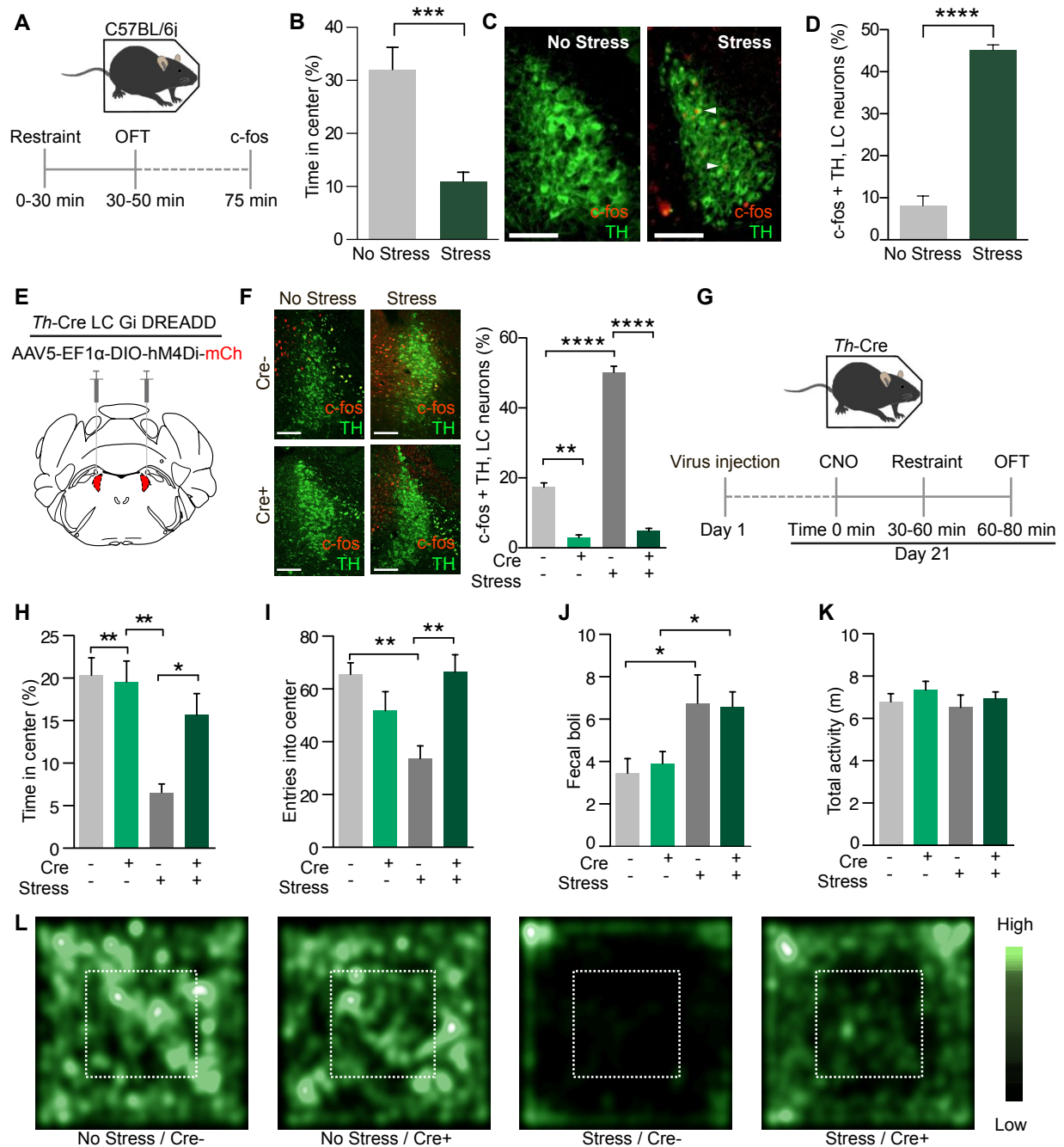
Figure 5.1 Selective inhibition of LC-NE neurons prevents stress-induced anxiety. (A) Cartoon of experimental paradigm for restraint stress-induced anxiety. **(B)** Stressed animals

207

spend significantly less time exploring the center of the OFT than non-stressed controls (Data represented as mean ± SEM, n=7-8/group: Student's t-test, p<0.001). **(C and D)** Representative immunohistochemistry and quantification show restraint stress increases c-fos immunoreactivity in LC neurons (Red=c-fos, green=tyrosine hydroxylase, arrows indicate example co-localization, scale bars= 100 μm; data represented as mean ± SEM, n=3 slices from 3 animals/group: Student's t-test, p<0.0001). See locomotor activity data in **Fig. S1. (E)** Cartoon depicting viral strategy. **(F and G)** Representative immunohistochemistry and quantification show hM4Di inhibition of LC neurons decreases c-fos immunoreactivity in LC neurons (Red=c-fos, green=tyrosine hydroxylase, Scale bars= 100 μm; data represented as mean ± SEM, n=3 slices from 3 animals/group: One-Way ANOVA, Bonferroni post-hoc, No stress/Cre$^-$ vs. No stress/Cre$^+$ **p<0.01, No stress/Cre$^-$ vs. Stress/Cre$^-$ ****p<0.0001, No stress/Cre$^-$ vs. Stress/Cre$^+$ ****p<0.0001, No stress/Cre$^+$ vs. Stress/Cre$^-$ ****p<0.0001, No stress/Cre$^+$ vs. Stress/Cre$^+$, not significant). **(G)** Cartoon of experimental paradigm for LC-NE inhibition during restraint stress-induced anxiety. **(H and I)** Inhibition of LC-NE neurons during stress blocks stress-induced anxiety. Data represented as mean ± SEM, n=8-13/group: One-Way ANOVA, Newman-Keuls post-hoc, No stress/Cre$^-$ vs. No stress/Cre$^+$, not significant, No stress/Cre$^-$ vs. Stress/Cre$^-$ **p<0.01, No stress/Cre$^-$ vs. Stress/Cre$^+$, not significant, No stress/Cre$^+$ vs. Stress/Cre$^-$ **p<0.01, No stress/Cre$^+$ vs. Stress/Cre$^+$, not significant). **(J)** Inhibition of LC-NE neurons has no effect on stress-induced bowel motility. Data represented as mean ± SEM, n= n=8-13/group: One-Way ANOVA, Newman-Keuls post-hoc, No stress/Cre$^-$ vs. No stress/Cre$^+$, not significant, No stress/Cre$^-$ vs. Stress/Cre$^-$ *p<0.05, No stress/Cre$^-$ vs. Stress/Cre$^+$ *p<0.05, No stress/Cre$^+$ vs. Stress/Cre$^-$, not significant, No stress/Cre$^+$ vs. Stress/Cre$^+$, not significant). **(K)** Inhibition of LC-

NE neurons has no effect on gross locomotor activity. Data represented as mean ± SEM. **(L)** Representative heat maps of activity during OFT.
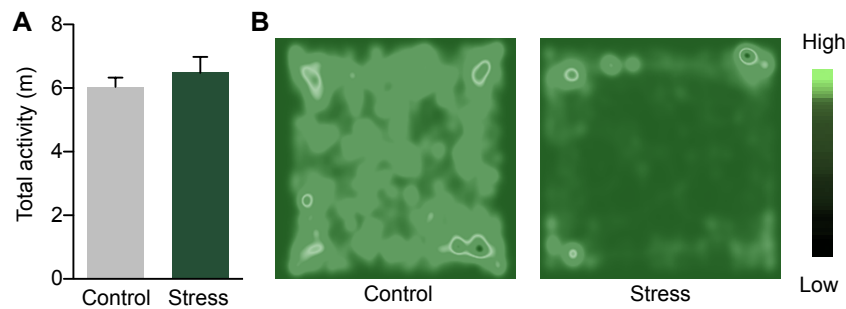
Figure 5.2 Restraint stress does not alter total locomotor activity in the OFT. Related data to Figure 5.1A-D (**A**) Restraint stress manipulation does not alter locomotor activity in the OFT. Data represented as mean ± SEM, n=7-8/group. (**B**) Representative heat maps of activity during OFT.

Optogenetic entrainment of high tonic LC-NE activity

LC-NE neurons are reported to respond vigorously to stress with a robust increase in tonic firing rate (Valentino and Van Bockstaele, 2008). While this physiological response has been observed by many groups in variety of species the precise behavioral output of such an increase has been previously inaccessible. We selectively targeted channelrhodopsin-2 (ChR2(H134)-eYFP) to LC-NE neurons of *Th*-Cre mice (*Th*-Cre[LC:ChR2)] and observed restricted eYFP labeling to the membranes of noradrenergic neurons of the LC (**Figure 5.3A-C**). Slice recordings show that this targeting is sufficient to generate an inward photocurrent and physiologically normal action potentials in response to 470 nm blue light (**Figure 5.3D & E).** To determine whether this optogenetic strategy could be used to exogenously elevate the tonic firing of LC-NE neurons in a sustained fashion, we performed slice physiology experiments which demonstrated that LC-NE neurons can fire photostimulated-action potentials at 5 Hz for as long as 30 minutes (**Figure 5.3F**). Furthermore, in *in vivo* extracellular recordings using a fiber optic-coupled multielectrode array (Sparta et al., 2011), we found that 5 Hz photostimulation produced responses similar to that evoked by stress (Bingham et al., 2011; Curtis et al., 2012) (**Figure 5.3G & H**). Interestingly, putative LC neurons that did not appear to be directly photosensitive (>10 ms spike latency) still show increased firing over time, perhaps due to well-known, tightly coupled nature of neurons in this structure (Alvarez et al., 2002; Ballantyne et al., 2004) (**Figure 5.3I**). Furthermore, indirect response of these neurons to photostimulation is highly correlated (r=0.89, p< 0.0001) to their baseline firing suggesting that some LC neurons are potentially more intrinsically excited by broader LC activity (**Figure 5.3J**). These findings indicate that optogenetic manipulation of LC-NE neurons can be used to sustain tonic firing of LC-NE that mimics their response to stress.
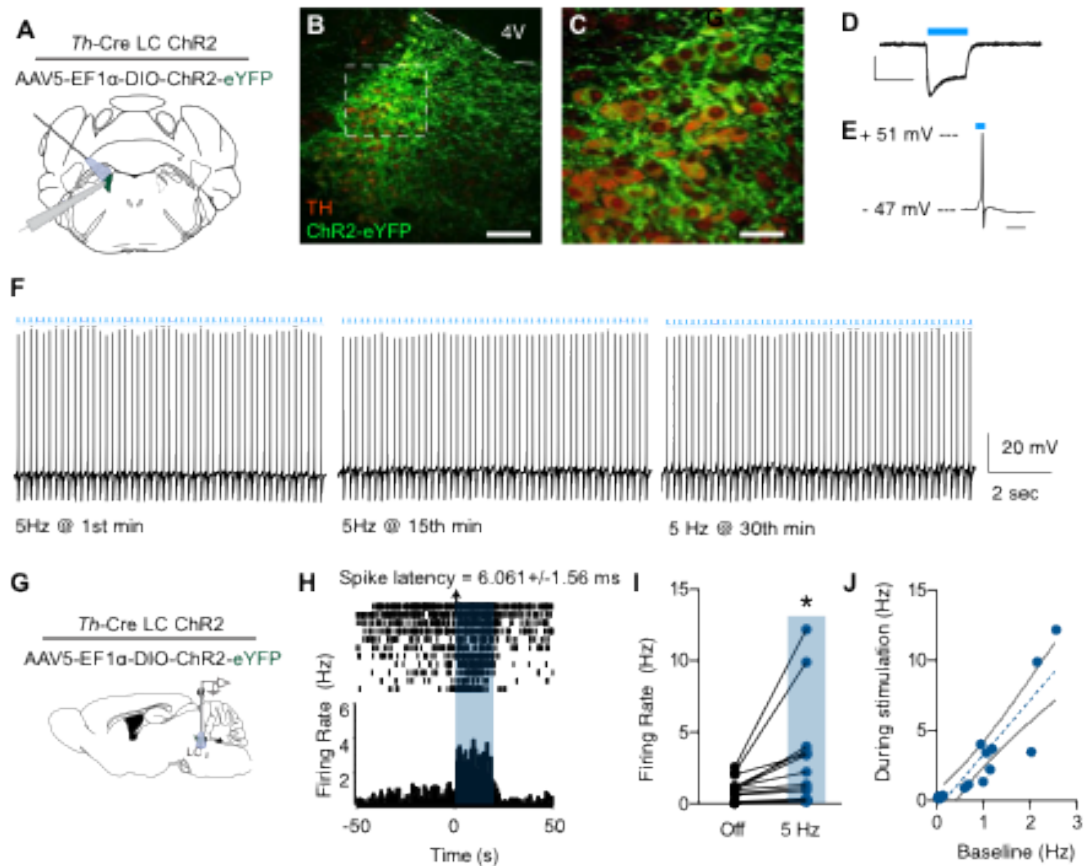
Figure 5.3 Optogenetic targeting to selectively increase tonic LC-NE activity. **(A)** Cartoon of viral strategy for slice experiments. **(B and C)** Representative immunohistochemistry show selective targeting of ChR2-eYFP to TH^{+} LC neurons (Red= tyrosine hydroxylase, green=ChR2-eYFP, 4V = 4th ventricle, Scale bars= 100 and 50 μm, respectively). **(D and E)** Whole cell current and voltage-clamp recordings of an LC-NE neuron expressing ChR2. D, scale bar is 200 pA x 100 ms and E, scale is 20 ms. **(F)** Slice recording of a single LC-NE neuron demonstrating action potentials over 30 min in response to 5 Hz 470 nm light pulses. **(G)** Cartoon of viral and multielectrode delivery for anesthetized, *in vivo* recordings. **(H)** Peristimulus time histogram (PSTH) showing increased LC neuron firing during a 20 s optical stimulation at 5 Hz. **(I)** Firing rate of n=16 cells before and during 5 Hz photostimulation (Paired Student's t-test, p<0.01). **(J)** Correlation of baseline activity to activity during photostimulation (r=0.8938, p<0.0001).

Increased LC-NE tonic neuronal firing is acutely anxiogenic

Using the same optogenetic strategy as above, we examined whether selectively increasing LC-NE tonic firing is sufficient to mimic acute stress-induced anxiety-like behaviors. We photostimulated (5 Hz, 10 ms pulse width, 473 nm) LC-NE neurons during two well-established assays of anxiety-like behavior, OFT and elevated zero maze (EZM) (Choleris et al., 2001; Shepherd et al., 1994) (**Figure 5.4A & B**). In the OFT, photostimulated Th-Cre$^{LC:ChR2}$ mice spent significantly less time exploring the center of the arena than did fluorophore expressing controls (Th-Cre$^{LC:eYFP}$) (**Figure 5.4C & D, Figure 5.5A & B**). Importantly, 5 Hz photostimulation does not affect total locomotor activity (**Figure 5.4E, Figure 5.5C**), suggesting 5Hz LC-NE tonic activity selectively drives anxiety-like behavior. Furthermore, 5 Hz photostimulation in the EZM also induced anxiety-like behavior in Th-Cre$^{LC:ChR2}$ animals compared to Th-Cre$^{LC:eYFP}$ controls. In the EZM, Th-Cre$^{LC:ChR2}$ spent less time in and entered the exposed areas of the EZM significantly less than Th-Cre$^{LC-eYFP}$ controls (**Figure 5.4F-H**). These experiments demonstrate that increasing the tonic firing rate of LC-NE neurons in the absence of a physical stressor is sufficient to produce robust anxiety-like behavior.
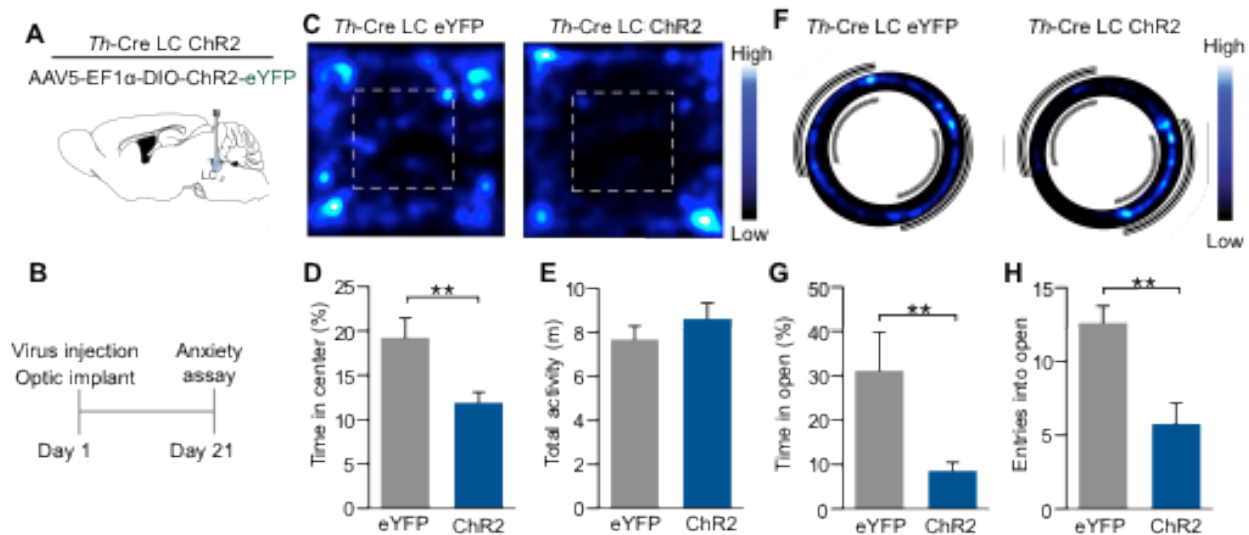
Figure 5.4 High tonic LC-NE neuronal activity is sufficient to induce anxiety-like behavior.

(A) Cartoon of viral and fiber optic delivery strategy. **(B)** Calendar of behavioral studies. **(C)** Representative heat maps of activity in the OFT. **(D)** 5 Hz photostimulation causes an anxiety-like phenotype in OFT of *Th*-Cre$^{LC:ChR2}$ animals compared to *Th*-Cre$^{LC:eYFP}$ controls (Data represented as mean ± SEM, n=10/group: Student's t-test, $p<0.01$) with **(E)** no change in locomotor activity (Data represented as mean ± SEM, n=10/group). See also **Fig. S2. (F)** Representative heat maps of activity in the EZM. **(G and H)** 5 Hz photostimulation causes an anxiety-like phenotype in EZM of *Th*-Cre$^{LC:ChR2}$ animals compared to *Th*-Cre$^{LC:eYFP}$ controls (Data represented as mean ± SEM, n=6-9/group; Student's t-test, $p<0.01$).
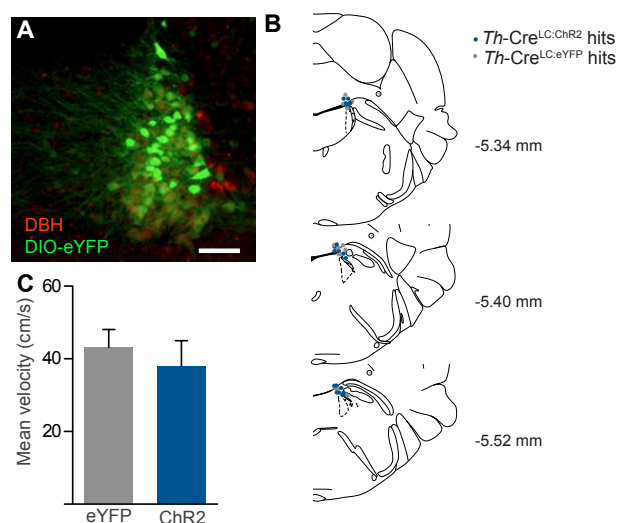
Figure 5.5 High tonic LC--NE neuronal activity is sufficient to induce anxiety-like behavior. Related data to Figure 5.4. **(A)** Representative immunohistochemistry shows selective targeting of AAV5-DIO-eYFP to DBH+ LC neurons of Th--CreLC:eYFP controls (Red= dopamine beta hydroxylase, green=DIO--eYFP, scale bars= 100 μm. **(B)** Fiber optic tip placements for the OFT and EZM experiments. Animals were excluded if the tip ended >1 mm dorsal of the LC or any caused significant lesion to the LC or 4th ventricle. For clarity, only hits of included mice for this experiment are shown. **(C)** There is also no change in mean velocity during the photostimulation in the OFT. Data represented as mean ± SEM, n=10/group.

LC-NE tonic activity drives a frequency-dependent aversion

Following the observation that increased tonic activity of LC-NE neurons alone is capable of driving anxiety-like behaviors; we next sought to determine whether this activity produced place aversion in the animals. First we performed slice electrophysiology experiments that demonstrated dynamic control of LC-NE firing at increasing frequencies while maintaining spike fidelity (**Figure 5.6A**). We next sought to determine acute behavioral valence in *Th*-Cre$^{LC:ChR2}$ and *Th*-Cre$^{LC:eYFP}$ mice at a range of photostimulation frequencies. To assess the positive or negative valence of the photostimulation we employed a real-time place-testing (RTPT) assay that triggers photostimulation upon the animal's entry into a chamber void of salient contextual stimuli (**Figure 5.6B**). This assay assesses native behavioral preference to photostimulation; regimes with a negative valence will cause an aversion from and those with a positive valence will drive a preference for the chamber paired with photostimulation (see Chapter 4) (Jennings et al., 2013; Kim et al., 2013a; Stamatakis and Stuber, 2012; Stamatakis et al., 2013; Tan et al., 2012). Without photostimulation and at low tonic firing rates similar to alert, awake LC activity (1 and 2 Hz) (Aston-Jones and Bloom, 1981a; Bloom, 1981; Carter et al., 2010, 2012) there was no observable shift in chamber preference compared to baseline or *Th*-Cre$^{LC:eYFP}$ control animals (**Figure 5.6C**). However, when we increased the frequency of photostimulation to induce a higher tonic firing rate of LC-NE neurons (5 and 10 Hz), we observed a significant frequency-dependent shift away from the photostimulation-paired chamber (**Figure 5.6C**). These data suggest that acutely increasing tonic firing of LC-NE neurons elicits a negative valence that is capable of biasing behavior to avoid the increased neuronal activity. Again, as we found in the anxiety-like behavioral assays, there was no change in gross locomotor activity during any of the frequencies tested (**Figure 5.6D & E, Figure 5.7A**

& B). To determine whether this negative valence was specifically due to increased tonic activity, we implemented the same RTPT assay using two different phasic photostimulation regimes (3 or 10 (10 ms) pulses at 10 Hz upon entry and every 30 s the mouse remains in the chamber). In the phasic photostimulation paradigm, we did not observe any negative or positive valence associated with phasic burst activity (**Figure 5.6F, Figure 5.7C & D**) in either regime. This finding is in line with the evidence that suggests phasic responses of LC-NE neurons are elicited by salient stimuli rather than stressful events (Aston-Jones and Bloom, 1981b; Bouret et al., 2012; Sara and Bouret, 2012).

While the RTPT assay provides clear evidence that increased tonic, but not phasic, activity of LC-NE neurons is acutely aversive, it does not provide information as to whether this activity is encoded and can be later retrieved to inform future behavior. A natural response to a stressful experience would be to avoid the context in which the stress occurred (Knoll and Carlezon, 2010; Ungless et al., 2010). To test whether increased tonic activity of LC neurons produces a learned change in behavior, we employed a Pavlovian conditioned place aversion (CPA) assay (Bruchas et al., 2009; Al-Hasani et al., 2013; Land et al., 2008, 2009). In this assay, *Th*-Cre$^{LC:ChR2}$ and *Th*-Cre$^{LC:eYFP}$ animals are exposed to two distinct visual contexts that have no initial bias. During two conditioning days, animals do not receive any optical stimulation in one context and receive high tonic stimulation (5 Hz, 10 ms pulse widths) in the other context (**Figure 5.6G**). When allowed to freely explore both chambers following conditioning, the *Th*-Cre$^{LC:ChR2}$ animals spent significantly less time in the chamber that was paired with high tonic photostimulation (**Figure 5.6H**). In contrast, *Th*-Cre$^{LC:eYFP}$ controls did not show a change in
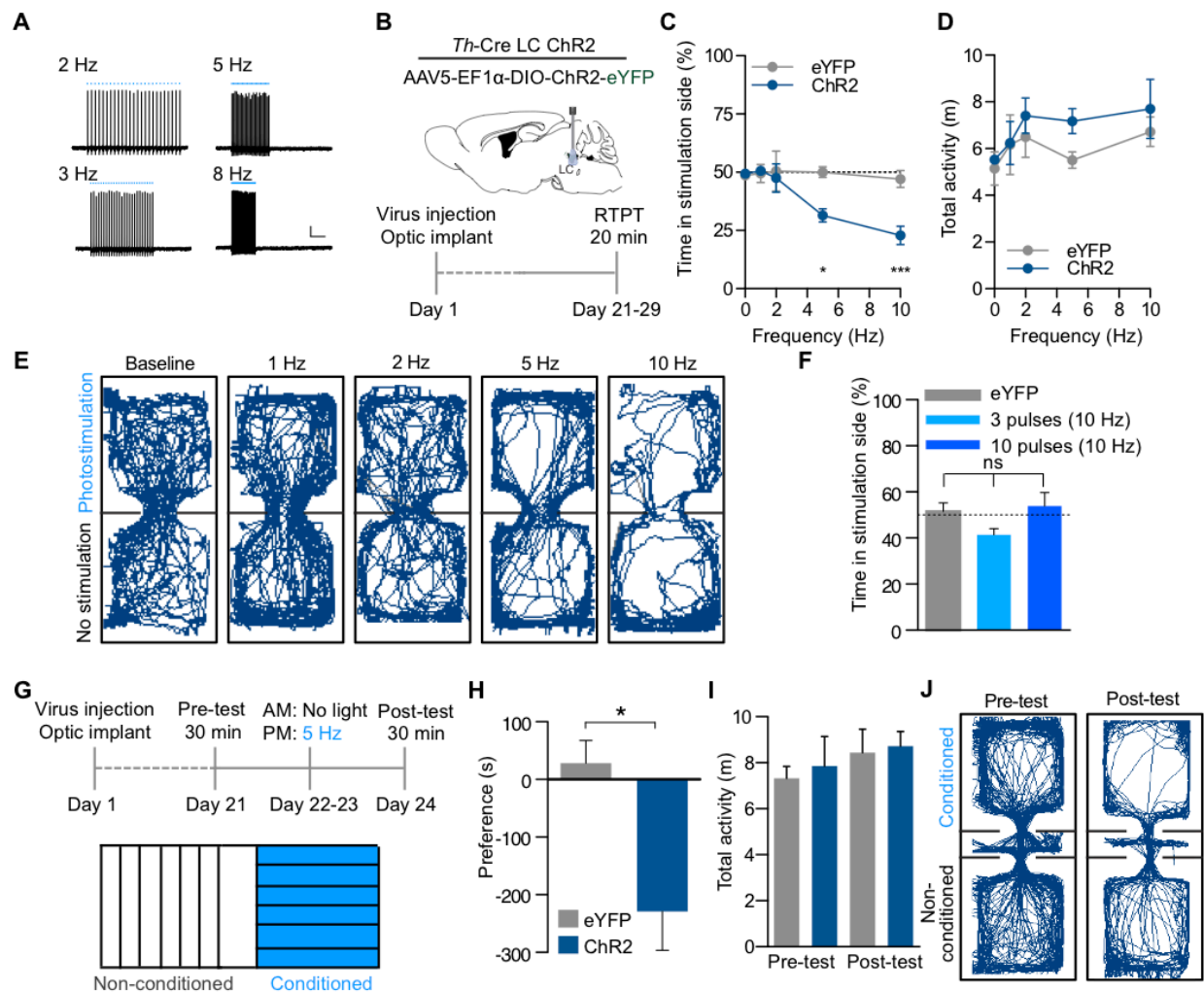
Figure 5.6 LC-NE photostimulation drives both real-time and learned aversions. (A) Current clamp whole cell recording with spike fidelity at 2, 3, 5 and 8 Hz. **(B)** Cartoon of viral and fiber optic delivery strategy and calendar of behavioral studies. **(C)** Frequency response of RTPT and **(D)** locomotor activity at 0, 1, 2, 5, and 10 Hz. Data represented as mean ± SEM, n=6-7/group: Two-Way ANOVA, Bonferroni post-hoc, 5 Hz ChR2 vs. 5 Hz eYFP *p<0.05, 10 Hz ChR2 vs. 10 Hz eYFP ***p<0.001. **(E)** Representative traces of behavior at different frequencies. **(F)** Phasic stimulation does not drive aversion, n=6/group. **(G)** Time line and cartoon of 5 Hz CPA experiment. **(H)** Mean preference (s) ± SEM, post-test minus pre-test (n=7-9; Student's t-test, p<0.05). **(I)** No locomotor effect in either pre- or post-test. **(J)** Representative traces of behavior in the pre- and post-test. See also **Figure 5.7.**

Figure 5.7 LC-NE pho... ...th real-time and learned aversions. Related da... ...e 5.6 (**A**) Representative traces of behavior at different frequen- cies for the *Th*-CreLC:eYFP animals. (**B**) Fiber optic tip placements for the RTPT frequency-response experiment. Animals were excluded if the tip ended >1 mm dorsal of the LC or any caused significant lesion to the LC or 4th ventricle. For clarity, only hits of included mice for this experiment are shown. (**C**) Phasic stimulation does not significantly alter locomotor activity, n=6/group. (**D**) Representative traces of behavior for the phasic regimes. (**E**) Representative traces of of *Th*-CreLC:eYFP behavior for the CPA assay in the pre- and post-test.

behavior from their initial exploration and neither group showed altered locomotor activity (**Figure 5.6I & J, Figure 5.7E**). These results suggest that the negative valence and anxiety-like behaviors previously observed during high tonic photostimulation of LC-NE neurons are capable of being learned and influencing future behavior; and suggest that, the high tonic state of LC-NE firing can inform behavior to avoid repeated exposure to conditions associated with stress-like conditions.

Photostimulation of galanin-containing LC-NE neurons is also sufficient to elicit aversion

In addition to the catalytic enzymes necessary for catecholamine production, a majority of LC-NE neurons are also known to produce the neuropeptide galanin and galanin immunoreactivity is widely used as an LC neuronal marker (Holets et al., 1988; Le Maître et al., 2013; Melander et al., 1986). Therefore, to further corroborate the results we observed using *Th*-Cre mice, we also used mice expressing Cre recombinase under the promoter for Galanin (*Gal*-Cre) (Gong et al., 2003, 2007; Wu et al., 2014). To validate and confirm loci of Galanin expression we first crossed these mice to a Cre-conditional tdTomato reporter line developed by the Allen Institute for Brain Science (Ai9) (Madisen et al., 2010). As predicted, we see dense, localized expression in the LC as well as the hypothalamus and brainstem (**Figure 5.7A & B**). We also observed some tdTomato$^+$ cells in regions that do not have mRNA for galanin in the adult mouse (cortex, hippocampus, thalamus, and amygdalar structures) (Lein et al., 2007). In each of these regions we identify transient mRNA expression throughout development (**Figure 5.9**) which would be sufficient to cause the recombination event needed to chronically express the reporter. However, this Cre driver remains a viable tool for selective targeting of the LC (**Figure 5.7C**), as seen when we selectively targeted ChR2(H134)-eYFP to LC-NE neurons of *Gal*-Cre mice (*Gal*-Cre$^{LC:ChR2}$) there was restricted eYFP labeling to the membranes of

noradrenergic neurons of the LC (**Figure 5.7D, Figure 5.10**). We found that eFYP expression was selective for LC-NE neurons (100% of eYFP expressing LC neurons were positive for the NE marker, dopamine beta hydroxylase (DBH^+)). However, we found that only 61.48% of LC-NE neurons expressed ChR2(H134)-eYFP in this model – significantly fewer than those targeted using the *Th*-Cre line (**Figure 5.7E, Figure 5.10**). To test whether tonic photostimulation of this subpopulation of galanin-containing, LC-NE neurons also produces aversion, the *Gal*-Cre$^{LC:ChR2}$ animals were tested in RTPT with and without photostimulation at 5 Hz. In these experiments, we found that increased tonic LC-NE stimulation in *Gal*-Cre$^{LC:ChR2}$ animals produced significant avoidance behavior, consistent with the behavior we observed under the same conditions in the *Th*-Cre$^{LC-ChR2}$ mice (**Figure 5.7F & G**). Using multiple, distinct *in vivo* LC-NE targeting strategies, these experiments further corroborate our findings that high tonic stimulation of LC-NE neurons drives an aversive behavioral response and further suggest that increased activity of the entire population of LC neurons may not be necessary to elicit aversive behavior.

CRH$^+$ neurons from the central amygdala send dense projections to the LC

Following multiple observations that exogenously increasing tonic firing of LC-NE neurons is sufficient to drive anxiety-like and aversion behaviors in the absence of stress, we sought to determine the endogenous substrate for such a change in firing. Previously, CRH has been suggested as a potential mechanism for stress-induced increases in LC activity (Curtis et al., 1997, 2001, 2012; Jedema and Grace, 2004; Page and Abercrombie, 1999; Reyes et al., 2008; Snyder et al., 2012; Valentino and Foote, 1988). Consistent with these studies, we found that systemic antagonism (Antalarmin HCl, 10 mg/kg, i.p.) of endogenous CRH action on CRHR1 receptors is sufficient to prevent stress-induced anxiety (**Figure 5.11A-D**) (Gafford et al., 2012; Heinrichs et al., 1994). We next sought to determine whether the action of CRH locally within
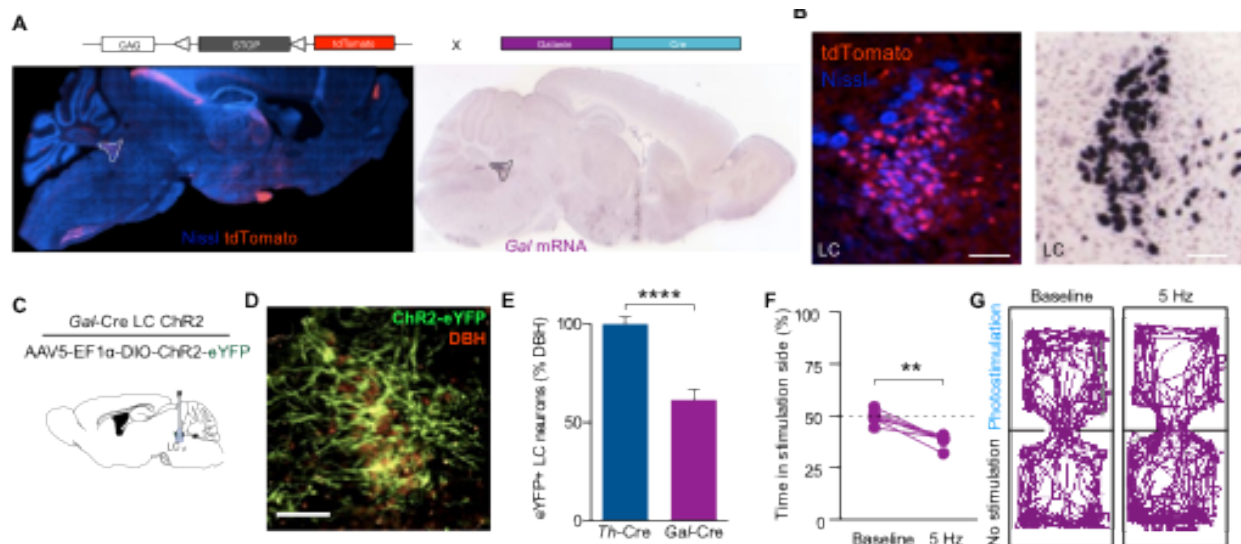
Figure 5.8 Galanin containing LC-NE neurons are sufficient to drive place aversion. (A and B) Galanin labeling in *Gal*-Cre x Ai9-tdTomato compared to *in situ* images from the Allen Institute for Brain Science in a sagittal section highlighting presence of galanin in the LC. All images show tdTomato (red) and Nissl (blue) staining. See also **Figure 5.9. (C)** Cartoon of viral and fiber optic delivery strategy for Gal-Cre experiment. **(D)** Image of ChR2-eYFP targeting to DBH$^+$ LC neurons. Scale bar=100 μm. **(E)** Quantification of Cre-dependent eYFP viral expression in the LC of *Th*-Cre and *Gal*-Cre mouse lines. Data represented as mean ± SEM, n=3 slices from 3 animals/group: Student's t-test, p<0.0001. See also **Figure 5.10. (F)** 5 Hz stimulation ofLC-Gal neurons drives aversion (n=6, Paired Student's t-test, p<0.01). **(G)** Representative traces of behavior at different frequencies.
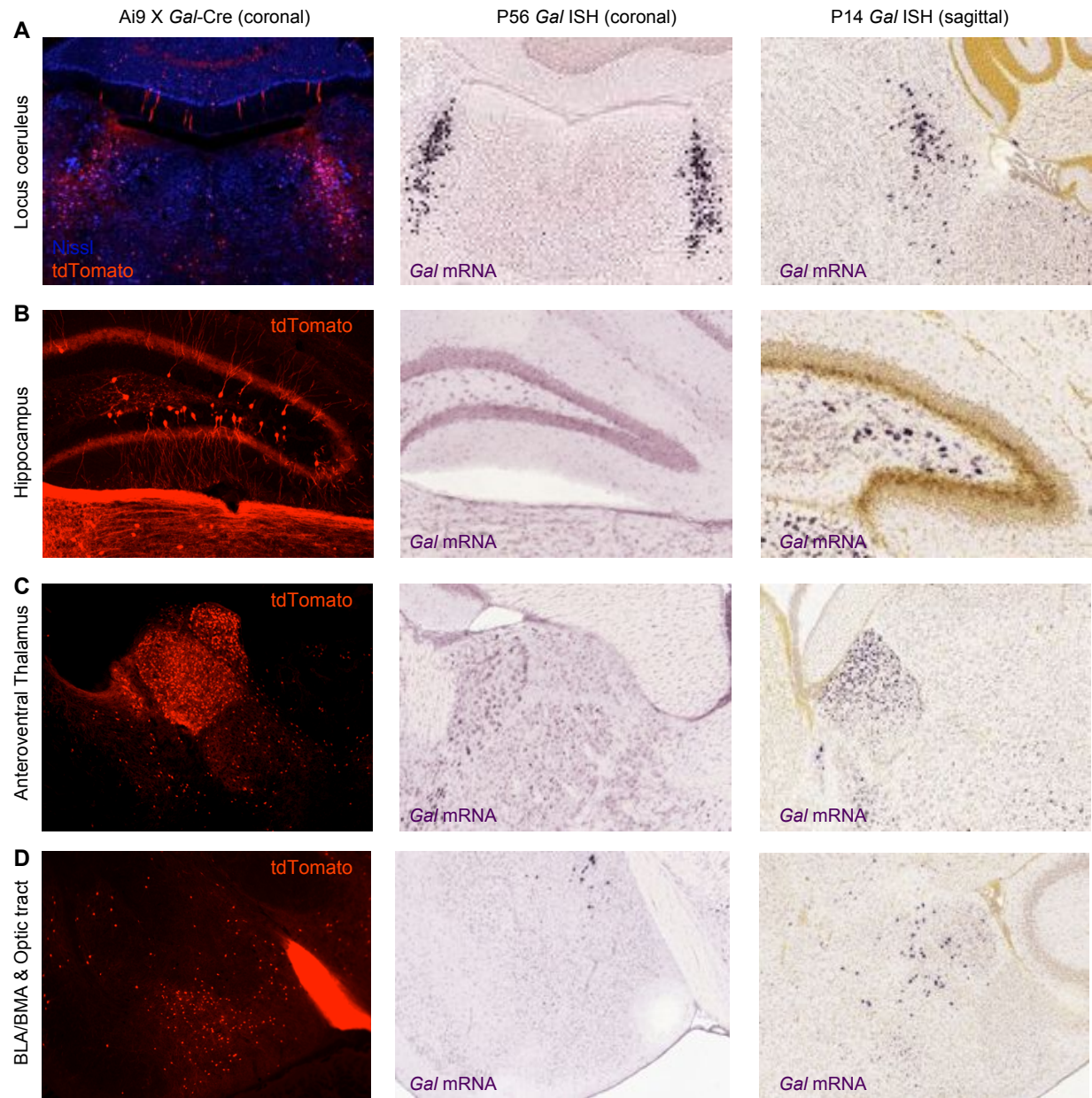
Figure 5.9 Cre-dependent tdTomato expression in adult Ai9 X *Gal*-Cre mice. Related data to Figure 5.8A & B. (**A**) Images show Cre-dependent reporter expression in adultAi9 X Gal-Cre mice (left panel), in situ hybridization for Gal in adult WT mice from the Allen Institute (middle panel), and in situ hybridization for Gal in P14 WT mice from the Allen Institute (right panel) for the (**A**) locus coeruleus, (**B**) hippocampus, (**C**) anteroventral thalamus, and (**D**) basolateral and basomedial amygdala. We did observe

any regions that contain Cre-dependent reporter expression that were not positive for Gal mRNA at some stage in development or in the adult animal.
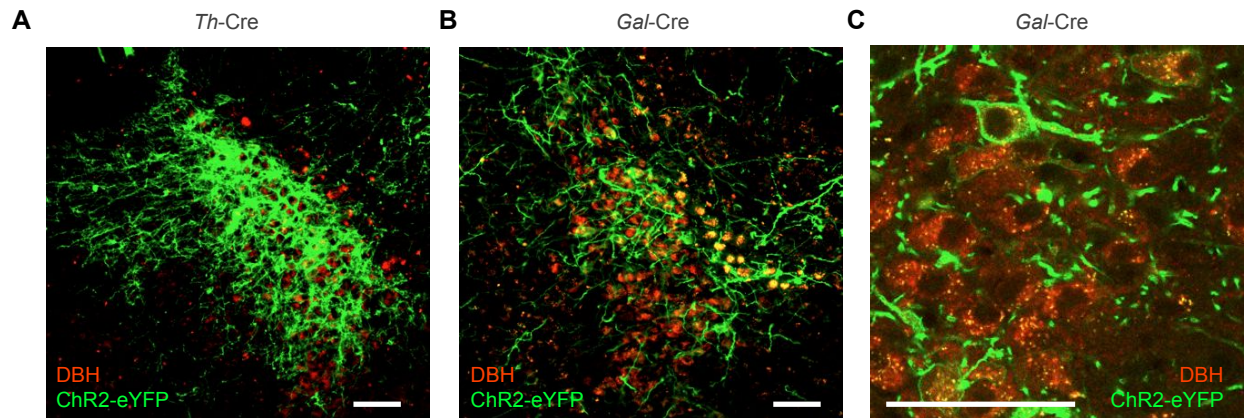
Figure 5.10 *Gal*-Cre mice can be used to effectively target a subset of LC neurons. Related data to Figure 5.8D & E. (**A**) Representative immunohstochemistry show selective targeting of ChR2--eYFP to DBH$^+$ LC neurons in *Th*-Cre mice (Red= tyrosine hydroxylase, green = ChR2-eYFP, Scale bar = 100 μm). (**B**) Representative immunohistochemistry show selective targeting of ChR2--eYFP to a subset of DBH+ LC neurons in *Gal*-Cre mice (Red= tyrosine hydroxylase, green = ChR2-eYFP, Scale bar = 100 μm). (**C**) High--power confocal micrograph depicting ChR2--eYFP membrane labeling in *Ga*l-*Cre* DBH$^+$ neurons.

the LC is responsible for CRH-dependent anxiety-like behavior. To do so, we utilized two retrograde tracing approaches to examine the potential sources of CRH input into the LC. First, we injected the tracer Fluorogold into the LC of wild-type mice (**Figure 5.11E**). Consistent with previous studies, this non-selective retrograde tracing approach revealed known inputs into the LC from the cortex, hypothalamus, and central amygdala - a known input and source of extrahypothalamic CRH (Bouret et al., 2003; Dimitrov et al., 2013; Reyes et al., 2008, 2011) (**Figure 5.11F, Figure 5.12**). We next used a dual injection strategy to anatomically isolate LC-projecting, CRH$^+$ neurons. To do so, we used mice expressing Cre under the promoter for CRH (*Crh*-Cre) mice (Taniguchi et al., 2011). We simultaneously injected a red-labeled retrograde tracer, Cholera Toxin Subunit B (CTB-594) (Conte et al., 2009), to the LC and the green-labeled AAV5-DIO-Ef1α-ChR2(H134)-eYFP to the CeA of these mice (*Crh*-Cre$^{CeA:ChR2}$; **Figure 5.11G**). From this approach we visualized *Crh*$^+$ neurons in the CeA project to the LC by observing significant colocalization of both fluorophores in single CeA neurons, indicating that these neurons project to the LC (**Figure 5.11H & I**). Finally, to examine CRH$^+$ terminal innervation of the LC, we only injected the Cre-dependent reporter AAV5-DIO-Ef1α-eYFP in the CeA of *Crh*-Cre mice (**Figure 5.11J**). We clearly observed projections from the CeA to the LC in both transverse and coronal sections (**Figure 5.11K-M**). These anatomical studies identify a discrete projection of *Crh*$^+$ neurons from the CeA to the LC that could act to provide the hypothesized CRH-induced increase in tonic LC activity.
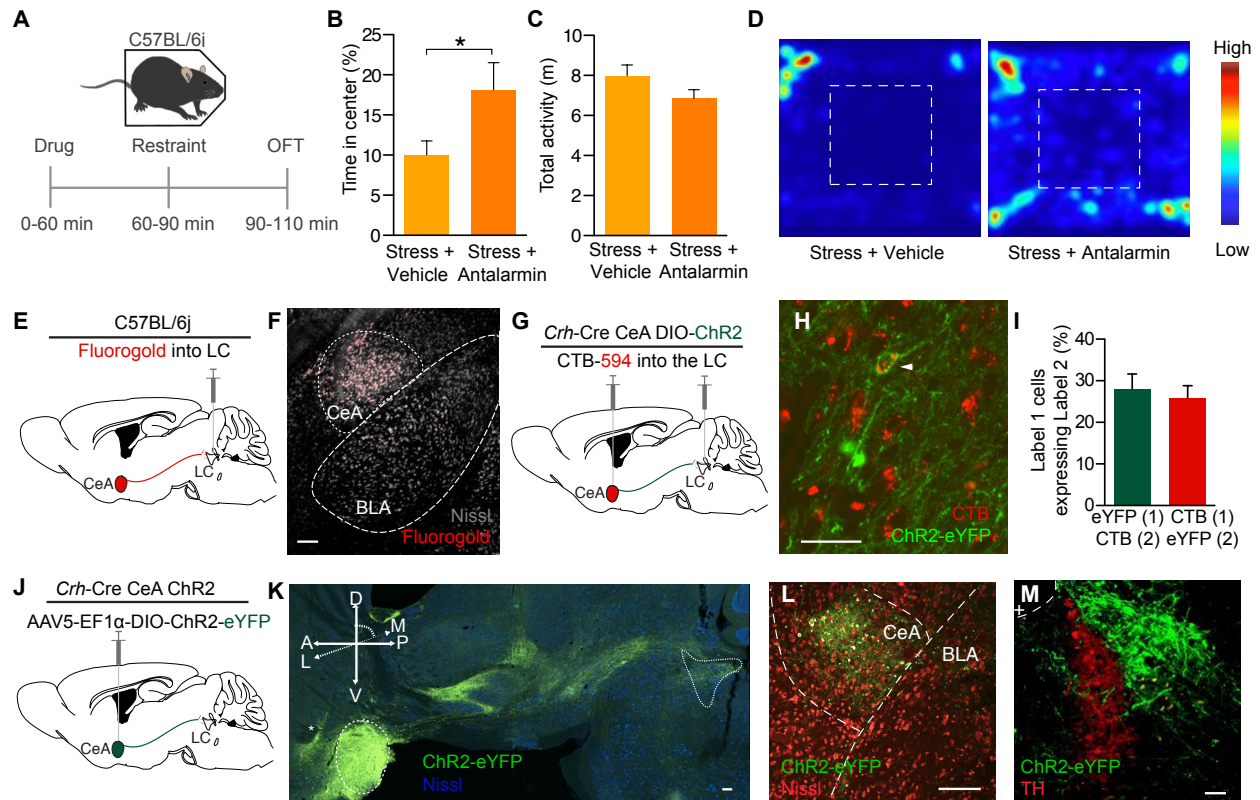
Figure 5.11 Identifying a CRH$^+$ CeA input to the LC. (A) Calendar of pharmacological experiment. **(B)** CRF-R1 antagonism blocks stress-induced anxiety-like behavior **(C)** with no significant effect on locomotor activity (n=6-8/group, Student's t-test, *p<0.05). **(D)** Representative heat maps show behavior in the OFT, hotter colors indicate more time spent in a position. **(E)** Cartoon depicting fluorgold tracing strategy. **(F)** Representative image shows robust retrograde labeling of the CeA (Fluorgold pseudocolored red, Nissl=grey). See also F **Figure 5.12 (G)** Cartoon depicting dual injection tracing strategy for CTB-594 and DIO-ChR2-eYFP. **(H)** Representative image shows retrograde labeling in CeA of CTB-594 (red) and anterograde labeling of CRH$^+$ cells (green). Arrow indicates example co-localization. **(I)** ~25% of each label co-labels with the other. **(J)** Cartoon depicting anterograde tracing strategy. **(K)** 71º off of sagittal, transverse slice of *Crh*-Cre mouse expressing DIO-eYFP in the CeA. Image shows intact projections from CeA to LC. Arrow indicates fiber optic placement. **(L and M)**

224

Coronal images depict robust eYFP labeling in the CeA and LC of the same mouse. All scale bars are 100 μm. + is in 4th ventricle.
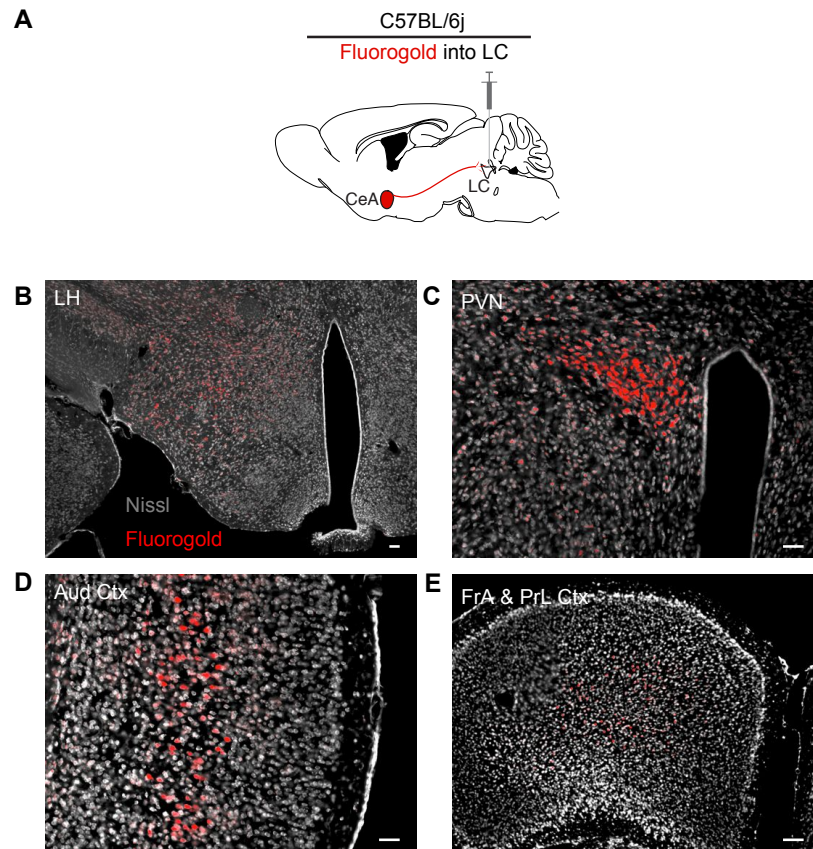
Figure 5.12 Retrograde fluorogold labeling in various forebrain regions. Related data to **Figure 5.11 E & F.** (**A**) Cartoon depicting fluorgold tracing strategy. Representative images shows retrograde labeling throughout in the (**B**) lateral hypothalamus (LH), (**C**) paraventricular nucleus of the hypothalamus (PVN), (**D**) auditory cortex (Aud Ctx), and (**E**) frontal association (FrA) and prelimbic cortex (PrL Ctx) paraventricular nucleus of the hypothalamus. In all images, fluorogold is psuedocolored red and Nissl is in grey. All scale bars are 100 μm.

Photoactivation of CRH[+] terminals in the LC causes increased tonic firing of LC neurons

After identifying the CRH$^+$ projection from the CeA to the LC, we sought to determine the effects of stimulating these terminals locally within the LC. In *Crh*-Cre$^{CeA-LC:ChR2}$ mice, we implanted multi-electrode arrays coupled to fiber optics into the LC and recorded LC activity before, during, and after photostimulation (**Figure 5.13A**). The CeA has been reported to spontaneously fire from 2-20 Hz (Ciocchi et al., 2010; Veinante and Freund-Mercier, 1998), so we used a 10 Hz photostimulation paradigm to maintain a physiologically-relevant frequency at the terminals. In recordings of 35 putative LC neurons from 5 different animals, we found a heterogeneous population of responses including increased firing in a significant proportion of cells (42.8% of observed putative LC units) (**Figure 5.13B-F, Figure 5.14A**). While the overall sample of neurons significantly increased firing (**Figure 5.13E & F**), we did observe a subset that decreased firing rate during photostimulation (**Figure 5.13H**). In cases where the firing rate increased the mean latency to increase was 344.6 ms, suggesting a neuromodulatory influence of the photostimulation (**Figure 5.13F & G**). Likewise, in cases where the firing rate decreased the mean latency to decrease was 360.0 ms (**Figure 5.13H & I**). Similarly to what we observed with direct LC-NE photostimulation (**Figure 5.3J**), we also observed that the increasing firing rates to *Crh*-Cre$^{CeA-LC:ChR2}$ photostimulation, are correlated (r=.70, p< 0.0001) to the baseline state of each neuron, again indicating that some LC neurons are innately more excitable by this projection than others. (**Figure 5.13J**). Importantly, the observed increase in firing following this selective photostimulation approach is consistent with other reports following either stress or exogenous application of CRH (Curtis et al., 1997; Jedema and Grace, 2004; Page and Abercrombie, 1999).

Stimulation of CRH$^+$ CeA terminals in the LC is aversive and anxiogenic

After identifying the CeA terminals to the LC as a projecting source of CRH$^+$ LC inputs, which are capable of increasing tonic activity, we next sought to test whether stimulation of these terminals would drive similar behavioral profiles to direct LC-NE stimulation or stress alone. In these experiments we used *Crh*-Cre$^{CeA-LC:ChR2}$ and *Crh*-Cre$^{CeA-LC:eYFP}$ animals with fiber optic implants over the LC (**Figure 5.13K**). Using the same stimulation procedure we used during *in vivo* recordings (10 Hz, 10 ms pulse width), we first observed that in the CPA assay (**Figure 5.13K**) photostimulation of CeA-LC CRH$^+$ terminals conditions a place aversion in *Crh*-Cre$^{CeA-LC:ChR2}$ compared to *Crh*-Cre$^{CeA-LC:eYFP}$ controls (**Figure 5.13L & M**). We next determined whether this stimulation was sufficient to induce anxiety-like behaviors in the EZM (**Figure 5.13N**). In *Crh*-Cre$^{CeA-LC:ChR2}$ animals, acute photostimulation produced significant anxiety-like behavior compared to *Crh*-Cre$^{CeA-LC:eYFP}$ controls (**Figure 5.13O, Figure 5.14B & C**). This anxiety-like behavior is similar to both direct LC-NE stimulation (**Figure 5.3**) or stress (**Figure 5.1A-D and Figure 5.11A-D**). Importantly, when we locally antagonize CRHR1 directly into the LC prior to photostimatulation (α-helical CRF 1 µg, intra-LC) this effect is completely reversed, suggesting that CRH release from CeA-LC terminals is the substrate responsible for the photostimulation-induced anxiety-like behavior (**Figure 5.13O, Figure 5.14B & C**). Furthermore, systemic antagonism of CRHR1 (Antalarmin HCl, 10 mg/kg, i.p.) prior to photostimulation of *Crh*-Cre$^{CeA-LC:ChR2}$ animals also prevents the induced anxiety-like behavior (**Figure 5.13P**). Taken together, these results suggest that the CRH$^+$ projection from the CeA to the LC carries both an aversive and anxiogenic component mediated through CRH$^+$ activation of CRHR1 in the LC. This is the first functional identification that CeA CRH projections to the LC can induce the negative affective behaviors associated with stress.

A *Crh*-Cre CeA ChR2
AAV5-EF1α-DIO-ChR2-eYFP

B Optically-responsive LC neuron

C Non-responsive LC neuron

D

E | **F** | **G** | **H** | **I** | **J**

K *Crh*-Cre CeA ChR2
AAV5-EF1α-DIO-ChR2-eYFP

Virus injection
Optic implant

Pre-test
30 min

AM: No light
PM: 5 Hz

Post-test
30 min

Day 1   Day 42   Day 43-44   Day 45

Non-conditioned   Conditioned

L Pre-test   Post-test

Conditioned

Non-conditioned

M

N *Crf*-Cre CeA ChR2
AAV5-EF1α-DIO-ChR2-eYFP

Virus injection

Optic & cannula
implantation

Drug   EZM

Day 1   Day 35   Time 0 min 60-67 min

Day 42

O

P

Q

CNO   473 nm   473 nm   CRHR1 antagonist

LC   LC   LC   CeA

hM4Di   ChR2   CRH   CRH+
TH+   TH+   CRH   ChR2
DBH+
Gal+

↓ stress-induced anxiety   ↑ anxiety aversion   ↑ anxiety aversion

228

Figure 5.13 CRH$^+$ CeA-LC terminals increase LC activity and drive anxiety through CRFR1 activation. (A) Cartoon of viral and multi-electrode array delivery for anesthetized, *in vivo* recordings. **(B and C)** Representative PSTHs of putative LC neurons responding to 20s of 10 Hz, 10 ms pulse width photostimulation (473 nm, ~10 mW). **(D)** Representative principal component analysis plot showing the first two principal components with clear clustering of units. **(E)** Total recorded sample shows significant increase in firing rate to 10 Hz photostimulation (n=35, Paired Student's t-test, p<0.01). **(F)** n=15 units increase firing rate by >10% during 10 Hz photostimulation (Paired Student's t-test, p<0.01). **(G)** Response latency following onset of photostimulation for cells that increase firing. **(H)** n=15 units decrease firing rate by >10% during 10 Hz photostimulation (Paired Student's t-test, p<0.01). See also **Fig. S7A**. **(I)** Response latency following onset of photostimulation for cells that increase firing. **(J)** Correlation of baseline activity to activity during photostimulation (r=0.7029, p<0.0001). **(K)** Cartoon of viral and fiber optic delivery strategy and calendar of CPA behavior. **(L and M)** *Crh*-Cre$^{CeA-LC:ChR2}$ show a significant CPA compared to *Crh*-Cre$^{CeA-LC:eYFP}$ controls. Representative traces of behavior in the pre- and post-test and mean preference (s) ± SEM, post-test minus pre-test (n=10-12/group; Student's t-test, p<0.05). **(N)** Cartoon of viral, cannula, and fiber optic delivery strategy and calendar of EZM behavior. **(O)** 10 Hz photostimulation causes an anxiety-like phenotype in EZM of *Crh*-Cre$^{CeA-LC:ChR2}$ animals compared to *Crh*-Cre$^{CeA-LC:eYFP}$ controls, which is reversed by intra-LC α-helical-CRF (αHCRF) pretreatment (Data represented as mean ± SEM, n=7/group: One-Way ANOVA, Newman-Keuls, *Crh*-Cre$^{CeA-LC:eYFP}$ vs. *Crh*-Cre$^{CeA-LC:ChR2}$ *p<0.05, Cre$^{CeA-LC:eYFP}$ vs. *Crh*-Cre$^{CeA-LC:ChR2+AHCRF}$ **p<0.01, Cre$^{CeA-LC:ChR2}$ vs. *Crh*-Cre$^{CeA-LC:ChR2+AHCRF}$ ***p<0.001). See also **Fig. S7B&C**. **(P)** Systemic CRHR1 antagonism

reverses photostimulation-induced anxiety-like behavior (n=6-8/group, Student's t-test, p<0.001). **(Q)** Model and summary of results. See also **Fig. S7D**.

Figure 5.14 CRH^{+} CeA-LC terminals increase LC activity and drive anxiety through CRFR1 activation. Related data to Figure 5.13. (A) n=5 units that did not increase or decrease firing by >10% during 10 Hz photostimulation. (B) Representative heat maps of activity in the EZM. (C) Cannula and fiber optic placements for the EZM experiments with *Crh*-Cre^{CeA-LC} animals. Animals were excluded if the fiber tip ended >1 mm dorsal of the LC or caused significant lesion to the LC or 4th ventricle. Additionally, cannulated mice were excluded if the final injection placement appeared to be >0.5mm from the LC. (D) Hypothetical model of downstream LC-NE influence on anxiety-like behaviors. Anterograde tracing of eYFP^{+} fibers from Th-Cre$^{LC-eYFP}$ mice reveals dense innervation in the CeA, BLA, and LS (red=Nissl, green – DIO-eYFP, scale bars =100 μm).

DISCUSSION

The LC-NE system has long been implicated as a key mediator of the central stress response (Koob, 1999). Observational electrophysiological studies across many species have identified that LC-NE neurons respond vigorously to stress and behavioral pharmacology has revealed a potential role for endogenous CRH in the generation of this response (Bingham et al., 2011; Cassens et al., 1981; Curtis et al., 1997, 2012; Francis et al., 1999; Lechner et al., 1997; Jedema and Grace, 2004; Page and Abercrombie, 1999; Reyes et al., 2008; Snyder et al., 2012; Valentino et al., 1991; Valentino and Foote, 1988; Valentino and Van Bockstaele, 2008). The current study, however, is the first to selectively manipulate LC-NE neurons in the context of stress and its resulting anxiety-like behaviors. Here, we report that the activity of LC-NE neurons is necessary to elicit acute stress-induced anxiety. Furthermore, selectively increasing the firing of LC-NE neurons is itself anxiogenic in the absence of stress. This same high tonic state has negative valence that can inform future behavior through learned association. Finally, optogenetic stimulation of CRH$^+$ CeA terminals into the LC replicates both the cellular profile and acute anxiogenic and aversive behavioral state of direct LC-NE high tonic stimulation (**Figure 5.13Q**).

LC activity during stress is necessary for acute stress-induced anxiety

While the observation of the LC response to stress has implicated the LC-NE system in negative affect associated with stress, it is only now, using a chemogenetic approach, that we can conclude that this activity is required for stress-induced anxiety. Many studies have indicated that noradrenergic tone is important for processing stressful stimuli, encoding fearful events, deciphering threatening versus non-threatening signals (Aston-Jones et al., 1999; Snyder et al.,

231

2012). The finding that activity of LC-NE neurons is necessary to transmit this information and produce stress-induced anxiety-like behavior extends our understanding of this system's role in the stress and the canonical "fight or flight" response. Interestingly, inhibition of the LC-NE system without stress did not affect baseline anxiety levels, suggesting that less LC activity is not necessarily anxiolytic. Furthermore, inhibiting LC-NE neurons during stress did not prevent other physiological readouts of stress, such as fecal output. It will be interesting to dissect whether other stress-induced behaviors such as analgesia (Bannister et al., 2009; Butler and Finn, 2009; Hickey et al., 2014) and reinstatement to drug seeking (Al-Hasani et al., 2013; Shaham et al., 2000) require intact LC-NE activity during stress.

The chemogenetic inhibition approach used here is temporally restricted due to the kinetics of CNO activity, and the neuromodulatory function of the DREADD receptors. Therefore it is difficult to precisely hypothesize when it would be crucial to inhibit LC-NE activity to prevent a stress-induced anxiety event. However, this initial study provides a clearer picture of how LC-NE activity during stress alters subsequent behavior. Additionally, it is quite possible that only a subset of LC-NE neurons are required for stress-induced anxiety and previous studies have indicated that the dorsal-ventral axis of the LC can have diverse actions (Hickey et al., 2014). Future studies will be necessary to elucidate whether the microanatomy and local neural circuits within the LC play an important role in stress-induced anxiety.

High tonic LC-NE neuronal activity can initiate anxiety-like behavior

Several recent studies have used optogenetics to generate binary control of acute anxiety (see Chapter 2) (Felix-Ortiz et al., 2013; Heydendael et al., 2014; Jennings et al., 2013; Kheirbek et al., 2013; Kim et al., 2013a, 2013b; Sidor et al., 2015; Tye et al., 2011). The circuits of the

extended amygdala and some of their projections into the mesolimbic dopamine system have demonstrated rapid onset and offset of anxiety that is likely mediated by small-molecule neurotransmission. Here, we demonstrate anxiety-like behavior generated by increasing the tonic activity of the neuromodulatory LC-NE system. While this activity generates anxiety on a short timescale (seconds to minutes), it is unlikely that the immediate (subsecond timescale) result of high tonic activity is anxiety. Rather, it is plausible that the LC serves to integrate information from numerous forebrain and sensory inputs and, over time, the persistent high tonic state feeds forward onto previously established anxiety circuits. This integration of information may serve to adjust the gain on these downstream systems to ultimately drive anxiety, an idea consistent with previous hypotheses on LC function (Koob, 1999). The extended amygdala is a potential candidate region where feed-forward, gain modulation could exist as there are reciprocal connections between the LC and multiple divisions of the amygdala (Bouret et al., 2003; Buffalari and Grace, 2007; Samuels and Szabadi, 2008) (**Figure 5.14D**). Importantly, this hypothetical model of LC modulation of anxiety circuitry is likely an endogenous mechanism given than the removal of the LC-NE system prevents stress-induced anxiety.

Furthermore, the LC is the primary source of norepinephrine for the mammalian forebrain (Berridge and Waterhouse, 2003; Sara, 2009). It is unlikely that increased noradrenergic tone throughout the brain and spinal cord is what mediates the transition to anxiety-like behavior. Rather, we suspect that particular efferent LC-NE projections likely mediate particular behavioral outcomes. For example, the LC projects into the basolateral amygdala and the lateral septum, both of which have been demonstrated to play a key role in the regulation of stress and anxiety-like behaviors (Anthony et al., 2014; Felix-Ortiz et al., 2013; Tye et al., 2011) (**Figure 5.14D**). This circuit-based theory of LC function is a helpful framework

towards understanding other LC functions such as attention, arousal, and as presented here, aversion.

High tonic LC-NE activity has a negative valence that can inform future behavior

The same optogenetic manipulation that incites anxiety also elicits aversive behaviors in both real-time and conditioned assays. These findings demonstrate that exogenously increasing LC tonic activity carries a significant negative valence. Mimicking the neuronal response to stress in these cells produces behavior similar to exposure to stressful stimuli. While previous studies have identified that the LC has increased immediate early gene expression during various forms of aversion (Sandner et al., 1993), this is the initial attempt to examine, in real-time, whether increased LC-NE activity is sufficient for these behaviors. In fact, we observe that high tonic stimulation of LC-NE neurons is aversive in both real-time and a Pavlovian conditioning paradigm. While this negative valence aligns with the previously discussed anxiogenic results, it elucidates three key components of the system. First, in the real-time aversion assay, the observed aversion behavior is frequency-dependent. In other words, low tonic stimulation that is similar to baseline awake LC activity (1-2 Hz) (Aston-Jones and Bloom, 1981a; Bloom, 1981; Carter et al., 2010, 2012) does not provide negative valence signals to the animal, but higher tonic states, similar to those evoked by stress (5-10 Hz) (Bingham et al., 2011; Cassens et al., 1981; Curtis et al., 1997, 2012; Francis et al., 1999; Lechner et al., 1997; Reyes et al., 2008; Valentino and Van Bockstaele, 2008; Valentino et al., 1991), drive aversion. Furthermore, phasic paradigms mimicking the intrinsic phasic bursting activity of LC neurons (Aston-Jones and Bloom, 1981b; Bouret et al., 2003, 2012; Tervo et al., 2014; Valentino and Foote, 1988), and similar to paradigms used to evoke real-time behavior in other catecholaminergic systems (see Chapters 2 & 4) (Adamantidis et al., 2011; Chaudhury et al., 2013; Kim et al., 2013b; Lammel et

al., 2012; Stamatakis and Stuber, 2012; Tsai et al., 2009; Tye et al., 2013; Witten et al., 2011), do not carry the same aversive signals to the animal. Finally, it appears that higher tonic frequencies potentially produce anxiety through negative affect. While it is generally thought that anxiety and aversion are both negative affective states, the two behavioral outputs are neurobiologically distinct in numerous systems (Kim et al., 2013a; Land et al., 2008) and can each exist without the other. In the case of the LC system, however, the observed anxiety-like behavior does seem to be driven by the aversive nature of the stimulation.

Galaninergic locus coeruleus neurons are sufficient to drive aversion

Previous studies have identified galanin as a common neuropeptide co-transmitter in the LC (Holets et al., 1988; Le Maître et al., 2013; Melander et al., 1986). This selective co-localization allows for a second means of genetically targeting LC neurons. While the *Gal*-Cre experiments support the findings targeting LC-NE neurons in *Th*-Cre mice, they also importantly show that a smaller subset of LC neurons can still maintain the same behavior. This observation suggests possible heterogeneity within the LC. It is now possible to directly compare Gal$^+$ and Gal$^-$ neurons using a Cre-OFF and Cre-ON system to express optogenetic or chemogenetic constructs in clearly segregated populations of LC neurons (Fenno et al., 2014; Saunders et al., 2012). Future work using these and other intersectional targeting strategies will help further dissect the role of this important structure in behavior.

The *Gal*-Cre experiments also point to a gap in our knowledge of the downstream substrate beyond LC-NE neurons. As previously discussed, it seems likely the LC operates with circuit-selectivity to mediate various behaviors, however, postsynaptic cellular mechanisms allow for orders of magnitude of more complexity. With at least nine different adrenergic

receptors and three different galanin receptors, that have nearly all been indicated in anxiety-like behaviors (Brunner et al., 2014; Dixit et al., 2014; Hanke et al., 2012; Kuteeva et al., 2008; Le Maître et al., 2013; Mantsch et al., 2010; Raskind et al., 2007; Wohleb et al., 2011), the combined circuit- and cellular-level dynamics of this system will provide significant challenges for the next series of studies.

CRH[+] CeA-LC terminals increase activity and drive anxiety through CRFR1 activation

Anatomical studies first identified the projection from the CeA to the LC (Van Bockstaele et al., 1996, 1998) and recent work has helped understand the molecular profile of these projections suggesting that CeA-LC projections are potentially glutamatergic and carry the neuropeptides dynorphin and CRH (Kravets et al., 2015; Reyes et al., 2008, 2011). Here, we identify that CRH^{+} neurons represent a clear subset of LC-projecting neurons that aligns with electron microscopy data from the terminal populations in the LC (Kravets et al., 2015; Reyes et al., 2008, 2011). Importantly, CRH^{+} CeA neurons have been shown to be a part of the protein kinase C d[-] subpopulation (Haubensak et al., 2010) of CeA neurons that have recently been shown to be distinct from those CeA neurons involved in conditioned fear and have a possible role in driving food consumption (Cai et al., 2014; Haubensak et al., 2010). This CRH[+] projection into the LC has been of particular interest for the possibility that this is a source of extrahypothalamic CRH that increases tonic LC firing during stress. Here, we see the overall population of recorded LC neurons does increase tonic firing following photostimulation of CRH[+] CeA-LC terminals. Unsurprisingly, however, this increase in activity was not ubiquitous. The diversity of observed responses likely represents an anatomical differentiation of LC neurons. It is quite possible that non-responding neurons do not receive innervation from the CeA and the difference in increased or decreased responses could be explained by a varied

expression of cell-surface receptors on the postsynaptic neurons. While the literature is clear that monosynaptic connections exist in this circuit (Kravets et al., 2015; Reyes et al., 2008, 2011), none of our recorded cells suggest any fast-acting neurotransmission. While this could be due to the potential for selection bias inherent in *in vivo* recordings (only firing neurons can be observed) or an artifact of slower acting neuropeptide/G-protein coupled receptor-mediated transmission, we cannot rule out the possibility of a polysynaptic mechanism. Future work to extensively investigate local GABAergic influence and other LC microcircuits will be necessary (Aston-Jones et al., 2004).

Importantly, however, spatially-isolated photostimulation of these terminals in the LC recapitulates the aversion and anxiety-like behaviors observed with both stress and direct LC photostimulation. Furthermore, the anxiety-like behavior can be prevented by local antagonism of CRHR1 in the LC. This finding suggests that photostimulation-induced release of CRH mediates these behaviors through action in the LC. In addition, the same behavior can be blocked by systemic antagonism of CRHR1. This systemic approach has previously been shown to be anxiogenic in the absence of stress (Heinrichs et al., 1994), but here, still in the absence of stress, the pharmacological manipulation is anxiolytic – reversing the photostimulation-induced anxiety.

Understanding the place of the LC in broader brain networks related to anxiety is crucial to understanding anxiogenesis and determining potential points for therapeutic intervention. While recent focus has been on fast-acting small-molecule transmission (glutamate/GABA) in the generation of anxiety states, the role of stress and neuromodulatory fight-or-flight systems has yet to be fully vetted. Understanding how the vast efferent projection network of the LC facilitates this anxiogenesis will be an important next step. While Anthony and colleagues (Anthony et al., 2014), clearly demonstrate the role of Crfr2$^+$ neurons of the lateral septum (LS)

in prolonged stress-induced anxiety, future work will be needed to investigate whether the known LC inputs into the LS acutely modulate this system and produce prolonged anxiety (Antonopoulos et al., 2004; Berridge et al., 1996; Bondi et al., 2007; Risold and Swanson, 1997). Additionally, the LC also has many known projections to other anxiogenic centers such as the amygdala including the basolateral amygdala and reciprocal projections back to the CeA which merit similar future investigation (Bouret et al., 2003; Buffalari and Grace, 2007; Samuels and Szabadi, 2008)(**Figure 5.14D**). Nevertheless, we report here that stress-induced increases in LC activity are both necessary and sufficient for anxiety-like behavior, collectively affirming the LC-NE system as a critical mediator of the acute behavioral stress response. Taken together, this study provides fundamental framework for understanding the mammalian brain circuitry responsible for the innate anxiety response.

MATERIALS AND METHODS

Experimental subjects

Adult (25–35 g) male C57BL/6J, *TH*-IRES-Cre, *Crh*-IRES-Cre, and *Gal*-Cre (all backcrossed to C57BL/6J mice for ~10 generations) were group-housed, given access to food pellets and water *ad libitum* and maintained on a 12 h:12 h light:dark cycle (lights on at 7:00 AM). All animals were held in a sound attenuated holding room facility in the lab 1 week prior to surgery, post-surgery and throughout the duration of the behavioral assays to minimize stress from transportation and disruption from foot traffic. All mice were handled and, where appropriate, connected to fiber optics and/or headstages two times a day for one week prior to experimental testing. All procedures were approved by the Animal Care and Use Committee of Washington University and conformed to US National Institutes of Health guidelines.

Viral preparation

Plasmids coding pAAV-EF1α-DIO-EFYP and pAAV-EF1α-double floxed-hChR2(H134R)-EYFP-WPRE-HGHpA, were obtained from Addgene (Addgene.org) originally from the Deisseroth Laboratory at Stanford University. The DNA was amplified with a Maxiprep kit (Promega) and packaged into AAV5 serotyped viruses by the WUSTL Hope Center Viral Core. The final viral concentration was 2-5 x 1012 genome vg/mL for the adeno-associated viruses. AAV5-EF1α-DIO-HM4Di-mCherry was purchased directly from the UNC Vector Core.

Table 5.1 Viral vectors used.

Plasmid	Source	Packaged by	Serotype	Titer
pAAV-EF1α-DIO-EFYP	Deisseroth Laboratory (Stanford)	WUSTL Hope Center Viral Core	AAV5	5 x 10^12 vg/ml
pAAV-EF1α-double floxed-hChR2(H134R)-EYFP-WPRE-HGHpA	Deisseroth Laboratory (Stanford)	WUSTL Hope Center Viral Core	AAV5	2 x 10^13 vg/ml
AAV5-EF1α-DIO-HM4Di-mCherry	Roth Laboratory (UNC)	UNC Vector Core	AAV5	3x10^12 VM/mL

Stereotaxic surgery

After the animals were acclimated to the holding facility for seven to nine days, they were anaesthetized in an induction chamber (4% Isolflurane) and placed in a stereotaxic frame (Kopf Instruments, Model 1900) where they were maintained at 1-2% isoflurane. A craniotomy was performed and mice were injected with 500 nl of AAV5-DIO-HM4Di, AAV5-DIO-ChR2 or AAV5-DIO-eYFP, Fluorogold, or CTB-594 unilaterally into the LC (stereotaxic coordinates from bregma: -5.45 anterior-posterior (AP), +/−1.25 medial-lateral (ML), −4.00 mm dorsal-ventral (DV)), or the CeA (-1.25 AP, +/- 2.75 ML, -4.75 DV). Mice were then implanted with metal cannula (PlasticsOne; coordinates adjusted from viral injection 0.00 AP, +/- 0.25 ML, +1.00 DV) or fiber optic implants (coordinates adjusted from viral injection 0.00 AP, +/- 0.25 ML, +1.00 DV)(Carter et al., 2010). Custom adapters (WUSTL Instrument Machine Shop) for the Kopf cannula holder (Model 1966) were used to implant the fiber optics(Sparta et al., 2011). The implants were secured using two bone screws (CMA, 743102) and affixed with dental cement (Lang Dental). Mice were allowed to recover for 3-6 weeks prior to behavioral testing; this interval also permitted optimal AAV expression and Cre recombinase activity.

Immunohistochemistry

Immunohistochemistry was performed as described (see Chapter 2) (Al-Hasani et al., 2013; Kim et al., 2013b). Briefly, mice were anesthetized with pentobarbital and transcardially perfused with ice-cold 4% paraformaldehyde in phosphate buffer (PB). Brains were dissected, post-fixed for 24 hr at 4 ºC and cryoprotected with solution of 30% sucrose in 0.1M PB at 4ºC for at least 24 hr, cut into 30 μm sections and processed for immunostaining. 30 μm brain sections were washed three times in PBS and blocked in PBS containing 0.5% Triton X-100 and

5% normal goat serum. Sections were then incubated for ~16 hr at room temperature in rabbit anti c-fos antibody (1:500, Santa Cruz), rabbit anti-DBH (1:2000, Millipore) and/or chicken anti-TH (1:2000, Aves Labs). Following incubation, sections were washed three times in PBS and then incubated for 2 hr at room temperature in Alexa Fluor 488 goat anti-mouse IgG (1:500, Invitrogen), Alexa Fluor 594 goat anti-rabbit IgG (1:500, Invitrogen), and/or goat anti-chicken Alexa Fluor 633(1:500, Invitrogen) were then washed three times in PBS and followed by three 10-min rinses in PB and mounted on glass slides with Hardset Vectashield (Vector Labs) for microscopy. All sections were imaged on both epifluorescent and confocal microscopes. Gain and exposure time were constant throughout each experiment, and all image groups were processed in parallel using Adobe Photoshop CS5 (Adobe Systems). IHC was quantified as previously described (see Chapter 2) (Al-Hasani et al., 2013; Kim et al., 2013b). Briefly, channels were separated, an exclusive threshold was set, and positive staining for each channel was counted in a blind-to-treatment fashion using Metamorph. The counts from each channel were then overlaid and percent of co-labeled cells were reported.

Antibody	Species	Dilution	Source
TH	Chicken	1:2000	Aves Labs
c-fos	Rabbit	1:500	Santa Cruz
DBH	Rabbit	1:2000	Millipore
Alexa Fluor 488 anti-mouse IgG	Goat	1:500	Invitrogen

Alexa Fluor 594 anti-rabbit IgG	Goat	1:500	Invitrogen
Alexa Fluor 633 anti-chicken IgG	Goat	1:500	Invitrogen
Alexa Fluor 594 anti-chicken IgG	Goat	1:500	Invitrogen

Table 5.2 Antibodies used.

Anatomical tracing

For retrograde tracing experiments (Fluorogold and CTB-594), the tracer was injected and the animal was allowed to recover for six days before perfusion. For anterograde viral tracing, the virus was injected and the animal was allowed to recover for six weeks before perfusion.

Stress-induced anxiety paradigm

Mice assigned to stress groups were restrained in 50 ml disposable conical tubes that were adapted for this purpose by drilling holes to permit air circulation and for the tail to be extended. For acute stress-induced anxiety-like behavior, mice were immobilized in the tube once for 30 minutes. Immediately following stress, animals were transferred to the open field (see below). Fecal boli were collected from both the tube and the open field. For the hM4Di experiments, mice were injected with CNO (10 mg/kg, i.p., 30 min prior to exposure to the restraint tube) (Armbruster et al., 2007; Li et al., 2013; Mahler et al., 2014; Penzo et al., 2015;

Vazey and Aston-Jones, 2014). For the CRF antagonism experiment, mice were injected with Antalarmin HCl (10 mg/kg, i.p., 30 min prior to exposure to the restraint tube).

Open Field Test (OFT)

OFT testing was performed in a square enclosure (50 x 50 cm) within a sound attenuated room maintained at 23ºC. Lighting was measured and stabilized at ~25 lux. For stress-induced experiments, we followed the above paradigm immediately prior to a 20 minute test. For optogenetic experiments, we connected *Th*-Cre[LC:ChR2] or *Th*-Cre[LC:eYFP] mice to fiber optic cables and placed them in the center of the open field and allowed them to roam freely for 21 min. Photostimulation alternated between off and on states in 3 min time segments, beginning with 3 min of no stimulation. For the photostimulated time segments, animals received 5 Hz (10 ms width) photostimulation (~10 mW light power). The open field was cleaned with 70% ethanol between each trial. Movements were video recorded and analyzed using Ethovision 8.5 (Noldus Information Technologies, Leesburg, VA). The center was defined as a square comprised of 50% the total area of the OFT. Time in the center was the primary measure of anxiety-like behaviors.

Slice preparation and solutions (experiments by performed by Chris Ford, PhD)

Following anesthesia, horizontal midbrain slices containing the LC (240 μm) were cut in ice-cold sucrose cutting solution that contained (mM): 75 NaCl, 2.5 KCl, 6 MgCl$_2$, 0.1 CaCl$_2$, 1.2 NaH$_2$PO$_4$, 25 NaHC0$_3$, 2.5 D-glucose, 50 sucrose; bubbled with 95% O$_2$/5% CO$_2$. Slices were incubated post-cutting at 35°C in oxygenated 95% O$_2$/5% CO$_2$ ACSF solution that contained (mM): 126 NaCl, 2.5 KCl, 1.2 MgCl$_2$, 2.5 CaCl$_2$, 1.2 NaH$_2$PO$_4$, 21.4 NaHCO$_3$, 11.1 D-glucose for 45 minutes before recording. During incubation, 10 μM MK-801 was included to reduce excitotoxicity and increase slice viability. Following incubation, slices were placed in a

recording chamber and constantly perfused with warm ACSF (34 ± 2°C) containing 100 µM picrotoxin, 10 µM DNQX and 1 µM idazoxan at 2 ml/min. Neurons were visualized with a BXWI51 microscope (Olympus) with infrared custom-built gradient contrast optics.

Slice electrophysiology (experiments by performed by Chris Ford, PhD)

Whole-cell current-clamp recordings were made as described (Courtney and Ford, 2014; Ford et al., 2009) using an Axopatch 200B amplifier (Molecular Devices). Patch pipettes (1.5-2 MΩ) were pulled from borosilicate glass (World Precision Instruments). The intracellular pipette solution contained 115 (mM): 115 K-methylsulphate, 20 NaCl, 1.5 $MgCl_2$, 10 HEPES(K), 10 BAPTA-tetrapotassium, 1mg/ml ATP, 0.1 mg/ml GTP, and 1.5 mg/ml phosphocreatine (pH 7.4, 275 mOsm). Data were acquired using an ITC-18 interface (Instrutech) and Axograph X (Axograph Scientific) at 10 KHz and filtered to 2KHz for voltage-clamp recordings. Widefield activation of ChR2 was activated with collimated light from a LED (470 nm) through the 40x water immersion objective.

In vivo electrophysiology

For light modulated responses, an array of 16 (35-µm tungsten wires, 150-µm spacing between wires, 150-µm spacing between rows, Innovative Physiology) was epoxied to a fiber optic and lowered into the LC of a lightly (<1% isoflurane) anesthetized, *Th*-Cre[LC:ChR2] (**Figure 5.3**) or *Crh*-Cre[CeA-LC:ChR2] animals (**Figure 5.13**). Two skull screws were arbitrarily placed anterior to bregma on either side of the midline and used to ground the electrode array. In either approach, voltage readings from each electrode were bandpass-filtered with activity between 250 and 8,000 Hz analyzed as spikes. LC cells were selected based on their stereotaxic position, baseline activity, and response to a toe pinch. The signal was amplified and digitally converted

using commercially available hardware and software (Omniplex and PlexControl, Plexon). Spikes were sorted using principal component analysis and/or evaluation of t-distribution with expectation maximization (Offline sorter, Plexon). Sorted units were analyzed using NeuroExplorer 3.0 and timestamps were exported for further analysis in Microsoft Excel and Matlab 7.12.

Elevated Zero Maze (EZM)

EZM testing was performed in a sound attenuated room maintained at 23ºC at 200 lux (see Chapter 2) (Bruchas et al., 2009; Kim et al., 2013b), and trials were performed in the afternoon between 13:00–16:00 hr. The EZM (Harvard Apparatus, Holliston, MA) had the following dimensions: 200 cm in circumference comprised of four 50 cm sections: two opened and two closed. The maze was elevated 50 cm above the floor, with a path width of 4 cm and a 0.5 cm lip on each open section. The maze was cleaned with 70% ethanol between trials. Prior to testing, *Th*-Cre$^{LC:ChR2}$, *Th*-Cre$^{LC:eYFP}$, *Crh*-Cre$^{CeA-LC:ChR2}$, or *Crh*-Cre$^{CeA-LC:eYFP}$ were connected to the fiber optic and placed at the threshold of a closed section facing the open section and allowed to roam freely for 7 min. *Th*-Cre animals received 5 Hz (10 ms width) and *Crh*-Cre animals received 10 Hz (10 ms width) photostimulation (~10 mW light power). For the CRFR1 antagonism experiments, mice were injected into the LC with α-helical CRF (1 µg, intra-LC, one hour prior to behavior, Tocris) or Antalarmin HCl (10 mg/kg, i.p., 30 min prior to behavior, Sigma). Movements were video recorded and analyzed using Ethovision 8.5 (Noldus Information Technologies, Leesburg, VA). Open section time and entries into the open section following a one-minute habituation were the primary measures of anxiety-like behaviors.

Conditioned Place Aversion

Th-Cre^LC:ChR2, *Th*-Cre^LC:eYFP, *Crh*-Cre^CeA-LC:ChR2, or *Crh*-Cre^CeA-LC:eYFP animals were trained in an unbiased, balanced three-compartment conditioning apparatus as described (Bruchas et al., 2009; Al-Hasani et al., 2013; Land et al., 2008, 2009). Briefly, mice were pre-tested by placing individual animals in the small central compartment and allowing them to explore the entire apparatus for 30 min. Time spent in each compartment was recorded with a video camera (ZR90; Canon) and analyzed using Ethovision 8.5 (Noldus). Mice were randomly assigned to photostimulation and no-photostimulation compartments and received no photostimulation in the morning and photostimulation (*Th*-Cre^LC:ChR2: 5 Hz, 10 ms pulses; *Crh*-Cre^CeA-LC:ChR2: 10 Hz, 10 ms pulses) in the afternoon at least 4 h after the morning training on two consecutive days. CPA was assessed on day 4 by allowing the mice to roam freely in all three compartments and recording the time spent in each. Scores were calculated by subtracting the time spent in the photostimulation-paired compartment post-test minus the pre-test.

Real-time Place Testing

Th-Cre^LC:ChR2, *Th*-Cre^LC:eYFP, *Gal*- Cre^LC:ChR2, *Crh*-Cre^CeA-LC:ChR2, or *Crh*-Cre^CeA-LC:eYFP animals were placed in a custom-made unbiased, balanced two-compartment conditioning apparatus (52.5 x 25.5 x 25.5 cm) as described previously (see Chapter 4) (Jennings et al., 2013; Kim et al., 2013a; Stamatakis and Stuber, 2012; Stamatakis et al., 2013; Tan et al., 2012). Mice were allowed to freely roam the entire apparatus for 20 min. Entry into one compartment triggered photostimulation of various frequencies (0, 1, 2, 5, 10 Hz, etc.) while the animal remained in the light-paired chamber. Entry into the other chamber ended the photostimulation. The side paired with photostimulation was counterbalanced across mice and across session. Time spent in each chamber and total distance traveled for the entire 20-minute trial was measured using Ethovision 8.5 (Noldus Information Technologies, Leesburg, VA).

Data Analysis/Statistics

All data expressed as mean ± SEM. Data were normally distributed, and differences between groups were determined using independent t-tests or one-way ANOVA, or two-way ANOVAs followed by *post hoc* Bonferroni comparisons if the main effect was significant at $p<0.05$. Statistical analyses were conducted using Prism 5.0 (GraphPad).

Genotyping of mouse lines

DNA was isolated from tail tissue obtained from weanling mice (21-28 days of age), and PCR screening was performed using the following primers: Cre recombinase (forward: 5'- GCA TTA CCG GTC GAT GCA ACG AGT GAT GAG-3' and reverse: 5'- GAG TGA ACG AAC CTG GTC GAA ATC AGT GCG-3') yielding a 400-bp PCR product in Cre positive animals. Fatty acid-binding protein intestinal primers (forward: 5'- TGG ACA GGA CTG GAC CTC TGC TTT CCT AGA-3' and reverse: 5'- TAG AGC TTT GCC ACA TCA CAG GTC ATT CAG-3') were used as positive controls and yield a 200-bp PCR product.

REFERENCES

Adamantidis, A.R., Tsai, H.-C., Boutrel, B., Zhang, F., Stuber, G.D., Budygin, E.A., Touriño, C., Bonci, A., Deisseroth, K., and de Lecea, L. (2011). Optogenetic interrogation of dopaminergic modulation of the multiple phases of reward-seeking behavior. J. Neurosci. Off. J. Soc. Neurosci. *31*, 10829–10835.

Alvarez, V.A., Chow, C.C., Van Bockstaele, E.J., and Williams, J.T. (2002). Frequency-dependent synchrony in locus ceruleus: role of electrotonic coupling. Proc. Natl. Acad. Sci. U. S. A. *99*, 4032–4036.

Anthony, T., Dee, N., Bernard, A., Lerchner, W., Heintz, N., and Anderson, D. (2014). Control of Stress-Induced Persistent Anxiety by an Extra-Amygdala Septohypothalamic Circuit. Cell *156*, 522–536.

Antonopoulos, J., Latsari, M., Dori, I., Chiotelli, M., Parnavelas, J.G., and Dinopoulos, A. (2004). Noradrenergic innervation of the developing and mature septal area of the rat. J. Comp. Neurol. *476*, 80–90.

Armbruster, B.N., Li, X., Pausch, M.H., Herlitze, S., and Roth, B.L. (2007). Evolving the lock to fit the key to create a family of G protein-coupled receptors potently activated by an inert ligand. Proc. Natl. Acad. Sci. U. S. A. *104*, 5163–5168.

Aston-Jones, G., and Bloom, F.E. (1981a). Activity of norepinephrine-containing locus coeruleus neurons in behaving rats anticipates fluctuations in the sleep-waking cycle. J. Neurosci. Off. J. Soc. Neurosci. *1*, 876–886.

Aston-Jones, G., and Bloom, F.E. (1981b). Norepinephrine-containing locus coeruleus neurons in behaving rats exhibit pronounced responses to non-noxious environmental stimuli. J. Neurosci. Off. J. Soc. Neurosci. *1*, 887–900.

Aston-Jones, G., Rajkowski, J., and Cohen, J. (1999). Role of locus coeruleus in attention and behavioral flexibility. Biol. Psychiatry *46*, 1309–1320.

Aston-Jones, G., Zhu, Y., and Card, J.P. (2004). Numerous GABAergic afferents to locus ceruleus in the pericerulear dendritic zone: possible interneuronal pool. J. Neurosci. Off. J. Soc. Neurosci. *24*, 2313–2321.

Ballantyne, D., Andrzejewski, M., Mückenhoff, K., and Scheid, P. (2004). Rhythms, synchrony and electrical coupling in the Locus coeruleus. Respir. Physiol. Neurobiol. *143*, 199–214.

Bannister, K., Bee, L.A., and Dickenson, A.H. (2009). Preclinical and early clinical investigations related to monoaminergic pain modulation. Neurother. J. Am. Soc. Exp. Neurother. *6*, 703–712.

Berridge, C.W., and Waterhouse, B.D. (2003). The locus coeruleus-noradrenergic system: modulation of behavioral state and state-dependent cognitive processes. Brain Res. Brain Res. Rev. *42*, 33–84.

Berridge, C.W., Bolen, S.J., Manley, M.S., and Foote, S.L. (1996). Modulation of Forebrain Electroencephalographic Activity in Halothane-Anesthetized Rat via Actions of Noradrenergic β-Receptors within the Medial Septal Region. J. Neurosci. *16*, 7010–7020.

Bingham, B., McFadden, K., Zhang, X., Bhatnagar, S., Beck, S., and Valentino, R. (2011). Early adolescence as a critical window during which social stress distinctly alters behavior and brain norepinephrine activity. Neuropsychopharmacol. Off. Publ. Am. Coll. Neuropsychopharmacol. *36*, 896–909.

Bloom, F.E. (1981). ACTIVITY OF NOREPINEPHRINE-CONTAINING NEURONS IN BEHAVING RATS ANTICIPATES THE SLEEP-WAKING CYCLE ' LOCUS COERULEUS FLUCTUATIONS IN. *1*, 876–886.

Van Bockstaele, E.J., Chan, J., and Pickel, V.M. (1996). Input from central nucleus of the amygdala efferents to pericoerulear dendrites, some of which contain tyrosine hydroxylase immunoreactivity. J. Neurosci. Res. *45*, 289–302.

Van Bockstaele, E.J., Colago, E.E., and Valentino, R.J. (1998). Amygdaloid corticotropin-releasing factor targets locus coeruleus dendrites: substrate for the co-ordination of emotional and cognitive limbs of the stress response. J. Neuroendocrinol. *10*, 743–757.

Bondi, C.O., Barrera, G., Lapiz, M.D.S., Bedard, T., Mahan, A., and Morilak, D.A. (2007). Noradrenergic facilitation of shock-probe defensive burying in lateral septum of rats, and modulation by chronic treatment with desipramine. Prog. Neuropsychopharmacol. Biol. Psychiatry *31*, 482–495.

Bouret, S., Duvel, A., Onat, S., and Sara, S.J. (2003). Phasic activation of locus ceruleus neurons by the central nucleus of the amygdala. J. Neurosci. Off. J. Soc. Neurosci. *23*, 3491–3497.

Bouret, S., Ravel, S., and Richmond, B.J. (2012). Complementary neural correlates of motivation in dopaminergic and noradrenergic neurons of monkeys. Front. Behav. Neurosci. *6*, 40.

Bruchas, M.R., Land, B.B., Lemos, J.C., and Chavkin, C. (2009). CRF1-R activation of the dynorphin/kappa opioid system in the mouse basolateral amygdala mediates anxiety-like behavior. PloS One *4*, e8528.

Brunner, S.M., Farzi, A., Locker, F., Holub, B.S., Drexel, M., Reichmann, F., Lang, A.A., Mayr, J.A., Vilches, J.J., Navarro, X., et al. (2014). GAL3 receptor KO mice exhibit an anxiety-like phenotype. Proc. Natl. Acad. Sci. U. S. A. *111*, 7138–7143.

Buffalari, D.M., and Grace, A.A. (2007). Noradrenergic modulation of basolateral amygdala neuronal activity: opposing influences of alpha-2 and beta receptor activation. J. Neurosci. Off. J. Soc. Neurosci. *27*, 12358–12366.

Butler, R.K., and Finn, D.P. (2009). Stress-induced analgesia. Prog. Neurobiol. *88*, 184–202.

Cai, H., Haubensak, W., Anthony, T.E., and Anderson, D.J. (2014). Central amygdala PKC-δ+ neurons mediate the influence of multiple anorexigenic signals. Nat. Neurosci. *17*, 1240–1248.

Carter, M.E., Yizhar, O., Chikahisa, S., Nguyen, H., Adamantidis, A., Nishino, S., Deisseroth, K., and de Lecea, L. (2010). Tuning arousal with optogenetic modulation of locus coeruleus neurons. Nat. Neurosci. *13*, 1526–1533.

Carter, M.E., Brill, J., Bonnavion, P., Huguenard, J.R., Huerta, R., and de Lecea, L. (2012). Mechanism for Hypocretin-mediated sleep-to-wake transitions. Proc. Natl. Acad. Sci. U. S. A. *109*, E2635–E2644.

Cassens, G., Kuruc, A., Roffman, M., Orsulak, P.J., and Schildkraut, J.J. (1981). Alterations in brain norepinephrine metabolism and behavior induced by environmental stimuli previously paired with inescapable shock. Behav. Brain Res. *2*, 387–407.

Chaudhury, D., Walsh, J.J., Friedman, A.K., Juarez, B., Ku, S.M., Koo, J.W., Ferguson, D., Tsai, H.-C., Pomeranz, L., Christoffel, D.J., et al. (2013). Rapid regulation of depression-related behaviours by control of midbrain dopamine neurons. Nature *493*, 532–536.

Chmielarz, P., Kuśmierczyk, J., Parlato, R., Schütz, G., Nalepa, I., and Kreiner, G. (2013). Inactivation of Glucocorticoid Receptor in Noradrenergic System Influences Anxiety- and Depressive-Like Behavior in Mice. PLoS ONE *8*, e72632.

Choleris, E., Thomas, a W., Kavaliers, M., and Prato, F.S. (2001). A detailed ethological analysis of the mouse open field test: effects of diazepam, chlordiazepoxide and an extremely low frequency pulsed magnetic field. Neurosci. Biobehav. Rev. *25*, 235–260.

Ciocchi, S., Herry, C., Grenier, F., Wolff, S.B.E., Letzkus, J.J., Vlachos, I., Ehrlich, I., Sprengel, R., Deisseroth, K., Stadler, M.B., et al. (2010). Encoding of conditioned fear in central amygdala inhibitory circuits. Nature *468*, 277–282.

Conte, W.L., Kamishina, H., and Reep, R.L. (2009). Multiple neuroanatomical tract-tracing using fluorescent Alexa Fluor conjugates of cholera toxin subunit B in rats. Nat. Protoc. *4*, 1157–1166.

Courtney, N.A., and Ford, C.P. (2014). The timing of dopamine- and noradrenaline-mediated transmission reflects underlying differences in the extent of spillover and pooling. J. Neurosci. Off. J. Soc. Neurosci. *34*, 7645–7656.

Curtis, a L., Lechner, S.M., Pavcovich, L. a, and Valentino, R.J. (1997). Activation of the locus coeruleus noradrenergic system by intracoerulear microinfusion of corticotropin-releasing factor: effects on discharge rate, cortical norepinephrine levels and cortical electroencephalographic activity. J. Pharmacol. Exp. Ther. *281*, 163–172.

Curtis, a L., Bello, N.T., and Valentino, R.J. (2001). Evidence for functional release of endogenous opioids in the locus ceruleus during stress termination. J. Neurosci. Off. J. Soc. Neurosci. *21*, RC152.

Curtis, A.L., Leiser, S.C., Snyder, K., and Valentino, R.J. (2012). Predator stress engages corticotropin-releasing factor and opioid systems to alter the operating mode of locus coeruleus norepinephrine neurons. Neuropharmacology *62*, 1737–1745.

Dimitrov, E.L., Yanagawa, Y., and Usdin, T.B. (2013). Forebrain GABAergic projections to locus coeruleus in mouse. J. Comp. Neurol. *521*, 2373–2397.

Dixit, M.P., Thakre, P.P., Pannase, A.S., Aglawe, M.M., Taksande, B.G., and Kotagale, N.R. (2014). Imidazoline binding sites mediates anticompulsive-like effect of agmatine in marble-burying behavior in mice. Eur. J. Pharmacol. *732*, 26–31.

Dunn, A.J., Swiergiel, A.H., and Palamarchouk, V. (2004). Brain circuits involved in corticotropin-releasing factor-norepinephrine interactions during stress. Ann. N. Y. Acad. Sci. *1018*, 25–34.

Felix-Ortiz, A.C., Beyeler, A., Seo, C., Leppla, C.A., Wildes, C.P., and Tye, K.M. (2013). BLA to vHPC inputs modulate anxiety-related behaviors. Neuron *79*, 658–664.

Fenno, L.E., Mattis, J., Ramakrishnan, C., Hyun, M., Lee, S.Y., He, M., Tucciarone, J., Selimbeyoglu, A., Berndt, A., Grosenick, L., et al. (2014). Targeting cells with single vectors using multiple-feature Boolean logic. Nat. Methods *11*, 763–772.

Foote, S.L., Aston-Jones, G., and Bloom, F.E. (1980). Impulse activity of locus coeruleus neurons in awake rats and monkeys is a function of sensory stimulation and arousal. Proc. Natl. Acad. Sci. U. S. A. *77*, 3033–3037.

Ford, C.P., Phillips, P.E.M., and Williams, J.T. (2009). The time course of dopamine transmission in the ventral tegmental area. J. Neurosci. Off. J. Soc. Neurosci. *29*, 13344–13352.

Francis, D.D., Caldji, C., Champagne, F., Plotsky, P.M., and Meaney, M.J. (1999). The role of corticotropin-releasing factor–norepinephrine systems in mediating the effects of early experience on the development of behavioral and endocrine responses to stress. Biol. Psychiatry *46*, 1153–1166.

Gafford, G.M., Guo, J.-D., Flandreau, E.I., Hazra, R., Rainnie, D.G., and Ressler, K.J. (2012). Cell-type specific deletion of GABA(A)α1 in corticotropin-releasing factor-containing neurons enhances anxiety and disrupts fear extinction. Proc. Natl. Acad. Sci. U. S. A. *109*, 16330–16335.

Gong, S., Zheng, C., Doughty, M.L., Losos, K., Didkovsky, N., Schambra, U.B., Nowak, N.J., Joyner, A., Leblanc, G., Hatten, M.E., et al. (2003). A gene expression atlas of the central nervous system based on bacterial artificial chromosomes. Nature *425*, 917–925.

Gong, S., Doughty, M., Harbaugh, C.R., Cummins, A., Hatten, M.E., Heintz, N., and Gerfen, C.R. (2007). Targeting Cre Recombinase to Specific Neuron Populations with Bacterial Artificial Chromosome Constructs. J. Neurosci. *27*, 9817–9823.

Gross, C., and Hen, R. (2004). The developmental origins of anxiety. Nat. Rev. Neurosci. *5*, 545–552.

Hanke, M.L., Powell, N.D., Stiner, L.M., Bailey, M.T., and Sheridan, J.F. (2012). Beta adrenergic blockade decreases the immunomodulatory effects of social disruption stress. Brain. Behav. Immun. *26*, 1150–1159.

Al-Hasani, R., McCall, J.G., Foshage, A.M., and Bruchas, M.R. (2013). Locus Coeruleus Kappa Opioid Receptors modulate Reinstatement of Cocaine Place Preference through a Noradrenergic Mechanism. Neuropsychopharmacology.

Haubensak, W., Kunwar, P.S., Cai, H., Ciocchi, S., Wall, N.R., Ponnusamy, R., Biag, J., Dong, H.-W., Deisseroth, K., Callaway, E.M., et al. (2010). Genetic dissection of an amygdala microcircuit that gates conditioned fear. Nature *468*, 270–276.

Heinrichs, S.C., Menzaghi, F., Pich, E.M., Baldwin, H.A., Rassnick, S., Britton, K.T., and Koob, G.F. (1994). Anti-stress action of a corticotropin-releasing factor antagonist on behavioral reactivity to stressors of varying type and intensity. Neuropsychopharmacol. Off. Publ. Am. Coll. Neuropsychopharmacol. *11*, 179–186.

Heydendael, W., Sengupta, A., Beck, S., and Bhatnagar, S. (2014). Optogenetic examination identifies a context-specific role for orexins/hypocretins in anxiety-related behavior. Physiol. Behav. *130*, 182–190.

Hickey, L., Li, Y., Fyson, S.J., Watson, T.C., Perrins, R., Hewinson, J., Teschemacher, A.G., Furue, H., Lumb, B.M., and Pickering, A.E. (2014). Optoactivation of locus ceruleus neurons evokes bidirectional changes in thermal nociception in rats. J. Neurosci. Off. J. Soc. Neurosci. *34*, 4148–4160.

Holets, V.R., Hökfelt, T., Rökaeus, Å., Terenius, L., and Goldstein, M. (1988). Locus coeruleus neurons in the rat containing neuropeptide Y, tyrosine hydroxylase or galanin and their efferent projections to the spinal cord, cerebral cortex and hypothalamus. Neuroscience *24*, 893–906.

Jedema, H.P., and Grace, A.A. (2004). Corticotropin-releasing hormone directly activates noradrenergic neurons of the locus ceruleus recorded in vitro. J. Neurosci. Off. J. Soc. Neurosci. *24*, 9703–9713.

Jennings, J.H., Sparta, D.R., Stamatakis, A.M., Ung, R.L., Pleil, K.E., Kash, T.L., and Stuber, G.D. (2013). Distinct extended amygdala circuits for divergent motivational states. Nature *496*, 224–228.

Kheirbek, M.A., Drew, L.J., Burghardt, N.S., Costantini, D.O., Tannenholz, L., Ahmari, S.E., Zeng, H., Fenton, A.A., and Hen, R. (2013). Differential control of learning and anxiety along the dorsoventral axis of the dentate gyrus. Neuron *77*, 955–968.

Kim, S.-Y., Adhikari, A., Lee, S.Y., Marshel, J.H., Kim, C.K., Mallory, C.S., Lo, M., Pak, S., Mattis, J., Lim, B.K., et al. (2013a). Diverging neural pathways assemble a behavioural state from separable features in anxiety. Nature *496*, 219–223.

Kim, T., McCall, J.G., Jung, Y.H., Huang, X., Siuda, E.R., Li, Y., Song, J., Song, Y.M., Pao, H.A., Kim, R.-H., et al. (2013b). Injectable, Cellular-Scale Optoelectronics with Applications for Wireless Optogenetics. Science *340*, 211–216.

Knoll, A.T., and Carlezon, W.A. (2010). Dynorphin, stress, and depression. Brain Res. *1314*, 56–73.

Konturek, P.C., Brzozowski, T., and Konturek, S.J. (2011). Stress and the gut: pathophysiology, clinical consequences, diagnostic approach and treatment options. J. Physiol. Pharmacol. Off. J. Pol. Physiol. Soc. *62*, 591–599.

Koob, G.F. (1999). Corticotropin-releasing factor, norepinephrine, and stress. Biol. Psychiatry *46*, 1167–1180.

Kravets, J.L., Reyes, B. a. S., Unterwald, E.M., and Van Bockstaele, E.J. (2015). Direct targeting of peptidergic amygdalar neurons by noradrenergic afferents: linking stress-integrative circuitry. Brain Struct. Funct. *220*, 541–558.

Kuteeva, E., Wardi, T., Lundström, L., Sollenberg, U., Langel, U., Hökfelt, T., and Ogren, S.O. (2008). Differential role of galanin receptors in the regulation of depression-like behavior and monoamine/stress-related genes at the cell body level. Neuropsychopharmacol. Off. Publ. Am. Coll. Neuropsychopharmacol. *33*, 2573–2585.

Lammel, S., Lim, B.K., Ran, C., Huang, K.W., Betley, M.J., Tye, K.M., Deisseroth, K., and Malenka, R.C. (2012). Input-specific control of reward and aversion in the ventral tegmental area. Nature *491*, 212–217.

Land, B.B., Bruchas, M.R., Lemos, J.C., Xu, M., Melief, E.J., and Chavkin, C. (2008). The dysphoric component of stress is encoded by activation of the dynorphin kappa-opioid system. J. Neurosci. Off. J. Soc. Neurosci. *28*, 407–414.

Land, B.B., Bruchas, M.R., Schattauer, S., Giardino, W.J., Aita, M., Messinger, D., Hnasko, T.S., Palmiter, R.D., and Chavkin, C. (2009). Activation of the kappa opioid receptor in the dorsal raphe nucleus mediates the aversive effects of stress and reinstates drug seeking. Proc. Natl. Acad. Sci. U. S. A. *106*, 19168–19173.

Larauche, M., Kiank, C., and Tache, Y. (2009). Corticotropin releasing factor signaling in colon and ileum: regulation by stress and pathophysiological implications. J. Physiol. Pharmacol. Off. J. Pol. Physiol. Soc. *60 Suppl 7*, 33–46.

Lechner, S.M., Curtis, a L., Brons, R., and Valentino, R.J. (1997). Locus coeruleus activation by colon distention: role of corticotropin-releasing factor and excitatory amino acids. Brain Res. *756*, 114–124.

Lein, E.S., Hawrylycz, M.J., Ao, N., Ayres, M., Bensinger, A., Bernard, A., Boe, A.F., Boguski, M.S., Brockway, K.S., Byrnes, E.J., et al. (2007). Genome-wide atlas of gene expression in the adult mouse brain. Nature *445*, 168–176.

Li, H., Penzo, M.A., Taniguchi, H., Kopec, C.D., Huang, Z.J., and Li, B. (2013). Experience-dependent modification of a central amygdala fear circuit. Nat. Neurosci. *16*, 332–339.

Madisen, L., Zwingman, T.A., Sunkin, S.M., Oh, S.W., Zariwala, H.A., Gu, H., Ng, L.L., Palmiter, R.D., Hawrylycz, M.J., Jones, A.R., et al. (2010). A robust and high-throughput Cre reporting and characterization system for the whole mouse brain. Nat. Neurosci. *13*, 133–140.

Mahler, S.V., Vazey, E.M., Beckley, J.T., Keistler, C.R., McGlinchey, E.M., Kaufling, J., Wilson, S.P., Deisseroth, K., Woodward, J.J., and Aston-Jones, G. (2014). Designer receptors show role for ventral pallidum input to ventral tegmental area in cocaine seeking. Nat. Neurosci. *17*, 577–585.

Le Maître, E., Barde, S.S., Palkovits, M., Diaz-Heijtz, R., and Hökfelt, T.G.M. (2013). Distinct features of neurotransmitter systems in the human brain with focus on the galanin system in locus coeruleus and dorsal raphe. Proc. Natl. Acad. Sci. U. S. A. *110*, E536–E545.

Mantsch, J.R., Weyer, A., Vranjkovic, O., Beyer, C.E., Baker, D. a, and Caretta, H. (2010). Involvement of Noradrenergic Neurotransmission in the Stress- but not Cocaine-Induced Reinstatement of Extinguished Cocaine-Induced Conditioned Place Preference in Mice: Role for beta-2 Adrenergic Receptors. Neuropsychopharmacol. Off. Publ. Am. Coll. Neuropsychopharmacol. *35*, 2165–2178.

Melander, T., Hökfelt, T., and Rökaeus, A. (1986). Distribution of galaninlike immunoreactivity in the rat central nervous system. J. Comp. Neurol. *248*, 475–517.

Olson, V.G., Rockett, H.R., Reh, R.K., Redila, V.A., Tran, P.M., Venkov, H.A., DeFino, M.C., Hague, C., Peskind, E.R., Szot, P., et al. (2011). The Role of Norepinephrine in Differential Response to Stress in an Animal Model of Posttraumatic Stress Disorder. Biol. Psychiatry *70*, 441–448.

Page, M.E., and Abercrombie, E.D. (1999). Discrete local application of corticotropin-releasing factor increases locus coeruleus discharge and extracellular norepinephrine in rat hippocampus. Synap. N. Y. N *33*, 304–313.

Penzo, M.A., Robert, V., Tucciarone, J., De Bundel, D., Wang, M., Van Aelst, L., Darvas, M., Parada, L.F., Palmiter, R.D., He, M., et al. (2015). The paraventricular thalamus controls a central amygdala fear circuit. Nature *advance online publication*.

Raskind, M.A., Peskind, E.R., Kanter, E.D., Petrie, E.C., Radant, A., Thompson, C.E., Dobie, D.J., Hoff, D., Rein, R.J., Straits-Tröster, K., et al. (2003). Reduction of nightmares and other PTSD symptoms in combat veterans by prazosin: a placebo-controlled study. Am. J. Psychiatry *160*, 371–373.

Raskind, M.A., Peskind, E.R., Hoff, D.J., Hart, K.L., Holmes, H.A., Warren, D., Shofer, J., O'Connell, J., Taylor, F., Gross, C., et al. (2007). A parallel group placebo controlled study of prazosin for trauma nightmares and sleep disturbance in combat veterans with post-traumatic stress disorder. Biol. Psychiatry *61*, 928–934.

Raskind, M.A., Peterson, K., Williams, T., Hoff, D.J., Hart, K., Holmes, H., Homas, D., Hill, J., Daniels, C., Calohan, J., et al. (2013). A Trial of Prazosin for Combat Trauma PTSD With Nightmares in Active-Duty Soldiers Returned From Iraq and Afghanistan. Am. J. Psychiatry *170*, 1003–1010.

Rasmussen, K., Strecker, R.E., and Jacobs, B.L. (1986). Single unit response of noradrenergic, serotonergic and dopaminergic neurons in freely moving cats to simple sensory stimuli. Brain Res. *369*, 336–340.

Reyes, B. a S., Drolet, G., and Van Bockstaele, E.J. (2008). Dynorphin and stress-related peptides in rat locus coeruleus: contribution of amygdalar efferents. J. Comp. Neurol. *508*, 663–675.

Reyes, B. a. S., Carvalho, A.F., Vakharia, K., and Van Bockstaele, E.J. (2011). Amygdalar peptidergic circuits regulating noradrenergic locus coeruleus neurons: linking limbic and arousal centers. Exp. Neurol. *230*, 96–105.

Risold, P.Y., and Swanson, L.W. (1997). Chemoarchitecture of the rat lateral septal nucleus. Brain Res. Brain Res. Rev. *24*, 91–113.

Samuels, E.R., and Szabadi, E. (2008). Functional Neuroanatomy of the Noradrenergic Locus Coeruleus: Its Roles in the Regulation of Arousal and Autonomic Function Part I: Principles of Functional Organisation. Curr. Neuropharmacol. *6*, 235–253.

Sandner, G., Oberling, P., Silveira, M.C., Di Scala, G., Rocha, B., Bagri, A., and Depoortere, R. (1993). What brain structures are active during emotions? Effects of brain stimulation elicited aversion on c-fos immunoreactivity and behavior. Behav. Brain Res. *58*, 9–18.

Sara, S.J. (2009). The locus coeruleus and noradrenergic modulation of cognition. Nat. Rev. Neurosci. *10*, 211–223.

Sara, S.J., and Bouret, S. (2012). Orienting and reorienting: the locus coeruleus mediates cognition through arousal. Neuron *76*, 130–141.

Saunders, A., Johnson, C.A., and Sabatini, B.L. (2012). Novel recombinant adeno-associated viruses for Cre activated and inactivated transgene expression in neurons. Front. Neural Circuits *6*, 47.

Schaefer, M.L., Wong, S.T., Wozniak, D.F., Muglia, L.M., Liauw, J.A., Zhuo, M., Nardi, A., Hartman, R.E., Vogt, S.K., Luedke, C.E., et al. (2000). Altered Stress-Induced Anxiety in Adenylyl Cyclase Type VIII-Deficient Mice. J. Neurosci. *20*, 4809–4820.

Shaham, Y., Highfield, D., Delfs, J., Leung, S., and Stewart, J. (2000). Clonidine blocks stress-induced reinstatement of heroin seeking in rats: an effect independent of locus coeruleus noradrenergic neurons. Eur. J. Neurosci. *12*, 292–302.

Shepherd, J.K., Grewal, S.S., Fletcher, A., Bill, D.J., and Dourish, C.T. (1994). Behavioural and pharmacological characterisation of the elevated "zero-maze" as an animal model of anxiety. Psychopharmacology (Berl.) *116*, 56–64.

Sidor, M.M., Spencer, S.M., Dzirasa, K., Parekh, P.K., Tye, K.M., Warden, M.R., Arey, R.N., Enwright, J.F., Jacobsen, J.P.R., Kumar, S., et al. (2015). Daytime spikes in dopaminergic activity drive rapid mood-cycling in mice. Mol. Psychiatry *5*.

Sim, H.-R., Choi, T.-Y., Lee, H.J., Kang, E.Y., Yoon, S., Han, P.-L., Choi, S.-Y., and Baik, J.-H. (2013). Role of dopamine D2 receptors in plasticity of stress-induced addictive behaviours. Nat. Commun. *4*, 1579.

Snyder, K., Wang, W.-W., Han, R., McFadden, K., and Valentino, R.J. (2012). Corticotropin-releasing factor in the norepinephrine nucleus, locus coeruleus, facilitates behavioral flexibility. Neuropsychopharmacol. Off. Publ. Am. Coll. Neuropsychopharmacol. *37*, 520–530.

Sparta, D.R., Stamatakis, A.M., Phillips, J.L., Hovelsø, N., van Zessen, R., and Stuber, G.D. (2011). Construction of implantable optical fibers for long-term optogenetic manipulation of neural circuits. Nat. Protoc. *7*, 12–23.

Stamatakis, A.M., and Stuber, G.D. (2012). Activation of lateral habenula inputs to the ventral midbrain promotes behavioral avoidance. Nat. Neurosci. *15*, 1105–1107.

Stamatakis, A.M., Jennings, J.H., Ung, R.L., Blair, G.A., Weinberg, R.J., Neve, R.L., Boyce, F., Mattis, J., Ramakrishnan, C., Deisseroth, K., et al. (2013). A unique population of ventral tegmental area neurons inhibits the lateral habenula to promote reward. Neuron *80*, 1039–1053.

Tan, K.R., Yvon, C., Turiault, M., Mirzabekov, J.J., Doehner, J., Labouèbe, G., Deisseroth, K., Tye, K.M., and Lüscher, C. (2012). GABA neurons of the VTA drive conditioned place aversion. Neuron *73*, 1173–1183.

Taniguchi, H., He, M., Wu, P., Kim, S., Paik, R., Sugino, K., Kvitsiani, D., Kvitsani, D., Fu, Y., Lu, J., et al. (2011). A resource of Cre driver lines for genetic targeting of GABAergic neurons in cerebral cortex. Neuron *71*, 995–1013.

Tervo, D.G.R., Proskurin, M., Manakov, M., Kabra, M., Vollmer, A., Branson, K., and Karpova, A.Y. (2014). Behavioral Variability through Stochastic Choice and Its Gating by Anterior Cingulate Cortex. Cell *159*, 21–32.

Tsai, H.-C., Zhang, F., Adamantidis, A., Stuber, G.D., Bonci, A., de Lecea, L., and Deisseroth, K. (2009). Phasic firing in dopaminergic neurons is sufficient for behavioral conditioning. Science *324*, 1080–1084.

Tye, K.M., Prakash, R., Kim, S.-Y., Fenno, L.E., Grosenick, L., Zarabi, H., Thompson, K.R., Gradinaru, V., Ramakrishnan, C., and Deisseroth, K. (2011). Amygdala circuitry mediating reversible and bidirectional control of anxiety. Nature *471*, 358–362.

Tye, K.M., Mirzabekov, J.J., Warden, M.R., Ferenczi, E.A., Tsai, H.-C., Finkelstein, J., Kim, S.-Y., Adhikari, A., Thompson, K.R., Andalman, A.S., et al. (2013). Dopamine neurons modulate neural encoding and expression of depression-related behaviour. Nature *493*, 537–541.

Ungless, M.A., Argilli, E., and Bonci, A. (2010). Effects of stress and aversion on dopamine neurons: implications for addiction. Neurosci. Biobehav. Rev. *35*, 151–156.

Valentino, R.J., and Van Bockstaele, E. (2008). Convergent regulation of locus coeruleus activity as an adaptive response to stress. Eur. J. Pharmacol. *583*, 194–203.

Valentino, R.J., and Foote, S.L. (1988). Corticotropin-releasing hormone increases tonic but not sensory-evoked activity of noradrenergic locus coeruleus neurons in unanesthetized rats. J. Neurosci. Off. J. Soc. Neurosci. *8*, 1016–1025.

Valentino, R.J., Page, M.E., and Curtis, a L. (1991). Activation of noradrenergic locus coeruleus neurons by hemodynamic stress is due to local release of corticotropin-releasing factor. Brain Res. *555*, 25–34.

Valentino, R.J., Page, M., Van Bockstaele, E., and Aston-Jones, G. (1992). Corticotropin-releasing factor innervation of the locus coeruleus region: distribution of fibers and sources of input. Neuroscience *48*, 689–705.

Vazey, E.M., and Aston-Jones, G. (2014). Designer receptor manipulations reveal a role of the locus coeruleus noradrenergic system in isoflurane general anesthesia. Proc. Natl. Acad. Sci. *111*, 3859–3864.

Veinante, P., and Freund-Mercier, M.-J. (1998). Intrinsic and extrinsic connections of the rat central extended amygdala: an in vivo electrophysiological study of the central amygdaloid nucleus. Brain Res. *794*, 188–198.

Witten, I.B., Steinberg, E.E., Lee, S.Y., Davidson, T.J., Zalocusky, K.A., Brodsky, M., Yizhar, O., Cho, S.L., Gong, S., Ramakrishnan, C., et al. (2011). Recombinase-driver rat lines: tools, techniques, and optogenetic application to dopamine-mediated reinforcement. Neuron *72*, 721–733.

Wohleb, E.S., Hanke, M.L., Corona, A.W., Powell, N.D., Stiner, L.M., Bailey, M.T., Nelson, R.J., Godbout, J.P., and Sheridan, J.F. (2011). β-Adrenergic receptor antagonism prevents anxiety-like behavior and microglial reactivity induced by repeated social defeat. J. Neurosci. Off. J. Soc. Neurosci. *31*, 6277–6288.

Wu, Z., Autry, A.E., Bergan, J.F., Watabe-Uchida, M., and Dulac, C.G. (2014). Galanin neurons in the medial preoptic area govern parental behaviour. Nature *509*, 325–330.

Chapter 6

Determining the downstream receptor and projection targets that mediate locus coeruleus-induced negative affective behaviors

Author contributions for the above citation:
*co-first author **J.G.M,** E.R.S., and M.R.B. designed all of the experiments and wrote the paper. **J.G.M.** performed all of the experiments except for the fast scan cyclic voltammetry (FSCV). E.R.S. and S.L.A. performed the immunohistochemistry. **J.G.M** and E.R.S. performed the *in vivo* electrophysiology experiments together and E.R.S analyzed the *in vivo* electrophysiology data. E.R.S. analyzed the behavior for Figures 6.6 & 6.7. Z.A. McElligot performed and analyzed the FSCV. G.D.S. supervised the FSCV. M.R.B. oversaw all of the work and helped write the paper. A similar, though distinct, chapter is contained in the dissertation of E.R.S. E.R.S. made the layouts for Figures 6.2-6.7.

SUMMARY

Increased tonic activity of locus coeruleus noradrenergic (LC-NE) neurons induces anxiety-like and aversive behavior. While some information is known about the afferent circuitry that endogenously drives this neural activity and behavior, the downstream receptors and anatomical projection targets that mediate these behaviors remain unresolved. Here we use a combination of *in vivo* optogenetics, behavioral pharmacology, single-unit electrophysiology and fast scan cyclic voltammetry to determine the neural substrates downstream of LC-NE activity. We show that β-adrenergic receptors mediate the anxiety-like phenotype of increased tonic LC-NE activity, while α1-adrenergic receptors mediate the real-time place aversion. Additionally, we demonstrate that norepinephrine release in the basolateral amygdala (BLA) alters BLA activity and increases anxiety-like and conditioned aversive behaviors, but not real-time place preference. These studies begin to illustrate how the complex efferent system of the LC-NE system selectively mediates different behaviors through distinct receptor and projection-selective mechanisms.

INTRODUCTION

After determining that increased tonic activity of LC-NE neurons drives negative affective behaviors in **Chapter** 5, we next sought to determine the downstream components of this system towards driving anxiety. Though **Chapter 5** investigated the circuitry upstream of the LC, we were careful to make our conclusions based on LC-NE cell activity rather than on downstream effectors (e.g. receptors, anatomical targets). With at least nine different adrenergic receptors and three different galanin receptors, that have nearly all been indicated in anxiety-like behaviors (Brunner et al., 2014; Dixit et al., 2014; Hanke et al., 2012; Kuteeva et al., 2008; Le

260

Maître et al., 2013; Mantsch et al., 2010; Raskind et al., 2007; Wohleb et al., 2011) and a widespread projection network through the brain and spinal cord (Berridge and Waterhouse, 2003; Sara, 2009), the downstream targets for these behaviors could quickly become complicated. The LC sends dense neuronal projections to the amygdala and extended amygdala, which are thought to be responsible for the widely known role of norepinephrine (NE) in affective behaviors (Berridge and Waterhouse, 2003; Davis, 1992; Valentino and Aston-Jones, 2010). In particular, noradrenergic cell firing in the LC has been shown to increase in the context of stressful stimuli (Abercrombie and Jacobs, 1987a, 1987b; Aston-Jones et al., 1999; Mana and Grace, 1997). While the anatomical projections from the LC and their cell types have been studied for several years, the precise mechanisms by which the LC generates its influence over basolateral amygdala (BLA) function remain undefined. In particular, how the LC-BLA projection integrates affective behavioral responses via specific receptor systems and cell activity is unknown.

To determine what downstream receptor systems might be involved in the anxiety-like and aversive behavior induced by high tonic LC-NE activity, we replicated experiments from **Chapter 5** (**Figure 5.4 and 5.6**) with systemic antagonism of either β-adrenergic receptors or α1-adrenergic receptors. These pilot experiments unexpectedly reveal that the observed anxiety-like and real-time aversion behaviors are mediated through different receptor systems. To determine the role of noradrenergic influence on BLA function and negative affective behavior we utilized optogenetic control of LC-NE inputs into the BLA. Here we directly tested whether NE release from LC terminals into the BLA can drive anxiety-like and aversive behavioral responses. We demonstrate that photostimulation of LC projections to the amygdala releases NE

to cause localized excitability. This increased noradrenergic tone is sufficient to produce anxiety-like and conditioned aversive behaviors.

RESULTS

The anxiety-like component of increased LC-NE tonic neuronal firing is mediated through β-adrenergic receptor activation

Using the same optogenetic strategy described in **Chapter 5** (**Figure 5.4**), we tested whether systemic antagonism could block the anxiogenic behavioral response induced by selectively increasing LC-NE tonic firing. 30 minutes prior to behavioral testing, we pre-treated animals with either the non-selective β-adrenergic receptor antagonist Propranolol HCl (10 mg/kg, i.p., Tocris) (Al-Hasani et al., 2013), the α1-adrenergic antagonist Prazosin HCl (1 mg/kg, Sigma) (Bortolozzi and Artigas, 2003), or a vehicle control. We next photostimulated (5 Hz, 10 ms pulse width, 473 nm) LC-NE neurons during access to elevated zero maze (EZM) (Choleris et al., 2001; Shepherd et al., 1994) (**Figure 6.1A & B**). As we saw in **Chapter 5,** 5 Hz photostimulation in the EZM induced anxiety-like behavior in *Th*-Cre[+] animals expressing ChR2 in the LC compared to *Th*-Cre[-] control animals that do not express ChR2 (**Figure 6.1C**). *Th*-Cre[+] animals that were pre-treated with Propranolol were not significantly different from controls, indicating that β-adrenergic antagonism blocked the effect of LC-NE photostimulation (**Figure 6.1C**). Importantly, this was not the case in the animals treated with Prazosin (**Figure 6.1C**). The blockade of α1-adrenergic receptors trended towards a more anxiogenic baseline state in the controls and a potentiation of the photostimulation-induced effect in the Cre[+] animals, but this trend was not significant. These experiments demonstrate that the anxiogenic state that is driven by increasing tonic firing of LC-NE neurons is meditated by β-adrenergic receptor activation.
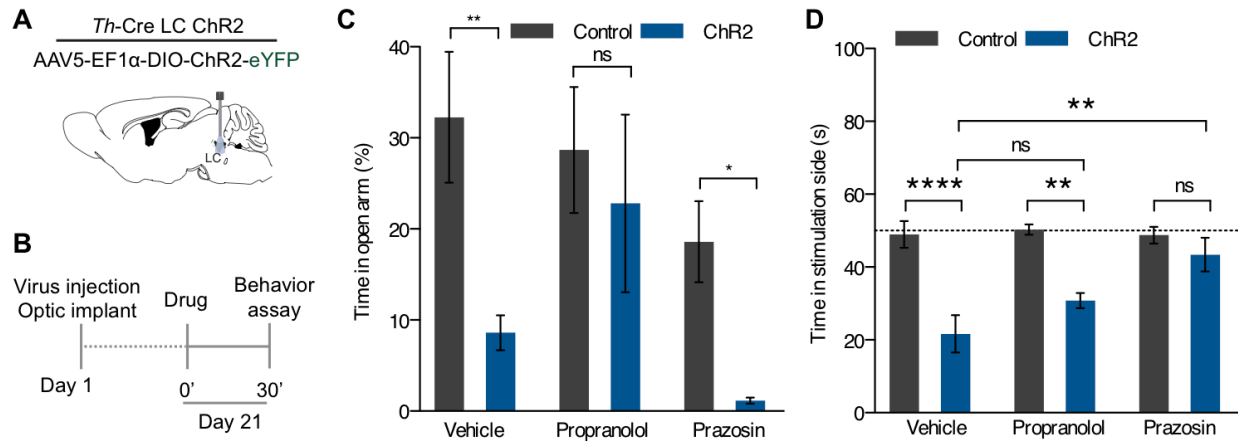
Figure 6.1 The anxiety-like and real-time place aversion behaviors induced by high tonic LC-NE activity are mediated by separate receptor systems. (A) Cartoon of viral and fiber optic delivery strategy. (B) Calendar of behavioral studies. (C) 5 Hz photostimulation causes an anxiety-like phenotype in EZM of *Th*-Cre[+] animals expressing ChR2 in the LC compared to *Th*-Cre[-] control animals that do not express ChR2. This effect is reversed by Propranolol pre-treatment, but not by Prazosin (Data represented as mean ± SEM, n=6-11/group; One-Way ANOVA, Bonferonni post-hoc, **p<0.01, *p<0.05, ns=no significance). (D) 5 Hz photostimulation causes a real-time place aversion in RTPT of *Th*-Cre[+] animals expressing ChR2 in the LC compared to *Th*-Cre[-] control animals that do not express ChR2. This effect is not reversed by Propranolol pre-treatment, but is by Prazosin (Data represented as mean ± SEM, n=6-10/group; One-Way ANOVA, Bonferonni post-hoc, ****p<0.0001, **p<0.01, ns=no significance).

The negative valence elicited by high tonic LC-NE activity is mediated by α1-adrenergic receptors

We next sought to determine whether this same systemic antagonism of β-adrenergic receptors could prevent the acute negative behavioral valence seen in the real-time place testing (RTPT) assay from **Chapter 5** (**Figure 5.6**). This assay assesses native behavioral preference to photostimulation (**see Chapters 4 & 5**) (Jennings et al., 2013; Kim et al., 2013a; Stamatakis and Stuber, 2012; Stamatakis et al., 2013; Tan et al., 2012). We previously demonstrated that 5 Hz photostimiluation of LC-NE neurons in this assay causes an aversion from the chamber paired with photostimulation (**Figure 5.6**). Similarly, when we replicated this experiment with vehicle controls, we see the same behavioral phenotype as before – *Th*-Cre+, ChR2-expressing animals have an aversion from the photostimulation-paired chamber compared to controls (**Figure 6.1D**). Surprisingly pre-treatment with Propranolol did not block this effect (**Figure 6.1D**). Even more unexpected, however, we found that pre-treatment with Prazosin did block the real-time place aversion (**Figure 6.1D**). These data suggest that the negative affective behaviors elicited by elevating LC tonic activity are separable behavior phenomenon. At the least the anxiety-like and real-time aversive components of these behaviors are mediate by different downstream receptor systems (anxiety-like behavior through β-adrenergic receptors and real-time aversion through α1-adrenergic receptors). Whether there is also a circuit-based mechanism for this segregation remains to be seen.

Optogenetic targeting of LC- NE neurons and their inputs to the BLA

After gaining some insight into the receptors through which increased tonic LC-NE activity induces behavioral responses, we next sought to test whether these same behaviors can

be generated by releasing NE at localized LC projection in the BLA. Using the same *Th*-Cre mice as above to genetically isolate LC-NE neurons, we injected Cre-dependent virus expressing channelrhodopsin-2 (AAV5-EF1α-DIO-ChR2-eYFP) into the LC and allowed six weeks for ChR2 expression to reach terminals within the BLA (LC-BLA[Th-Cre]; **Figures 6.2 A-D and 6.3 A,B**).
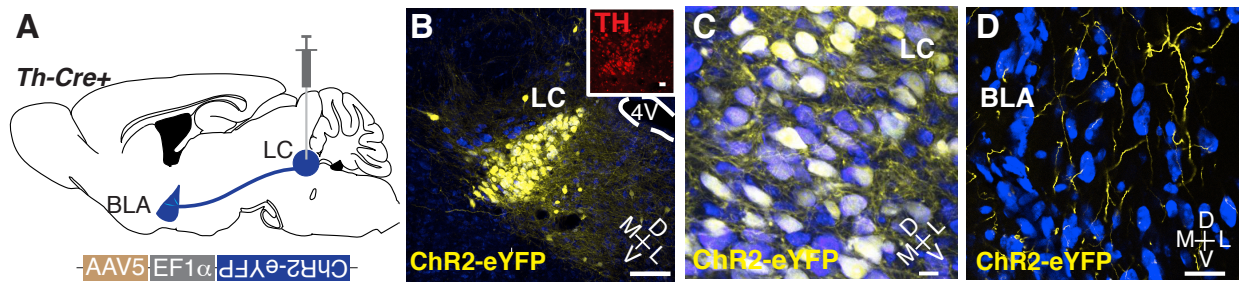
Figure 6.2 Expression of AAV5-EF1α-DIO-ChR2-eYFP in *Th*-Cre[+] mice. (A) Cartoon of viral injection and fiber optic implantation. **(B)** ChR2-eYFP (yellow), Nissl (blue), and tyrosine hydroxylase (TH; red) (inset, TH (red), scale bar = 25 μm) expression in LC (scale bar = 50 μm). **(C)** ChR2-eYFP (yellow) and Nissl (blue) in locus coeruleus (scale bar = 100 μm). **(D)** LC terminals expressing ChR2-eYFP (yellow) amongst BLA neurons (Nissl (blue)) (scale bar = 20 μm).
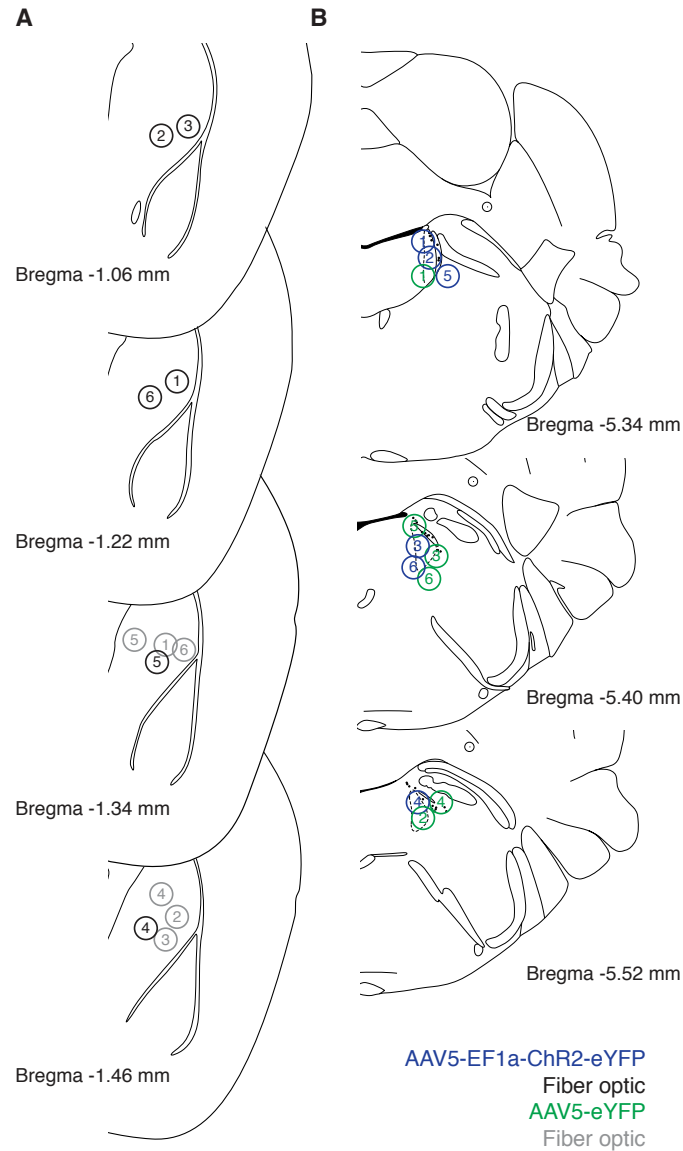
Figure 6.3 Viral expression and fiber optic hit maps in the LC and BLA, respectively, of
***Th*-Cre[+] mice (a)** Unilateral ferrule implant placement for AAV5-EF1α-DIO-ChR2-eYFP
(black) and AAV5-EF1α-DIO-eYFP (grey) in BLA for 6 individual animals each. **(b)** Unilateral
viral expression of AAV5-EF1α-DIO-ChR2-eYFP (blue) and AAV5-EF1α-DIO-eYFP (green)
in locus coeruleus for 6 individual animals each. Numbers indicate individual animals and viral
label was generally present throughout the intended target.

Photostimulation of LC-BLA terminals releases NE

In **Chapter 5**, we demonstrated optogenetic control of LC-NE neurons (**Figure 5.3**). However, these studies did not examine where the observed spiking activity caused release of neurotransmitters, particularly NE. To test whether photostimulation of LC-BLA$^{Th\text{-}Cre}$ projections resulted in NE release at terminals, we collaborated with the Stuber lab at the University of North Carolina (UNC). After injecting LC-BLA$^{Th\text{-}Cre}$ mice with AAV5-EF1α-DIO-ChR2-eYFP, we sent the animals to UNC for Zoe McElligot to acutely slice for fast-scan cyclic voltammetry (FSCV). A carbon fiber microelectrode was positioned in the amygdala and slices were stimulated with a 473 nm LED for 30x, 5-ms pulses at 10 Hz (**Figure 6.4A**). Oxidative and reductive currents were observed following photostimulation displaying characteristic catecholamine cyclic voltammograms and uptake similar to NE (t1/2 = 2.0 ± 0.2 s, **Figure 6.4B**). Following 20 minutes of consistent baseline NE oxidative current, 1 µM reserpine (an inhibitor of vesicular monoamine transporters) was perfused on the slices to deplete catecholamine from the terminals projecting from the LC (Dahlström et al., 1965). Reserpine treatment significantly depleted evoked terminal NE (31.6 +\- 1.0 % of baseline, **Figures 6.4C & D**) confirming optically-evoked NE release in this isolated LC-BLA$^{Th\text{-}Cre}$ projection. This study demonstrates that long-range BLA projections from the LC can be photostimulated to induce NE release.

Photostimulation of LC-BLA terminals modulates

BLA neurons have well reported responses to exogenous application of NE (Buffalari and Grace, 2007). We next sought to determine if the optically-evoked endogenous NE release would mimic the responses of BLA neurons to exogenous NE. To do so, we examined BLA single-unit activity in LC-BLA$^{Th\text{-}Cre}$ mice using 16-channel microelectrode arrays coupled to a fiber optic implant (optrode arrays) (Sparta et al., 2011). These optrode arrays were used to isolate and
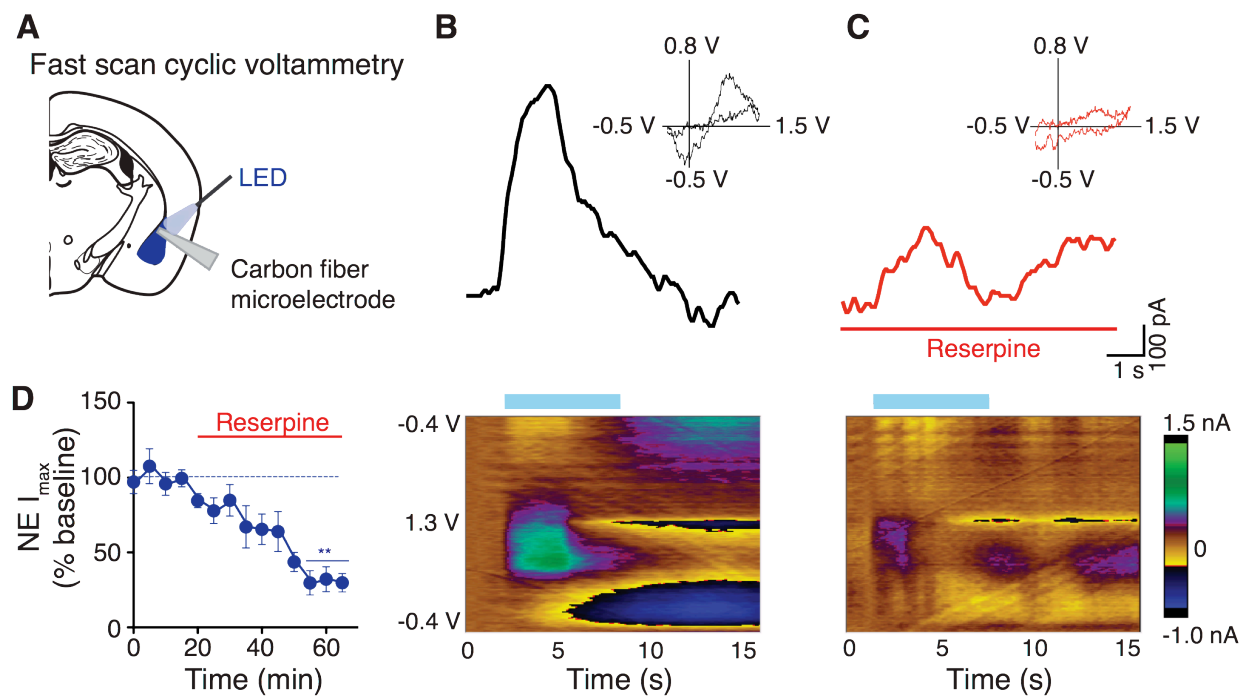
Figure 6.4 Photostimulation of locus coeruleus terminals in the BLA releases norepinephrine. (**A**) Fast scan cyclic voltammetry schematic. (**B-C**) Oxidative and reductive currents (with representative voltammograms below) in response to photostimulation are attenuated by reserpine (1 µM). (**D**) Attenuation in NE oxidative current in response to reserpine (1 µM; **p < 0.01; paired Student's t-tests to baseline; n = 3 pairs; mean ± S.E.M).
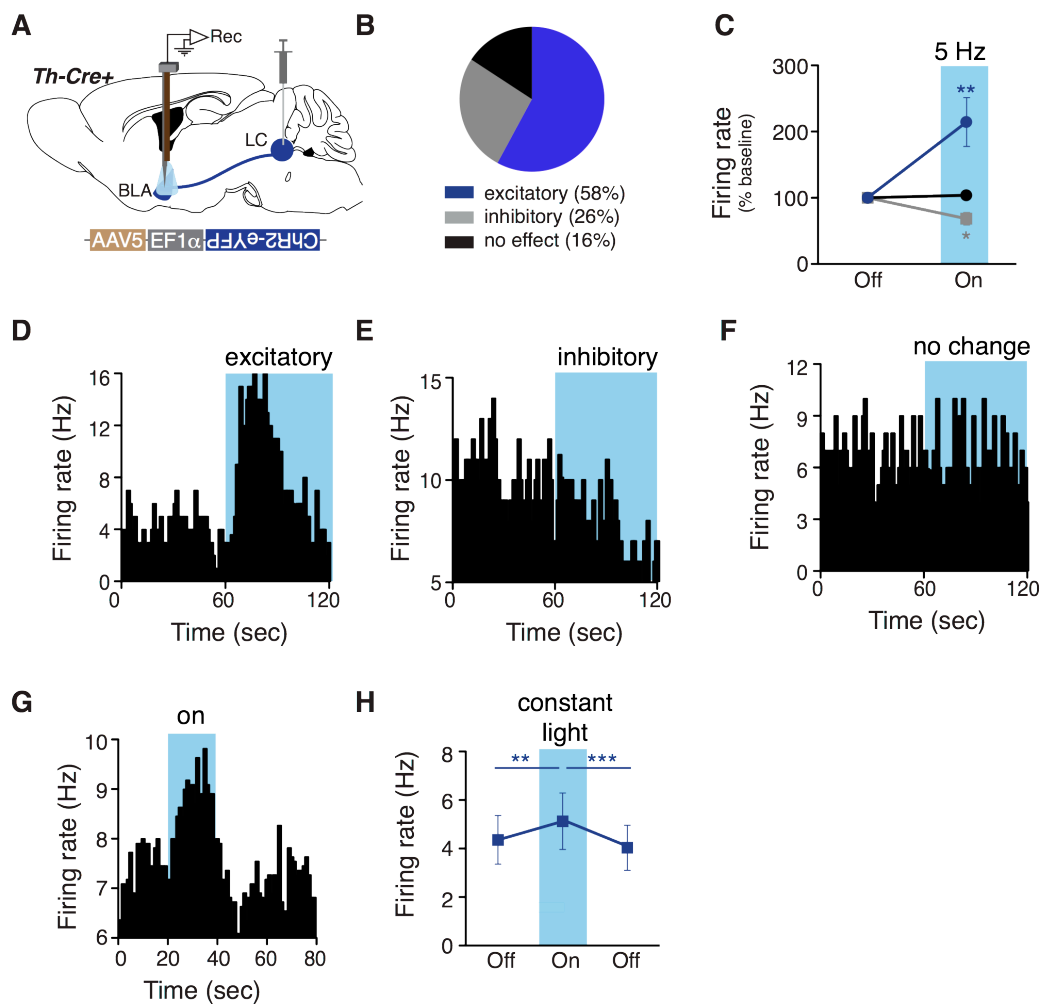
Figure 6.5. Photostimulation of LC terminals in the BLA alters neuronal excitability. (A) Schematic illustrating single-unit extracellular recording paradigm of BLA neurons presynaptically modulated by ChR2-expressing LC-BLA terminals. **(B)** Distribution of differential firing rates present in BLA neurons following LC-BLA terminal photostimlation. **(C)** Photostimulation (5 Hz) of LC terminals in the BLA shows neurons that either increase (excitatory; blue; n = 12; **$p < 0.01$, paired Student's t-test), decrease (inhibitory; grey; n = 5; *$p < 0.05$, paired Student's t-test), or show no change (black; n = 3) in firing rate. Representative histograms (1 sec bin) of isolated single-units showing increase **(D)**, decrease **(E)**, or no change **(F),** in neuronal firing in response to photostimulation (473 nm, 5 Hz, 3 min). **(G)** Representative histogram (1 sec bin) of isolated single-unit shows an increase in neuronal firing in response to constant photostimulation (473, constant light, 20 sec, 5 mW). **(H)** Neuronal firing rate increases in response to 20 sec (473 nm, constant light) photostimulation and returns to baseline values in the absence of light (** $p < 0.01$, ***$p < 0.001$, One-Way Repeated Measures ANOVA followed by Bonferroni post hoc comparison test).

record BLA single-unit activity before, during, and after photostimulation of LC-BLA$^{Th\text{-}Cre}$ projections (473 nm, 5 Hz, 10 ms pulse width) (**Figure 6.5A**). In these experiments photostimulation of LC-BLA$^{Th\text{-}Cre}$ terminals caused a significant increase in firing frequency in 58% of units recorded in the BLA, while some cells showed inhibitory responses (26%), and some showed no response (16%) (**Figures 6.5B-F**). Responses are also shown from isolated units receiving constant light stimulation (**Figures 6.5G,H**). Together, these heterogeneous firing properties are consistent with previous studies using iontophoresis of norepinephrine to the region, and further highlight the complex pharmacological activity of NE in this structure (Buffalari and Grace, 2007; Ferry et al., 1997; Huang et al., 1996). These results demonstrate that photostimulation of LC terminals in the BLA causes varied responses in BLA firing rate, with a majority of observed units increasing in response the terminal photostimulation.

Optogenetic targeting of LC-NE projections to the BLA promotes anxiety-like behavior

After identifying the LC terminals to the BLA as a projecting source of NE, which is capable of increasing BLA activity, we next sought to test whether stimulation of these terminals would drive similar behavioral profiles to direct LC-NE stimulation. Fiber optics were implanted at LC-NE terminal sites in the BLA of LC-BLA$^{Th\text{-}Cre}$ mice (**Figures 6.6A and 6.3A & B**). Photostimulation of LC-BLA$^{Th\text{-}Cre}$ terminals using the parameters that induce anxiety-like behavior at LC-NE cell bodies in **Chapter 5** (5 Hz) resulted in a significant decrease in time spent in the open area of the elevated zero maze (EZM) (**Figures 6.6B & C**) with no significant change in general locomotor activity (**Figures 6.6D-F**). This experiment shows stimulation of a subset of LC-NE fibers, only those projecting to the BLA, is sufficient to induce anxiety-like behavior.

271
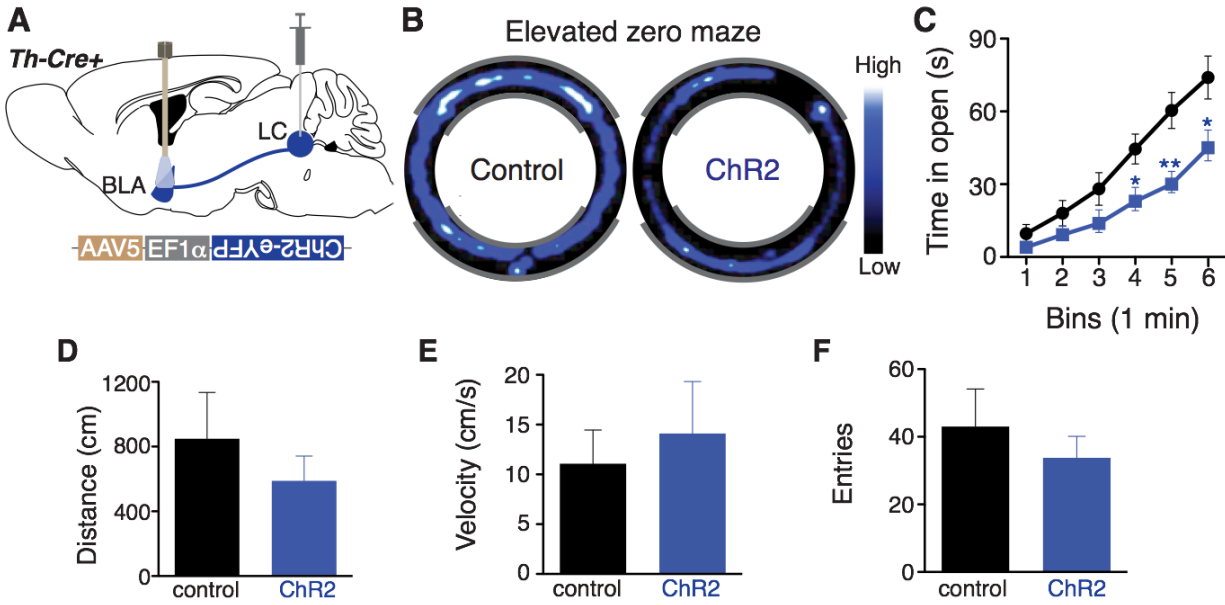
Figure 6.6. Photostimulation of LC terminals in the BLA induces anxiety-like behavior. (**A**) Viral injection and fiber optic implants in LC-BLA[Th-Cre] mice. (**B**) Colorized heat maps of elevated zero maze activity (EZM) of control and ChR2 animals. (**C**) Cumulative open arm time course of photostimulated ChR2 (blue, n = 8) and control animals (black; n = 7) (5 Hz, 10 ms pulses; * $p < 0.05$, ** $p < 0.01$, via multiple Student's t-tests; mean ± SEM). Control (black; n = 6) and ChR2 (blue; n = 8) expressing animals: travel similar distances (**D**), have similar velocities (**E**), and make similar number of entries (**F**) into open arms of EZM.

21

LC-BLA$^{Th\text{-}Cre}$ terminal stimulation is sufficient to condition place aversion, but does not drive a real-time place aversion

Following the observation that stimulation of LC-BLA fibers alone is capable of driving anxiety-like behaviors, we next tested whether this same stimulation produces a learned change in behavior. Similarly to **Chapter 5**, (**Figure 5.6**) we employed a Pavlovian conditioned place aversion (CPA) assay (Bruchas et al., 2009; Al-Hasani et al., 2013; Land et al., 2008, 2009). When allowed to freely explore both chambers following two conditioning days of photostimulation of LC-BLA$^{Th\text{-}Cre}$ terminals (5 Hz, 10 ms), the animals expressing ChR2-eYFP spent significantly less time in the chamber that was paired with photostimulation compared to eYFP-expressing controls (**Figure 6.7A-C**). Neither group of mice had significant changes in locomotor activity before, during, or after conditioning (**Figure 6.7D**). These results suggest that the negative affect produced by LC-BLA$^{Th\text{-}Cre}$ photostimulation is capable of being learned and biasing behavior away from contexts in which the experience took place. This finding is also consistent with prior work showing a role for noradrenergic influence in fear-related memory formation (Debiec and Ledoux, 2004).

These experiments, however, do not assess whether or not the stimulation itself has a negative valence. Surprisingly, when LC-BLA$^{Th\text{-}Cre}$ animals are tested in the RTPT paradigm there was no aversion at either 5 Hz (**Figures 6.7E & F**) or 60 Hz photostimulation (**Figures 6.7G & H**). This finding is particularly interesting in light of the systemic pharmacology experiments (**Figure 6.1**) and suggests that perhaps the negative valence of LC-NE stimulation is produced via another circuit. It is also possible that the neuromodulatory effects on this circuit potentially require a learning component compared to acute activation of similar neurotransmitter pathways (GABA/Glutamate) (Haubensak et al., 2010; Kim et al., 2013a).

273
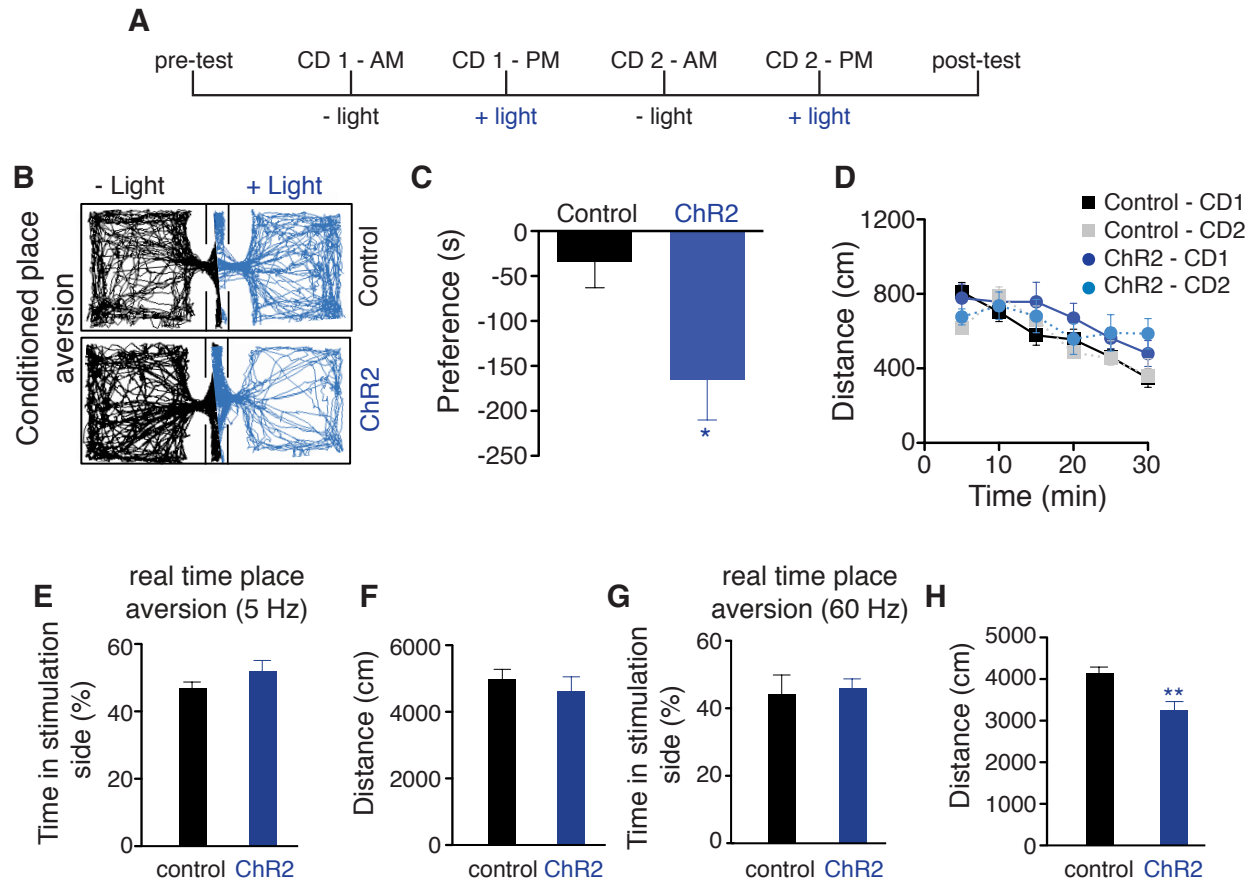
Figure 6.7. Photostimulation of LC terminals in the BLA induces aversive behavior. (**A**) Conditioned place aversion (CPA) behavioral diary. (**B**) Representative CPA traces. (**C**) ChR2 (blue; n = 9) show an aversive response to chamber paired with photostimulation compared to controls (black; n = 8) (*p < 0.05; unpaired t-test) following two days of conditioning with (**D**) no differences in locomotor behavior during conditioning day 1 (CD1) and or conditioning day 2 (CD2) in CPA. (**E**) ChR2 (blue; n = 9) and viral control mice (black; n = 9) do not show real-time place aversion to a photostimulation (5 Hz) paired chamber and (**F**) do not show any difference in distance traveled during real time place aversion. (**G**) ChR2 (blue; n = 5) and viral control mice (black; n = 4) do not show real time place aversion to a photostimulation (60 Hz) paired chamber. (**H**) ChR2 (blue; n =5) travel less distance than viral control mice (black; n = 4) in real-time place aversion with 60 Hz photostimulation.

23

Taken together these data suggest that LC-BLA projections release NE into the BLA, which can cause increased neuronal excitability and facilitate condition aversive and anxiety-like behavioral responses. It is possible that the neuronal activity responses and behavior are mediated by β-adrernergic receptors and unlikely to be mediated by α1-adrenergic receptors. These data provide a critical framework for understanding the downstream influence of the LC-NE system in the BLA as it relates to anxiety-like and aversive behavioral states.

DISCUSSION

Though LC-NE neurons contain numerous co-transmitters (Berridge and Waterhouse, 2003), NE is considered the primary effector released from these neurons. Here we show that NE activates multiple receptors for the generation of unique negative affective behaviors. The observation that these behaviors segregate by receptor system foreshadows an elegant, but complicated future in dissecting the role of the LC-NE system in behavior.

The BLA is an important component in the neural circuitry of negative affective behavior (Davidson, 2002; Davis, 1992). Activation of BLA cell bodies and their projections to the ventral hippocampus mediate anxiety-like behavior (Felix-Ortiz et al., 2013; Tye et al., 2011). The BLA receives noradrenergic input from the LC (Asan, 1998; Fallon et al., 1978) and NE increases in the BLA following stress events (Galvez et al., 1996; Hatfield et al., 1999). Here we use FSCV to show that Th^+ positive neurons from the LC release NE in the amygdala. Previous studies have demonstrated that noradrenergic cell firing in the LC increases tonic drive (5-8Hz) following stressful stimuli (see **Chapter 5**) (Abercrombie and Jacobs, 1987a, 1987b; Aston-Jones et al., 1999; Mana and Grace, 1997). We also demonstrate that selective activation of terminals from these neurons (5Hz) increases the excitatory drive of BLA neurons *in vivo*. Additionally, we show that stimulation of LC terminals in the BLA causes robust increases in

anxiety-like and conditioned aversive behavior suggesting a strong role of NE in mediating these behaviors. However, given that the LC terminals likely release more than NE, the postsynaptic neuronal responses and their subsequent behavioral outputs may potentially be mediated through a different mechanism of action. While there is some concern that photostimulation of LC-BLA$^{Th\text{-}Cre}$ causes backpropagating action potential to LC-NE cell bodies, the observation that this stimulation does not replicate all of the behavioral phenotypes seen in **Chapter 5** (i.e. no RTPT) suggests there is at least some degree of circuit isolation in these studies. Future work should strive to account for such a possibility either by genetically isolating the projection (Fenno et al., 2014) or pharmacologically inactivating backpropagation (Stuber et al., 2011).

To further solidify the role of NE in mediating anxiogenic behavior, future studies should combine photostimulation of LC-BLA$^{Th\text{-}Cre}$ with local infusion of adrenergic antagonists in the BLA. However, these data could prove difficult to interpret as antagonists would not target specific cell types and could "spill over" from the predominately glutamatergic BLA to the neighboring GABAergic CeA (Carlsen, 1988; McDonald, 1982; Smith and Paré, 1994). These experiments represent an ideal application of optofluidic neural probes (**Chapter 4**), where spatial restriction of both pharmacological agents and photostimulation will be required. While isolation of the specific contributions of different receptor subtypes to NE- mediated anxiety-like behavior and aversion could be challenging via classical pharmacological methods, other modern techniques, such as DREADD and optically-sensitive GPCRs, show potential in dissecting these contributions.

Taken together, our results demonstrate that LC-NE downstream influence on negative affective behaviors is an elegant and complex system likely involving many different postsynaptic receptor systems and anatomical projection targets. These findings have broad

implications for our understanding of the mechanisms of stress-induced and anxiety disorders and suggest that further study of these noradrenergic circuits and signaling pathways should greatly advance our current understanding of these pathologies.

MATERIALS & METHODS

Animals

Adult (25–35 g) male C57BL/6J and TH::IRES-Cre backcrossed to C57BL/6J mice were group-housed, given access to food and water ad libitum and maintained on a 12 h:12 h light:dark cycle. All animals were held in a facility in the lab 1 week prior to surgery, post-surgery and throughout the duration of the behavioral assays to minimize stress from transportation and disruption from foot traffic. All procedures were approved by the Animal Care and Use Committee of Washington University and conformed to US National Institutes of Health guidelines.

Viral preparation

Plasmids encoding pAAV-EF1α-DIO-eYFP [final titer 5 x 1012 vg/ml], pAAV-EF1α-double floxed-hChR2(H134R)-eYFP-WPRE-HGHpA [final titer 2 x 1013 vg/ml], were obtained from Addgene (Addgene.org) originally from the Deisseroth Laboratory at Stanford University. The DNA was amplified with a Maxiprep kit (Promega) and packaged into AAV5 serotyped viruses by the WUSTL Hope Center Viral Core.

Stereotaxic surgery

Mice were anaesthetized in an induction chamber (5% isoflurane) and placed in a stereotaxic frame (Kopf Instruments, Model 1900) where they were maintained at 1-2% isoflurane throughout the procedure. A craniotomy was performed and mice were injected as

follows. For locus coeruleus terminal studies, 1 μl of AAV5- DIO-ChR2 or AAV5-DIO-eYFP was injected unilaterally into the locus coeruleus at stereotaxic coordinates from bregma: -5.45 mm anterior-posterior (AP), ± 1.25 mm medial-lateral (ML), -3.65 mm dorsal-ventral (DV). Mice were then implanted with chronic fiber optic implants with coordinates adjusted from viral injection to 0.00 mm 30(AP), ± 0.25 mm (ML), and +1.00 mm (DV). The fiber optic implants were secured using two bone screws (CMA, 743102) and affixed with TitanBond (Horizon Dental Products) and dental cement (Lang Dental) (McCall et al., 2013). Mice were allowed to recover for at least 3-6 weeks prior to behavioral testing; this interval also permitted optimal AAV expression and Cre recombinase activity.

General Behavior Notes

Behavioral assays were performed in a sound attenuated room maintained at 23°C. Lighting was measured and stabilized at ~ 4 lux for anxiety tests and ~200 lux for place testing. All behavioral apparatuses were cleaned with 70% ethanol in between animals. In each assay, animals received constant photostimulation throughout the entire trial. AAV5-DIO-ChR2 and AAV5-DIO-eYFP animals received 5 ms pulses of 10 Hz photostimulation (473 nm). Movements were video recorded and analyzed using Ethovision Software.

Elevated Zero Maze (EZM)

The EZM (Harvard Apparatus) was made of grey plastic, 200 cm in circumference, comprised of four 50 cm sections (two opened and two closed). The maze was elevated 50 cm above the floor and had a path width of 4 cm with a 0.5 cm lip on each open section. Animals were connected to cables coupled to a function generator, positioned head first into a closed arm, and allowed to roam freely for 6 min. Mean open arm time was the primary measure of anxiety-like behavior.

Conditioned Place Aversion (CPA)

Mice were trained in an unbiased, balanced three compartment conditioning apparatus as previously described (Al-Hasani et al., 2013; Kim et al., 2013b). Briefly, mice were pre-tested by placing individual animals in the small central compartment and allowing them to explore the entire 31apparatus for 30 min. Time spent in each compartment was recorded with a video camera (ZR90; Canon) and analyzed using Ethovision 8.5 (Noldus). Mice were randomly assigned to light and no-light compartments and received no light in the morning and light (5 Hz for LC-BLA) in the afternoon at least 4 h after the morning training on two consecutive days. CPA was assessed on day 4 by allowing the mice to roam freely in all three compartments and recording the time spent in each. Scores were calculated by subtracting the time spent in the light stimulus-paired compartment post-test minus the pre-test.

Real Time Place Testing (RTPT)

Mice were placed into a custom-made unbiased, balanced two-compartment conditioning apparatus (52.5 x 25.5 x 25.5 cm) as previously described (Stamatakis and Stuber, 2012) and allowed to freely roam the entire apparatus for 20 min. Entry into one compartment triggered constant photostimulation (5 Hz for LC-BLA; ~10 mW light power) while the animal remained in the light-paired chamber. Entry into the other chamber ended the photostimulation. The side paired with photostimulation was counterbalanced across mice. Time spent in each chamber and total distance traveled for the entire 20 min trial was measured using Ethovision 8.5 (Noldus). Data are expressed as mean +/- S.E.M percent time spent in photostimulation-paired chamber.

Voltammetry

Slice voltammetry experiments were performed as previously described (Stamatakis et al., 2013). Briefly, mice were anesthetized (Euthasol) and perfused with ice-cold sucrose aCSF (in

mM: 225 sucrose, 119 NaCl, 1.0 NaH2PO4, 4.9 MgCl2, 0.1 CaCl2, 26.2 NaHCo3, 1.25 glucose). Following rapid decapitation, slices were prepared 32 on a vibratome (VT-1000, Leica Microsystems) and allowed to rest for at least 30 min in oxygenated aCSF (in mM: 119 NaCl, 2.5 KCl, 1.0 NaH2PO4, 1.3 MgCl2, 2.5 CaCl2, 26.2 NaHCO3, and 11 glucose) at 35oC prior to placement in the recording chamber where slices were perfused with oxygenated aCSF at 37oC at a rate of 2 ml/min. Carbon fiber microelectrodes (CFME, 75 μm in length) were lowered into 300 μM coronal slices and placed where the densest ChR2-eYFP expression was observed (CeA/BLA border) of THLC::ChR2 mice. To detect NE, the CFME was ramped from -0.4 V to 1.3 V versus a Ag/AgCl reference electrode (in the bath) at a rate of 400 V/s at 10 Hz. Slices were stimulated with 30 pulses of a blue LED (Thorlabs, 473 nm, 5 ms pulse width, 1 mW) via a 40X objective at 10 Hz every 5 minutes to release NA. Electrochemical data was collected and analyzed via custom software (Tar Heel CV, HD CV, Labview). Following collection, background subtracted cyclic voltammograms (CVs) were transformed with a Fast Fourier Transformation (Bucher et al., 2013). CVs had characteristic oxidation and reduction peaks coinciding with catecholamine detection (ox: 600-700 mV red: -200-300 mV). Oxidative currents were analyzed at the peak of the oxidative potential for individual experiments. Clearance half-life (t1/2) was measured in Clampfit 10.2 (Molecular devices) as previously described (McElligott et al., 2013).

In vivo electrophysiology

Spontaneous single unit activity was recorded as previously described (Kim et al., 2013b; Sparta et al., 2011). Briefly, mice were lightly anesthetized (1% isoflurane), placed in a stereotactic frame and two skull screws were placed on either side of the midline to ground the electrode array. The recording apparatus consisted of a 16-channel (35-μm tungsten wires, 150-

μm spacing between wires, 150-33 μm spacing between rows, Innovative Physiology) electrode array. This array was epoxied to a fiber optic and lowered into the BLA (stereotaxic coordinates from bregma: -1.3 mm (AP), ± 2.9 mm (ML) and -4.9 mm (DV). Extracellular recordings were taken from LC-BLA$^{Th\text{-}Cre}$ mice   and its corresponding viral control mice. Spontaneous and photostimulated neuronal activity was recorded from each electrode, bandpass-filtered with activity between 250 and 8,000 Hz, and analyzed as spikes. Voltage signals were amplified and digitally converted using OmniPlex and PlexControl (Plexon). For LC-BLA$^{Th\text{-}Cre}$ recordings, 3 min of baseline recordings were made followed by 3 min of 5 Hz photostimulation (10 ms pulses, 10 mW) and then another 3 min post- stimulation (off, on, off). Principle component analysis and/or evaluation of t-distribution with expectation maximization was used to sort spikes using Offline Sorter (Plexon).

Statistics/Data Analysis

All data are expressed as mean ± SEM. Statistical significance was taken as *p < 0.05, **p < 0.01, ***p < 0.001, as determined by the Student's t-test (paired and unpaired): One-Way Analysis of Variance (ANOVA) or One-Way Repeated Measures ANOVA, followed by Dunnett's or Bonferroni post hoc tests as appropriate. Statistical analyses were performed in GraphPad Prism 5.0.

REFERENCES

Abercrombie, E.D., and Jacobs, B.L. (1987a). Single-unit response of noradrenergic neurons in the locus coeruleus of freely moving cats. I. Acutely presented stressful and nonstressful stimuli. J. Neurosci. Off. J. Soc. Neurosci. *7*, 2837–2843.

Abercrombie, E.D., and Jacobs, B.L. (1987b). Single-unit response of noradrenergic neurons in the locus coeruleus of freely moving cats. II. Adaptation to chronically presented stressful stimuli. J. Neurosci. Off. J. Soc. Neurosci. *7*, 2844–2848.

Asan, E. (1998). The catecholaminergic innervation of the rat amygdala. Adv. Anat. Embryol. Cell Biol. *142*, 1–118.

Aston-Jones, G., Rajkowski, J., and Cohen, J. (1999). Role of locus coeruleus in attention and behavioral flexibility. Biol. Psychiatry *46*, 1309–1320.

Berridge, C.W., and Waterhouse, B.D. (2003). The locus coeruleus-noradrenergic system: modulation of behavioral state and state-dependent cognitive processes. Brain Res. Brain Res. Rev. *42*, 33–84.

Bortolozzi, A., and Artigas, F. (2003). Control of 5-hydroxytryptamine release in the dorsal raphe nucleus by the noradrenergic system in rat brain. Role of alpha-adrenoceptors. Neuropsychopharmacol. Off. Publ. Am. Coll. Neuropsychopharmacol. *28*, 421–434.

Bruchas, M.R., Land, B.B., Lemos, J.C., and Chavkin, C. (2009). CRF1-R activation of the dynorphin/kappa opioid system in the mouse basolateral amygdala mediates anxiety-like behavior. PloS One *4*, e8528.

Brunner, S.M., Farzi, A., Locker, F., Holub, B.S., Drexel, M., Reichmann, F., Lang, A.A., Mayr, J.A., Vilches, J.J., Navarro, X., et al. (2014). GAL3 receptor KO mice exhibit an anxiety-like phenotype. Proc. Natl. Acad. Sci. U. S. A. *111*, 7138–7143.

Bucher, E.S., Brooks, K., Verber, M.D., Keithley, R.B., Owesson-White, C., Carroll, S., Takmakov, P., McKinney, C.J., and Wightman, R.M. (2013). Flexible software platform for fast-scan cyclic voltammetry data acquisition and analysis. Anal. Chem. *85*, 10344–10353.

Buffalari, D.M., and Grace, A.A. (2007). Noradrenergic modulation of basolateral amygdala neuronal activity: opposing influences of alpha-2 and beta receptor activation. J. Neurosci. Off. J. Soc. Neurosci. *27*, 12358–12366.

Carlsen, J. (1988). Immunocytochemical localization of glutamate decarboxylase in the rat basolateral amygdaloid nucleus, with special reference to GABAergic innervation of amygdalostriatal projection neurons. J. Comp. Neurol. *273*, 513–526.

Choleris, E., Thomas, a W., Kavaliers, M., and Prato, F.S. (2001). A detailed ethological analysis of the mouse open field test: effects of diazepam, chlordiazepoxide and an extremely low frequency pulsed magnetic field. Neurosci. Biobehav. Rev. *25*, 235–260.

Dahlström, A., Fuxe, K., and Hillarp, N.-åke (1965). Site of Action of Reserpine. Acta Pharmacol. Toxicol. (Copenh.) *22*, 277–292.

Davidson, R.J. (2002). Anxiety and affective style: role of prefrontal cortex and amygdala. Biol. Psychiatry *51*, 68–80.

Davis, M. (1992). The role of the amygdala in fear and anxiety. Annu. Rev. Neurosci. *15*, 353–375.

Debiec, J., and Ledoux, J.E. (2004). Disruption of reconsolidation but not consolidation of auditory fear conditioning by noradrenergic blockade in the amygdala. Neuroscience *129*, 267–272.

Dixit, M.P., Thakre, P.P., Pannase, A.S., Aglawe, M.M., Taksande, B.G., and Kotagale, N.R. (2014). Imidazoline binding sites mediates anticompulsive-like effect of agmatine in marble-burying behavior in mice. Eur. J. Pharmacol. *732*, 26–31.

Fallon, J.H., Koziell, D.A., and Moore, R.Y. (1978). Catecholamine innervation of the basal forebrain. II. Amygdala, suprarhinal cortex and entorhinal cortex. J. Comp. Neurol. *180*, 509–532.

Felix-Ortiz, A.C., Beyeler, A., Seo, C., Leppla, C.A., Wildes, C.P., and Tye, K.M. (2013). BLA to vHPC inputs modulate anxiety-related behaviors. Neuron *79*, 658–664.

Fenno, L.E., Mattis, J., Ramakrishnan, C., Hyun, M., Lee, S.Y., He, M., Tucciarone, J., Selimbeyoglu, A., Berndt, A., Grosenick, L., et al. (2014). Targeting cells with single vectors using multiple-feature Boolean logic. Nat. Methods *11*, 763–772.

Ferry, B., Magistretti, P.J., and Pralong, E. (1997). Noradrenaline modulates glutamate-mediated neurotransmission in the rat basolateral amygdala in vitro. Eur. J. Neurosci. *9*, 1356–1364.

Galvez, R., Mesches, M.H., and McGaugh, J.L. (1996). Norepinephrine release in the amygdala in response to footshock stimulation. Neurobiol. Learn. Mem. *66*, 253–257.

Hanke, M.L., Powell, N.D., Stiner, L.M., Bailey, M.T., and Sheridan, J.F. (2012). Beta adrenergic blockade decreases the immunomodulatory effects of social disruption stress. Brain. Behav. Immun. *26*, 1150–1159.

Al-Hasani, R., McCall, J.G., Foshage, A.M., and Bruchas, M.R. (2013). Locus Coeruleus Kappa Opioid Receptors modulate Reinstatement of Cocaine Place Preference through a Noradrenergic Mechanism. Neuropsychopharmacology.

Hatfield, T., Spanis, C., and McGaugh, J.L. (1999). Response of amygdalar norepinephrine to footshock and GABAergic drugs using in vivo microdialysis and HPLC. Brain Res. *835*, 340–345.

Haubensak, W., Kunwar, P.S., Cai, H., Ciocchi, S., Wall, N.R., Ponnusamy, R., Biag, J., Dong, H.-W., Deisseroth, K., Callaway, E.M., et al. (2010). Genetic dissection of an amygdala microcircuit that gates conditioned fear. Nature *468*, 270–276.

Huang, C.C., Hsu, K.S., and Gean, P.W. (1996). Isoproterenol potentiates synaptic transmission primarily by enhancing presynaptic calcium influx via P- and/or Q-type calcium channels in the rat amygdala. J. Neurosci. Off. J. Soc. Neurosci. *16*, 1026–1033.

Jennings, J.H., Sparta, D.R., Stamatakis, A.M., Ung, R.L., Pleil, K.E., Kash, T.L., and Stuber, G.D. (2013). Distinct extended amygdala circuits for divergent motivational states. Nature *496*, 224–228.

Kim, S.-Y., Adhikari, A., Lee, S.Y., Marshel, J.H., Kim, C.K., Mallory, C.S., Lo, M., Pak, S., Mattis, J., Lim, B.K., et al. (2013a). Diverging neural pathways assemble a behavioural state from separable features in anxiety. Nature *496*, 219–223.

Kim, T., McCall, J.G., Jung, Y.H., Huang, X., Siuda, E.R., Li, Y., Song, J., Song, Y.M., Pao, H.A., Kim, R.-H., et al. (2013b). Injectable, Cellular-Scale Optoelectronics with Applications for Wireless Optogenetics. Science *340,* 211–216.

Kuteeva, E., Wardi, T., Lundström, L., Sollenberg, U., Langel, U., Hökfelt, T., and Ogren, S.O. (2008). Differential role of galanin receptors in the regulation of depression-like behavior and monoamine/stress-related genes at the cell body level. Neuropsychopharmacol. Off. Publ. Am. Coll. Neuropsychopharmacol. *33*, 2573–2585.

Land, B.B., Bruchas, M.R., Lemos, J.C., Xu, M., Melief, E.J., and Chavkin, C. (2008). The dysphoric component of stress is encoded by activation of the dynorphin kappa-opioid system. J. Neurosci. Off. J. Soc. Neurosci. *28*, 407–414.

Land, B.B., Bruchas, M.R., Schattauer, S., Giardino, W.J., Aita, M., Messinger, D., Hnasko, T.S., Palmiter, R.D., and Chavkin, C. (2009). Activation of the kappa opioid receptor in the dorsal raphe nucleus mediates the aversive effects of stress and reinstates drug seeking. Proc. Natl. Acad. Sci. U. S. A. *106*, 19168–19173.

Le Maître, E., Barde, S.S., Palkovits, M., Diaz-Heijtz, R., and Hökfelt, T.G.M. (2013). Distinct features of neurotransmitter systems in the human brain with focus on the galanin system in locus coeruleus and dorsal raphe. Proc. Natl. Acad. Sci. U. S. A. *110,* E536–E545.

Mana, M.J., and Grace, A.A. (1997). Chronic cold stress alters the basal and evoked electrophysiological activity of rat locus coeruleus neurons. Neuroscience *81*, 1055–1064.

Mantsch, J.R., Weyer, A., Vranjkovic, O., Beyer, C.E., Baker, D. a, and Caretta, H. (2010). Involvement of Noradrenergic Neurotransmission in the Stress- but not Cocaine-Induced Reinstatement of Extinguished Cocaine-Induced Conditioned Place Preference in Mice: Role for beta-2 Adrenergic Receptors. Neuropsychopharmacol. Off. Publ. Am. Coll. Neuropsychopharmacol. *35*, 2165–2178.

McDonald, A.J. (1982). Cytoarchitecture of the central amygdaloid nucleus of the rat. J. Comp. Neurol. *208*, 401–418.

McElligott, Z.A., Fox, M.E., Walsh, P.L., Urban, D.J., Ferrel, M.S., Roth, B.L., and Wightman, R.M. (2013). Noradrenergic synaptic function in the bed nucleus of the stria terminalis varies in animal models of anxiety and addiction. Neuropsychopharmacol. Off. Publ. Am. Coll. Neuropsychopharmacol. *38*, 1665–1673.

Raskind, M.A., Peskind, E.R., Hoff, D.J., Hart, K.L., Holmes, H.A., Warren, D., Shofer, J., O'Connell, J., Taylor, F., Gross, C., et al. (2007). A parallel group placebo controlled study of prazosin for trauma nightmares and sleep disturbance in combat veterans with post-traumatic stress disorder. Biol. Psychiatry *61*, 928–934.

Sara, S.J. (2009). The locus coeruleus and noradrenergic modulation of cognition. Nat. Rev. Neurosci. *10*, 211–223.

Shepherd, J.K., Grewal, S.S., Fletcher, A., Bill, D.J., and Dourish, C.T. (1994). Behavioural and pharmacological characterisation of the elevated "zero-maze" as an animal model of anxiety. Psychopharmacology (Berl.) *116*, 56–64.

Smith, Y., and Paré, D. (1994). Intra-amygdaloid projections of the lateral nucleus in the cat: PHA-L anterograde labeling combined with postembedding GABA and glutamate immunocytochemistry. J. Comp. Neurol. *342*, 232–248.

Sparta, D.R., Stamatakis, A.M., Phillips, J.L., Hovelsø, N., van Zessen, R., and Stuber, G.D. (2011). Construction of implantable optical fibers for long-term optogenetic manipulation of neural circuits. Nat. Protoc. *7*, 12–23.

Stamatakis, A.M., and Stuber, G.D. (2012). Activation of lateral habenula inputs to the ventral midbrain promotes behavioral avoidance. Nat. Neurosci. *15*, 1105–1107.

Stamatakis, A.M., Jennings, J.H., Ung, R.L., Blair, G.A., Weinberg, R.J., Neve, R.L., Boyce, F., Mattis, J., Ramakrishnan, C., Deisseroth, K., et al. (2013). A unique population of ventral tegmental area neurons inhibits the lateral habenula to promote reward. Neuron *80*, 1039–1053.

Stuber, G.D., Sparta, D.R., Stamatakis, A.M., van Leeuwen, W.A., Hardjoprajitno, J.E., Cho, S., Tye, K.M., Kempadoo, K.A., Zhang, F., Deisseroth, K., et al. (2011). Excitatory transmission from the amygdala to nucleus accumbens facilitates reward seeking. Nature *475*, 377–380.

Tan, K.R., Yvon, C., Turiault, M., Mirzabekov, J.J., Doehner, J., Labouèbe, G., Deisseroth, K., Tye, K.M., and Lüscher, C. (2012). GABA neurons of the VTA drive conditioned place aversion. Neuron *73*, 1173–1183.

Tye, K.M., Prakash, R., Kim, S.-Y., Fenno, L.E., Grosenick, L., Zarabi, H., Thompson, K.R., Gradinaru, V., Ramakrishnan, C., and Deisseroth, K. (2011). Amygdala circuitry mediating reversible and bidirectional control of anxiety. Nature *471*, 358–362.

Valentino, R., and Aston-Jones, G. (2010). Special issue on neuropeptides in stress and addiction: Overview. Brain Res. *1314*, 1–2.

Wohleb, E.S., Hanke, M.L., Corona, A.W., Powell, N.D., Stiner, L.M., Bailey, M.T., Nelson, R.J., Godbout, J.P., and Sheridan, J.F. (2011). β-Adrenergic receptor antagonism prevents anxiety-like behavior and microglial reactivity induced by repeated social defeat. J. Neurosci. Off. J. Soc. Neurosci. *31*, 6277–6288.

Chapter 7

Further discussion and future directions

PART 1: The development and application of cellular-scale optoelectronic devices for wireless manipulation of intact mammalian neural circuitry

To date, the primary implementation of the technologies presented in **Part 1** has been in "proof-of-principle" experiments. Initially, Tae-il Kim and I devised a means to combine many different functional electronic modalities into a single, ultrathin device (**Chapter 2**, **Figure 2.1**). These ultrathin (~20 μm), flexible devices allow for electrophysiological, optical, and thermal observation of brain tissue as well as wireless photostimulation. We devised a means to implant this thin interface into the brain using a removable insertion needle that temporarily binds to the flexible device with a biodissolvable adhesive (**Figure 2.1D**). By utilizing the well-established reward-related circuitry of the ventral tegmental area dopamine (VTA-DA) system, we were able to demonstrate that these devices can safely and effectively integrate with awake, behaving animals as small as a C57Bl/6 mouse (**Figure 2.1G**). Furthermore, we for the first time, directly addressed the role of tonic VTA-DA activity in anxiety-like behavior (**Figure 2.28**).

In an effort to facilitate the widespread distribution of this new technology Tae-il, Gunchul Shin, and I prepared a detailed protocol explaining every step of the fabrication and use these first generation devices (**Chapter 3**). Though this protocol is specific to these devices, the principles of both the materials science and the neuroscience approaches presented are portable to other endeavors such as the fabrication of other flexible optoelectronic technologies (**Figure 3.1-3.3**) and/or the general stereotaxic surgery (**Figure 3.5**).

Though the devices detailed in **Chapters 2 & 3** enable previously impossible experimental power for wireless photostimulation, they are limited greatly in their scope for other wireless perturbations such as local pharmacological manipulations in the deep brain.

Local pharmacology is a powerful tool in dissecting both neural circuits and endogenous receptor/ligand systems (Parker et al., 2010; Stachniak et al., 2014). However, to date, localized fluid delivery has relied exclusively on tethered approaches. Together, Jaewoong Jeong and I achieved wireless fluid delivery that can be paired with photostimulation (**Chapter 4**). These optofluidic neural probes can deliver up to four different fluids (**Figure 4.1 & 4.6**) and we have shown utility in viral gene transfer (**Figure 4.10**), local pharmacology (**Figure 4.11**), and paired optogenetic and pharmacological manipulation (**Figure 4.12**). Here we again returned to the well-established VTA-DA system to demonstrate the latter combinatorial approach. Following the extensive progress that had recently been made in the VTA-DA field (Gunaydin et al., 2014; Kim et al., 2012, 2013; Lammel et al., 2011, 2012, 2015; Stamatakis et al., 2013; Stuber et al., 2015; Tsai et al., 2009; Witten et al., 2011), we isolated a distinct projection to photostimulate and antagonize dopamine D_1 receptors (DRD1) (**Figure 4.12**). The isolation of this projection greatly increased the selectivity of our approach in **Chapter 2** (**Figure 2.11**) and revealed a role for this particular projection in the real-time place preference assay (**Figure 4.12**).

All of the devices presented in **Part 1** represent first forays into new technology. Following the initial proof-of-principle experiments presented here, there are myriad of ways to expand application of the technology.

Enhanced spatial targeting using independently-controlled μ-ILEDs

A major motivation and primary strength of the μ-ILED approach to photostimulation is the ability to spatially restrict the path of light (**Figure 2.23**) (Kim et al., 2013). At the time that we began work on these devices the most celebrated approach to directing the light path was feeding a fiber optic cable through a beveled cannula (Tye et al., 2011). Contemporaneous

development of optical waveguide-based probes (Zorzos et al., 2010, 2012) achieved marked success in spatial targeting of light, but failed to implement these impressive devices into experiments with behaving animals. While these waveguides provide impressive optical abilities, their rigid design and cumbersome optical coupling have limited their use in the field. μ-ILED devices, however, should be capable of spatial targeting beyond what we have so far presented. The initial devices used an array of four μ-ILEDs all under the same control. Gunchul Shin has since developed μ-ILED devices that have two μ-ILEDs separated by 1 mm that can be independently controlled. These "bidirectional" devices provide a first concept towards enhanced spatial targeting with μ-ILEDs and we have demonstrated their utility dissecting the microanatomy of the nucleus accumbens. Ream Al-Hasani and I have recently identified a functional anatomical segregation within dynorphin-expressing neurons of the nucleus accumbens (**Appendix 1**). Here we show that activation of dynorphin neurons in the dorsal shell of the nucleus accumbens (NAcSh) drives a preference behavior and activation of dynorphin neurons in the ventral NAcSH drives an aversion behavior. Using Gunchul's devices we were able to demonstrate that this behavioral diversity can be elicited in the same animal by shifting the spatial targeting of photostimulation between dorsal to ventral (**Figure A1.3 and A1.4**).

While the dynorphin experiments show the promise of spatial selectivity using μ-ILEDs, there likely remain greater spatial targeting achievements. One can imagine flexible devices that insert between the hippocampus and cortex of mouse brain or along sulci in higher mammals that would allow spatially segregated targeting of different regions. Other possible schemes could involve flexible net-like devices that could overlay the cortex (Viventi et al., 2010, 2011), providing numerous independently-addressable μ-ILEDs. One such exciting application that exploits the spatial properties of independently-addressable μ-ILEDs is using optogenetics for

cochlear stimulation. Preliminary studies have already shown that such an approach is feasible with µ-ILEDs (Hernandez et al., 2014), but soft, flexible devices with independently-addressable µ-ILEDs that could wrap along the cochlea similar to traditional cochlear implants could help refine the sensitivity of such prosthetics (Clark, 2015). Such devices could greatly aid study of larger network dynamics with the fine control of optogenetics. Furthermore, the independently-addressable µ-ILEDs could also access different wavelengths to either provide combined stimulation/inhibition or to activate discrete opsins targeted to distinct cell-types along a similar projection (Chuong et al., 2014; Klapoetke et al., 2014; Lin et al., 2013).

Miniaturization of the harvesting antenna

The initial power harvesting antennas that we presented were relatively large (~2 g) and most of this weight resulted from a reliance on a standard, commercially available rigid printed circuit board. By printing the same circuitry on flexible Kapton film we were able to reduce the weight of the harvester to ~700 mg. These lightweight devices, however, still require external mounting and would interfere with more ethologically-relevant behaviors such as social interaction. Following our work from **Chapter 2** (Kim et al., 2013), Sung il Park in the Rogers group has worked diligently to reduce the size of the power harvester needed to power the µ−ILEDs. The ultimate goal of this work is to achieve a miniaturized power harvester capable of being embedded completely under the scalp of an animal. Sung il achieved an order of magnitude reduction in weight by increasing the operating frequency of the harvesters (Park, 2013). The original harvesters operated at ~900 MHz and an increase to 1.5 GHz, resulted in substantially smaller harvesters (**Figure 7.1A & B**). These devices were operational and proved sufficient for Ed Siuda and myself to demonstrate that wireless activation of Gs-signaling in CAMKIIα^+ neurons the BLA is sufficient for anxiety-like behavior in the light-dark box assay

(**Figure 7.1C-F**). Importantly, this assay involves the animal entering an enclosed environment and would be incompatible with tethered fiber optic system. After this initial reduction in size, Sung il once again increased the operating frequency to allow for further miniaturization of the harvesters. Now with harvesters optimized near 2.4 GHz, the devices are an order of magnitude lighter ~60 mg and can easily be implanted under the scalp (**Figure 7.1G**). Proof of principle experiments
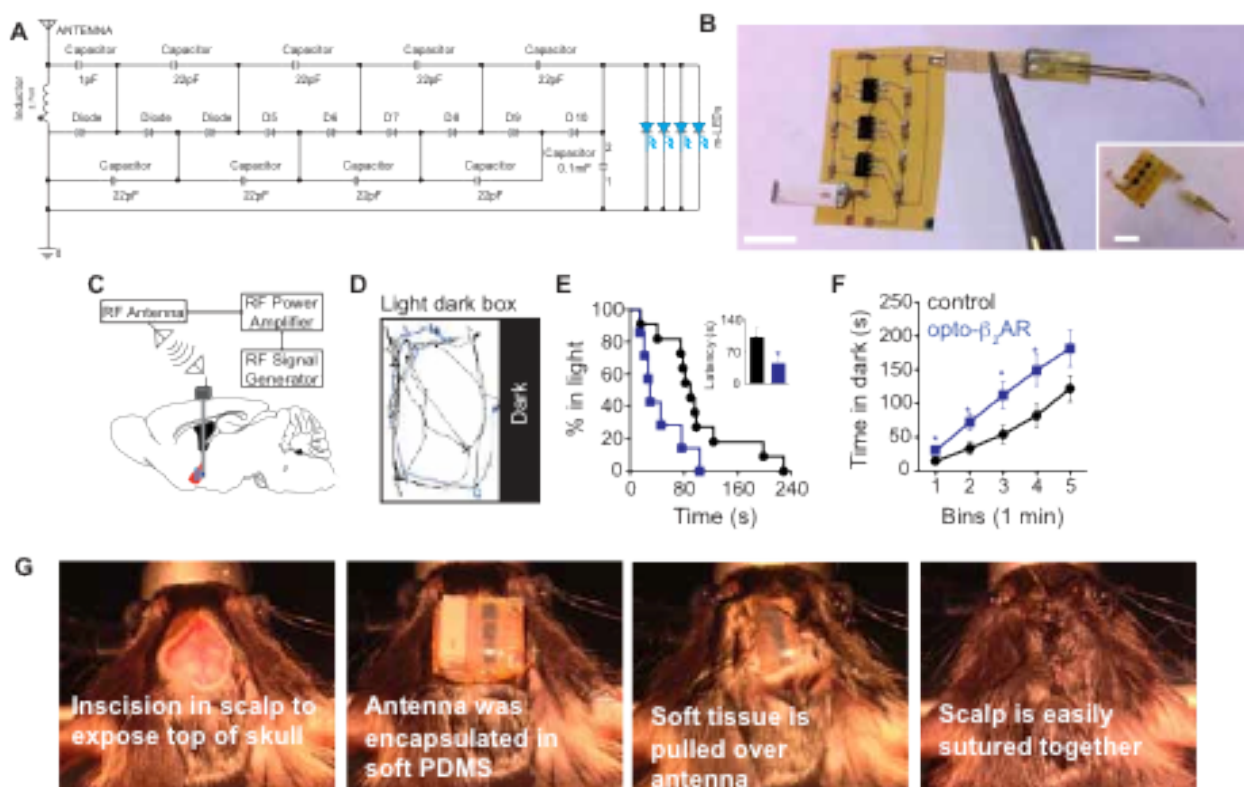
Figure 7.1: **Ongoing work to reduce the size of the RF energy harvester.** (**A**) Circuit diagram of an energy harvester operating at 1.5 Ghz. It consists of antenna, impedance matching circuits,

Cockcroft-Walton multiplier, and micro-LEDs. (**B**) Radiofrequency power harvester with μ-LEDs. μ-LEDs are detachable from the harvester as shown in the inset. Scale bars = 5 mm. (**C**) Viral injection site, unilateral μ-ILED implant and brief overview of wireless transmission system. (**D**) Representative traces of individual control (black) and individual opto-β_2AR (blue) animal in light dark box behavioral assay. (**E**) Wireless photostimulation of mice expressing opto-β_2AR (blue; n = 7) in the BLA enter the dark box faster than viral controls (black; n = 11) (* $p < 0.05$; log-rank (Mantel-Cox) Test) (inset * $p < 0.05$; Students' unpaired t-test). (**F**) Opto-β_2AR animals (blue) spend more time in the dark box than viral controls (black) (*$p < 0.05$; multiple Student's unpaired t-tests). All data expressed as mean ± SEM. All light pulses are 473 nm, 1 W/cm^2. (**G**) Demonstration of subcutaneous implantation of 2.4 GHz RF harvesters. (**A & B**) Data generated by Sung il Park, Rogers Group, University of Illinois at Urbana-Champaign (**C-F**) Data generated and analyzed by Edward R. Siuda, Jordan G. McCall, and Martin J. Schmidt. (**G**) Data generated by Jordan G. McCall.

using these devices are underway, but these miniaturized harvesters may prove difficult to implement with freely behaving animals due to the limitations of RF power harvesting.

Limitations of radiofrequency power scavenging

The wireless capabilities of the devices presented in **Chapters 2 & 3** (Kim et al., 2013; McCall et al., 2013) are all based on the concept of radiofrequency power harvesting from intentionally broadcasted sources. This powering scheme is advantageous because it allows the user to wirelessly operate the devices while foregoing both an onboard battery and a processor of some kind to determine the parameters of photostimulation (the latter is avoided by manipulating the broadcasted RF signal). However, the intentionally broadcasted RF signal is linearly polarized. This polarization limits the angle at which the broadcasted signal can be efficiently harvested for power of the μ–ILEDs. Practically speaking, this property can greatly limit the ability to deliver effective wireless photostimulation. As discussed briefly in **Chapter 3** (McCall et al., 2013), the use of multiple broadcast antennas arranged purposefully can overcome some of these polarity issues. However, the increase in operating frequency that allows for miniaturization of the harvester makes these devices inherently more prone to polarity issues. These issues can be problematic. Despite the use of multiple broadcasting antennas, there can often be numerous "dead zones" or areas where there is insufficient RF radiation to power the devices in a behavioral arena. This likely did not affect our behavioral results in (**Figure 7.1C-F**) as we were using an optically-sensitive GPCR with a activation time that outlasts the period of photostimulation (Airan et al., 2009), but users wishing to use a faster acting channel or pump (Mattis et al., 2012) may face hurdles. This limitation is likely a greater concern in the 2.4 GHz subcutaneous versions of the harvesters.

Despite the limitations introduced by the higher operating frequency, the goal of miniaturization is a worthy target. One possible solution is to use the implanted nature of these devices to harness the tissue of the animal as a greater harvesting platform (Peyman et al., 2001; Poon et al., 2010). Such an approach would allow smaller harvesters that are not nearly as effected by the head direction of the animal (as the whole body of the animal could be used to help capture RF energy). Another approach would be to supplement the small-scale harvesters with a small battery that engages when power is lost. This would eliminate dead zones, but the battery and its interface to the harvester may prove too large to have the device remain subcutaneous. It is also possible that such a strategy would need a miniaturized microcontroller to ensure proper control of the photostimulation. Finally, and perhaps most promising, is the prospect of moving away from high frequency RF scavenging altogether. Lower frequency RF (~13 MHz) such as that used for Near Field Communication (NFC) can similarly be used for energy transfer from an initiator antenna to power a passive target, in this case an μ–ILED array (S.n et al., 2012). A similar approach was recently demonstrated using a resonant cavity to broadcast circularly polarized RF signals to nearby RF harvesting coils for wireless photostimulation in mice (Ho et al., 2015). In that particular case, the resonant cavity inherently restricts the operating distance and types of behavior accessible to this technology. The NFC initiator-based approach also sacrifices the distance at which the devices can be wirelessly powered (high frequency RF can operate μ–ILEDs at ~2 m, low frequency is likely close to 10 cm). However, the NFC initiator can be many different shapes and could presumably be form-fitted to any behavioral environment. Assuming three-dimensional access to the environment in which the subject was freely moving, it should be possible to maintain efficient photostimulation without limitations of polarity or "dead spot" areas in the field using an NFC initiator approach.

295

Furthermore, NFC should easily accommodate underwater scenarios that are difficult with high frequency RF or battery-based systems (Zoksimovski et al.) and the technology is already being used for bidirectional information exchange which would easily enable physiological monitoring systems such as electroencephalography (Bertrand, 2015).

Increasing the functionality and accessibility of optofluidic neural probes

The optofluidic neural probes presented in **Chapter 4** foreshadow a number of parallel advances in wireless neural interface technologies including therapeutic approaches accessing the peripheral nervous system (Minev et al., 2015), the expansion of *in vivo* photoconversion of caged ligands (Kramer et al., 2013; Polosukhina et al., 2012; Tochitsky et al., 2014), and improved wireless photostimulation schemes based on battery-powered microprocessors (Iwai et al., 2011; Lee et al., 2015). The designs we present in **Chapter 4** can be modified to address each one of these exciting new directions. Local delivery of drugs into the spinal cord and peripheral nervous system could provide opportunities for better pain management and/or aid in regeneration of damaged nerves (Minev et al., 2015; Richards and McMahon, 2013; Scheib and Höke, 2013). Such delivery may be more readily achieved using these thin, flexible microfluidic channels. Likewise, the integration of the optofluidic neural probes with UV spectrum (~405 nm) μ-ILEDs that Gunchul Shin has recently developed will hopefully expand the applicability of these devices to wild-type animals and increase the chance of therapeutic translation using caged compounds (Banghart and Sabatini, 2012; Kramer et al., 2013). Finally, it is worth noting that the wireless scheme presented in **Chapter 4** is unique from those presented in **Chapters 2 & 3**. Using a battery-powered microprocessor insures equivalent efficiency of the μ-ILEDs regardless of the position or orientation of the animal in space, thus providing another solution to the polarity issues discussed above. While these battery-powered designs are larger (~1.8 g) than the

current generation of RF harvesters, size reduction for devices intended exclusively for photostimulation are immediately possible. The power requirements for the µ−ILED is substantially less than that of the Joule heaters needed for fluid delivery, so such a device would only need a single battery. Furthermore, control of the pulse paradigm for photostimulation could be removed from the on-board microcontroller and instead controlled remotely by pulsing the IR signal. In other words, if the microcontroller was reduced to serve as an I/O gate to the µ−ILEDs then the IR signal could be pulsed to any desired parameters. Such modifications could likely make a wireless photostimulation device weighing less than 500 mg that would not suffer any orientation limitations.

Unlike the ultrathin, flexible multimodal µ−ILED devices presented in **Chapters 2 & 3** (Kim et al., 2013; McCall et al., 2013), the optofluidic neural probes presented in **Chapter 4** are fabricated from readily available and/or 3D-printable materials in a standard lab environment. However, accessibility to these devices is limited to how the fluid chambers are filled (see **Chapter 4 Materials & Methods**). The current design only allows each set of four chambers to be filled a single time. Ideally, access to the fluidic channels would be limitless. In tethered approaches, fluid supply is never an issue and certainly not the limiting step towards adopting the technique. Development of a cartridge system that could reversibly connect to the microfluidic channels is one possibility for overcoming this hurdle. In this case, fluid could be filled into limitless disposable cartridges and once the fluid is dispensed from all chambers in the cartridge, the entire cartridge is replaced. The primary challenge with this idea will be the creation of fluid interconnects that remain patent between cartridges, but such a goal should be achievable.

Even though each device and technology platform introduced in **Part 1** has room for improvement and modification, each device design is ready to address new biological questions.

In large part, these tools were developed to help us answer previously intractable questions concerning the locus coeruleus noradrenergic system. Though application of these technologies to locus coeruleus circuitry has begun (**Figure 2.23, Figure 7.1C-F**), much more work will be needed to better understand how this system regulates such a broad range of behaviors. In **Part 2**, we began a relatively gross modern dissection of LC-NE circuitry in negative affect. With the help of the technology from **Part 1**, we can uncover more of the fundamental nature of LC-NE mediated behaviors.

PART 2: Dissecting the role of locus coeruleus circuitry in negative affective behaviors

The locus coeruleus noradrenergic (LC-NE) system has been known to be involved in central stress response for many decades (Koob, 1999). While numerous groups have observed that the LC-NE electrophysiological activity increases in response to stressors (Bingham et al., 2011; Cassens et al., 1981; Curtis et al., 1997, 2012; Francis et al., 1999; Lechner et al., 1997; Jedema and Grace, 2004; Page and Abercrombie, 1999; Reyes et al., 2008; Snyder et al., 2012; Valentino et al., 1991; Valentino and Foote, 1988; Valentino and Van Bockstaele, 2008), the underlying circuitry and cellular dynamics of this response have not previously been fully elucidated. Recent advances in cell-type selective control of neural circuitry, namely optogenetics and chemogenetics, provide an ideal toolbox for furthering our understanding of this small, pontine brain structure. Indeed, one of the earliest *in vivo* optogenetics studies targeted the LC-NE cell bodies to understand this structure's role in arousal (Carter et al., 2010). The bidirectional control of arousal through LC-NE cell bodies by Carter et al., 2010 demonstrated the powerful command this small brainstem structure can have on gross behavioral states. This early observation, though striking, left much unexplored territory for the LC which is known have roles in stress responses (Koob, 1999), attention (Sara, 2009; Sara and Bouret,

298

2012), and descending pain modulation (Jones, 1991) among other behavioral outputs (Berridge and Waterhouse, 2003; Sara, 2009). In order to better understand how the LC-NE system mediates these and other behaviors, more detailed studies were necessary to dissect the underlying circuitry. The studies presented in **Chapters 5 & 6** are the first to selectively manipulate LC-NE neurons in the context of stress and the resulting anxiety-like behaviors and are the first to explore afferent and efferent projections from this structure with regard towards negative affective behavior.

In **Chapter 5,** we report that the activity of LC-NE neurons is necessary to elicit acute stress-induced anxiety (**Figure 5.1**). Furthermore, selectively increasing the firing of LC-NE neurons is itself anxiogenic in the absence of stress (**Figure 5.4**). This same high tonic state has negative valence that can be learned to influence future behavior (**Figure 5.6).** Interestingly, this negative valence can be generated by a subset of LC-NE neurons that express the neuropeptide Galanin (**Figure 5.8**). In an effort to understand the endogenous afferent circuitry that mediates these effects we traced CRH$^+$ inputs from the central amygdala (CeA) to the LC (**Figure 5.11**). Optogenetic stimulation of CRH$^+$ CeA terminals into the LC replicates both the cellular activity profile and acute anxiogenic and aversive behavioral state of direct LC-NE high tonic stimulation (**Figure 5.13**).

Following these experiments, we sought to determine what downstream brain regions and receptor systems could be targets to drive the negative affective behaviors mediated by the LC. In **Chapter 6**, I observed that the anxiogenic and aversive components of LC activation may be mediated through two different adrenergic receptor systems (**Figure 6.1**). In an effort to understand where these effects are mediated, Ed Siuda and I identified an anxiogenic and aversive efferent projection from the LC to the basolateral amygdala (BLA) (**Figure 6.6 and**

6.7). Increased tonic stimulation of this projection releases norepinephrine (NE) into the BLA (**Figure 6.4**) and alters BLA single unit activity similarly to exogenously applied NE (**Figure 6.5**) (Buffalari and Grace, 2007). In the behaving animal, stimulation of these LC-BLA terminals drives similar anxiety-like behavior and conditions an aversion similar to direct LC-NE cell body stimulation (**Figure 6.6**, **Figure 7.2A**). Together these findings suggest a critical amygdalar-coerulear network in the mediation of stress-induced anxiety (**Figure 7.2 B**). Understanding these circuits in the context of natural behaviors will require further study, but there is undoubtedly a wealth of knowledge to be gained by further circuit dissection of the LC-NE system.
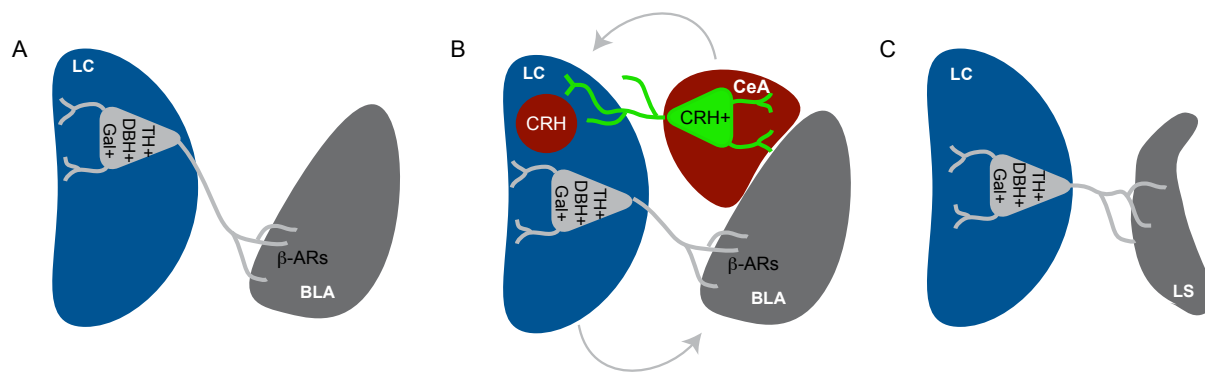
Figure 7.2 Possible models for LC-NE mediated stress-induced negative affective behaviors. (**A**) **Chapter** 6 indicates that LC-BLA projections likely mediate acute stress-induced anxiety, possibly through local β-adrenergic receptors. (**B**) Proposed model of feed-forward circuit between the LC and the amygdala that could possibly drive persistent and/or chronic anxiety. (**C**) Anthony et al. 2014 presented the lateral septum (LS) as a region mediating persistent stress-induced anxiety, the LC sends projections to this region which could play a role in sustained stress-induced anxiety.

Considerations when using Cre-driver lines for cell-type selective targeting

Much of the data presented in this dissertation was gathered using various Cre-driver lines (e.g. *Th*-Cre, *CRH*-Cre, *Gal*-Cre*, Dyn*-Cre, etc.). While these mouse lines can enable cell-type selective expression of constructs using Cre-dependent viral vectors, it is important to consider the limitations of these animals. Recent work highlighted various Cre-driver lines commonly used to target VTA-DA neurons may target slightly different populations within and near this brain region (Lammel et al., 2015). While there is significant controversy concerning this work (Stuber et al., 2015), it is important to appreciate that no Cre-driver system is likely perfect. In our hands with the *Gal*-Cre mouse, using a Cre-dependent reporter mouse, we observed Cre-dependent activity in brain regions that should be absent of Galanin in the adult (**Figure 5.9**). After a thorough investigation using the Allen Brain Atlas of the Developing Mouse Brain, we determined that the ectopic reporter expression was due to recombination from transient Galanin (and therefore Cre) expression during development. After histological evaluation in the adult mouse, we believe that this appearance of "leaky" Cre expression is likely an artifact brought on through development. Such developmental changes of Cre expression have been observed before (Bruchas et al., 2011) and the extent to which they can bias results will depend on each mouse line and each experiment. Importantly, following histological examination in all of the mouse lines we used in **Part 1** and **Part 2**, we do no believe there is cause for concern in interpreting our data.

Single-unit electrophysiology qualifications and future alternatives

The single-unit electrophysiological studies of LC neurons presented in **Chapters 5 & 6** were all performed in isofluorane-anesthetized animals. While the LC is still active under light

(<~1%) isofluorane anesthesia, its activity is significantly reduced and can be dampened completely with higher levels of isofluorane (Gompf et al., 2009). Conversely, significant LC activation can reverse the effects of isofluorane anesthesia (Vazey and Aston-Jones, 2014). Significant effort was taken to perform these experiments at the lowest possible level of anesthetic that still maintains an anesthetized state of the animal (~0.7%). That being said, the basal activity of LC neurons and the likelihood of observing an LC neuron were both likely decreased in all of the recording experiments. This side effect of the experimental preparation introduces an inherent selection bias as one can only record from neurons that are observably active. Though attempts were made to record from the LC of awake, behaving animals the signal-to-noise ratio was not ideal to isolate single LC neurons. An important future step in understanding LC-NE function will be to observe the activity of these neurons during naturalistic behaviors (e.g. during the stress experience and/or the expression of anxiety-like behaviors. One possible approach would be to visualize the LC-NE neurons using a genetically targeted fluorescent Ca^{2+} indicator paired with a deep brain implanted gradient-index (GRIN) lens and miniature fluorescent microscope (Hamel et al., 2015; Jennings et al., 2015; Ziv et al., 2013). While the temporal resolution of *in vivo* Ca^{2+} imaging is much slower than single-unit electrophysiology, there should be valuable information gained from the visualization of these neurons in awake, behaving animals. Even at a reduced temporal resolution, gross alterations in LC-NE activity should be observable with *in vivo* Ca^{2+} imaging. Such observational studies would greatly inform how the LC processes stressful events and induces negative affective behavior.

The implementation of deep brain microendoscopy can be challenging, however, due to the invasive nature of the implanted GRIN lens. Fiber photometry represents a less invasive

opportunity to resolve population activity with genetically targeted fluorescent Ca^{2+} indicators (Cui et al., 2013, 2014). While this approach likely does not yield much greater information that multiunit activity would at cell bodies, the technique can be used to observe Ca^{2+} activity in terminal fields (Gunaydin et al., 2014). This feature of the technology would be very powerful in understanding the dynamics of long-range projections into and out of the LC. Furthermore, it is possible that the flexible photodetector presented in **Chapters 2 & 3** could be adapted for similar purposes (**Figure 2.1, Figure 3.3**).

Temporal limitations and the implications for persistent and chronic stress-induced anxiety

While these studies are the first of their kind to dissect LC function with cell-type- and projection-selective targeting, there remain many limitations in the interpretation of the data. The necessity of the LC-NE system in stress-induced anxiety was shown by cell-type selective chemogenetic inhibition of LC-NE neurons (**Figure 5.1**). This approach is somewhat temporally ambiguous due to the onset kinetics of CNO and the Gi-coupled DREADD receptor. We chose this tool purposefully as it should enable inhibition of LC activity for an extended period of time (~1 hour). However, because LC activity was likely dampened during both the stressor and the test of stress-induced anxiety-like behavior, it is difficult to know the contribution of increased LC activity to either. Inhibitory optogenetic constructs are much more temporally precise, however achieving equivalent inhibition via illumination across a large area can be problematic. Not only are there concerns of tissue heating (Yizhar et al., 2011), but the first generation optogenetic constructs can lead to altered cell activity after the inhibition has ceased (Raimondo et al., 2012).

Similar to the temporal concerns of the inhibition experiments, all of our studies in **Chapters 5 & 6** relate only the acute phase of stress-induced anxiety. While we suggest that LC activity may work in a feed-forward loop through the amygdala to promote an anxiety-like state it is unclear at this time if LC-NE activity alone can sustain such a loop. Experiments that acutely increase LC tonic activity prior to anxiety testing (rather than during) and those addressing chronic LC activation (see below) can help address these outstanding questions. Recent evidence has shown that persistent stress-induced anxiety is mediated through $CRFR2^+$ cells in the lateral septum (Anthony et al., 2014). It is possible that the LC mediates acute anxiety-like behavior through a projection to the BLA (**Figure 7.2A**), while modulating more long-term stress-induced anxiety through inputs into the lateral septum (**Figure 5.14, Figure 7.2C**).

Do diverging projections explain diverging behaviors?

A central question underlying LC-NE research is how a small structure with such ubiquitous innervation of the forebrain can selectively contribute to a wide array of physiological and behavioral functions as it does? Our work here (**Chapters 5 & 6**) begins to illustrate a circuit-based mechanism for this diversity. First, in **Chapter 5** we demonstrate that only a subset of neurons are required to sufficiently drive a real-time place aversion (**Figure 5.8**) and that sparse innervation from the CeA is sufficient for both learned aversion and anxiety-like behavior (**Figure 5.13**). Next, in **Chapter 6** we show that anxiety-like and real-time place aversion are mediated by two separate downstream adrenergic receptor systems (**Figure 6.1**) and that the anxiety-like behavior is likely mediated through β-adrenergic receptors activated by LC projections to the BLA (**Figures 6.1, 6.4, 7.1, 7.2A**). This divisibility of behavioral output suggests that subsets of LC neurons with different efferent projection targets can drive distinct

LC-mediated behaviors. It will be important to extend these findings to other behaviors, particularly other stress-induced behaviors as described below.

The next generation of functional circuit dissection should access finer selectivity than the research presented here. Combinatorial approaches that utilize intersectional genetics as well as projection-selective viral gene transfer will greatly enhance our ability to decipher complex circuitry *in vivo* (Fenno et al., 2014; Madisen et al., 2015; Saunders et al., 2012; Stamatakis et al., 2013). We previously suggested that a similar approach be taken using the *Gal*-Cre mice to selectively target LC-NE neurons that do not express Galanin (i.e. using the Cre-OFF system (Saunders et al., 2012), but such an approach could be used in combination with retrograde viral targeting to yield, projection- and perhaps synapse-selective cell-type selective control of neuronal subtypes (Goshen et al., 2011; Krashes et al., 2014; Ogawa et al., 2014; Watabe-Uchida et al., 2012).

Exploring LC-NE activity in other stress-related behaviors

Stress-induced anxiety and aversion represents only a subset of known behavioral responses to stress (Bruchas et al., 2011; Butler and Finn, 2009; Weninger et al., 1999). Several stress-induced behaviors are known to be influenced or mediated by NE, including stress-induced relapse to drug seeking (Weinshenker and Schroeder, 2007) and stress-induced analgesia (Butler and Finn, 2009). Exploring the possibility of these behaviors being mediated by LC efferent projections is a compelling next step.

Stress-induced relapse

While it is possible the NE involved in other stress-induced behaviors could come from the other A1/A2 noradrenergic neurons of the brainstem (Erb et al., 2000; Shaham et al., 2000),

preliminary data indicates that tonic activation of the LC-NE system is sufficient for reinstatement of a cocaine place preference (**Appendix 2, Figure A2.1**). While these data need to be extended and replicated, the findings represent an interesting observation that goes against the accepted dogma in the addiction field (Weinshenker and Schroeder, 2007). The LC-NE system has not been considered a mediator of stress-induced relapse since an early pharmacological study asserted that the mechanism was independent of LC activity (Shaham et al., 2000). While this study and others (Delfs et al., 2000) clearly demonstrated the involvement of A1/A2 noradrenergic neurons in these behaviors, the data are not sufficient to rule out a role for the LC-NE system. Furthermore, our lab has recently shown that the LC does have an important role in kappa opioid-induced reinstatement to cocaine place preference (Al-Hasani et al., 2013). Future studies will be necessary to determine if the reinstatement behavior induced by tonic activation of LC-NE cell bodies is truly mirroring stress-induced reinstatement. However, the tools now exist for elegant dissection of this behavior to demonstrate both the necessary and sufficient components of the system paralleling the approach used in **Chapter 5**.

Beyond using selective modulation of LC-NE cell bodies in drug seeking behavior, it will also be important to investigate the underlying circuit mechanisms of such behavior. For example, the efferent projections from the LC that mediate reinstatement behavior may not be the same as those that mediate anxiety-like or aversion behaviors. While it is possible that the negative affective behaviors induced by tonic activation of the LC fibers in the BLA can drive reinstatement behavior (Bruchas et al., 2009, 2011; Land et al., 2009), it is also possible that the LC-NE system can mitigate reinstatement from direct activation of the VTA-DA system (Mejías-Aponte et al., 2009; Velásquez-Martinez et al., 2012) (**Figure 7.3A**). Furthermore, the afferent circuitry that activates the LC-NE system during such behavior could be independent of the

amygdala as the VTA-DA system (among many others) has direct input into the LC as well (Deutch et al., 1986).
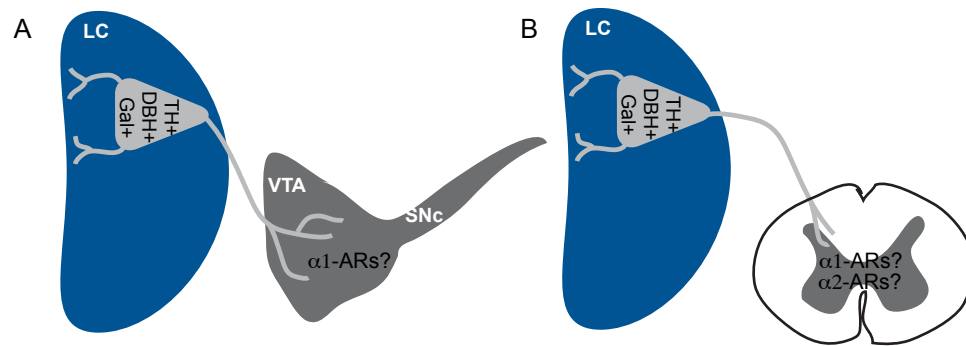
Figure 7.3 Possible models for the role of LC-NE in other stress-induced behaviors. (**A**) Stress-induced reinstatement of drug seeking could possible be mediated in part by LC projection into the VTA that activates α1-adrenergic receptors or by activating the anxiety-related circuits in **Figure 7.2**. (**B**) Stress-induced analgesia may be mediated by descending projections into the spinal cord via α1-adrenergic andor α2-adrenergic receptors.

Stress-induced analgesia

The LC-NE system has a well-established role in the descending modulation of pain (Jones, 1991; Liu et al., 2008; Millan, 2002; Ossipov et al., 2010; Tsuruoka et al., 2010). Furthermore, NE and its receptor systems are known mediators of stress-induced analgesia (Buerkle and Yaksh, 1998; Butler and Finn, 2009; Howe et al., 1983). The link between these two observations, however, has yet to be clearly made. Recently both our group (**Appendix 2, Figure A2.2**) and another (Hickey et al., 2014) have demonstrated that increased tonic LC-NE activity can drive antinociception in both mice and rats, respectively. This selective increased activity mimics stress-induced anxiety (**Figure 5.4**), but whether the same can be said for stress-induced analgesia remains to be seen. Selective inhibition of LC-NE neurons during stress will

be important to determine whether there is physiological relevance to the findings in **Figure A2.2** and Hickey et al., 2014.

The study of descending modulation of pain by the LC-NE system is clear example of a case where integration between **Part 1** and **Part 2** of this dissertation would be fruitful (**Figure 7.3B**). As previously discussed, integration of the optofluidic neural probes (**Chapter 4**) with the spinal cord is a promising future direction. In the case of descending LC-NE projections, the ability to optically stimulate LC-NE terminals within the spinal cord would provide direct evidence that the analgesic effect of LC-NE stimulation is via descending projections rather than through central modulation in the amygdala or elsewhere. Furthermore, local pharmacology in the spinal cord could help to resolve the receptor systems mediating any observed effects. Beyond local modulation in the spinal cord, Hickey et al., 2014 presented evidence of a dorsal-ventral shift between pronociception and antinociception in the LC. Using independently-addressable µ-ILEDs such as those used in **Appendix 1**, could help decipher the contribution and significance of this anatomical functional segregation within the LC proper.

Stress-induced arousal disorders

The LC-NE system is intimately involved in the regulation of arousal states (Aston-Jones and Bloom, 1981; Carter et al., 2010, 2012; Foote et al., 1980; Sara and Bouret, 2012). While the awake state seems to be mediated by the presence of any tonic activity (Aston-Jones and Bloom, 1981; Bloom, 1981; Carter et al., 2010), we now know that increased tonic activity mimics the behavioral phenotypes of stress (**Figures 5.4, 5.6, 5.8, 5.13, 6.1, 6.6**). The connection between stress, anxiety, arousal and the LC-NE system is likely a continuum: the more LC-NE activity, the more arousal, the more anxiety-like behavior. While we believe that LC activation likely

adjusts the gain on downstream anxiety systems (e.g. BLA activity), we have not examined the long-term consequences of exogenously increasing LC activity. **Chapters 5 & 6** only test acute anxiety-like and aversive states. It is possible that chronic, long-term activation of LC-NE cell bodies would produce a state of hyperarousal a known symptom of post-traumatic stress disorder (Krystal and Neumeister, 2009). Once again, utilizing some of the technology presented in Part 1 can now more directly test such a hypothesis. Wireless μ-ILED devices that utilize RF power harvesting are suitable for long-term photostimulation in a homecage environment. Thus, one could directly test the behavioral effects of chronic LC stimulation. Wireless optogenetics, however, are not necessary for such a design. It would also be possible to mimic chronic activation of the LC by targeting the Gq-coupled DREADD receptor to LC-NE neurons and deliver CNO via an osmotic pump. While the time-frame of this design would be limited by the CNO exposure, it would certainly allow for long-term activation of LC-NE neurons.

Closing thoughts

While both **Part 1** and **Part 2** of this dissertation provide new tools for interrogating neural function and insight into the role of LC-NE system in stress-induced behaviors, each **Part** is only a very early step in these processes. Flexible, wireless neural probes ultimately have the potential clinical translation. Perhaps not with optogenetics in mind, but less invasive and less cumbersome medical devices are promising future applications of these kinds of technology. With a clearer understanding of the function of the LC-NE system in stress-induced behaviors, it is even possible that such technologies could be used to ameliorate psychiatric disorders, relieve pain, or prevent the deleterious effects of chronic stress and axnxiety.

MATERIALS & METHODS

Stereotaxic surgery

Mice were anaesthetized in an induction chamber (5% isoflurane) and placed in a stereotaxic frame (Kopf Instruments, Model 1900) where they were maintained at 1-2% isoflurane throughout the procedure. Following craniotomy mice were injected bilaterally with 1.2 μl of either lenti-EF1α-GFP or lenti-CaMKIIα-optoβ$_2$AR-mCherry in the basolateral amygdala at stereotaxic coordinates from bregma: -1.3 mm (AP), ± 2.9 mm (ML) and -4.9 mm (DV). For wireless μ-ILED BLA studies, animals were injected unilaterally, not bilaterally. Mice were then implanted with chronic fiber optic implants or μ-ILED wireless devices with coordinates adjusted from viral injection to 0.00 mm (AP), ± 0.00 mm (ML), and +1.00 mm (DV). For bio-dissolvable samples, the device was implanted at the desired target, ACSF was applied to the portion of the device that remained outside of the skull to facilitate dissolution of the adhesive, and then the epoxy needle was removed after a delay of 15 min (Kim et al., 2013; McCall et al., 2013). The fiber optic implants and wireless μ-ILED devices were secured using two bone screws (CMA, 743102) and affixed with TitanBond (Horizon Dental Products) and dental cement (Lang Dental) (McCall et al., 2013). Mice were allowed to recover for at least 3-6 weeks prior to behavioral testing; this interval also permitted optimal viral expression.

Wireless powering and RF powering scavenger for wireless optogenetics

Wireless powering of the μ-ILED devices was adapted as previously described (Kim et al., 2013; McCall et al., 2013). The wireless power transmitter includes an RF signal generator (Agilent N5181A), a power supply (Agilent U8031A), a RF power amplifier (Empower RF Systems 1119-BBM3K5KHM), an RF signal splitter (RF Lambda RFLT2W0727GN), and two panel antennas (ARC Wireless ARC-PA2419B01). The RF signal generator is internally

modulated to delivery sufficient power to light the μ-iLEDs at the given stimulation protocol (10 Hz, 50 ms pulse widths). The RF power amplifier that is powered by the power supply enlarges the modulated RF signal from the RF signal generator. The RF power is then transmitted from the panel antenna to the headstage power harvesters. The RF signal generator has a power output from -10 to 0 dBm at 1.5 GHz, optimized daily to ensure equivalent light power throughout the space of the LDB assay. Mice with chronically implanted μ-ILED devices were acutely connected to the headstage power harvesters immediately prior to any wireless photostimulation.

Behavior – Light/Dark Box (LDB)

Behavioral assays were performed in a special sound attenuated room maintained at 23°C. Lighting was measured and stabilized at ~ 4 lux for anxiety tests and ~200 lux for place testing. All behavioral apparatuses were cleaned with 70% ethanol in between animals. In each assay, animals received constant photostimulation throughout the entire trial. For all behavioral experiments, lenti-EF1α-GFP and lenti-CaMKIIα-optoβ₂AR-mCherry received 5 sec of constant photostimulation (473 nm) followed by 5 sec of no light throughout the entire trial. Movements were video recorded and analyzed using Ethovision Software. The LDB was a 50 x 50 cm square plexiglass enclosure with a 16.5 cm x 49 cm dark insert. For testing, animals were connected to wireless harvester and placed into the corner of the open enclosure and allowed to roam freely for 10 min.

REFERENCES

Airan, R.D., Thompson, K.R., Fenno, L.E., Bernstein, H., and Deisseroth, K. (2009). Temporally precise in vivo control of intracellular signalling. Nature *458*, 1025–1029.

Anthony, T., Dee, N., Bernard, A., Lerchner, W., Heintz, N., and Anderson, D. (2014). Control of Stress-Induced Persistent Anxiety by an Extra-Amygdala Septohypothalamic Circuit. Cell *156*, 522–536.

Aston-Jones, G., and Bloom, F.E. (1981). Activity of norepinephrine-containing locus coeruleus neurons in behaving rats anticipates fluctuations in the sleep-waking cycle. J. Neurosci. Off. J. Soc. Neurosci. *1*, 876–886.

Banghart, M.R., and Sabatini, B.L. (2012). Photoactivatable neuropeptides for spatiotemporally precise delivery of opioids in neural tissue. Neuron *73*, 249–259.

Berridge, C.W., and Waterhouse, B.D. (2003). The locus coeruleus-noradrenergic system: modulation of behavioral state and state-dependent cognitive processes. Brain Res. Brain Res. Rev. *42*, 33–84.

Bertrand, A. (2015). Distributed signal processing for wireless EEG sensor networks. IEEE Trans. Neural Syst. Rehabil. Eng. Publ. IEEE Eng. Med. Biol. Soc.

Bloom, F.E. (1981). ACTIVITY OF NOREPINEPHRINE-CONTAINING NEURONS IN BEHAVING RATS ANTICIPATES THE SLEEP-WAKING CYCLE ' LOCUS COERULEUS FLUCTUATIONS IN. *1*, 876–886.

Bruchas, M.R., Land, B.B., Lemos, J.C., and Chavkin, C. (2009). CRF1-R activation of the dynorphin/kappa opioid system in the mouse basolateral amygdala mediates anxiety-like behavior. PloS One *4*, e8528.

Bruchas, M.R., Schindler, A.G., Shankar, H., Messinger, D.I., Miyatake, M., Land, B.B., Lemos, J.C., Hagan, C.E., Neumaier, J.F., Quintana, A., et al. (2011). Selective p38α MAPK deletion in serotonergic neurons produces stress resilience in models of depression and addiction. Neuron *71*, 498–511.

Buerkle, H., and Yaksh, T.L. (1998). Pharmacological evidence for different alpha 2-adrenergic receptor sites mediating analgesia and sedation in the rat. Br. J. Anaesth. *81*, 208–215.

Buffalari, D.M., and Grace, A.A. (2007). Noradrenergic modulation of basolateral amygdala neuronal activity: opposing influences of alpha-2 and beta receptor activation. J. Neurosci. Off. J. Soc. Neurosci. *27*, 12358–12366.

Butler, R.K., and Finn, D.P. (2009). Stress-induced analgesia. Prog. Neurobiol. *88*, 184–202.

Carter, M.E., Yizhar, O., Chikahisa, S., Nguyen, H., Adamantidis, A., Nishino, S., Deisseroth, K., and de Lecea, L. (2010). Tuning arousal with optogenetic modulation of locus coeruleus neurons. Nat. Neurosci. *13*, 1526–1533.

Carter, M.E., Brill, J., Bonnavion, P., Huguenard, J.R., Huerta, R., and de Lecea, L. (2012). Mechanism for Hypocretin-mediated sleep-to-wake transitions. Proc. Natl. Acad. Sci. U. S. A. *109*, E2635–E2644.

Chuong, A.S., Miri, M.L., Busskamp, V., Matthews, G.A.C., Acker, L.C., Sørensen, A.T., Young, A., Klapoetke, N.C., Henninger, M.A., Kodandaramaiah, S.B., et al. (2014). Noninvasive optical inhibition with a red-shifted microbial rhodopsin. Nat. Neurosci. *17*, 1123–1129.

Clark, G.M. (2015). The multi-channel cochlear implant: Multi-disciplinary development of electrical stimulation of the cochlea and the resulting clinical benefit. Hear. Res. *322*, 4–13.

Cui, G., Jun, S.B., Jin, X., Pham, M.D., Vogel, S.S., Lovinger, D.M., and Costa, R.M. (2013). Concurrent activation of striatal direct and indirect pathways during action initiation. Nature *494*, 238–242.

Cui, G., Jun, S.B., Jin, X., Luo, G., Pham, M.D., Lovinger, D.M., Vogel, S.S., and Costa, R.M. (2014). Deep brain optical measurements of cell type-specific neural activity in behaving mice. Nat. Protoc. *9*, 1213–1228.

Delfs, J.M., Zhu, Y., Druhan, J.P., and Aston-Jones, G. (2000). Noradrenaline in the ventral forebrain is critical for opiate withdrawal-induced aversion. Nature *403*, 430–434.

Deutch, A.Y., Goldstein, M., and Roth, R.H. (1986). Activation of the locus coeruleus induced by selective stimulation of the ventral tegmental area. Brain Res. *363*, 307–314.

Erb, S., Hitchcott, P.K., Rajabi, H., Mueller, D., Shaham, Y., and Stewart, J. (2000). Alpha-2 Adrenergic Receptor Agonists Block Stress-Induced Reinstatement of Cocaine Seeking. Neuropsychopharmacology *23*, 138–150.

Fenno, L.E., Mattis, J., Ramakrishnan, C., Hyun, M., Lee, S.Y., He, M., Tucciarone, J., Selimbeyoglu, A., Berndt, A., Grosenick, L., et al. (2014). Targeting cells with single vectors using multiple-feature Boolean logic. Nat. Methods *11*, 763–772.

Foote, S.L., Aston-Jones, G., and Bloom, F.E. (1980). Impulse activity of locus coeruleus neurons in awake rats and monkeys is a function of sensory stimulation and arousal. Proc. Natl. Acad. Sci. U. S. A. *77*, 3033–3037.

Gompf, H., Chen, J., Sun, Y., Yanagisawa, M., Aston-Jones, G., and Kelz, M.B. (2009). Halothane-induced hypnosis is not accompanied by inactivation of orexinergic output in rodents. Anesthesiology *111*, 1001–1009.

Goshen, I., Brodsky, M., Prakash, R., Wallace, J., Gradinaru, V., Ramakrishnan, C., and Deisseroth, K. (2011). Dynamics of retrieval strategies for remote memories. Cell *147*, 678–689.

Gunaydin, L.A., Grosenick, L., Finkelstein, J.C., Kauvar, I.V., Fenno, L.E., Adhikari, A., Lammel, S., Mirzabekov, J.J., Airan, R.D., Zalocusky, K.A., et al. (2014). Natural neural projection dynamics underlying social behavior. Cell *157*, 1535–1551.

Hamel, E.J.O., Grewe, B.F., Parker, J.G., and Schnitzer, M.J. (2015). Cellular Level Brain Imaging in Behaving Mammals: An Engineering Approach. Neuron *86*, 140–159.

Al-Hasani, R., McCall, J.G., Foshage, A.M., and Bruchas, M.R. (2013). Locus Coeruleus Kappa Opioid Receptors modulate Reinstatement of Cocaine Place Preference through a Noradrenergic Mechanism. Neuropsychopharmacology.

Hernandez, V.H., Gehrt, A., Reuter, K., Jing, Z., Jeschke, M., Mendoza Schulz, A., Hoch, G., Bartels, M., Vogt, G., Garnham, C.W., et al. (2014). Optogenetic stimulation of the auditory pathway. J. Clin. Invest. *124*, 1114–1129.

Hickey, L., Li, Y., Fyson, S.J., Watson, T.C., Perrins, R., Hewinson, J., Teschemacher, A.G., Furue, H., Lumb, B.M., and Pickering, A.E. (2014). Optoactivation of locus ceruleus neurons evokes bidirectional changes in thermal nociception in rats. J. Neurosci. Off. J. Soc. Neurosci. *34*, 4148–4160.

Ho, J.S., Tanabe, Y., Iyer, S.M., Christensen, A.J., Grosenick, L., Deisseroth, K., Delp, S.L., and Poon, A.S.Y. (2015). Self-tracking Energy Transfer for Neural Stimulation in Untethered Mice. ArXiv150301493 Phys. Q-Bio.

Howe, J.R., Wang, J.Y., and Yaksh, T.L. (1983). Selective antagonism of the antinociceptive effect of intrathecally applied alpha adrenergic agonists by intrathecal prazosin and intrathecal yohimbine. J. Pharmacol. Exp. Ther. *224*, 552–558.

Iwai, Y., Honda, S., Ozeki, H., Hashimoto, M., and Hirase, H. (2011). A simple head-mountable LED device for chronic stimulation of optogenetic molecules in freely moving mice. Neurosci. Res. *70*, 124–127.

Jennings, J.H., Ung, R.L., Resendez, S.L., Stamatakis, A.M., Taylor, J.G., Huang, J., Veleta, K., Kantak, P.A., Aita, M., Shilling-Scrivo, K., et al. (2015). Visualizing hypothalamic network dynamics for appetitive and consummatory behaviors. Cell *160*, 516–527.

Jones, S.L. (1991). Descending noradrenergic influences on pain. Prog. Brain Res. *88*, 381–394.

Kim, K.M., Baratta, M.V., Yang, A., Lee, D., Boyden, E.S., and Fiorillo, C.D. (2012). Optogenetic Mimicry of the Transient Activation of Dopamine Neurons by Natural Reward Is Sufficient for Operant Reinforcement. PLoS ONE *7*, e33612.

Kim, T., McCall, J.G., Jung, Y.H., Huang, X., Siuda, E.R., Li, Y., Song, J., Song, Y.M., Pao, H.A., Kim, R.-H., et al. (2013). Injectable, Cellular-Scale Optoelectronics with Applications for Wireless Optogenetics. Science *340*, 211–216.

Klapoetke, N.C., Murata, Y., Kim, S.S., Pulver, S.R., Birdsey-Benson, A., Cho, Y.K., Morimoto, T.K., Chuong, A.S., Carpenter, E.J., Tian, Z., et al. (2014). Independent optical excitation of distinct neural populations. Nat. Methods *11*, 338–346.

Koob, G.F. (1999). Corticotropin-releasing factor, norepinephrine, and stress. Biol. Psychiatry *46*, 1167–1180.

Kramer, R.H., Mourot, A., and Adesnik, H. (2013). Optogenetic pharmacology for control of native neuronal signaling proteins. Nat. Neurosci. *16*, 816–823.

Krashes, M.J., Shah, B.P., Madara, J.C., Olson, D.P., Strochlic, D.E., Garfield, A.S., Vong, L., Pei, H., Watabe-Uchida, M., Uchida, N., et al. (2014). An excitatory paraventricular nucleus to AgRP neuron circuit that drives hunger. Nature *507*, 238–242.

Krystal, J.H., and Neumeister, A. (2009). Noradrenergic and serotonergic mechanisms in the neurobiology of posttraumatic stress disorder and resilience. Brain Res. *1293*, 13–23.

Lammel, S., Ion, D.I., Roeper, J., and Malenka, R.C. (2011). Projection-Specific Modulation of Dopamine Neuron Synapses by Aversive and Rewarding Stimuli. Neuron *70*, 855–862.

Lammel, S., Lim, B.K., Ran, C., Huang, K.W., Betley, M.J., Tye, K.M., Deisseroth, K., and Malenka, R.C. (2012). Input-specific control of reward and aversion in the ventral tegmental area. Nature *491*, 212–217.

Lammel, S., Steinberg, E.E., Földy, C., Wall, N.R., Beier, K., Luo, L., and Malenka, R.C. (2015). Diversity of transgenic mouse models for selective targeting of midbrain dopamine neurons. Neuron *85*, 429–438.

Land, B.B., Bruchas, M.R., Schattauer, S., Giardino, W.J., Aita, M., Messinger, D., Hnasko, T.S., Palmiter, R.D., and Chavkin, C. (2009). Activation of the kappa opioid receptor in the dorsal raphe nucleus mediates the aversive effects of stress and reinstates drug seeking. Proc. Natl. Acad. Sci. U. S. A. *106*, 19168–19173.

Lee, S.T., Williams, P.A., Braine, C.E., Lin, D.-T., John, S.W.M., and Irazoqui, P.P. (2015). A Miniature, Fiber-Coupled, Wireless, Deep-Brain Optogenetic Stimulator. IEEE Trans. Neural Syst. Rehabil. Eng. *PP*, 1–1.

Lin, J.Y., Knutsen, P.M., Muller, A., Kleinfeld, D., and Tsien, R.Y. (2013). ReaChR: a red-shifted variant of channelrhodopsin enables deep transcranial optogenetic excitation. Nat. Neurosci. *16*, 1499–1508.

Liu, L., Tsuruoka, M., Maeda, M., Hayashi, B., Wang, X., and Inoue, T. (2008). Descending modulation of visceral nociceptive transmission from the locus coeruleus/subcoeruleus in the rat. Brain Res. Bull. *76*, 616–625.

Madisen, L., Garner, A.R., Shimaoka, D., Chuong, A.S., Klapoetke, N.C., Li, L., van der Bourg, A., Niino, Y., Egolf, L., Monetti, C., et al. (2015). Transgenic Mice for Intersectional Targeting of Neural Sensors and Effectors with High Specificity and Performance. Neuron *85*, 942–958.

Mattis, J., Tye, K.M., Ferenczi, E.A., Ramakrishnan, C., O'Shea, D.J., Prakash, R., Gunaydin, L.A., Hyun, M., Fenno, L.E., Gradinaru, V., et al. (2012). Principles for applying optogenetic tools derived from direct comparative analysis of microbial opsins. Nat. Methods *9*, 159–172.

McCall, J.G., Kim, T., Shin, G., Huang, X., Jung, Y.H., Al-Hasani, R., Omenetto, F.G., Bruchas, M.R., and Rogers, J.A. (2013). Fabrication and application of flexible, multimodal light-emitting devices for wireless optogenetics. Nat. Protoc. *8*, 2413–2428.

Mejías-Aponte, C.A., Drouin, C., and Aston-Jones, G. (2009). Adrenergic and noradrenergic innervation of the midbrain ventral tegmental area and retrorubral field: prominent inputs from medullary homeostatic centers. J. Neurosci. Off. J. Soc. Neurosci. *29*, 3613–3626.

Millan, M.J. (2002). Descending control of pain. Prog. Neurobiol. *66*, 355–474.

Minev, I.R., Musienko, P., Hirsch, A., Barraud, Q., Wenger, N., Moraud, E.M., Gandar, J., Capogrosso, M., Milekovic, T., Asboth, L., et al. (2015). Biomaterials. Electronic dura mater for long-term multimodal neural interfaces. Science *347*, 159–163.

Ogawa, S.K., Cohen, J.Y., Hwang, D., Uchida, N., and Watabe-Uchida, M. (2014). Organization of monosynaptic inputs to the serotonin and dopamine neuromodulatory systems. Cell Rep. *8*, 1105–1118.

Ossipov, M.H., Dussor, G.O., and Porreca, F. (2010). Central modulation of pain. J. Clin. Invest. *120*, 3779–3787.

Park, S.I. (2013). EHANCEMENT OF WIRELESS POWER TRANSMISSION INTO BIOLOGICAL TISSUES USING A HIGH SURFACE IMPEDANCE GROUND PLANE. Prog. Electromagn. Res. *135*, 123–136.

Parker, K.E., McCall, J.G., and Will, M.J. (2010). Basolateral amygdala opioids contribute to increased high-fat intake following intra-accumbens opioid administration, but not following 24-h food deprivation. Pharmacol. Biochem. Behav. *97*, 262–266.

Peyman, A., Rezazadeh, A.A., and Gabriel, C. (2001). Changes in the dielectric properties of rat tissue as a function of age at microwave frequencies. Phys. Med. Biol. *46*, 1617–1629.

Polosukhina, A., Litt, J., Tochitsky, I., Nemargut, J., Sychev, Y., De Kouchkovsky, I., Huang, T., Borges, K., Trauner, D., Van Gelder, R.N., et al. (2012). Photochemical Restoration of Visual Responses in Blind Mice. Neuron *75*, 271–282.

Poon, A.S.Y., O'Driscoll, S., and Meng, T.H. (2010). Optimal Frequency for Wireless Power Transmission Into Dispersive Tissue. IEEE Trans. Antennas Propag. *58*, 1739–1750.

Raimondo, J.V., Kay, L., Ellender, T.J., and Akerman, C.J. (2012). Optogenetic silencing strategies differ in their effects on inhibitory synaptic transmission. Nat. Neurosci. *15*, 1102–1104.

Richards, N., and McMahon, S.B. (2013). Targeting novel peripheral mediators for the treatment of chronic pain. Br. J. Anaesth. *111*, 46–51.

Sara, S.J. (2009). The locus coeruleus and noradrenergic modulation of cognition. Nat. Rev. Neurosci. *10*, 211–223.

Sara, S.J., and Bouret, S. (2012). Orienting and reorienting: the locus coeruleus mediates cognition through arousal. Neuron *76*, 130–141.

Saunders, A., Johnson, C.A., and Sabatini, B.L. (2012). Novel recombinant adeno-associated viruses for Cre activated and inactivated transgene expression in neurons. Front. Neural Circuits *6*, 47.

Scheib, J., and Höke, A. (2013). Advances in peripheral nerve regeneration. Nat. Rev. Neurol. *9*, 668–676.

Shaham, Y., Highfield, D., Delfs, J., Leung, S., and Stewart, J. (2000). Clonidine blocks stress-induced reinstatement of heroin seeking in rats: an effect independent of locus coeruleus noradrenergic neurons. Eur. J. Neurosci. *12*, 292–302.

S.n, A.U.N., T.v, P., H.s, J., Ganapathi, K., B.k, P., C.m, R., and R, S.N. (2012). Near Field Communication – Applications and Performance Studies. In Wireless Networks and Computational Intelligence, K.R. Venugopal, and L.M. Patnaik, eds. (Springer Berlin Heidelberg), pp. 1–10.

Stachniak, T.J., Ghosh, A., and Sternson, S.M. (2014). Chemogenetic synaptic silencing of neural circuits localizes a hypothalamus→midbrain pathway for feeding behavior. Neuron *82*, 797–808.

Stamatakis, A.M., Jennings, J.H., Ung, R.L., Blair, G.A., Weinberg, R.J., Neve, R.L., Boyce, F., Mattis, J., Ramakrishnan, C., Deisseroth, K., et al. (2013). A unique population of ventral tegmental area neurons inhibits the lateral habenula to promote reward. Neuron *80*, 1039–1053.

Stuber, G.D., Stamatakis, A.M., and Kantak, P.A. (2015). Considerations when using cre-driver rodent lines for studying ventral tegmental area circuitry. Neuron *85*, 439–445.

Tochitsky, I., Polosukhina, A., Degtyar, V.E., Gallerani, N., Smith, C.M., Friedman, A., Van Gelder, R.N., Trauner, D., Kaufer, D., and Kramer, R.H. (2014). Restoring Visual Function to

Blind Mice with a Photoswitch that Exploits Electrophysiological Remodeling of Retinal Ganglion Cells. Neuron *81*, 800–813.

Tsai, H.-C., Zhang, F., Adamantidis, A., Stuber, G.D., Bonci, A., de Lecea, L., and Deisseroth, K. (2009). Phasic firing in dopaminergic neurons is sufficient for behavioral conditioning. Science *324*, 1080–1084.

Tsuruoka, M., Wang, D., Tamaki, J., and Inoue, T. (2010). Descending influence from the nucleus locus coeruleus/subcoeruleus on visceral nociceptive transmission in the rat spinal cord. Neuroscience *165*, 1019–1024.

Tye, K.M., Prakash, R., Kim, S.-Y., Fenno, L.E., Grosenick, L., Zarabi, H., Thompson, K.R., Gradinaru, V., Ramakrishnan, C., and Deisseroth, K. (2011). Amygdala circuitry mediating reversible and bidirectional control of anxiety. Nature *471*, 358–362.

Vazey, E.M., and Aston-Jones, G. (2014). Designer receptor manipulations reveal a role of the locus coeruleus noradrenergic system in isoflurane general anesthesia. Proc. Natl. Acad. Sci. *111*, 3859–3864.

Velásquez-Martinez, M.C., Vázquez-Torres, R., and Jiménez-Rivera, C. a (2012). Activation of alpha1-adrenoceptors enhances glutamate release onto ventral tegmental area dopamine cells. Neuroscience *216*, 18–30.

Viventi, J., Kim, D.-H., Moss, J.D., Kim, Y.-S., Blanco, J.A., Annetta, N., Hicks, A., Xiao, J., Huang, Y., Callans, D.J., et al. (2010). A Conformal, Bio-Interfaced Class of Silicon Electronics for Mapping Cardiac Electrophysiology. Sci. Transl. Med. *2*, 24ra22–ra24ra22.

Viventi, J., Kim, D.-H., Vigeland, L., Frechette, E.S., Blanco, J.A., Kim, Y.-S., Avrin, A.E., Tiruvadi, V.R., Hwang, S.-W., Vanleer, A.C., et al. (2011). Flexible, foldable, actively multiplexed, high-density electrode array for mapping brain activity in vivo. Nat. Neurosci. *14*, 1599–1605.

Watabe-Uchida, M., Zhu, L., Ogawa, S.K., Vamanrao, A., and Uchida, N. (2012). Whole-Brain Mapping of Direct Inputs to Midbrain Dopamine Neurons. Neuron *74*, 858–873.

Weinshenker, D., and Schroeder, J.P. (2007). There and back again: a tale of norepinephrine and drug addiction. Neuropsychopharmacol. Off. Publ. Am. Coll. Neuropsychopharmacol. *32*, 1433–1451.

Weninger, S.C., Dunn, A.J., Muglia, L.J., Dikkes, P., Miczek, K.A., Swiergiel, A.H., Berridge, C.W., and Majzoub, J.A. (1999). Stress-induced behaviors require the corticotropin-releasing hormone (CRH) receptor, but not CRH. Proc. Natl. Acad. Sci. *96*, 8283–8288.

Witten, I.B., Steinberg, E.E., Lee, S.Y., Davidson, T.J., Zalocusky, K.A., Brodsky, M., Yizhar, O., Cho, S.L., Gong, S., Ramakrishnan, C., et al. (2011). Recombinase-driver rat lines: tools,

techniques, and optogenetic application to dopamine-mediated reinforcement. Neuron *72*, 721–733.

Yizhar, O., Fenno, L.E., Davidson, T.J., Mogri, M., and Deisseroth, K. (2011). Optogenetics in Neural Systems. Neuron *71*, 9–34.

Ziv, Y., Burns, L.D., Cocker, E.D., Hamel, E.O., Ghosh, K.K., Kitch, L.J., El Gamal, A., and Schnitzer, M.J. (2013). Long-term dynamics of CA1 hippocampal place codes. Nat. Neurosci. *16*, 264–266.

Zoksimovski, A., Sexton, D., Stojanovic, M., and Rappaport, C. Underwater electromagnetic communications using conduction – Channel characterization. Ad Hoc Netw.

Zorzos, A.N., Boyden, E.S., and Fonstad, C.G. (2010). Multiwaveguide implantable probe for light delivery to sets of distributed brain targets. Opt. Lett. *35*, 4133–4135.

Zorzos, A.N., Scholvin, J., Boyden, E.S., and Fonstad, C.G. (2012). Three-dimensional multiwaveguide probe array for light delivery to distributed brain circuits. Opt. Lett. *37*, 4841–4843.

Appendix 1

Distinct subpopulations of nucleus accumbens dynorphin neurons drive aversion or reward

Author contributions for the above citation:
*Co-first author R.A. and **J.G.M** designed and performed experiments, collected and analyzed data, and wrote the manuscript. A.M., G.P.S and J.M.B performed experiments and collected data. G.S., C.P. and S.I.P designed and fabricated the wireless bidirectional μ-iLED devices and RF power harvesters. C.M.M., N.A.C and T.L.K designed and performed *in vitro* whole cell recordings. M.J.K and B.B.L generated the Dyn-Cre mouse line. J.A.R. helped design and oversee the wireless device operation. M.R.B. helped design and oversee experiments, and wrote the manuscript.

SUMMARY

Both the nucleus accumbens (NAc) and the dynorphinergic system are widely implicated in motivated behaviors. Prior studies have shown that activation of the dynorphin-kappa opioid receptor (KOR) system can lead to aversive, dysphoria-like behavior. However, the endogenous sources of dynorphin in these circuits remain unknown. We investigated whether dynorphinergic neuronal firing in the NAc is sufficient to induce aversive behaviors. We found that photostimulation of dynorphinergic cells in the dorsal NAc shell induces robust place preference and is positively reinforcing in an operant paradigm, whereas activation of dynorphin neurons in the ventral NAc shell elicits robust conditioned and real-time aversive behavior via KOR activation. These results show a previously unknown, discrete NAc subregion of dynorphin-containing cells in the ventral shell that selectively drive aversive behavior. Understanding the regional specificity by which NAc dynorphinerigic cells regulate aversion provides valuable insight into the motivated behaviors dysregulated in stress and psychiatric disease.

INTRODUCTION

It is now widely thought that many mood disorders are associated with major disruption of the brain's reward circuitry (Nestler and Carlezon, 2006). The nucleus accumbens (NAc) is a key region within this circuitry with major projections from the ventral tegmental area (VTA), medial prefrontal cortex (mPFC), basolateral amygdala (BLA) and the hippocampus (Russo and Nestler, 2013). Recent studies have identified the striatum as crucial for integrating behavioral responses to both positive and negative reinforcement (Castro and Berridge, 2014; Everitt and Robbins, 2005; Kravitz et al., 2012). Furthermore, it is thought that negative emotional states are what mediate and perpetuate the phases of depression as well as increase susceptibility to drug abuse. NAc neuronal activity is consistently reduced in major depression in humans (Drevets et

321

al., 1992; Mayberg et al., 2000) and is thought to reflect loss of reward function that drives common symptoms such as anhedonia (Russo and Nestler, 2013). In order to better understand these processes, it is important to dissect how neuromodulator systems within specific subregions of the brain function to influence negative emotional states, represented by changes in motivated behavior.

The kappa opioid receptor (KOR) system has recently been identified as one such prominent neuromodulator system for regulating motivated behavior and is highly implicated in stress-induced dysphoria and vulnerability to drug abuse. Its peptide dynorphin (Dyn), which is cleaved from the precursor prodynorphin, endogenously activates KORs (Chavkin et al., 1982). Dyn is known to mediate negative emotional states, with KOR agonists inducing place aversions, depression-like behavior, and dysphoria in human and animal models (Mucha et al., 1985; Pfeiffer et al., 1986; Shippenberg et al., 2007). Notably, direct infusion of KOR agonists into the NAc mediates conditioned place aversion (Bals-Kubik et al., 1989), and local antagonism of KOR in this region prevents depression-like behavioral responses (Land et al., 2009; Shirayama et al., 2004). Furthermore, Dyn-containing axon terminals and cell bodies are located in the NAc (Van Bockstaele et al., 1995). Additionally, a number of studies have shown recruitment of the Dyn/KOR system in the NAc following compulsive drug taking (Daunais et al., 1993; Fagergren et al., 2003; Hurd et al., 1992; Lindholm et al., 2000; Schlussman et al., 2005; Solecki et al., 2009). It is thought that monoamine output within the NAc is tightly regulated via presynaptic KORs on serotonergic and dopaminergic cells in the region, ultimately acting to suppress release of dopamine and serotonin. However, the mechanisms and role of Dyn-containing circuits in the regulation of KOR-mediated negative affective behaviors remain unresolved (Bruchas et al., 2010, 2011).

Here we directly ascertained the sufficiency of local Dyn release within the NAc shell to drive aversive behavior. We hypothesized that photostimulation of Dyn-containing cells in the NAc shell will drive an aversion behavior in a real-time place testing paradigm using a new form of birdirectional wireless μ-ILED optogenetic technology, a conditioned place testing paradigm and an operant self-stimulation paradigm. We report a distinct subpopulation of ventral NAc Dyn-containing cells that when activated produce robust aversive behavioral responses, whereas stimulation of a nearby dorsal NAc site engages positively reinforced motivated behaviors.

RESULTS

Activation of dynorphinergic cells in the NAc shell drives both aversion and reward

To determine key sites of Dyn influence throughout the brain we generated a Dyn-tdTomato-reporter mouse by crossing preprodynorphin-IRES-Cre (Dyn-IRES-Cre) mice to Allen Institute for Brain Science tdTomato flox-stop reporter line (Ai9) (Madisen et al., 2010) **(Figure A1.1A, Figure A1.2).** This new mouse line (Dyn-Cre^{tdTomato}) is useful for Cre-dependent expression/excision in selected Dyn-circuits and provides a representative map of Dyn expressing cells, Dyn axon projections, and terminal fields. We first characterized Dyn expression across the full brain of these mice, comparing our Dyn-Cre^{tdTomato} expression side-by-side with *in situ* hybridization data **(Figure A1.1B)** to confirm soma specific labeling in well known Dyn enriched regions. Using Dyn-Cre^{tdTomato} mice we visualized an abundance of Dyn-containing cells within the NAc, in direct line with current literature **(Figure A1.1C)**. In addition, we found robust Dyn-induced tdTomato expression in the hippocampus, bed nucleus of the stria
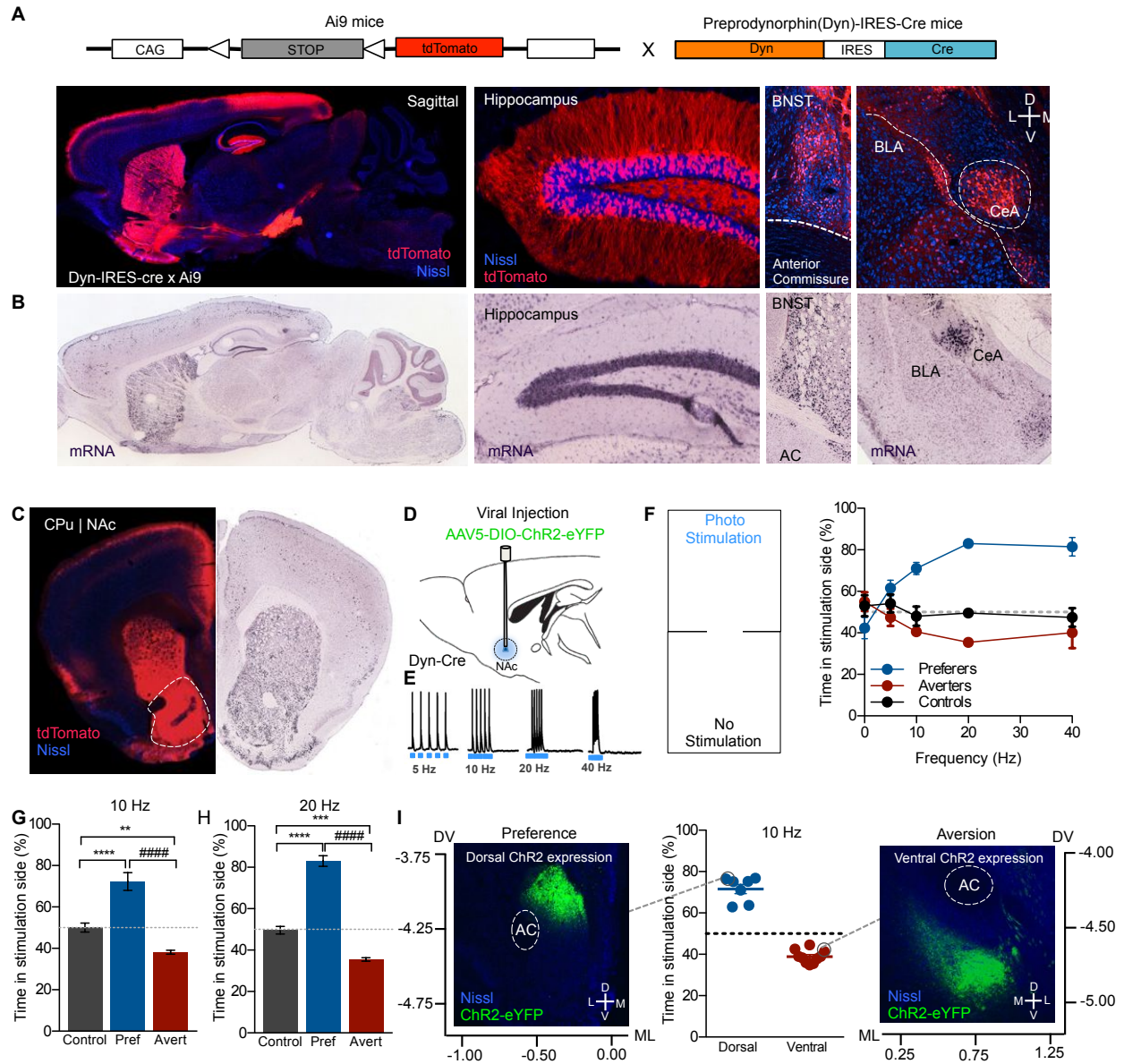
Figure A1.1: **Photostimulation of dynorphinergic cells in the NAc shell drives and aversion and reward**. **A**. Dyn labeling in Dyn-IRES-cre x Ai9-tdTomato compared to *in situ* images from the **B**. Allen Institute for Brain Science in a sagittal section highlighting presence of Dyn in the striatum, the hippocampus, BNST, amygdala, hippocampus and substantia nigra. All images show tdTomato (red) and Nissl (blue) staining. **C**. Coronal section highlighting dynorphinergic cell labeling in the NAc as compared to the Allen Institute for Brain Science. **D**. Cartoon depicting virus and fiber optic placement. **E**. Whole cell slice recording showing that dynorphinergic cells in the NAc shell fire optically stimulated action potentials from 5-40 Hz. **F**. Cartoon of real time place testing set up and a frequency response curve showing two distinct groups 'preferers' and 'averters' spend significantly more time in the stimulated and non-stimulated side, respectively, following 10, 20 and 40 Hz stimulation (Data represented as mean ± SEM, n=6: Two-Way ANOVA, interaction effect between groups and frequency, $p<0.0001$) in a real-time place testing paradigm **G.** At 10 Hz preferers and averters show a significant preference or aversion compared to one another and controls (Data represented as mean ± SEM, n=5-8: One-Way ANOVA, Bonferroni post-hoc, control *vs* preferers ****$p<0.0001$, control *vs* averters **$p<0.01$, preferers *vs* averters ####$p<0.0001$). **H**. At 20 Hz preferers and averters show a significant preference or aversion compared to one another and controls (Data represented as mean ± SEM, n=6: One-Way ANOVA, Bonferroni post-hoc, control *vs* preferers ****$p<0.0001$, control *vs* averters ***$p<0.001$, preferers *vs* averters ####$p<0.0001$). **I.** Scatter plot for preferers and averters at following 10Hz photostimulation, with representative IHC showing that preferers show dorsal ChR2 expression whereas averters show ventral ChR2 expression (n=7-10).
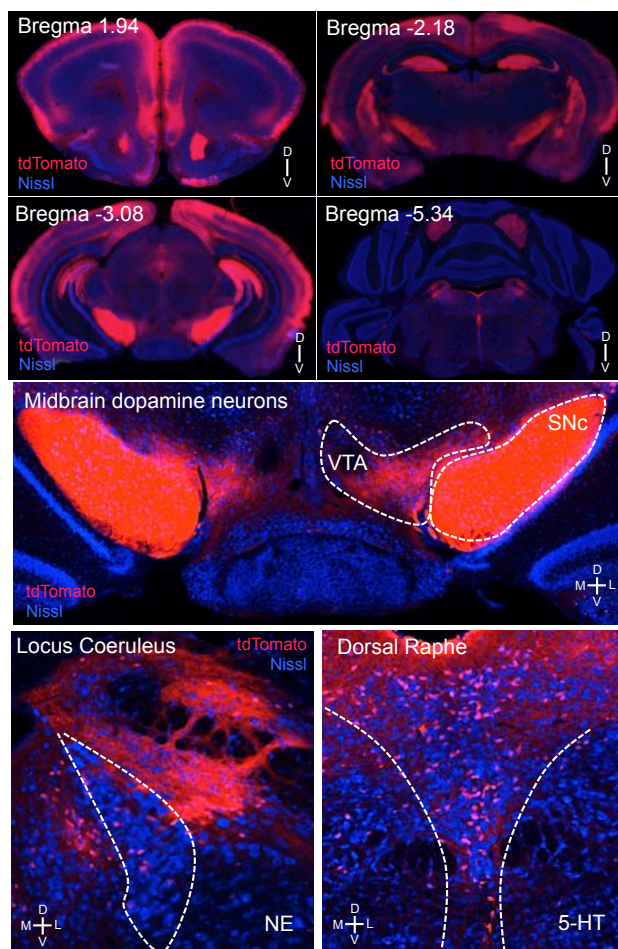
Figure A1.2 Additional Dyn labeling in Dyn-IRES-cre x Ai9-tdTomato throughout the brain. A. Bregma 1.94, coronal section including the cortex and NAc. **B.** Bregma -2.18, coronal section including the hippocampus and tracts through the cerebral peduncle. **C.** Bregma -3.08, coronal section including the substantia nigra and the VTA. **D.** Bregma -5.34, coronal section including the parabrachial nucleus and the colliculus **E.** Dynorphinergic labeling in the dopamine rich areas of the ventral tegmental area and the substantia nigra. **F.** Dynorphinergic labeling in the locus coeruleus and **G.** the dorsal raphe. Images are representative of three separate brains imaged in their entirety.

terminalis, basolateral amygdala, central nucleus of the amygdala, throughout the cortex, caudate putamen, globus pallidus, the dopamine rich areas of the ventral tegmental area and the substania nigra, dorsal raphe and locus coeruleus **(Figure A1.1A, Figure A1.2A-G)**.

To dissect the role of NAc Dyn-containing cells, we utilized *in vivo* optogenetics to selectively target these neurons and assess their ability to be photostimulated **(Figure A1.1D)**. However, due to the novelty of this Dyn-Cre mouse line we first determined whether photostimulation of Dyn-containing cells could elicit action potentials at multiple frequencies in slice. We injected AAV5-DIO-ChR2-eYFP into the NAc of Dyn-Cre mice and performed whole-cell electrophysiology. We found robust intact spike fidelity at frequencies of 5 Hz, 10Hz and 20Hz (1 ms pulse width), which was not maintained at 40 Hz **(Figure A1.1E)**.

Prior reports have suggested that the Dyn/KOR system mediates negative emotional states through increased Dyn expression in the NAc, contributing to the dysphoria associated with depression and drug dependence. However, the endogenous source of Dyn in these responses has not been previously shown (Britton et al., 1982; Bruchas et al., 2010; Knoll et al., 2011; Lindholm et al., 2000; Mucha et al., 1985; Pfeiffer et al., 1986; Rylkova et al., 2009; Schlosburg et al., 2013; Shippenberg et al., 2007). Given the location of Dyn-containing cells in the NAc, we first hypothesized that photostimulation of NAc-Dyn neurons will produce aversive behaviors. To test this hypothesis we injected AAV5-DIO-ChR2-eYFP,chronically implanted a fiber optic into the NAc shell of Dyn-Cre positive and Dyn-Cre negative mice and used a real-time place-testing paradigm (RTPT) **(Figure A1.1F)**. During this 20 min behavioral test, photostimulation occurs in real-time only upon entry into the counterbalanced designated chamber (Carter et al., 2010; Stamatakis and Stuber, 2012; Tan et al., 2012). Behavioral data are then calculated as time spent in the photostimulation- paired chamber, expressed as a percentage

of total time. In this experiment we also assessed the efficacy of photostimulated cell firing *in vivo* in producing real-time behavioral responses, as compared to the *in vitro* whole-cell recordings. In accordance with our hypothesis, we show that photostimulation of Dyn-containing cells in the NAc shell over the same range of frequencies, 5Hz, 10Hz and 20Hz produces a significant real-time aversion behavior, that plateaued at 40Hz, correlating with the *in vitro* whole-cell recordings **(Figure A1.1E)**. However a subgroup of mice showed a robust preference behavior when compared to controls. We therefore defined these two groups as real time 'averters' or 'preferers'. Our data show a significant interaction between the preferers, averters, controls and the frequency of photostimulation **(Figure A1.1F)**. In addition, *in vivo* 10Hz and 20Hz stimulation produced a significant real-time place-preference and aversion in the preferers as well as the averters, respectively, compared either to control or to one another **(Figure A1.1 G and H)**. To investigate what may drive these opposing behavioral states between preferers and averters we carefully examined the anatomical distribution of viral expression within the NAc shell of each individual mouse and group. Interestingly, we identified that mice which exhibited a preference behavior, showed isolated dorsal viral expression in the NAc shell whereas mice which exhibited an aversion behavior showed a more ventral pattern of viral expression **(Figure A1.1I)**. These results suggest that photostimulation of Dyn-containing cells in discrete subregions within the NAc shell can drive opposing behaviors with distinct positive or negative valence. These data indicate that photostimulation of Dyn-containing cells in the dorsal NAc drives a real-time place preference whereas photostimulation of Dyn-containing cells in the ventral NAc drives a real-time place aversion.

Spatially discrete targeting of NAc dyn-containing cells engages both preference and aversion in the same animal

To further investigate the subregional distinction in behavior within the NAc shell and to enable precise, discrete spatial targeting we used a novel modified form of our recently developed wireless μ-ILED devices (Kim et al., 2013; McCall et al., 2013). We reconfigured the original wireless μ-ILED devices to produce a device that allows isolated and directionally controlled light to specific NAc subregions. In this case we positioned one μ-ILED to target the dorsal NAc and the other the ventral NAc shell **(Figure A1.3A, Figure A1.4)**, separated by a distance of 1 mm. These devices are wirelessly controlled using an RF power source, which can either stimulate each μ-ILED independently or both together simultaneously **(Figure A1.3B, Figure A1.4)**. These devices provide discrete spatial targeting and importantly allow us to photostimulate each region to drive opposing behaviors within the same individual mouse. Following viral injections of AAV5-DIO-ChR2-eYFP into the NAc shell of Dyn-Cre positive and Dyn-Cre negative mice, with expression spanning both dorsal and ventral co-ordinates, devices were implanted into mice and used in the real-time place preference paradigm **(Figure A1.3C)**. Here we show that within the same mouse we can selectively photostimulate the ventral NAc, to produce a real time aversion or we can photostimulate the dorsal NAc to drive a real time preference **(Figure A1.3D, E & F)**. In addition, photostimulation of Dyn-containing cells in either the dorsal or the ventral NAc shell does not induce any significant changes in locomotor activity compared to controls (Fig 2F). In addition, we wanted to investigate if targeting these distinct regions in the NAc induced anxiety behavior, since recent reports have implicated the KOR/Dyn system in anxiety-like behavioral responses (Bruchas et al., 2009; Knoll et al., 2011).
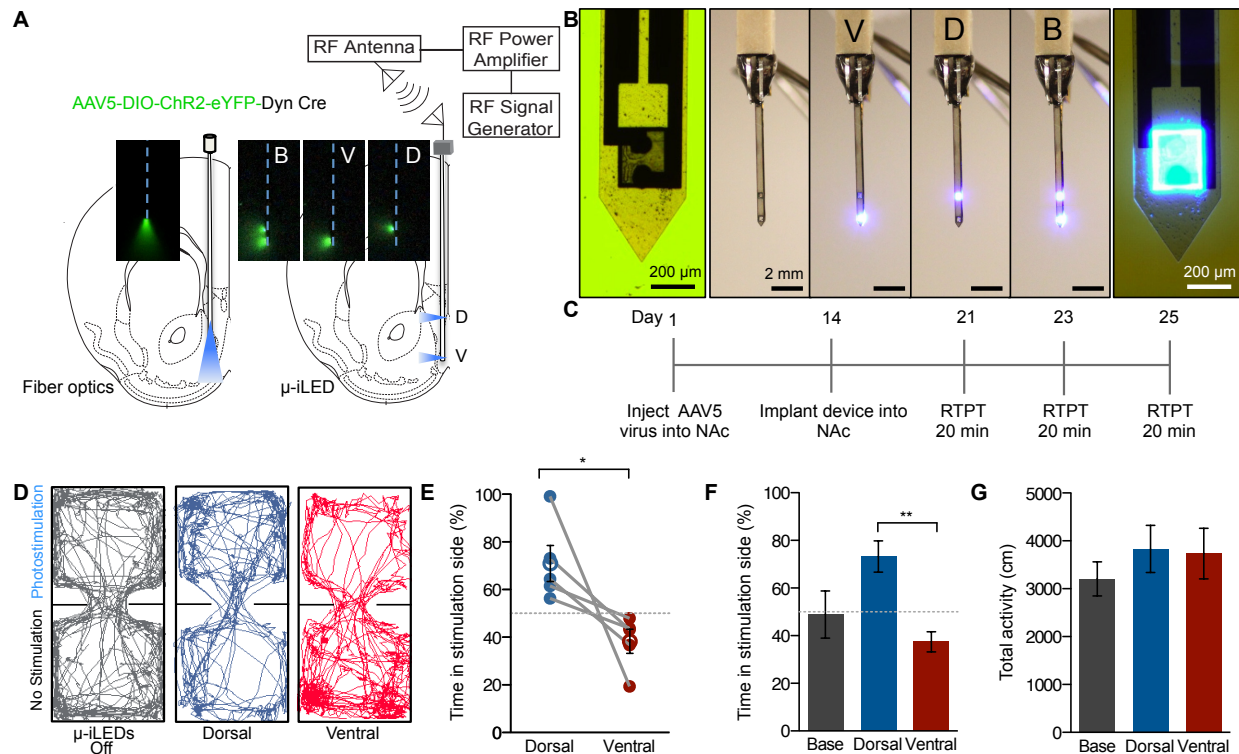
Figure A1.3 Discrete spatial targeting drives preference and aversion in the same animal.
A. Directionally-controlled light spread of μ-iLED devices has advantages over fiber optics for isolating subregions of NAc as demonstrated in the fluorescein images. **B.** Images of an ultrathin (~10-50 μm), flexible integrated system. Light can be isolated to either dorsal or ventral NAc **C.** Behavioral calendar outlining the design of the experimental procedure. **D.** Examples of real-time mouse behavioral traces following no stimulation, ventral or dorsal wireless photostimulation. **E.** An aversion and preference real-time behavior following stimulation of the ventral and dorsal NAc shell within each individual mouse (Data represented as mean ± SEM, n=5: Student's t-test, p=0.05). **F.** Stimulation with dorsal LED drives a real-time place preference but stimulation with ventral LED drives an aversion, which are significantly different from one another (Data represented as mean ± SEM, n=6: One-Way ANOVA, Bonferroni post-hoc **p<0.01) **G.** No significant difference in locomotor activity measured during a 20 min trial between all groups (Data represented as mean ± SEM, n=6).

A Antenna 1.5 GHz & 2.4 GHz

B

5 mm   5 mm

C   1.5 GHz   2.4 GHz

V →   ← D

5 mm   5 mm   5 mm

D Peak: 465 nm

E

F

331

Figure A1.4 Fabrication details for the bidirectional μ-iLED devices. A. Circuit diagram of wireless energy harvester operating at 1.5Ghz and 2.4 GHz. It consists of antennas, impedance matching circuits, Cockcroft-Walton multiplier, and

blue-LED. **B.** An image showing the device plus the harvester that wirelessly powers the device. **C.** An image of the μ-iLED connected to the harvester that can power either the dorsal or ventral μ-iLED at different carrier frequencies. **D.** Light emission spectrum of blue LED which has the peak wavelength of 465 nm **E.** Light output-Current-Voltage (L-I-V) characteristics of injectable LED device. **F.** No significant difference in mean velocity measured during a 20 min trial between all groups (Data represented as mean ± SEM, n=6).
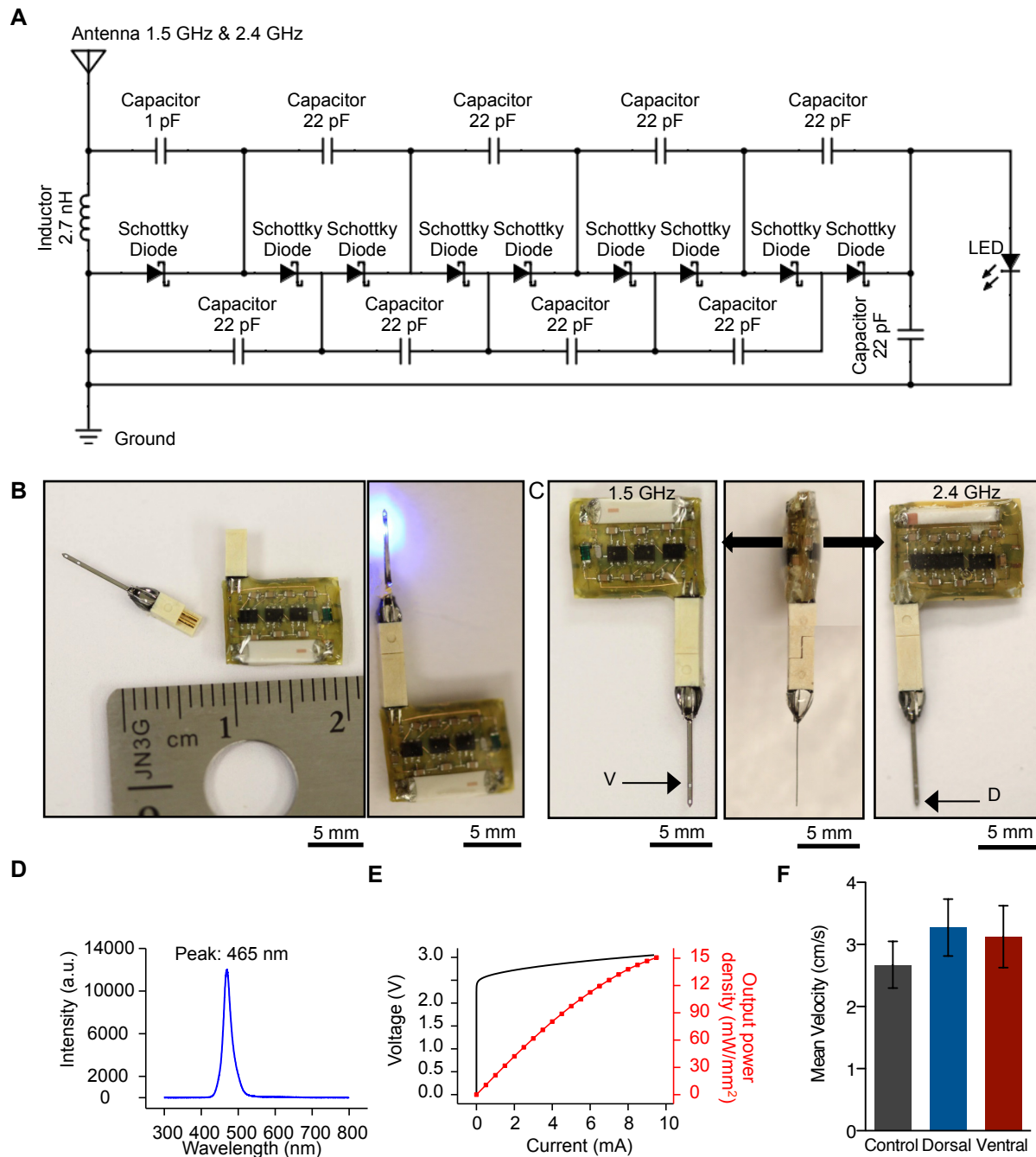
Together, these data support the hypothesis that activation of Dyn-containing cells in the ventral NAc shell drives an aversion behavior. These novel devices also demonstrate that within the same animal we can cause a preference behavior by stimulating Dyn-containing cells in the dorsal NAc shell. Bidirectional µ-ILED control adds confidence to the current findings and suggests that stimulation of the subsets of neurons within the NAc dynorphinergic system is capable of dynamic engagement of either positive or negative behavioral valence. Furthermore, because these devices are ultrathin, minimally invasive, (Kim et al., 2013) and target both dorsal and ventral NAc, there is limited likelihood that dorsal lesions from our earlier fiber optic implantation **(Figure A1.1)** influence the observed behavioral responses.

Aversion following photostimulation of Dyn-containing neurons in the ventral NAc shell requires KOR activity

Current research indicates a role for NAc KORs in aversive negative affective behaviors involved in stress, dysphoria and drug abuse (Bals-Kubik et al., 1989; Land et al., 2009; Mucha et al., 1985; Shippenberg et al., 2007; Solecki et al., 2009). Therefore, we hypothesized that activation of kappa opioid receptors following the photostimulated-release of Dyn in the ventral NAc is one of the key underlying mechanisms for the observed aversion behavior.

From this point onward we modified our virus volume and co-ordinates to specifically target either the dorsal or ventral NAc shell. We also injected Cre-negative control mice in either the dorsal and ventral NAc and saw no effect of photostimulation in either group. Based on the results from our whole cell slice recordings and *in vivo* frequency response data we photostimulated at 10 Hz with a 10 ms pulse width to elicit action potential firing, evoke release of Dyn, remain physiologically-relevant and to maintain spike fidelity. We first assessed how

photostimulation of Dyn-containing cells in the ventral NAc shell drives an aversion in a conditioned place preference paradigm. This behavioral model is a form of pavlovian conditioning used to measure the motivational or aversive effects of an associated experience. The key component of this model is the learning aspect, which was absent in our RTPT paradigm **(Figure A1.1).** We showed that in a y-maze conditioning paradigm **(Figure A1.5A)** we are able to condition mice to the photostimulation of Dyn-containing cells in the ventral Nac to drive an aversion behavior, which is consistent with our earlier findings. In addition, conditioned photostimulation of dorsal Nac shell was able to drive a significant preference behavior when compared to controls and to each other **(Figure A1.5B, C & D)**.

To test the hypothesis that the aversion behavior is driven by the release of Dyn from cells within the ventral NAc shell acting on KOR we locally infused the long acting KOR antagonist NorBNI (2.5μg/1μl) (Bruchas et al., 2007; Al-Hasani et al., 2013; Melief et al., 2010) into the ventral NAc shell, 14 days after site specific viral (AAV5-DIO-ChR2-eYFP) injection in to the ventral NAc **(Figure A1.5A)**. Importantly, injection of NorBNI into the ventral NAc shell was able to significantly block the aversion seen following photostimulation of Dyn-containing cells **(Figure A1.5B, C, D)** with no observed change in locomotor activity **(Figure A1.5E)**. These findings identify the aversion behavior mediated following photostimulation of Dyn-containing cells in the ventral NAc as KOR-mediated, acting locally within the NAc itself, consistent with prior studies using exogenous ligand infusions within this region (Castro and Berridge, 2014; Land et al., 2009; Shippenberg et al., 2007).
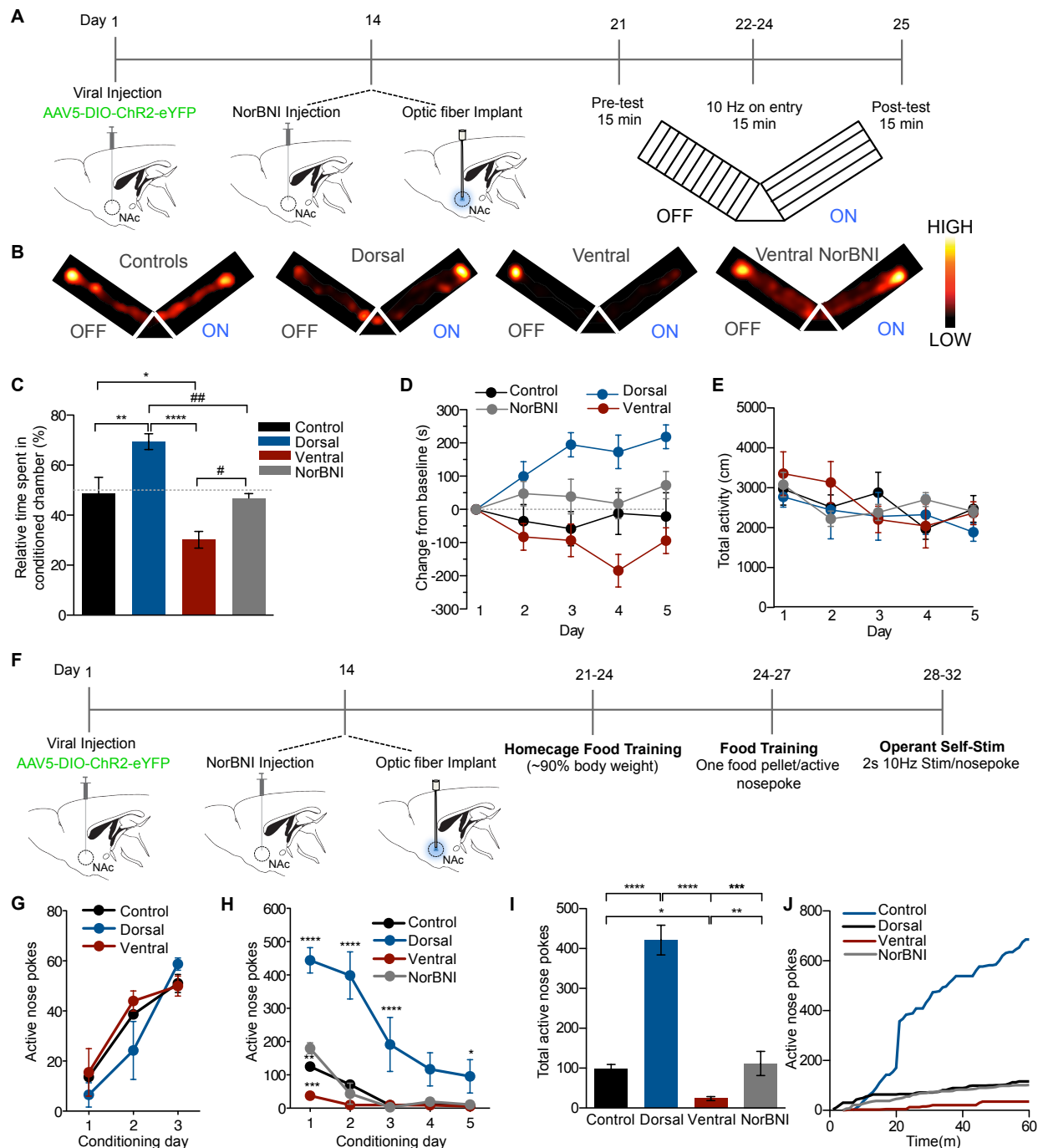
Figure A1.5 Aversion following photostimulation of Dyn-containing neurons in the ventral NAc shell requires KOR activity. **A**. Calendar outlining experimental procedure for the Y-maze paradigm. **B**. Representative heat map of activity during post-test day 5. **C**. Mice injected and photostimulated in the dorsal NAc show a significant increase in % time spent in

conditioned arm of the Y-maze whereas mice stimulated in the ventral NAc show an aversion (Data represented as mean ± SEM, n=8-13: One-Way ANOVA, Bonferroni post-hoc, control *vs* dorsal **$p<0.01$, Control *vs* ventral *$p<0.05$, dorsal *vs* ventral ****$p<0.0001$, dorsal *vs* ventral NorBNI ##$p<0.01$, ventral *vs* ventral NorBNI #$p<0.05$. **D.** Change from baseline measured across all 5 days of the y-maze paradigm (Data represented as mean ± SEM, n=8-13, Two-Way ANOVA, interaction effect between groups and days, $p<0.0001$) **E**. No significant difference in locomotor activity measured during a 20 min trial between all groups (Data represented as mean ± SEM, n=8-13). **F.** Calendar outlining experimental procedure for the operant self-stimulation paradigm. **G**. No significant difference in active nose pokes for food reward between all groups (Data represented as mean ± SEM, n=6-7). **H**. Data showing number of nose pokes across 5 days of operant self-stimulation. Dorsally injected mice show significantly increased active nose pokes, compared to controls and ventrally injected mice, which show a significant reduction in nose pokes following photostimulation (Data represented as mean ± SEM, n=6-7: Two Way repeated measures ANOVA, Bonferroni post-hoc; dorsal vs controls, ventral and ventral NorBNI on day 1,2,3 ****$p<0.0001$, dorsal vs control and ventral on day 4 *$p<0.05$, control vs ventral on day 1 **$p<0.01$, ventral vs ventral NorBNI ***$p<0.001$. **I**. Significant differences in total nose pokes on day and day 2 following photostimulation (Data represented as mean ± SEM, n=6-7: One-Way ANOVA, bonferroni post-hoc, control vs dorsal ****$p<0.0001$, control vs ventral *$p<0.05$, dorsal vs ventral ****$p<0.0001$, dorsal vs ventral NorBNI ****$p<0.0001$, ventral vs ventral NorBNI **$p<0.01$. J. Representative 60 min trials for each group.

Distinct NAc dynophin populations in operant stimulation produce positive and negative responses

The operant self-stimulation paradigm is unique in that it demonstrates the ability of a mouse to establish response habits similar to those exhibited to natural rewards. Here we assessed the contribution of dorsal and ventral NAc shell Dyn-containing neurons in self-stimulation. Importantly, all groups of mice, whether injected with AAV5-DIO-ChR2-eYFP in Dyn-Cre mice, in either the dorsal or ventral NAc, were able to learn to poke for a food reward **(Figure A1.5F and G)**. Following food training the food pellet was replaced with a 2s (10Hz, 10ms pulse width) photo-stimulation, which was delivered following a nose poke. The dorsally injected mice continued to show positive reinforcement behavior but the number of nose pokes increased 5-fold following photostimulation, emphasizing the highly rewarding nature of self-stimulation of this NAc shell subregion **(Figure A1.5G, H, I)**. However, both the controls and the ventrally-injected mice decreased their number of nose pokes following photostimulation. While both were significantly different compared to the dorsally injected mice, the ventrally injected mice showed a significant decrease in the number of nose pokes compared to controls **(Figure A1.5G, H, I)**. The aversive nature of the photostimulation in the ventral NAc shell mice suggest that it is strong enough to mute the extinction burst seen during the first day of photostimulation and accelerate extinction following food training. The extinction burst is characteristic in the operant model but in the case of this experiment is highly interesting as the ventrally-injected mice show an acceleration in extinction and overall reduced nose pokes for photostimulation whereas the dorsal mice maintain an increased number of nose pokes due to the rewarding nature of the stimulation **(Figure A1.1G, H, I)**. These operant self-stimulation data

further suggest that there is a dynamic relationship between the positively reinforcing and aversive nature of stimulating distinct subpopulations of NAc shell Dyn-containing cells.

DISCUSSION

In the present study we identify that photostimulation of Dyn-containing cells in discrete subregions within the NAc shell drive opposing motivational behavioral states. We show that photostimulation of Dyn cells in the ventral NAc shell drives aversion behavior whereas photostimulation in the dorsal NAc shell drives a preference/reward behavior. This is the first study to our knowledge to report a distinction in aversion and reward behavior within the NAc shell via dynorphin-containing cells and here we demonstrate this using three different behavioral paradigms; real-time place testing using bidirectional wireless µ-ILED technology, conditioned place testing and operant self-stimulation.

Previous studies reported that the Dyn/KOR system mediates negative emotional states through increased Dyn expression in the NAc, contributing to the dysphoria associated with depression, drug dependence and withdrawal but the mechanisms for engagement of dynorphin circuitry are unknown (Britton et al., 1982; Bruchas et al., 2009; Knoll et al., 2011; Lindholm et al., 2000; Mucha et al., 1985; Pfeiffer et al., 1986; Rylkova et al., 2009; Schlosburg et al., 2013; Shippenberg et al., 2007). In this study we are able to show that activation of Dyn-containing cells within a distinct region of the NAc shell, the ventral NAc shell, drives an aversion behavior, as demonstrated in a real-time place preference paradigm. Few reports have extensively investigated regional distinctions within the NAc that might mediate differences in aversion and reward behaviors. However, it has recently been shown that the rostrodorsal quadrant of the medial NAc shell contains a specialized opioid hedonic hotspot in rats, which traditionally

338

mediates an increase in "liking" following mu opioid receptor (MOR) activation, however a role

has also been identified for both delta opioid receptors (DOR) and KOR (Castro and Berridge,

2014). Within this recent body of work, a separate suppressive cold spot in the caudal half of the

shell was identified in which each opioid stimulation oppositely reduced sucrose positive

"liking" reactions (Castro and Berridge, 2014). In addition to these interesting findings this

group also identified several anatomical differences between NAc opioid control of "liking"

verses "wanting" of feeding (Castro and Berridge, 2014). These results highlight anatomical

heterogeneity of the NAc, but also show that this is localized to opioid reward related functions

in the medial shell that includes a role for KOR system. While using different species and

behavioral model we report here a consistent heterogeneity within the NAc shell, where selective

photostimulation of the endogenous Dyn-containing cells in the dorsal NAc shell drives a

preference/reward behavior but photostimulation of Dyn neurons in the ventral shell drives an

aversion behavior. Further, a recent study has found that prodynorphin content specifically in the

ventral NAc shell is dramatically increased following 12 hour long access heroin self-

administration, and that escalation of this drug-seeking behavior was suppressed following

treatment with the long acting KOR antagonist NorBNI (Schlosburg et al., 2013). These recent

findings further support our present data, and suggest that the release of Dyn in distinct

subregions within the NAc shell drives opposing motivated behavioral states.

To discretely isolate these small subregions of the accumbens within a single animal, we

modified our original wireless, spatially-targeted μ-ILED devices (Kim et al., 2013; McCall et

al., 2013) to enable independent illumination of either the ventral or dorsal region of the NAc

within the same mouse. A device with these capabilities has not been previously used, but here

we generated a modified version of them to directly test the question of spatial segregation of

reward and aversion within the NAc shell. Here we adapted the connection and powering schemes of the μ-ILED devices to provide multiple channels of independent optical control. Using these devices we were able to drive a real-time aversion and reward behavior within the same mouse confirming that engaging Dyn neurons in these discrete regions mediates opposing behaviors. Importantly, we also found that stimulating these distinct regions does not mediate an anxiety-like behavior, consistent with previous reports that identify the basolateral amygdala and the central nucleus of the amygdala as the key KOR site involved in the mediation of anxiety-like behaviors (Bruchas et al., 2009; Knoll et al., 2011).

These μ-ILED devices could be easily modified for other potential uses, for example the μ-ILEDs can be differentially spaced and/or oriented to target different regions or subregions within the brain. Additional μ-ILEDs can be added to the device to target larger brain regions or multiple subregions in a dorsal-ventral axis, such as layers of the cortex, or other similar structures. μ-ILEDs of different wavelengths could also be added enabling photoactivation or inhibition of various opsin constructs within the same structure. The wireless capabilities also enable us to carry out optogenetic experiments within the home cage itself, which are more difficult using traditional fiber optic tethering.

Looking closely at the neurobiological sources of Dyn and KOR in the NAc, it is widely known that Dyn is predominantly expressed in medium spiny neurons within the NAc that coexpress dopamine D1 receptors (Ghazarossian et al., 1980; Raynor et al., 1994); however, there are also input projections from other structures that could also release Dyn, for example the ventral pallidum and the lateral hypothalamus (Baldo et al., 2003; Groenewegen et al., 1999; Haber et al., 1985; Peyron et al., 1998). It is reported that postsynaptic KOR in the NAc are on dendrites of most medium spiny neurons but reside predominantly on the dopamine D2

expressing medium spiny neurons (Svingos et al., 1999). KORs are also widely known to be expressed on presynaptic terminals of glutamate, serotonin and dopamine projections into the NAc (Bruchas et al., 2011; Hjelmstad and Fields, 2001; Land et al., 2009; Schindler et al., 2012; Svingos et al., 1999). In light of this we hypothesized that the Dyn-mediated aversion in the ventral NAc is driven by activation of KOR locally in the NAc. In both a conditioned place preference and an operant self-stimulation paradigm we show that NorBNI is able to block the aversion behavior following photostimulation of Dyn neurons in the ventral NAc shell, thereby identifying that aversion behavior in the ventral NAc is mediated by a local KOR dependent mechanism.

Photostimulation of Dyn-containing cells in the dorsal NAc drives a preference/reward behavior in all of the three paradigms. Interestingly, Berridge's group are the first to report positive rewarding effects for kappa activation but this was restricted to the rostrodorsal shell hotspot as all other areas produced negative effects (Castro and Berridge, 2014). They suggest that the anatomical specificity gates the valence of KOR effects in the NAc. Though this is certainly a consideration in the present study it is important to note that the Dyn-containing cells we are photostimulating also express dopamine D1 receptors so it is certainly likely that upon photostimulation we are in fact likely mimicking D1 receptor activation which would in turn induce a preference/reward behavior. In fact, optogenetic stimulation of the direct pathway, Dyn/Dopamine receptor-1 (D1-R) containing neurons in the dorsal striatum has been shown to be rewarding in several contexts (Kravitz et al., 2012). Here we have shown that we can produce the same behavior but by targeting a more discrete region dorsal NAc. Further investigation is warranted to identify whether the preference behavior is KOR-dependent or more likely consistent with the well-established D1 receptor mediated effect.

The key finding of the present study is that we have identified two distinct subregions within the NAc shell that drive opposing behavioral valences. The elegant work of Thompson and Swanson (2010) identified that within the NAc network nodes exist which are localized and restricted to specific subdivisions within a region, which is why regions such as the hedonic hotspot have been considered important (Thompson and Swanson, 2010). Furthermore, it is the distinct projections to and from these discrete regions that will help us to understand what is driving the unique behavioral outputs in this present study. To begin investigating these projections we will use a combination of the Dyn-reporter mouse (Dyn-Cre^{tdTomato}) generated and viral tracing approaches. We have characterized Dyn expression across the full brain of these mice, comparing our results with data freely available from the Allen Institute for Brain Science (Lein et al., 2007). This mouse line is useful for Cre-dependent expression/excision in selected Dyn-circuits, provides us with a new map of Dyn expressing cells, and a simple way to easily trace dynorphinergic axon projections and terminal fields.

Here we identified two distinct subregions within the NAc shell, which drive opposing behaviors through activation of the KOR/Dyn system. Photostimulation of Dyn-containing neurons in the ventral NAc shell causes a KOR dependent aversive behavior whereas photostimulation of Dyn-containing neurons in the dorsal NAc shell causes preference. Understanding the circuitry that mediate motivated behaviors is critical in furthering our understanding of positive and negative affective states that contribute to mood disorders, addiction and depression.

MATERIALS & METHODS

Experimental subjects

342

Adult (25–35 g) male preprodynorphin-IRES-Cre (Dyn-Cre) mice were group-housed, given access to food pellets and water *ad libitum* and maintained on a 12 h:12 h light:dark cycle (lights on at 7:00 AM). All animals were kept in a sound attenuated, isolated holding facility in the lab one week prior to surgery, post-surgery and throughout the duration of the behavioral assays to minimize stress. All procedures were approved by the Animal Care and Use Committee of Washington University and conformed to US National Institutes of Health guidelines.

Generation and breeding of Pdyn-IRES-Cre mice and Ai9-x Pdyn-IRES-Cre

Pdyn-IRES-Cre mice were kindly provided by Bradford Lowell's lab (Krashes et al., 2014) see for details. The mice were bred in our facilities by crossing the pdyn-IRES-Cre mice with C57BL/6 wildtype mice and backcrossed for seven generations. These mice were then crossed to Ai9-tdtomato mice on C57BL/6 background, bred and backcrossed for seven generations.

Stereotaxic viral injection surgery

After the animals were acclimatized to the holding facility for seven to nine days, the mice were anaesthetized in an induction chamber (4% Isoflurane) and placed into a stereotaxic frame (Kopf Instruments, Model 1900) where they were maintained at 1-2% isoflurane. We performed a craniotomy and unilaterally injected, using a blunt needle (86200, Hamilton Company, Reno, NV), 300 nl of AAV5-DIO-ChR2-eYFP or AAV5-DIO-eYFP (Hope Center Viral Vector Core, viral titre 2 x 10^13 vg/ml) into either the dorsal NAc (stereotaxic coordinates from bregma: +1.30 anterior-posterior (AP), +/−0.5 medial-lateral (ML), −4.25 mm dorsal-ventral (DV)) or ventral NAc (stereotaxic coordinates from bregma: +1.30 (AP), +/−0.5 (ML), −4.75 mm (DV), followed by fiber optic implantation (Sparta et al., 2012). We secured the

implants using two bone screws and constructed a chronic headcap using dental cement (Lang Dental, Wheeling, IL). Mice were allowed to recover for three weeks prior to behavioral testing, permitting optimal expression of ChR2 in the Dyn-Cre cell bodies.

NorBNI local Infusion: Two weeks post viral injection the mice were locally injected with NorBNI in the ventral NAc (2.5µg/1µl) (co-ordinates stated above) followed by the optic fiber implantation to allow optimal expression of both ChR2 and NorBNI. All mice were allowed at least one week to recover post surgery before beginning experimentation, well within the ideal limits of norBNI antagonism and ChR2 expression.

Slice electrophysiology

We performed whole-cell electrophysiology experiments similar to those published (Sparrow et al., 2012). Briefly, mice were rapidly decapitated under isoflurane anesthesia, and 300uM coronal slices containing the NAc were prepared on a vibratome (Leica VT1200). The brains were removed and placed in ice-cold modified high sucrose artificial cerebrospinal fluid (aCSF) (see supplemental experimental procedures for details). Slices were then transferred to normal aCSF (see supplemental experimental procedures for details) maintained at approximately 30 degrees (Warner Instruments, Hamden, Connecticut). Slices were placed in a holding chamber (Warner Instruments, Hamden, CT), and were allowed to rest for one hour, and remained there until used. Slices were continuously bubbled with a 95% O_2 / 5% CO_2 mixture throughout slicing and experiments. Thin-walled borosilicate glass capillary recording electrodes (3–6 MΩ) were pulled on a Flaming-Brown Micropipette Puller (Sutter Instruments). Following rupture of the cell membrane, cells were allowed to rest and equilibrate to the intracellular

344

recording solutions (below). Input resistance was monitored continuously throughout the experiment, and when input resistance deviated by more than 20% the experiment was discarded.

All brains were checked for light-evoked action potentials in the NAc using a potassium-gluconate based internal (see supplemental experimental procedures for details). Those brains in which action potentials were not obtained or injections were missed were discarded and not used for further experimentation. Action potentials were light evoked (1msec stimulation) at frequencies from 5-40 Hz to check spike fidelity of light-evoked responses.

Real-time Place Testing

We used custom-made unbiased, balanced two-compartment conditioning apparatus (52.5 x 25.5 x 25.5 cm) as described previously (Jennings et al., 2013; Stamatakis and Stuber, 2012). Mice were allowed to freely roam the entire apparatus for 20 min. Entry into one compartment triggered constant photostimulation at either 5Hz, 10Hz, 20Hz or 40Hz (473 nm, 10 ms pulse width, ~10 mW light power) while the animal remained in the light-paired chamber. Entry into the other chamber ended the photostimulation. The side paired with photostimulation was counterbalanced across mice. Time spent in each chamber and total distance traveled for the entire 20-minute trial was measured using Ethovision 8.5 (Noldus Information Technologies, Leesburg, VA).

Wireless Powering and RF Powering Scavenger

Wireless powering of the μ-ILED devices was adapted as previously described (Kim et al., 2013; McCall et al., 2013) The RF scavenger consists of antennas, impedance matching circuits and Cockcroft-Walton voltage multiplier. The wireless power transmitter includes an RF signal generator (Agilent N5181A), a power supply (Agilent U8031A), a RF power amplifier

(Empower RF Systems 1119-BBM3K5KHM), an RF signal splitter (RF Lambda RFLT2W0727GN), and two panel antennas (ARC Wireless ARC-PA2419B01). The RF signal generator is internally modulated to delivery sufficient power to light the μ-ILEDs at the given stimulation protocol (10 Hz, 50 ms pulse widths). The RF power amplifier that is powered by the power supply enlarges the modulated RF signal from the RF signal generator. The RF power is then transmitted from the panel antenna to the headstage power harvesters. The RF signal generator has a power output from -10 to 0 dBm at 1.5 GHz & 2.4 GHz for each LEDs, optimized daily to ensure equivalent light power throughout the space of the LDB assay. Mice with chronically implanted μ-ILED devices were acutely connected to the headstage power harvesters immediately prior to any wireless photostimulation.

Y-Maze Conditioned Place Testing

Mice were placed in a 3-chambered environment compatible with fiber-optics coupled to 473 nm laser as previous described (Kim et al., 2013). Initially, on day one the mice have free access to all chambers without stimulation (pre-test) to show no bias between the 2 larger, cue-distinct environments. This is followed by three conditioning days where upon entry into one chamber photostimulation (10 Hz, 10 ms pulse width) occurs in real-time and when the animal leaves this compartment photostimulation ends. On post-test day 5 mice have free access to all chambers without stimulation to assess whether a preference or aversion association has been made with the paired context. Data were calculated as time spent in each chamber and entries into the photostimulation- paired chamber with control animals showing equal time spent in each chamber and an aversive response being time reduced from 50%.

Operant Self-Stimulation

Mice are initially food deprived to 90% of their body weight and trained to nose-poke for food pellets for 4 days in a modular test chamber for mice (17.8 cm x 15.2 cm x 18.4 cm) (Med Associates Inc., St. Albans, VT). This was used in conjunction with either Ethovision (Noldus, Leesburg, VA) or Med Associates program. This was followed by operant self-stimulation where upon an active nose poke the mice receive a 2 second photo-stimulation (10 Hz, 10 ms pulse width stimulation) on a fixed ratio-1 schedule for a 1 hour session. For operant self-stimulation the mice are connected to a laser via a tether than runs through the top of the chamber. An Arduino (Arduino, http://www.arduino.cc) is programed and connected to the laser and chamber so upon nose poking the 2 second 10 Hz, 10 ms pulse width photostimulation is administered. This was paired with a cue light and a tone. A poke at the inactive nose poke resulted in no stimulation, cue light or tone. The data were calculated as total number of nosepokes at the active and inactive for each day over the course of 5 days.

For all behavioral experiments at the end of each study, animals were perfused with 4% paraformaldehyde followed by anatomical analysis to confirm injection sites and cell type-specific expression.

Statistics

All data are expressed as mean ± SEM. Statistical significance was taken as $*p < 0.05$, $**p < 0.01$, $***p < 0.001$, $****p < 0.0001$ as determined by a One-Way Analysis of Variance (ANOVA) or a Two-Way Repeated Measures ANOVA followed by a Bonferroni *post hoc* tests as appropriate. Statistical analyses were performed in GraphPad Prism 5.0.

REFERENCES

Baldo, B.A., Daniel, R.A., Berridge, C.W., and Kelley, A.E. (2003). Overlapping distributions of orexin/hypocretin- and dopamine-beta-hydroxylase immunoreactive fibers in rat brain regions mediating arousal, motivation, and stress. J. Comp. Neurol. *464*, 220–237.

Bals-Kubik, R., Herz, A., and Shippenberg, T.S. (1989). Evidence that the aversive effects of opioid antagonists and kappa-agonists are centrally mediated. Psychopharmacology (Berl.) *98*, 203–206.

Van Bockstaele, E.J., Gracy, K.N., and Pickel, V.M. (1995). Dynorphin-immunoreactive neurons in the rat nucleus accumbens: ultrastructure and synaptic input from terminals containing substance P and/or dynorphin. J. Comp. Neurol. *351*, 117–133.

Britton, D.R., Koob, G.F., Rivier, J., and Vale, W. (1982). Intraventricular corticotropin-releasing factor enhances behavioral effects of novelty. Life Sci. *31*, 363–367.

Bruchas, M.R., Land, B.B., Aita, M., Xu, M., Barot, S.K., Li, S., and Chavkin, C. (2007). Stress-induced p38 mitogen-activated protein kinase activation mediates kappa-opioid-dependent dysphoria. J. Neurosci. Off. J. Soc. Neurosci. *27*, 11614–11623.

Bruchas, M.R., Land, B.B., Lemos, J.C., and Chavkin, C. (2009). CRF1-R activation of the dynorphin/kappa opioid system in the mouse basolateral amygdala mediates anxiety-like behavior. PloS One *4*, e8528.

Bruchas, M.R., Land, B.B., and Chavkin, C. (2010). The dynorphin/kappa opioid system as a modulator of stress-induced and pro-addictive behaviors. Brain Res. *1314*, 44–55.

Bruchas, M.R., Schindler, A.G., Shankar, H., Messinger, D.I., Miyatake, M., Land, B.B., Lemos, J.C., Hagan, C.E., Neumaier, J.F., Quintana, A., et al. (2011). Selective p38α MAPK deletion in serotonergic neurons produces stress resilience in models of depression and addiction. Neuron *71*, 498–511.

Carter, M.E., Yizhar, O., Chikahisa, S., Nguyen, H., Adamantidis, A., Nishino, S., Deisseroth, K., and de Lecea, L. (2010). Tuning arousal with optogenetic modulation of locus coeruleus neurons. Nat. Neurosci. *13*, 1526–1533.

Castro, D.C., and Berridge, K.C. (2014). Opioid hedonic hotspot in nucleus accumbens shell: mu, delta, and kappa maps for enhancement of sweetness "liking" and "wanting." J. Neurosci. Off. J. Soc. Neurosci. *34*, 4239–4250.

Chavkin, C., James, I.F., and Goldstein, A. (1982). Dynorphin is a specific endogenous ligand of the kappa opioid receptor. Science *215*, 413–415.

Daunais, J.B., Roberts, D.C., and McGinty, J.F. (1993). Cocaine self-administration increases preprodynorphin, but not c-fos, mRNA in rat striatum. Neuroreport *4*, 543–546.

Drevets, W.C., Videen, T.O., Price, J.L., Preskorn, S.H., Carmichael, S.T., and Raichle, M.E. (1992). A functional anatomical study of unipolar depression. J. Neurosci. Off. J. Soc. Neurosci. *12*, 3628–3641.

Everitt, B.J., and Robbins, T.W. (2005). Neural systems of reinforcement for drug addiction: from actions to habits to compulsion. Nat. Neurosci. *8*, 1481–1489.

Fagergren, P., Smith, H.R., Daunais, J.B., Nader, M.A., Porrino, L.J., and Hurd, Y.L. (2003). Temporal upregulation of prodynorphin mRNA in the primate striatum after cocaine self-administration. Eur. J. Neurosci. *17*, 2212–2218.

Ghazarossian, V.E., Chavkin, C., and Goldstein, A. (1980). A specific radioimmunoassay for the novel opioid peptide dynorphin. Life Sci. *27*, 75–86.

Groenewegen, H.J., Wright, C.I., Beijer, A.V., and Voorn, P. (1999). Convergence and segregation of ventral striatal inputs and outputs. Ann. N. Y. Acad. Sci. *877*, 49–63.

Haber, S.N., Groenewegen, H.J., Grove, E.A., and Nauta, W.J. (1985). Efferent connections of the ventral pallidum: evidence of a dual striato pallidofugal pathway. J. Comp. Neurol. *235*, 322–335.

Al-Hasani, R., McCall, J.G., Foshage, A.M., and Bruchas, M.R. (2013). Locus Coeruleus Kappa Opioid Receptors modulate Reinstatement of Cocaine Place Preference through a Noradrenergic Mechanism. Neuropsychopharmacol. Off. Publ. Am. Coll. Neuropsychopharmacol.

Hjelmstad, G.O., and Fields, H.L. (2001). Kappa opioid receptor inhibition of glutamatergic transmission in the nucleus accumbens shell. J. Neurophysiol. *85*, 1153–1158.

Hurd, Y.L., Brown, E.E., Finlay, J.M., Fibiger, H.C., and Gerfen, C.R. (1992). Cocaine self-administration differentially alters mRNA expression of striatal peptides. Brain Res. Mol. Brain Res. *13*, 165–170.

Jennings, J.H., Sparta, D.R., Stamatakis, A.M., Ung, R.L., Pleil, K.E., Kash, T.L., and Stuber, G.D. (2013). Distinct extended amygdala circuits for divergent motivational states. Nature *496*, 224–228.

Kim, T., McCall, J.G., Jung, Y.H., Huang, X., Siuda, E.R., Li, Y., Song, J., Song, Y.M., Pao, H.A., Kim, R.-H., et al. (2013). Injectable, cellular-scale optoelectronics with applications for wireless optogenetics. Science *340*, 211–216.

Knoll, A.T., Muschamp, J.W., Sillivan, S.E., Ferguson, D., Dietz, D.M., Meloni, E.G., Carroll, F.I., Nestler, E.J., Konradi, C., and Carlezon, W.A., Jr (2011). Kappa opioid receptor signaling in the basolateral amygdala regulates conditioned fear and anxiety in rats. Biol. Psychiatry *70*, 425–433.

Krashes, M.J., Shah, B.P., Madara, J.C., Olson, D.P., Strochlic, D.E., Garfield, A.S., Vong, L., Pei, H., Watabe-Uchida, M., Uchida, N., et al. (2014). An excitatory paraventricular nucleus to AgRP neuron circuit that drives hunger. Nature *507*, 238–242.

Kravitz, A.V., Tye, L.D., and Kreitzer, A.C. (2012). Distinct roles for direct and indirect pathway striatal neurons in reinforcement. Nat. Neurosci. *15*, 816–818.

Land, B.B., Bruchas, M.R., Schattauer, S., Giardino, W.J., Aita, M., Messinger, D., Hnasko, T.S., Palmiter, R.D., and Chavkin, C. (2009). Activation of the kappa opioid receptor in the dorsal raphe nucleus mediates the aversive effects of stress and reinstates drug seeking. Proc. Natl. Acad. Sci. U. S. A. *106*, 19168–19173.

Lein, E.S., Hawrylycz, M.J., Ao, N., Ayres, M., Bensinger, A., Bernard, A., Boe, A.F., Boguski, M.S., Brockway, K.S., Byrnes, E.J., et al. (2007). Genome-wide atlas of gene expression in the adult mouse brain. Nature *445*, 168–176.

Lindholm, S., Ploj, K., Franck, J., and Nylander, I. (2000). Repeated ethanol administration induces short- and long-term changes in enkephalin and dynorphin tissue concentrations in rat brain. Alcohol Fayettev. N *22*, 165–171.

Madisen, L., Zwingman, T.A., Sunkin, S.M., Oh, S.W., Zariwala, H.A., Gu, H., Ng, L.L., Palmiter, R.D., Hawrylycz, M.J., Jones, A.R., et al. (2010). A robust and high-throughput Cre reporting and characterization system for the whole mouse brain. Nat. Neurosci. *13*, 133–140.

Mayberg, H.S., Brannan, S.K., Tekell, J.L., Silva, J.A., Mahurin, R.K., McGinnis, S., and Jerabek, P.A. (2000). Regional metabolic effects of fluoxetine in major depression: serial changes and relationship to clinical response. Biol. Psychiatry *48*, 830–843.

McCall, J.G., Kim, T., Shin, G., Huang, X., Jung, Y.H., Al-Hasani, R., Omenetto, F.G., Bruchas, M.R., and Rogers, J.A. (2013). Fabrication and application of flexible, multimodal light-emitting devices for wireless optogenetics. Nat. Protoc. *8*, 2413–2428.

Melief, E.J., Miyatake, M., Bruchas, M.R., and Chavkin, C. (2010). Ligand-directed c-Jun N-terminal kinase activation disrupts opioid receptor signaling. Proc. Natl. Acad. Sci. U. S. A. *107*, 11608–11613.

Mucha, R.F., Millan, M.J., and Herz, A. (1985). Aversive properties of naloxone in non-dependent (naive) rats may involve blockade of central beta-endorphin. Psychopharmacology (Berl.) *86*, 281–285.

Nestler, E.J., and Carlezon, W.A., Jr (2006). The mesolimbic dopamine reward circuit in depression. Biol. Psychiatry *59*, 1151–1159.

Peyron, C., Tighe, D.K., van den Pol, A.N., de Lecea, L., Heller, H.C., Sutcliffe, J.G., and Kilduff, T.S. (1998). Neurons containing hypocretin (orexin) project to multiple neuronal systems. J. Neurosci. Off. J. Soc. Neurosci. *18*, 9996–10015.

Pfeiffer, A., Brantl, V., Herz, A., and Emrich, H.M. (1986). Psychotomimesis mediated by kappa opiate receptors. Science *233*, 774–776.

Raynor, K., Kong, H., Chen, Y., Yasuda, K., Yu, L., Bell, G.I., and Reisine, T. (1994). Pharmacological characterization of the cloned kappa-, delta-, and mu-opioid receptors. Mol. Pharmacol. *45*, 330–334.

Russo, S.J., and Nestler, E.J. (2013). The brain reward circuitry in mood disorders. Nat. Rev. Neurosci. *14*, 609–625.

Rylkova, D., Shah, H.P., Small, E., and Bruijnzeel, A.W. (2009). Deficit in brain reward function and acute and protracted anxiety-like behavior after discontinuation of a chronic alcohol liquid diet in rats. Psychopharmacology (Berl.) *203*, 629–640.

Schindler, A.G., Messinger, D.I., Smith, J.S., Shankar, H., Gustin, R.M., Schattauer, S.S., Lemos, J.C., Chavkin, N.W., Hagan, C.E., Neumaier, J.F., et al. (2012). Stress produces aversion and potentiates cocaine reward by releasing endogenous dynorphins in the ventral striatum to locally stimulate serotonin reuptake. J. Neurosci. Off. J. Soc. Neurosci. *32*, 17582–17596.

Schlosburg, J.E., Whitfield, T.W., Jr, Park, P.E., Crawford, E.F., George, O., Vendruscolo, L.F., and Koob, G.F. (2013). Long-term antagonism of κ opioid receptors prevents escalation of and increased motivation for heroin intake. J. Neurosci. Off. J. Soc. Neurosci. *33*, 19384–19392.

Schlussman, S.D., Zhou, Y., Bailey, A., Ho, A., and Kreek, M.J. (2005). Steady-dose and escalating-dose "binge" administration of cocaine alter expression of behavioral stereotypy and striatal preprodynorphin mRNA levels in rats. Brain Res. Bull. *67*, 169–175.

Shippenberg, T.S., Zapata, A., and Chefer, V.I. (2007). Dynorphin and the pathophysiology of drug addiction. Pharmacol. Ther. *116*, 306–321.

Shirayama, Y., Ishida, H., Iwata, M., Hazama, G.-I., Kawahara, R., and Duman, R.S. (2004). Stress increases dynorphin immunoreactivity in limbic brain regions and dynorphin antagonism produces antidepressant-like effects. J. Neurochem. *90*, 1258–1268.

Solecki, W., Turek, A., Kubik, J., and Przewlocki, R. (2009). Motivational effects of opiates in conditioned place preference and aversion paradigm--a study in three inbred strains of mice. Psychopharmacol. Berl *207*, 245–255.

Sparrow, A.M., Lowery-Gionta, E.G., Pleil, K.E., Li, C., Sprow, G.M., Cox, B.R., Rinker, J.A., Jijon, A.M., Peňa, J., Navarro, M., et al. (2012). Central neuropeptide Y modulates binge-like

ethanol drinking in C57BL/6J mice via Y1 and Y2 receptors. Neuropsychopharmacol. Off. Publ. Am. Coll. Neuropsychopharmacol. *37*, 1409–1421.

Sparta, D.R., Stamatakis, A.M., Phillips, J.L., Hovelsø, N., van Zessen, R., and Stuber, G.D. (2012). Construction of implantable optical fibers for long-term optogenetic manipulation of neural circuits. Nat. Protoc. *7*, 12–23.

Stamatakis, A.M., and Stuber, G.D. (2012). Activation of lateral habenula inputs to the ventral midbrain promotes behavioral avoidance. Nat. Neurosci. *15*, 1105–1107.

Svingos, A.L., Colago, E.E., and Pickel, V.M. (1999). Cellular sites for dynorphin activation of kappa-opioid receptors in the rat nucleus accumbens shell. J. Neurosci. Off. J. Soc. Neurosci. *19*, 1804–1813.

Tan, K.R., Yvon, C., Turiault, M., Mirzabekov, J.J., Doehner, J., Labouèbe, G., Deisseroth, K., Tye, K.M., and Lüscher, C. (2012). GABA neurons of the VTA drive conditioned place aversion. Neuron *73*, 1173–1183.

Thompson, R.H., and Swanson, L.W. (2010). Hypothesis-driven structural connectivity analysis supports network over hierarchical model of brain architecture. Proc. Natl. Acad. Sci. U. S. A. *107*, 15235–15239.

Appendix 2

Supplementary locus coeruleus experiments

SUMMARY

Stress-induced anxiety and aversion represents only a subset of known behavioral responses to stress (Bruchas et al., 2011a; Butler and Finn, 2009; Weninger et al., 1999). Several stress-induced behaviors are known to be influenced or mediated by NE, including stress-induced relapse to drug seeking (Weinshenker and Schroeder, 2007) and stress-induced analgesia (Butler and Finn, 2009). Exploring the possibility of these behaviors being mediated by LC efferent projections is a compelling next step. This appendix contains two sets of preliminary data evoking a high tonic (5 Hz) state of LC. In all cases the LC is targeting using *Th*-Cre mice and AAV5-EF1α-DIO-ChR2-EYFP. The controls are AAV5-EF1α-DIO-EYFP The first is a study of reinstatement of a cocaine conditioned place preference, the second is battery pain-related assays.

Potential role of LC-NE neurons in reinstatement of cocaine place preference

Mice were trained in an unbiased, balanced three-compartment conditioning apparatus as described (Land et al., 2009; Bruchas et al., 2011). On pre-conditioning day, day 1, mice were allowed free access to all three chambers for 30 min. Time spent in each compartment was recorded with a video camera (ZR90; Canon) and analyzed using Ethovision 8.5 (Noldus). Mice were randomly assigned to saline and drug compartments and received a saline injection in the morning (10 ml/kg, s.c.) and a cocaine injection (15 mg/kg, s.c.) in the afternoon, at least 4 h after the morning training on 3 consecutive days (days 2-4). To test for cocaine place preference (day 5) the mice were allowed free access to the three chambers. Scores were calculated by subtracting the time spent in the drug-paired compartment post-test minus the pre-test. This was followed by 3 days of extinction training (days 6–8) during which saline (10 ml/kg, s.c.) was

injected in both the morning and afternoon prior to placement into isolated conditioning compartments. Mice were tested for extinction of place preference on day 9 with free access to all three chambers. Mice were considered to have extinguished cocaine preference if scores fell within 15% of their initial preference scores. Mice that did not meet these criteria were excluded from the study. Mice that extinguished continued on to the reinstatement phase. On day 10, mice were exposed to five minutes of 5 Hz, 10 ms photostimulation.

Reinstatement was measured as time (s) in drug-paired chamber on day 10 minus time spent in drug-paired chamber following extinction training. Mice that did not reinstate to photostimulation were exposed on the following day to a priming injection of cocaine (15 mg/kg, s.c.) and placed in the apparatus and allowed free access to all compartments (data not shown). Reinstatement scores were calculated by subtracting the time spent in the cocaine side post-test minus the extinction test as previously described (Bruchas et al., 2011, Land et al, 2009).
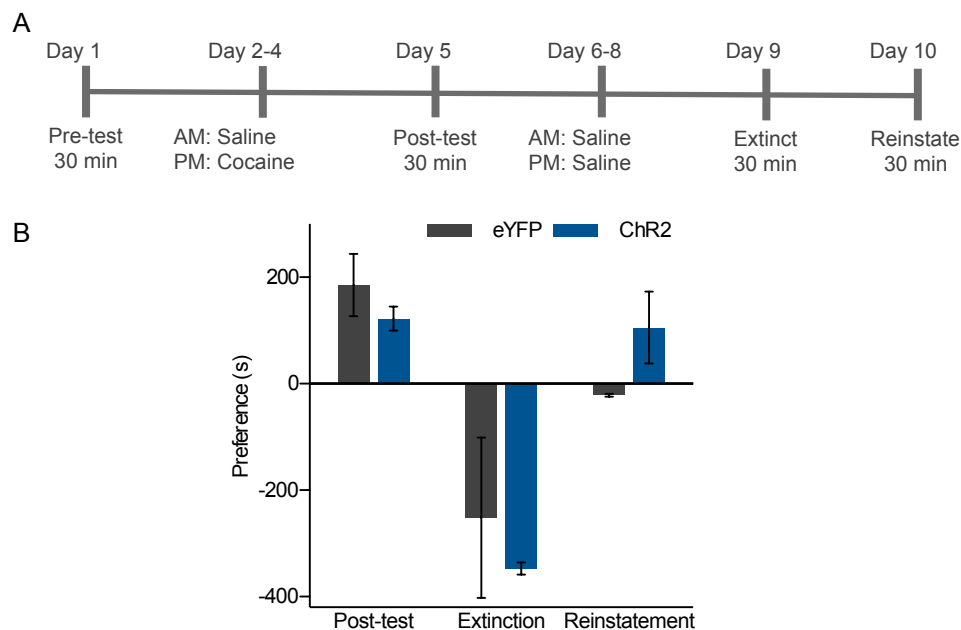
Figure A2.1 Potential role of LC-NE neurons in reinstatement of cocaine place preference.
(**A**) Time line of CPP/reinstatement experiment (**B**) Data represent the mean preference (s) ±
SEM, n=4/group. All included animals reached extinction criteria on Day 9 and received 5
minutes of 5 Hz stimulation prior to post-test on Day 10.

High tonic LC-NE activity is antinociceptive

Plantar test (Hargreaves Method)

Mice were acclimated to a 30ºC glass platform for two hours prior to testing. Radiant
heat was applied to each hindpaw and withdrawal latency was measured over 5 trials (15 min
ITI). Conditions were counterbalanced to get baseline withdrawal latency for each mouse. 5 Hz
photostimulation began 5 s before the first trial.

Hot plate test

Mice were habituated to the testing room for two hours prior to testing. The hot plate was
heated to 55ºC. 5 s before the trial, 5 Hz photostimulation began. The animal was placed on the
hot plate and a timer started. Time ended with any of the following behaviors: animal lifts
hindpaw and clearly licks, animal jumps off plate, or timer reaches 30 s. Only one trial per
animal was recorded.

Von Frey test

Calibrated Von Frey filaments were used to assess formalin-induced mechanical
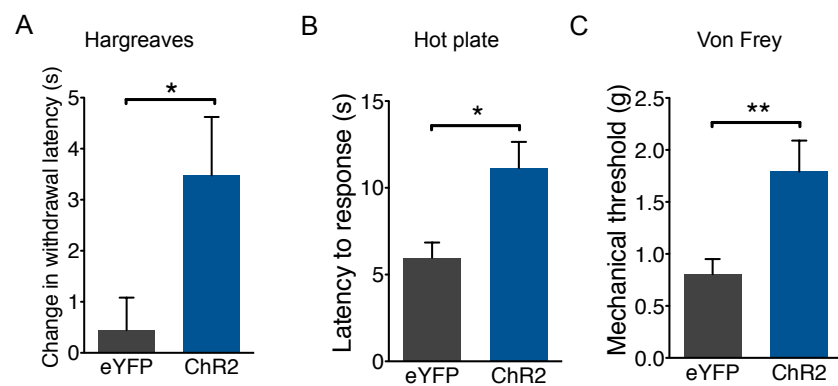hypersensitivity as previously described (Kolber et al., 2010).

eYFP   ChR2

Preference (s)

A Hargreaves   B Hot plate   C Von Frey

Figure A2.2 High tonic LC-NE activity is antinocieptive. 5 Hz stimulation blunts thermal nociception in the (**A**) plantar and (**B**) hot plate tests. 5 Hz stimulation of LC-NE cell bodies reverse mechanical hypersensitivity in (**C**) the Von Frey test. Data shown as mean +/- SEM. n=6/group. **p<0.01, *p<0.05 Student's t-test.

REFERENCES

Bruchas, M.R., Schindler, A.G., Shankar, H., Messinger, D.I., Miyatake, M., Land, B.B., Lemos, J.C., Hagan, C.E., Neumaier, J.F., Quintana, A., et al. (2011a). Selective p38α MAPK deletion in serotonergic neurons produces stress resilience in models of depression and addiction. Neuron *71*, 498–511.

Bruchas, M.R., Schindler, A.G., Shankar, H., Messinger, D.I., Miyatake, M., Land, B.B., Lemos, J.C., Hagan, C.E., Neumaier, J.F., Quintana, A., et al. (2011b). Selective p38α MAPK deletion in serotonergic neurons produces stress resilience in models of depression and addiction. Neuron *71*, 498–511.

Butler, R.K., and Finn, D.P. (2009). Stress-induced analgesia. Prog. Neurobiol. *88*, 184–202.

Kolber, B.J., Montana, M.C., Carrasquillo, Y., Xu, J., Heinemann, S.F., Muglia, L.J., and Gereau, R.W. (2010). Activation of metabotropic glutamate receptor 5 in the amygdala modulates pain-like behavior. J. Neurosci. Off. J. Soc. Neurosci. *30,* 8203–8213.

Land, B.B., Bruchas, M.R., Schattauer, S., Giardino, W.J., Aita, M., Messinger, D., Hnasko, T.S., Palmiter, R.D., and Chavkin, C. (2009). Activation of the kappa opioid receptor in the dorsal raphe nucleus mediates the aversive effects of stress and reinstates drug seeking. Proc. Natl. Acad. Sci. U. S. A. *106,* 19168–19173.

Weinshenker, D., and Schroeder, J.P. (2007). There and back again: a tale of norepinephrine and drug addiction. Neuropsychopharmacol. Off. Publ. Am. Coll. Neuropsychopharmacol. *32*, 1433–1451.

Weninger, S.C., Dunn, A.J., Muglia, L.J., Dikkes, P., Miczek, K.A., Swiergiel, A.H., Berridge, C.W., and Majzoub, J.A. (1999). Stress-induced behaviors require the corticotropin-releasing hormone (CRH) receptor, but not CRH. Proc. Natl. Acad. Sci. *96*, 8283–8288.